Biomaterials Science

ROYAL SOCIETY OF CHEMISTRY

REVIEW

View Article Online
View Journal | View Issue

Cite this: *Biomater. Sci.*, 2025, **13**, 9

Hijacking plant skeletons for biomedical applications: from regenerative medicine and drug delivery to biosensing

Elham Asadian,[a,b] Samin Abbaszadeh,[c] Fatemeh Ghorbani-Bidkorpeh,[d] Saman Rezaei,[c] Bo Xiao,*[e] Hélder A. Santos *[f,g] and Mohammad-Ali Shahbazi *[f]

The field of biomedical engineering continually seeks innovative technologies to address complex healthcare challenges, ranging from tissue regeneration to drug delivery and biosensing. Plant skeletons offer promising opportunities for these applications due to their unique hierarchical structures, desirable porosity, inherent biocompatibility, and adjustable mechanical properties. This review comprehensively discusses chemical principles underlying the utilization of plant-based scaffolds in biomedical engineering. Highlighting their structural integrity, tunable properties, and possibility of chemical modification, the review explores diverse preparation strategies to tailor plant skeleton properties for bone, neural, cardiovascular, skeletal muscle, and tendon tissue engineering. Such applications stem from the cellulosic three-dimensional structure of different parts of plants, which can mimic the complexity of native tissues and extracellular matrices, providing an ideal environment for cell adhesion, proliferation, and differentiation. We also discuss the application of plant skeletons as carriers for drug delivery due to their structural diversity and versatility in encapsulating and releasing therapeutic agents with controlled kinetics. Furthermore, we present the emerging role played by plant-derived materials in biosensor development for diagnostic and monitoring purposes. Challenges and future directions in the field are also discussed, offering insights into the opportunities for future translation of sustainable plant-based technologies to address critical healthcare needs.

Received 24th July 2024,
Accepted 5th October 2024

DOI: 10.1039/d4bm00982g

rsc.li/biomaterials-science

1. Introduction

In recent years, there has been growing interest in exploring plant skeletons as potential candidates for biomedical applications. Plant skeletons, with their diverse and complex hierarchical structures, composed primarily of cellulose, hemicellulose, and lignin, are biocompatible platforms that possess adjustable mechanical properties and sustainability. The biomimicking structures found in various parts of plants, including stems, leaves, and fruits, have captured the attention of researchers seeking novel biomaterials for a wide range of biomedical applications, including tissue engineering, drug delivery, medical biosensing, and beyond.

Since their inception, tissue engineering and regenerative medicine have witnessed a remarkable evolution driven by the continuous pursuit of innovative solutions for tissue repair and regeneration. This dynamic field has continuously pushed the boundaries of scientific understanding and technological advancement to address the pressing need for effective therapies to treat injuries and diseases that impair tissue function.[1] Historically, the field gained momentum with the introduction of 3D cell culture media, which enabled researchers to mimic the complexity of native tissue microenvironments more accurately. This shift was necessitated by the inherent limitations of traditional 2D cell culture methods, which fail to recapitulate the three-dimensional architecture and cellular interactions present *in vivo*.[2,3] Concurrently, the utilization of acel-

[a]*Medical Nanotechnology and Tissue Engineering Research Center, Shahid Beheshti University of Medical Sciences, 19689-17313 Tehran, Iran*
[b]*Department of Tissue Engineering and Applied Cell Sciences, School of Advanced Technologies in Medicine, Shahid Beheshti University of Medical Sciences, 19689-17313 Tehran, Iran*
[c]*Department of Pharmacology and Toxicology, School of Pharmacy, Urmia University of Medical Sciences, Urmia, Iran*
[d]*Department of Pharmaceutics and Pharmaceutical Nanotechnology, School of Pharmacy, Shahid Beheshti University of Medical Sciences, Tehran, Iran*
[e]*Personalized Drug Therapy Key Laboratory of Sichuan Province, Department of Pharmacy, Sichuan Provincial People's Hospital, University of Electronic Science and Technology of China, Chengdu 610072, China. E-mail: bxiao@uestc.edu.cn*
[f]*Department of Biomaterials and Biomedical Technology, The Personalized Medicine Research Institute (PRECISION), University Medical Center Groningen, University of Groningen, Antonius Deusinglaan 1, 9713 AV Groningen, Netherlands. E-mail: m.a.shahbazi@umcg.nl*
[g]*Drug Research Program, Division of Pharmaceutical Chemistry and Technology, University of Helsinki, Helsinki FI-00014, Finland. E-mail: h.a.santos@umcg.nl*

lular scaffolds emerged as a promising strategy, providing structural support and biochemical cues for cell adhesion and proliferation. Even though the extracellular matrix (ECM) microstructure of decellularized tissues/organs is pivotal in guiding cell behaviour and directing cellular responses, several associated limitations such as donor tissue availability, variability in scaffold bioactivity, ethical considerations surrounding tissue sourcing, procedural costs, and risks of inflammatory responses have prompted investigations into novel scaffold materials and fabrication techniques. In this respect, one of the alternative approaches that has gained attention in the past few years is the utilization of biomimetic scaffolds.

As Paracelsus famously quoted: "*The art of healing comes from nature, not from the physician. Therefore, the physician must start from nature, with an open mind*". This philosophy has inspired scientists to explore the concept of utilizing "Natural Biotemplates" as potential scaffold materials.[4] In recent years, plant-derived skeletons have emerged as new game changers in regenerative medicine, presenting a paradigm shift in the field. Within this framework, the plant kingdom offers numerous advantages as a sustainable and renewable option. The hierarchical structure of plant tissues provides a natural framework with exquisite anisotropy that mimics the complexity of native tissues, facilitating cellular adhesion, proliferation, and differentiation. In addition, leaves exhibit a sophisticated network of natural vasculature and wood possesses a multiscale porosity ranging from nano to micro levels, creating an intricate fluidic transport system that enables the effective exchange of nutrients, oxygen, and metabolic waste products. This inherent capability of plant-derived scaffolds to support dynamic fluidic processes enhances tissue viability and functionality in engineered constructs. Moreover, the abundance and diversity of plant species enable the selection of materials with tailored mechanical properties, ranging from flexible and elastomeric properties found in leaves to rigid and load-bearing characteristics inherent in wood. Additionally, plant-derived scaffolds boast inherent biocompatibility, biodegradability, and low immunogenicity, minimizing adverse reactions and promoting tissue integration. Furthermore, the renewable and sustainable nature of plant resources ensures a reliable and environmentally friendly supply chain, addressing concerns regarding scalability and ecological impact. Harnessing the array of these appealing properties, plant-based skeletons represent a promising avenue for advancing the field of tissue engineering and regenerative medicine towards more efficient and sustainable solutions.[5–7]

In addition to tissue engineering, the versatility of plant-derived materials has led to their exploration in drug delivery systems, where they can serve as carriers for therapeutic agents, ensuring targeted and controlled release.[8,9] Furthermore, the presence of enzymes and other biomolecules within plant structures has sparked interest in utilizing these materials for biosensing applications, enabling the development of sensitive and selective detection platforms for various analytes. The hierarchical structure and large surface area of plant-derived materials facilitate efficient analyte capture and signal transduction, leading to enhanced sensor performance.[10,11]

The purpose of the present review is to explore the potential applicability and expanding utilization of plant-derived scaffolds in revolutionizing biomedical technologies. Our review focuses on various preparation protocols, including decellularization and delignification processes, through which plant-based constructs become prepared for further functionalization and implantation *in vivo*. The subsequent section discusses the extent and success of these treatments, which should be monitored *via* various characterization techniques. Following this, various functionalization methods, including chemical functionalization and physical coating, will be explored to further modify the physicochemical properties of the prepared scaffolds, rendering them suitable for use as scaffolds in bone, neural, cardiovascular, skeletal muscle, and tendon tissue regeneration. The final part of the review will provide an overview of the applications of plant-derived platforms in the design and construction of biosensors. All of these components are schematically outlined in Scheme 1.

2. Advantages of plant-based scaffolds in medicine

Plant-based scaffolds offer several advantages for biomedical application, making them a valuable resource in the field: (i) *Biocompatibility*: Plant-based materials generally exhibit excellent compatibility, meaning they can integrate well with human tissues, minimizing adverse immune reactions. This makes them ideal for supporting the growth and development of new tissues in regenerative medicine; (ii) *Biodegradability*: These scaffolds naturally decompose within the body as new tissues form, eliminating the need for invasive surgical removal and reducing the risk of long-term complications; (iii) *Mechanical properties*: Plant-derived scaffolds can be engineered to mimic the mechanical properties of natural tissues, providing the necessary support while maintaining flexibility and durability; (iv) *Porous structure*: The inherent porous structure of plant materials facilitates cell infiltration, nutrient diffusion, and waste removal, which are critical for tissue regeneration; (v) *Chemical functionalization*: Plant-based scaffolds can be easily modified with functional groups to enhance cell attachment, proliferation, and differentiation, further supporting tissue engineering goals; and (vi) *Sustainability and availability*: Plant materials are abundant, renewable, and often more cost-effective compared with synthetic or animal-derived alternatives, making them an attractive option for eco-friendly and sustainable development in tissue engineering. Due to the above benefits, the usage of plant skeleton is a hot topic and many research studies have focused on optimal isolation of plant skeleton, and are described in the coming section.

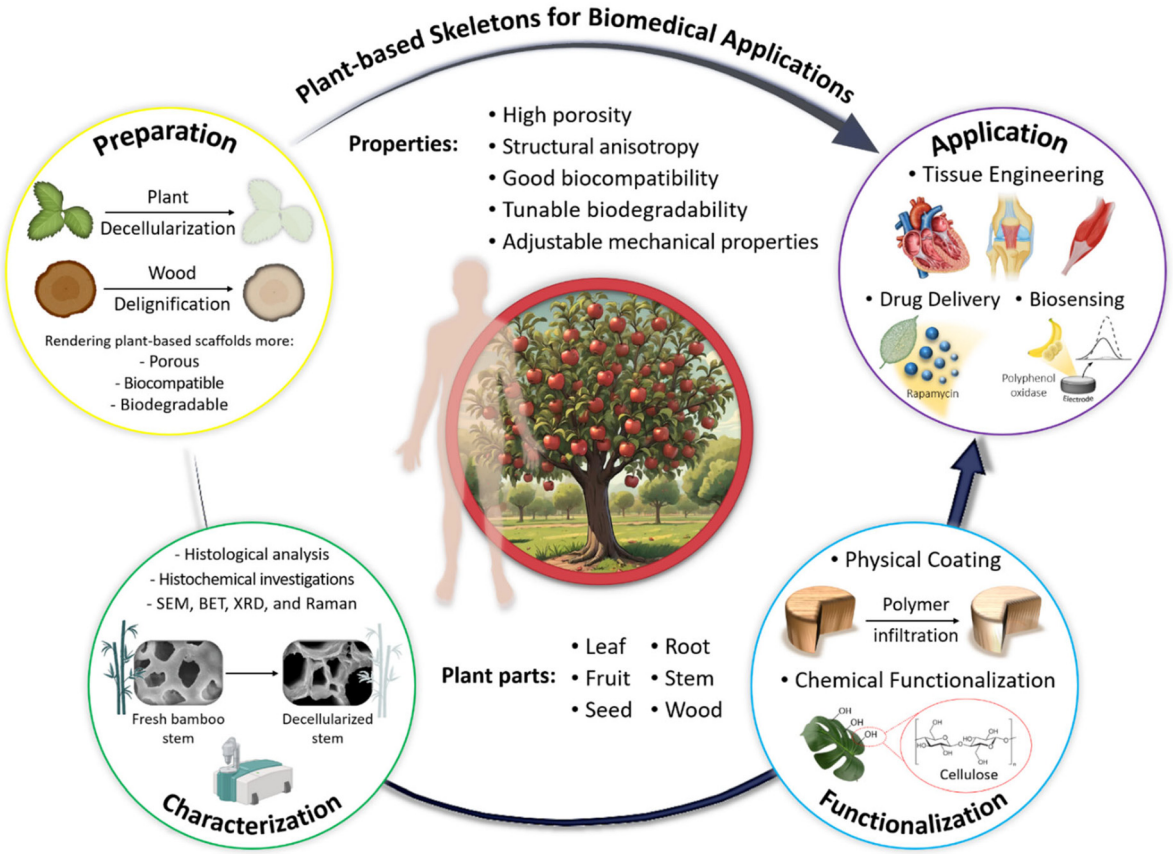

Scheme 1 Unveiling the potential of plant-based skeletons for biomedical applications. A comprehensive schematic illustration of how plant-based scaffolds can be explored for various biomedical applications *via* scaffold preparation, physicochemical characterization, and then structural functionalization for innovative uses in tissue engineering, drug delivery, and biosensing.

3. Preparation protocols of plant skeleton-derived scaffolds

Three-dimensional (3D) scaffolds represent a paradigm shift in the realm of tissue engineering, offering distinct advantages over traditional two-dimensional (2D) substrates. By mimicking the intricate spatial architecture of native tissues, 3D scaffolds provide a favorable microenvironment for cell proliferation, differentiation, and tissue organization. This spatial mimicry enhances cell–cell interactions and promotes tissue-specific functionality, which is critical for the successful development of functional engineered tissues. Moreover, 3D porous scaffolds provide a high surface area and physiologically relevant environment, which allow the penetration of nutrients and oxygen, augment cell attachment sites, and provide mechanical support for imitating the behavior of natural tissues, thereby facilitating cell proliferation and tissue growth.[12–14]

The construction of 3D scaffolds for tissue engineering encompasses a diverse array of methodologies, each tailored to achieve specific structural and functional requirements. Common processing techniques include electrospinning, solvent casting, and 3D bioprinting, using either natural or synthetic biomaterials.[15,16] While versatile, these techniques usually encounter difficulties in accurately reproducing the intricate microenvironment in the native biological tissues. Decellularization techniques, on the other hand, offer a unique advantage by utilizing native organs and tissues as scaffolds. Through the removal of cellular components, the ECM of native organs and tissues is preserved, providing a natural, biomimetic scaffold that retains the complex architecture and biochemical cues crucial for tissue regeneration.[17,18] Despite the notable advantages, the adoption of decellularized organs and tissues in tissue engineering is accompanied by several inherent limitations, such as substantial financial outlays, restricted donor availability, necessity of intricate and specialized processing techniques, as well as ethical considerations pertaining to organ sourcing. Concerns regarding potential immunogenic responses due to the persistence of cell remnants post-decellularization highlight the need for alternative approaches.[19,20] Consequently, there is an urgent need within the field to explore and develop alternative strategies that address these challenges and offer a more pragmatic solution for tissue engineering endeavors.

In this regard, the application of plant-derived skeletons in tissue engineering offers several advantages, including cost-efficiency, sustainability, availability, structural diversity, adequate biocompatibility, and flexibility in processing, along with potential for functionalization.[4] Moreover, plant-based scaffolds originating from stems, roots, leaves, fruits, vegetables, and wood have shown promise in supporting the growth and differentiation of various cell types, presenting a promising route for advancing biomedical applications, where creating functional and biocompatible scaffolds is crucial for successful tissue regeneration.[8,21] In the context of employing scaffolds derived from plant skeletons for tissue engineering, it is essential to implement strategies for eliminating certain constituents that inherently pose a significant barrier to cell infiltration and nutrient diffusion and impede comprehensive tissue integration. These processes, namely "plant decellularization" and "wood delignification", render the scaffold more porous, flexible, and conducive to cell infiltration. As an initial phase in the exploration of plant-derived scaffolds for tissue engineering applications, the processes of decellularization and delignification will be elucidated in the ensuing sections, explaining their complex mechanisms and functions.

3.1. Decellularization of plant scaffolds

Decellularization refers to specialized techniques used in tissue engineering and regenerative medicine involving the removal of cellular components from tissues and organs, leaving behind an acellular scaffold primarily composed of the ECM. Decellularization techniques have long been utilized to develop ECM-rich acellular scaffolds from mammalian tissues using various techniques, including chemical, physical, and enzymatic methods.[22,23] Following these efforts, researchers have extended decellularization methodologies to encompass plant tissues, aiming to exploit the advantages of their structural properties.[7,24]

Plants are primarily composed of complex cellular structures arranged into an inherent interconnected network of vessels, veins, and specialized tissues. During the decellularization processes of plant tissues, the cellular components, including the plant cells themselves, are removed from the plant scaffolds. This involves the elimination of cell membranes, organelles, and genetic material (*e.g.*, DNA and RNA). The residues after decellularization are primarily the ECM and other structural components of the plant tissues, such as cellulose, hemicellulose, lignin, and matrix proteins. These residues provide a framework for cell attachment, migration, and proliferation, and the predefined vascular system can potentially be repurposed to support nutrient and oxygen transportation in the engineered tissues.

3.1.1. Detergent-based decellularization techniques. In the context of decellularization, detergents are the most widely used chemicals to eliminate the cellular components from tissues or organs, leaving behind an acellular scaffold.[25–35] They play a crucial role in breaking down cell membranes and solubilizing cellular components, allowing for the removal of cellular materials. Plant decellularization has been performed using both ionic (*e.g.*, sodium dodecyl sulfate, SDS) and non-ionic (*e.g.*, Triton X-100 and Tween 20) detergents.[36–43]

Ionic detergents are powerful cell-lysing agents due to their amphiphilic properties. The hydrophobic portions of the detergents interact with the cell membrane lipids, whereas their hydrophilic segments interact with the surrounding aqueous environment. As a result, they have the capacity to fully solubilize cell and nucleic membranes, resulting in the breakdown and solubilization of cellular components. They are also capable of fully denaturing proteins, which aids in the elimination of cellular components from tissues or organs.[44] These solubilization and denaturation processes are crucial steps in achieving successful decellularization and preparing acellular scaffolds. It is worth noting that, although SDS is effective at removing cell nuclei, it can also be disruptive to the ECM and denature proteins, underscoring the requirement for careful optimization of the decellularization protocol to balance effective decellularization with the preservation of ECM integrity.[36,37] It is also worth noting that SDS is toxic to the organism if it remains in the decellularized plant tissues. Hence, it is essential to find effective methods to remove the residual SDS after the decellularization process. Using a calcium chloride ($CaCl_2$) solution post-decellularization with SDS has been found to be an effective method for eliminating the residual SDS from the tissues.[29,32,34,36,38,45] When a solution containing a high concentration of $CaCl_2$ salt (generally 100 mM) is introduced after SDS treatment, it disrupts the micelles formed by the surfactants and helps to remove any residual SDS by causing it to precipitate out of the solution. This process effectively reduces SDS concentration, minimizing potential toxicity and ensuring the biosafety of the resulting acellular scaffold.[29]

Apart from ionic detergents, non-ionic surfactants have been utilized in the course of plant decellularization. They have shown potential for disrupting DNA–protein, lipid–lipid, and lipid–protein interactions, while maintaining native protein structures.[46,47] Previous investigations have revealed that using a Triton X-100 solution, especially in conjunction with a bleach solution following SDS treatment, results in a more efficient decellularization process.[28,42,43,48] The Triton X-100/bleach solution serves as a supplementary step to the SDS treatment, augmenting the decellularization process by facilitating the removal of residual cellular components that remain in the tissues after the initial SDS treatment. The process helps remove residual SDS, disrupt cell membranes, solubilize proteins, and increase the overall processing efficiency. Fig. 1 provides a schematic illustration of the various steps involved in the decellularization process using detergents and chemical reagents.

3.1.2. Detergent-free decellularization methods. Although detergents, such as SDS and Triton X-100, are effective at producing cell-free plant-derived scaffolds, they are associated with a set of potential disadvantages. The issues regarding residual cellular components and chemicals, alterations in the ECM structure, and potential cytotoxicity, along with environmental considerations, have motivated researchers to develop

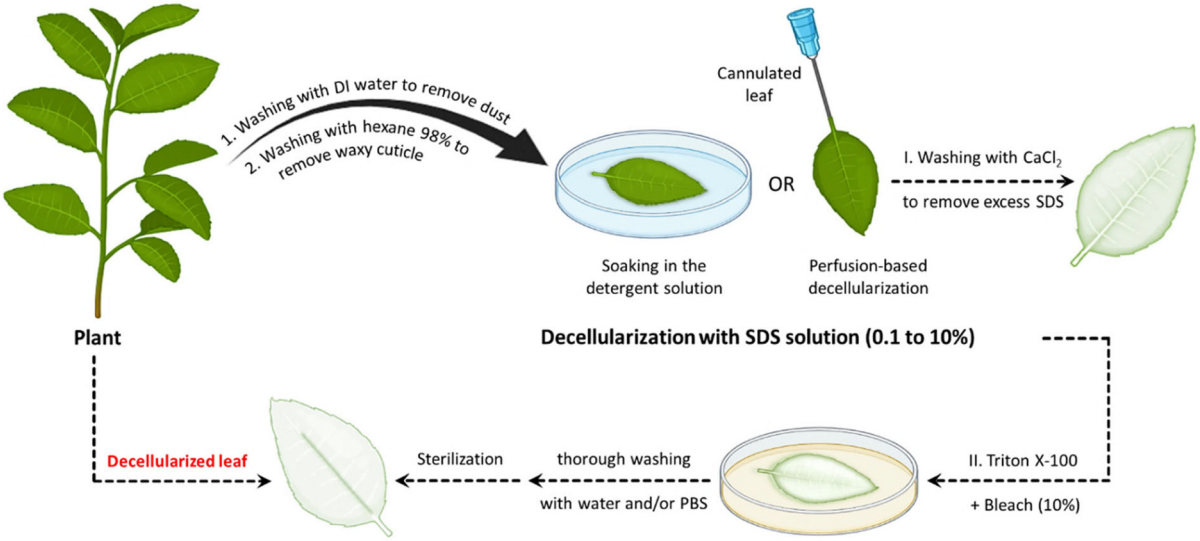

Fig. 1 Schematic representation of the plant decellularization process. The typical protocol for plant decellularization generally comprises several steps, including cutting the tissue into the desired size and shape for the intended application, followed by washing with water to remove any possible debris and dust. Subsequently, the leaf is incubated in hexane (98%) to dissolve the waxy cuticle layer from the leaf's surface. The leaf tissue can be either perfused (if it has vascular channels) or soaked (mainly in the case of vegetal and fruit samples) in the SDS decellularization solution. The SDS concentration and the decellularization time may vary, depending on both the size and thickness of the tissue type and plant species. Moreover, agitation or gentle mechanical stimulation (*e.g.*, shaking or stirring) can aid in the removal of cellular materials. After co-incubation with the decellularization solution for an appropriate period, the tissue is rinsed thoroughly with distilled water or a buffer solution to remove residual chemicals. In order to ensure the elimination of residual SDS, the samples can be washed with a $CaCl_2$ solution, greatly reducing the SDS extraction time. Triton X-100 and bleach treatments can be used after SDS decellularization to help remove any residual cellular components and increase the processing efficiency. After performing the required analysis (*e.g.*, histological and biochemical assays) to confirm the removal of cellular materials, the decellularized scaffold is typically sterilized using ethanol (70%) or 1% streptomycin/penicillin and 1% amphotericin B to ensure that it is free from any microbial and bacterial contaminants.

or refine protocols to address these challenges in plant decellularization.

In 2011, Bar-Shai *et al.* reported on the successful decellularization of green macroalgae to prepare seaweed cellulose-based scaffolds for tissue engineering applications.[49] They argued that seaweed, due to its lignin-free cell wall, tends to be more amenable for the decellularization process. This characteristic makes the decellularization process for macroalgae easier and more cost-effective. Two types of green seaweed (*i.e.*, *Enteromorpha* spp. and *Cladophora* spp.) were firstly boiled in acetone to eliminate pigments (chlorophyll) and proteins. The residual biomass underwent a bleaching process in an acetate buffer bath in the presence of sodium chlorite ($NaClO_2$), with the aim of inducing bleaching and eliminating structurally simpler polysaccharides. The resulting bleached samples were then subjected to an alkylation process in a sodium hydroxide (NaOH, 20%, w/v) bath to remove any excess lipids. Finally, to facilitate the removal of any excess polysaccharides that might have remained in close proximity to the cell walls, the macroalgae were placed in a 5% v/v hydrochloric acid (HCl) solution at 100 °C for 10 min, followed by rinsing with distilled water until a neutral pH was achieved. It has been shown that the proposed protocol is able to effectively decellularize the seaweed samples, leaving behind an intact cellulose ECM. The results demonstrated the applicability of an alkaline solution to remove excessive lipids and hemicellulose in the cell wall.

Following this preliminary study, alkali treatment using an NaOH solution was used to decellularize *Ficus religiosa* and *Camellia japonica* leaves.[50,51] Compared with detergent-based approaches, alkali treatment stands out as a notably swifter decellularization method. The process in alkaline media typically took only 30–120 min, depending on the type of leaf species, in stark contrast to the days often required for decellularization using SDS solutions. *Ficus religiosa* leaves treated with an NaOH solution under autoclave conditions have shown a considerable reduction in hemicellulose content, from 31% to 9.2% after 1 h.[50] Significant color alteration and initial lamina peeling were recorded when using alkaline decellularization. However, post-treatment processes, such as sonication and brushing, may be necessary to ensure complete lamina removal. Using a bleach solution also facilitated the decolorization of the decellularized leaf vein.[51]

An alternative, detergent-free approach for plant decellularization, aimed at removing DNA and cellular components, draws inspiration from a "skeletonization" protocol traditionally employed for the extraction of soft tissues from leaves. This method diverges from the detergent-based protocols adapted from well-established mammalian tissue decellularization techniques using gentler reaction conditions, namely

more prolonged incubation time in a bleach (sodium hypochlorite, NaClO) and sodium bicarbonate ($NaHCO_3$) solution at lower temperatures (60–70 °C).[52,53] The combination of bleaching agents as strong oxidizers and $NaHCO_3$ as a pH buffering agent has displayed potential in effectively separating vascular tissues from soft tissues.[54] This method is likely to be applicable across a broad range of plant species and can be utilized on both stems and leaves, being capable of effectively eliminating genetic materials and cell residues, while preserving the native topographical features and avoiding significantly disrupting the soft tissue structures.[52] As previously mentioned, the decellularization protocol can be customized to suit specific specimens. Increasing bath temperatures may expedite clearing times, albeit with the potential risk of damaging the soft tissues. Factors, including reaction temperature, incubation time, and the concentration of bleach solution, can be adjusted to accelerate or decelerate the decellularization process. As compared with the SDS-based decellularization protocol, decellularized samples prepared using this approach also exhibited a reduced cytotoxic influence on cell growth, in particular when washed with a Tris-HCl buffer (10 mM, pH 8.5) post-decellularization.[52]

In a comparative study, Aswathy *et al.* investigated the effect of various decellularization techniques on bamboo stems.[55] Various decellularizing solutions were employed, including (i) a bleach (NaClO) solution (H), (ii) SDS in a bleach solution (S/H), (iii) Triton X-100 in a bleach solution (T/H), and (iv) Triton X-100 + SDS in a bleach solution (S/T/H). The decellularization (pigmentation loss and increased translucence) results revealed that bamboo stems treated with S/H and S/T/H solutions were decellularized within 24 h, whereas prolonging the time to 48 h showed no significant differences between these two treatment groups in terms of DNA content.

Utilizing nuclease enzymes is another promising strategy for preparing decellularized plant-derived scaffolds, offering a high degree of specificity in removing genetic materials.[54] In order to explore the applicability of enzymatic decellularization to the fabrication of acellular plant scaffolds, deoxyribonuclease I (DNase I) was applied to remove cellular materials from cultured plant cells (tobacco BY-2 cells and rice cells) and tissue (tobacco hairy roots).[56] Unlike detergent-based decellularization methods, an enzymatic approach is able to effectively remove DNA molecules from the matrices while retaining proteins, as evidenced by the expression of recombinant enhanced green fluorescent protein (EGFP). The DNA content was reduced by 97.93% (from 1503 ± 459 for the control group to 31 ± 5 ng/sample for the + DNase group), whereas 36% protein retention was observed in the + DNase group. Moreover, DNase treatment at a concentration of 1 mg mL^{-1} for 30 min was more effective at reducing DNA levels, as compared with Triton X-100 treatment, which required overnight exposure. These results highlight the efficiency and applicability of employing enzymes for plant decellularization, suggesting that this approach holds promise for future research and applications.

Supercritical carbon dioxide ($scCO_2$) has also been proposed as a promising alternative to detergent-based decellularization methods.[57] $scCO_2$ is a state of CO_2 where it is held at a temperature and pressure above its critical point. In the case of CO_2, this critical point occurs at approximately 7.38 MPa and 31.1 °C. In the supercritical state, CO_2 exhibits both gas and liquid properties, and has the density of a liquid and the diffusivity of a gas, allowing it to penetrate materials in the same way as a solvent. As a result, $scCO_2$ is an appealing candidate for decellularization, given its ability to extract, dissolve, and separate various compounds without leaving behind potentially harmful residues. Spinach leaf was successfully decellularized using $scCO_2$ in the presence of peracetic acid (PAA; 2% v/v) as the most efficacious co-solvent. As compared with time-consuming detergent-based decellularization protocols (≈170 h), the $scCO_2$-assisted technique can obtain decellularized plant materials within 4 h, avoiding the harsh reaction conditions and toxic chemical reagents frequently used in the former cases. When moderate pressure is applied along with a PAA solution, the fluid gains the ability to efficiently remove cellular materials from plants, creating a scaffold that is compatible with biological tissues. Pressure plays a key role in allowing CO_2 to transition into a liquid state, creating the conditions for $scCO_2$ to infiltrate plant cells. It works by traversing the plant cell wall, moving through the cell membrane and, once inside, acting as a highly effective solvent. This movement of supercritical CO_2 leads to a decrease in the pH level of the cytoplasm, a process catalyzed by carbonic acid. The presence of PAA has been shown to enhance this effect even more. Consequently, cell metabolism is disrupted, and crucial enzymes are removed. Importantly, this process does not compromise the overall structure of the plant scaffolds.[54,57]

Table 1 lists the decellularization approaches used so far to eliminate the genetic materials and cellular components of various plant tissues and species. It is important to note that the choice of detergent and decellularization protocol should be carefully optimized to achieve a balance between the effective removal of cellular materials and the preservation of the ECM's integrity and bioactivity. This ensures that the resulting acellular scaffold provides an appropriate environment for subsequent tissue engineering or transplantation applications. As deduced from the reaction conditions, in the context of plant species characterized by soft tissues, such as *Borassus flabellifer* (Linn.) (BF), a decellularization protocol employing mild conditions can be implemented. This protocol entails the utilization of a 0.5% w/v SDS solution at ambient room temperature, with a recommended duration of 12–16 h for the decellularization process.[58,59] Conversely, for plant species with more robust and intricate vasculature structures (*e.g.*, spinach, parsley, and cabbage), a more rigorous decellularization approach was adopted. This involved the immersion of the plant materials in potent ionic detergents, including SDS (ranging in concentration from 0.1 to 10%), for a prolonged incubation time (from 2 to 7 days). This process may be supplemented by an incubation phase in a Triton X-100/bleach solution for a period of 24–48 h to ensure the complete

Table 1 Various protocols used for plant decellularization in biomedical applications

	Decellularizing agent (s)	Plant species	Decellularization condition	Recellularization	Ref.
Detergent-based decellularization techniques	SDS	Apple hypanthium tissue	- Immersion of samples in an SDS solution (0.5% w/v) with shaking for 12 h at 160 rpm at room temperature - Washing and incubating the resulting cellulose scaffolds in PBS for 6 hours, followed by sterilization with streptomycin/penicillin (1%) and amphotericin B (1%)	NIH3T3 fibroblasts, mouse C2C12 muscle myoblasts, and human HeLa epithelial cells	25
		Apple, broccoli, sweet pepper, carrot, persimmon, and jujube	- Immersion of fruit samples in an SDS solution (0.5% w/v) while shaking at 180 rpm for 48 h - Washing three times with PBS and twice with ethanol (70%, v/v) - Sterilization with penicillin/streptomycin and amphotericin B (1%, w/v) for 6 h	Induced pluripotent stem cells (iPSCs)	60
		Leek	- Washing the samples with water under vacuum for 3 h and keeping them at −80 °C overnight - Soaking the samples in an SDS solution (1% w/v) at 37 °C for 5 days, followed by washing several times with water and PBS (pH 7.4) - Placing in absolute ethanol at 65 °C for about 24 h to remove chlorophyll - Washing with PBS and kept in PBS overnight at 37 °C in order to remove excess ethanol	SH-SY5Y human neuroblastoma cells	61
		Carrot, broccoli, cucumber, potato, apple, asparagus, green onion, leek, and celery	- Submerging in an SDS solution (1% w/v) and shaking at 70 rpm at 25 °C for 3 weeks (the SDS solution was refreshed weekly) - Washing twice with PBS at 60 rpm and incubating with streptomycin/penicillin (1%) in PBS at 60 rpm overnight	C2C12 and human skeletal muscle cells (HSMCs)	35
		Borassus flabellifer (Linn.) (BF) immature endosperm	- Detaching the seed coat of the BF endosperm (endocarp) manually - Incubating the fleshy endosperm in an SDS solution (0.5% w/v) for 12–16 h at even room temperature or 25 ± 2 °C - Washing the decellularized samples with a PBS solution (pH 7.4) multiple times and finally with water	MG63 cells, L929 cells	58 and 59
	SDS + $CaCl_2$	Asparagus	- Placing the samples in an SDS solution (0.1% w/v) while shaking for 48 hours at 180 rpm at room temperature - Washing with a PBS solution followed by incubating for 12 h - Incubating in $CaCl_2$ (100 mM) for 24 h at room temperature - Washing with water and sterilizing in 70% ethanol overnight	—	45
		Golden delicious apple, carrot, and celery	- Immersion in an SDS solution (0.1% w/v) for 48 h at room temperature under continuous shaking at 180 rpm (at 24 h, the SDS solution was renewed, and the samples were sonicated for 5 min at 40 °C) - Incubating in $CaCl_2$ (100 mM) solution for 24 h, followed by washing three times in distilled water - Sterilization with penicillin/streptomycin (1%) and amphotericin B (1%) for 3 h while shaking at 140 rpm - Disinfecting in 70% ethanol solution for 1 h	3T3-L1 preadipocytes, MC3T3-E1 pre-osteoblasts, L929 cells	36
		McIntosh apple	- Decellularizing in an SDS solution (0.1% w/v) for two days and washing with water - Overnight incubation in $CaCl_2$ (100 mM) solution to remove the remaining SDS surfactant - Sterilizing with 70% ethanol for 30 min, followed by washing with water	MC3T3-E1 pre-osteoblasts	38
	SDS + Triton X-100/ bleach solution	Parsley leaves and stems	- Immersing in an SDS (10×) solution for 5 days with gentle agitation - Incubating in a Triton-X-100 (0.1%, v/v)/bleach (10%, v/v) solution for 48 h - Incubation in hexane (98%) for 1 min to remove the waxy cuticle, followed by washing with PBS and incubating in water for least 2 days	Human dermal fibroblasts (hDFs) and mesenchymal stem cells (MSCs)	27
		Baby spinach leaves, hybrid cherry tomato plant, aquatic plant *A. borealis*, and lucky bamboo	- Perfusion decellularization of spinach, tomato, and aquatic leaves through the petiole, while soaking *A. borealis* and lucky bamboo in an SDS solution (1% w/v) for 2 days - Decellularizing with an aqueous solution of Triton X-100 (0.1%, w/v)/$NaClO_2$ (10%, w/v) for 2 days - Flushing with water for an additional 48 h	Melanoma SK-MEL-28 and prostate PC3 cells	37
		Aptenia cordifolia	- Washing the leaves with 10% Dulbecco's phosphate-buffered saline (DPBS) and hexanes (98%) to remove the cuticles - Perfusing the leaves with an SDS solution (10% w/v) for 24 h followed by $NaClO_2$ bleach (1.2%) containing Triton X-100 (0.5%) for 24 h - Washing with water for 24 h to remove the residual detergents and bleach	Human breast cancer line MDA-MB231	39

Table 1 *(Contd.)*

	Decellularizing agent (s)	Plant species	Decellularization condition	Recellularization	Ref.
Detergent-free methods	Acetone + $NaClO_2$ + NaOH	Macroalgae species (*Ulva* sp. and *Cladophora* sp.)	- Boiling in an acetone (20%) bath at 60 °C for 60 min in order to remove pigments (chlorophyll) and proteins - Boiling in an acetate buffer bath containing $NaClO_2$ (20%, w/v) at 60 °C for 6–8 h, initiating the bleaching and removal of simpler structure polysaccharides - Washing with water, followed by treatment in an NaOH bath (20%, w/v) at 60 °C for 8–10 h to eliminate all excessive lipids - Washing with water and boiling in an HCl solution (5%, v/v) at 100 °C for 10 min - Incubating overnight at room temperature to remove all excessive polysaccharides followed by washing with water until a neutral pH is reached	NIH3T3-GFP-actin fibroblast	49
	NaOH treatment	*Camellia japonica*	- Submerging in water (95 °C) for 10 min, followed by placing it in an NaOH solution (5%, w/v) at 90 °C (30 to 120 min, depending on the species) - Sonicating the leaves and brushing them to remove cell fragments - Immersing in a bleach solution for 1 min, washing twice with PBS to remove the bleach	Mouse myoblast cells (C2C12)	51
		Ficus religiosa	- Immersing leaves in an NaOH solution (4%, w/v) and keeping them in an autoclave at 120 °C for 60 min under pressurized (15 lbs) conditions - Washing the alkali-treated leaves with water and rupturing the waxy layer with a smooth brush until the superficial layers are removed completely	Human MSCs (hMSCs)	50
	NaClO + $NaHCO_3$	*Ficus hispida*	- Immersing leaf samples in a bleach (NaClO, 5%) solution containing $NaHCO_3$ (3%, v/v) at 60–70 °C - After decolorizing, the samples were submerged in water for 1–2 min to remove excess bleach solution	Human dermal fibroblast (hDF) cells	52
	Enzymatic decellularization (DNase I)	Tobacco BY-2 and rice cells, and tobacco hairy roots	- Lyophilized BY-2 cell materials and pulverized rice matrices were incubated in DNase I enzyme (1 mg mL^{-1}) in a PBS solution containing Mg^{2+} (0.492 mM) and Ca^{2+} (0.9 mM) - Degassing the solution under vacuum for 5 min to release the trapped air - Incubating at 37 °C for 30 min, followed by washing with PBS (4 times)	Human foreskin fibroblasts (hFFs)	56
	Supercritical CO_2 ($scCO_2$)	Baby spinach leaves, sweet mint plants, celery stalks, and curly parsley	- Removing the wax cuticles by washing with hexane and PBS solutions - Placing the individual leaves in a vented 15 mL conical tube with 5 mL of PAA co-solvent and placing 3 tubes in a 600 mL pressure sealed vessel - Introducing the liquid CO_2 (medical grade of 99.9% purity) into the vessel while the pressure was increased to 0.55 MPa (at 3.2–5 cubic meters per cycle) - When the desired condition was achieved (*i.e.*, 17.23 MPa and 33 °C), the process was performed for 180 min - Slowly releasing the pressure at the end of the reaction and flushing the leaves with bleach for 8 h, followed by washing with water for 24 h	Human dermal fibroblast (hDF) cells	57

removal of plant cellular materials. Furthermore, in the case of porous tissues, such as apple hypanthium, immersion in a detergent solution with gentle stirring can be effective, whereas in that of more rigid leaves with veins, perfusion decellularization methods are commonly employed. Perfusion involves the circulation of the decellularization solution through the tissues, ensuring an even distribution. Temperature can influence the decellularization rate, with higher temperatures potentially accelerating this process. Finally, thorough rinsing and washing steps are essential to eliminate residual detergents and cell remnants. These parameters collectively dictate the success of the decellularization process and must be tailored to the specific characteristics of plant tissues. A summary of the characteristic features of each approach from different aspects is given in Table 2.

3.2. Delignification and bleaching

Wood is a complex biological material composed primarily of polysaccharides (cellulose and hemicellulose) and lignin, along with various other minor extractive components (Fig. 2). Cellulose is the most abundant component in wood, accounting for approximately 40–50% of its mass. It is a linear polymer composed of glucose units connected by β-1,4-glycosidic bonds. The organized arrangement of cellulose in the form of microfibrils endows wood with a fibrous structure, contributing to its rigidity, as well as tensile strength and stiffness. The cellulose microfibrils embedded in the hemicellulose–lignin matrix provide a balance between strength and flexibility, enabling the wood to bear loads and resist deformation. Hemicellulose, comprising approximately 15–35% of wood

Table 2 The characteristic features of detergent-based and detergent-free approaches for plant decellularization

Aspect	Detergent-based techniques	Detergent-free techniques
Cell removal	More effective at complete removal with uniform decellularization	May leave residual cellular material
ECM preservation	May damage the ECM structure	Better preservation of the ECM structure
Risk of toxic residues	Detergent residues might affect biocompatibility	No risk of chemical toxicity
Time & complexity	Time-consuming with extensive washing steps	Generally simpler and faster
Applicability	Suitable for most types of plant tissues	Limited to softer or less dense plant tissues
Environmental impact	Contamination with chemical detergents	Eco-friendly without harsh chemicals

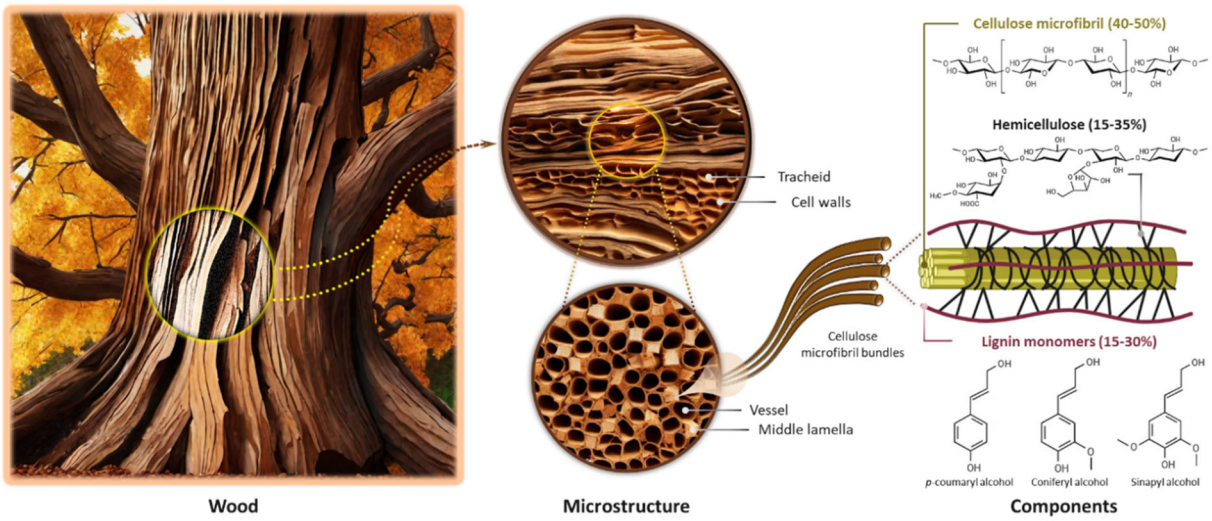

Fig. 2 The wood microstructures and its components. Wood is a hierarchical structure composed of vessels, tracheids, and fibers. The main components of cell walls are cellulose, hemicellulose, and lignin. Cellulose is a linear homopolymer formed through β (1 → 4) glycosidic linkages of glucose units. Unlike cellulose, hemicellulose is a branched polymer of various sugar units, including glucose, xylose, mannose, and others. Lignin is an amorphous polymer with a complex chemical structure. Its main precursors are *p*-coumaryl, coniferyl, and sinapyl alcohols. The percentage of wood components varies from one species to another. Softwoods (gymnosperms) generally have higher cellulose and lignin contents than hardwoods (angiosperms).

mass, forms a matrix around cellulose microfibrils and provides flexibility to the cell walls, making the wood less prone to breakage. It also plays the role of a binder between cellulose fibers and lignin molecules, improving the overall structural integrity of the wood. Lignin, constituting 15–30% of wood mass, is a complex and amorphous polymer made up of phenolic compounds. It acts as a glue, binding cellulose and hemicellulose together; hence, it is an essential agent in facilitating the creation of robust wood matrices, which provides rigidity and significantly enhances the mechanical characteristics of the wood.[62–65]

The delignification of wood is a technical process involving the selective dissolution or removal (partial or total) of lignin, a complex polymeric substance, from the lignocellulosic matrix of wood fibers.[66,67] This procedure aims to alter the composition of the wood structures by employing chemical,[63,67,68] enzymatic,[69–71] and thermal[72,73] treatments, resulting in a reduction in lignin contents while preserving the natural hierarchical structures and the inherent fiber directionalities of the original wood. Lignin extraction is mainly performed to attain distinct material properties such as enhanced pulp quality for paper production,[62,74,75] improved accessibility of cellulose for bioconversion processes,[76] and the creation of modified wood products with specific characteristics (*e.g.*, high porosity),[77–80] along with improved permeability and hydrophilicity due to the increased amounts of accessible hydroxyl groups.[68,81–84] However, it should be taken into consideration that, although lignin extraction from the cell walls leads to increased porosity without compromising fundamental structural stability, the extensive removal of lignin (in particular from the middle lamella region) would result in the detachment of wood cells.[66] Generally speaking, since lignin contributes significantly to the strength and structural integrity of wood, the delignification process can reduce the mechanical properties of wood fibers, making them weaker and more prone to damage.[85,86]

3.2.1. Thermal treatment. Thermal treatment has a historical precedent as one of the early approaches used for partial delignification of wood and for modifying its properties for various purposes. The underlying reason behind the thermal delignification process lies in the inherent structural characteristics of wood. As mentioned above, wood exhibits a hierarchi-

cal cell structure, comprising intertwined cellulose, hemicellulose, and lignin matrices, with cellulose microfibrils embedded in a lignin-rich matrix providing structural integrity at the microscopic level. Cellulose and hemicellulose are polysaccharides composed of simpler sugar units linked together. In contrast, lignin possesses a complex, intricate polymeric structure, resulting from the oxidative coupling of three main cinnamyl alcohol-based phenolic monomers: *p*-coumaryl alcohol, coniferyl alcohol, and sinapyl alcohol.[87] The chemical structures of these monomers are shown in Fig. 3a. These monolignols contribute to the formation of three main lignin units: 4-hydroxyphenyl (H), guaiacyl (G), and syringyl (S).[88] The final structure of lignin is formed *via* the radical coupling of these three subunits, resulting in a highly branched, cross-linked network. The monomers are interconnected by various types of chemical bond, including ether (C–O) bonds and carbon–carbon (C–C) linkages, with β-O-4 linkages being the most prevalent and prominent type of bond in the lignin structure (Fig. 3b).[89] There are variations between the lignin composition and the proportions of these three units, corresponding to different cell and plant types (*i.e.*, softwoods and hardwoods). However, the precise arrangement of these units and linkages can vary, contributing to the diversity of lignin structures observed in different plant species and tissues, and providing mechanical support to plant tissues.

The heat treatment involves subjecting the wood (or other lignocellulosic materials) to elevated temperatures in the absence of oxygen, or with a limited oxygen supply. Applying heat to wood can break down the lignin and other organic components, resulting in partial delignification, which makes

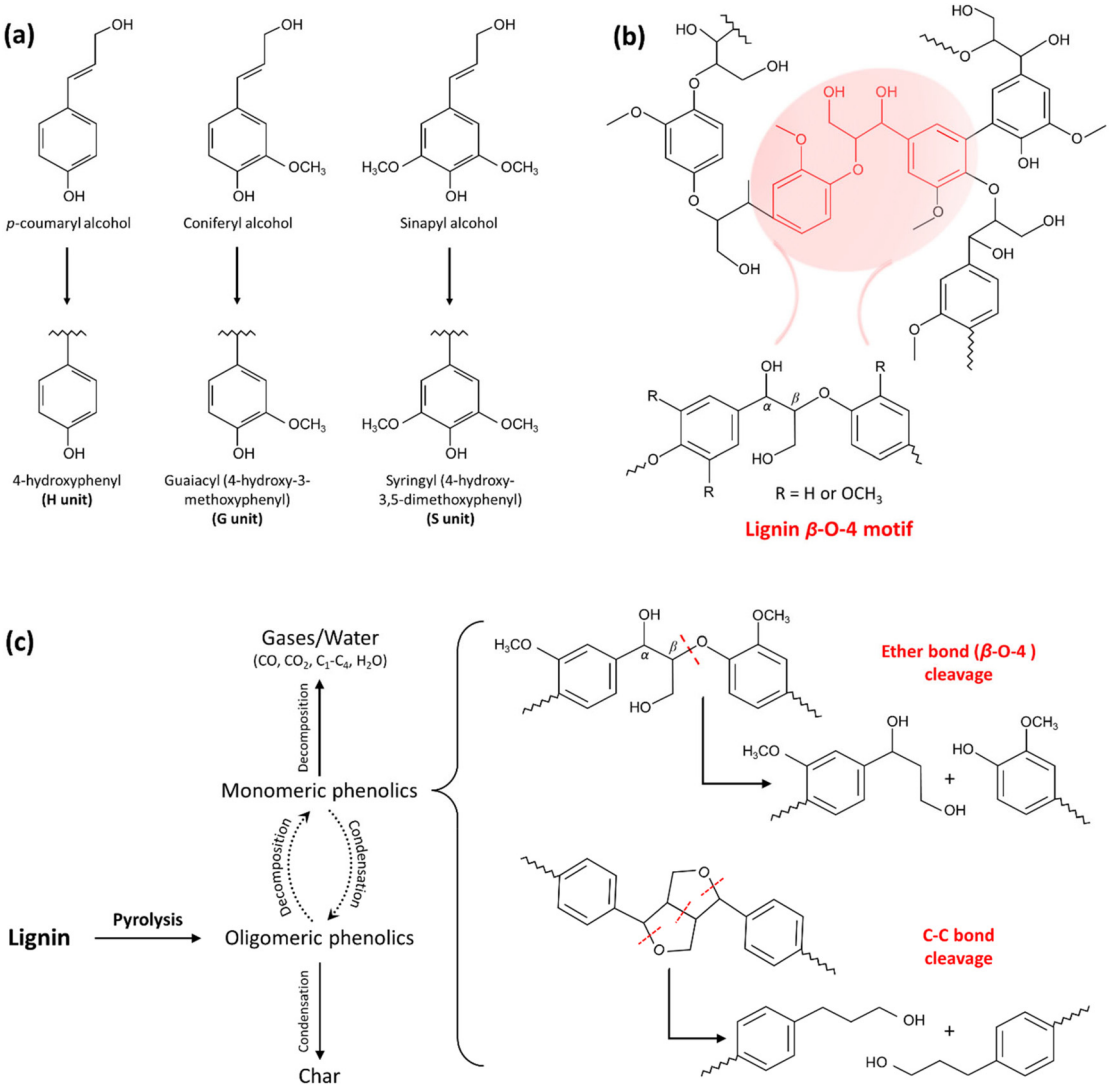

Fig. 3 The chemical structures of lignin and its pyrolysis products. (a) Chemical structures of lignin monolignols composed of *p*-coumaryl alcohol, coniferyl alcohol, and sinapyl alcohol that contribute to the formation of three main lignin units: 4-hydroxyphenyl (H), guaiacyl (G), and syringyl (S). (b) Simplified chemical structures of lignin showing the lignin β-O-4 motif. (c) The mechanism of lignin pyrolysis and the products after thermal treatment. (Reproduced from ref. 101 with permission from Elsevier Ltd. Copyright 2019.) The cleavage of constituent bonds involved in the structure and the production of smaller fragments results in the solubilization of lignin to some extent.

the wood more pliable and easier to process.[90] The heat treatment process induces alterations in the chemical compositions of wood through the degradation of cell wall compounds and extractives, as shown in Table 3. Although differential thermal analysis (DTA) of various types of lignocellulosic materials reveals distinctive patterns, their thermal degradation behavior follows a common characteristic. Within the 100–180 °C temperature range, the wood experiences a drying phase characterized by the progressive loss of free water followed by bound water. Hence, the distinct peak that emerges from DTA analysis in this temperature range corresponds to the humidity elimination.[91] In the absence of oxygen (pyrolysis conditions), the thermal stability order of wood components is generally as follows: lignin > cellulose > hemicellulose.[92] Hemicellulose demonstrates an early susceptibility to thermal degradation, and as a result, it is the primary structural constituent that undergoes thermal alteration, even at relatively mild temperatures during pyrolysis processes.[91,92] Wood degradation commences with the deacetylation process of hemicellulose constituents, associated with the liberation of acetic acid. This liberated acetic acid is assumed to play a pivotal role as a catalyst for depolymerization, inducing an additional catalytic effect on carbohydrate cleavage, thereby inducing a reduction in the degree of polymerization in the polysaccharide matrix.[90] The acid-catalyzed degradation of pentoses and hexoses in the structures results in the generation of furfural and hydroxymethyl furfural, respectively, as well as formaldehyde and various other aldehydes (produced from lignin units Cγ). Hydroxyl functional groups are also decreased, due to the dehydration reactions of hemicellulose.[93] The elevated temperatures (230 °C) are associated with a reduction in some hemicellulose contents (*e.g.*, xylose and mannose), along with the total decomposition and disappearance of other sugars (*e.g.*, arabinose and galactose).[94]

The cellulose content of the wood, on the other hand, exhibits less susceptibility to heat treatment. This is likely to be due to its inherent crystalline structures, which endow the wood with thermal stability. In addition, the strong intermolecular hydrogen bonds present in the cellulose molecules contribute to its resistance to thermal decomposition.[90,91] Previous investigations mainly revealed an increase in crystallinity with increased temperature. The degradation process of less ordered and amorphous cellulose at high temperatures (generally above ≈200 °C) contributes to an enhancement in the cellulose crystallinity index (CI).[95–97] It is also worthy of mention that, although the majority of studies indicate an increase in the CI of lignocellulosic samples following thermal treatment, in the case of certain species (*e.g.*, *Cryptomeria japonica* timber), cellulose crystallinity decreased.[98,99] The increase in crystallinity is significantly influenced by the humidity level. A study by Bhuiyan *et al.* demonstrated that, under a high humidity environment, the crystallization degree was twice that observed under completely dry conditions.[100]

Compared with cellulose and hemicellulose units, lignin demonstrates slower decomposition rates, spanning a wider temperature profile (typically from 200 to 500 °C), due to its complex structure comprising phenolic and aromatic rings conjugated by carbon–carbon and ether bonds.[91] As shown in Fig. 3c, the lignin decomposition starts with depolymerization, during which the lignin polymer begins to break down into smaller molecular fragments.[92,101]

This involves the cleavage of various chemical bonds in the lignin structures, including β-O-4 linkages, α-O-4 linkages, and other ether and carbon–carbon bonds. As mentioned previously, β-O-4 linkages containing both ether and C_α–C_β bonds are the most predominant bonds in the lignin structure. Ether linkages, in comparison with C–C ones, typically exhibit comparatively lower bond strength and are more readily cleaved.[87] During lignin decomposition, various functional groups (*e.g.*, methyl, ethyl, and hydroxyl groups) attached to the aromatic rings can undergo dealkylation and dehydroxylation reactions. These contribute to the formation of lighter, hydroxyl group-bearing water-soluble phenolic compounds, and other aromatic derivatives.[90,102] As the lignin fragments undergo further decomposition, some of the generated phenolic compounds can undergo condensation reactions, in which they react with each other to form larger aromatic molecules ("lignin autocondensation"). During this process, the cleavage of ether linkages in lignin, particularly the β-O-4 linkage, results in the creation of both free phenolic hydroxyl groups and α/β-carbonyl groups. These reactive functional groups play a crucial role in the formation of cross-links through the creation of methylene bridges.[90,95] The high temperatures can also result in the release of volatile gases, such as CO_2, methane, and various hydrocarbons. If the temperature becomes high enough and the process is sustained, the remaining carbon-rich residues can undergo further changes and eventually turn into charcoal (Fig. 3c).[101]

The final result of thermal treatment is an increase in dimensional stability, along with a substantial decrease in the hygroscopicity of the delignified wood (DW). However, thermal treatment is associated with loss of mechanical strength and

Table 3 Chemical transformations in various components of wood after heat treatment

Wood heat treatment			
Hemicellulose	Cellulose	Lignin	Extractives
• Dehydration • Deacetylation • Depolymerization	• Increased crystallinity degree	• Structural changes • Free molecules • Condensation reactions • Cross-linking	• Volatile organic compounds (VOC) emissions • Formation of new compounds

increased brittleness of timbers.[90,95] In order to preserve the inherent anisotropic structure and prevent the disintegration of the original wood template, a very slow heating rate was applied. It was found that using a heating rate as low as 0.5–1 °C min^{-1} effectively preserved the original cellular structured networks of the pyrolyzed wood, even when subjected to elevated temperatures up to 800–1000 °C (under an argon atmosphere).[73,103]

Thermal delignification in the presence of water (*i.e.*, hydrothermal conditions) has also been shown to play a pivotal role in decreasing the temperatures required for delignification, while increasing the lignin removal efficiency.[72,101] Water, as a heat transfer medium, allows for more precise temperature control during the delignification process. The steam generated at elevated temperatures can penetrate the porous structures of wood, facilitating the breakdown and removal of lignin, as well as hemicellulose hydrolysis. High temperatures alone can promote combustion, but the introduction of water vapor helps maintain a non-combustible environment, ensuring that the wood remains intact.[104] Moreover, the thermal delignification efficiency can be improved even more by using various catalysts[101] or combining it with certain methods, such as microwave assistance.[105] Microwave-assisted thermal delignification turns the process into a more energy-efficient and cost-effective strategy. It should be taken into consideration that the efficiency of wood thermal treatment and the properties of the final products are highly dependent on a plethora of factors, including the treatment time and temperature, the heating rate, the initial moisture content, and the type of wood species.[90,91,106]

3.2.2. Biological delignification. In natural environments, wood degradation is caused by enzymatic activity facilitated by microorganisms, especially fungi.[107] In other words, certain microorganisms (*e.g.*, white-rot fungi and bacteria) have enzymes that can break down lignin. Previous studies have revealed that among various fungi (*e.g.*, white-rot, brown-rot, and soft-rot fungi), only white-rot fungi possess the ability to selectively degrade lignin.[108] White rot, characterized by the decomposition of wood induced by basidiomycete fungi, has actually shown a remarkable ability to break down lignin extensively, including the heavily lignified middle lamella.[108,109] Blanchette *et al.* investigated the chemical components of the fungi–DW.[109] Their results revealed that the percentage of lignin in sound birch wood (19.8%) was decreased to 15.9%, 10.9%, 14.4%, and 18.8% in the entire decay in the presence of *Cerrena unicolor*, *Ganoderma applanatum*, *Ischnoderma resinosum*, and *Poria medulla-panis* fungi, respectively. However, in the white-pocket rot areas (*i.e.*, where affected woods are transformed into a white or yellowish color due to the breakdown of lignin and cellulose compounds), the lignin percentage was measured as 1.8%, 1.1%, 2.5%, and 2.8%, respectively. It has been argued that the fungal hyphae (the threadlike cells of the fungus located in cell lumens) can generate a lignin-degrading system. This consists of extracellular enzymes or is potentially an oxidizing system with the ability to target the compounds in the middle lamella for degradation while preserving the secondary wall.[109,110]

The impact of fungal treatment on the morphological characteristics and chemical composition, in particular the delignification degree, of wood species depends on various factors, namely the specific wood species, the particular white-rot fungus strain, and the duration of exposure to the fungal agents.[110] For instance, among three different white-rot fungi, including *Phanerochaete chrysosporium*, *Ganoderma adspersum*, and *Ganoderma applanatum*, it was observed that the decay rate of balsa wood was significantly higher when subjected to *G. applanatum*. The morphological delignification profiles of balsa wood incubated with the white-rot fungus *G. applanatum* at different time intervals are illustrated in Fig. 4b–j. As seen from the scanning electron microscopy (SEM) images, after exposure to fungi for 4 weeks, an initial decay stage is observed, with minimal alterations in the wood structures during this early phase. However, as the fungal colonization progresses (between 6 and 8 weeks), more substantial structural changes become evident, with some cell walls being destroyed while others remain unaffected. Following a 10-week exposure, the balsa wood underwent significant decay, with the majority of cell walls being destroyed, resulting in the formation of considerable gaps between the rays. The weight loss was incremental, from 15% to 25%, 35%, 45%, and finally 55%, when the wood was exposed to the *G. applanatum* fungus for 4, 6, 8, 10, and 12 weeks, respectively.[110]

Wood-rotting fungi indeed produce enzymes known as "ligninolytic oxidoreductases", often referred to as "ligninases", that play a crucial role in lignin depolymerization and degradation.[106,108] There are several types of ligninolytic peroxidases, including lignin peroxidases (LiP), manganese peroxidases (MnP), and versatile peroxidases (VP), that take part in enzymatic delignification.[111] Ligninolytic peroxidases, as the name implies, are peroxidase enzymes that use hydrogen peroxide (H_2O_2) as a co-substrate to catalyze the oxidation of lignin and lignin-related compounds, as shown in Fig. 5.[106,112] Laccases also have the potential to contribute to lignin breakdown. They are multi-copper oxidase enzymes that use molecular oxygen (O_2) as the primary oxidizing agent. Unlike the peroxidases typically produced by white-rot fungi, laccases can be produced by both white-rot and brown-rot fungi, as well as other microorganisms, and they have a broader range of functions beyond lignin degradation.[66] In general, laccases primarily catalyze the oxidation of phenolic compounds, including lignin. They are less selective for lignin-related compounds as compared with lignin peroxidases, which have a higher specificity for lignin.[112]

Although ligninolytic oxidoreductases are crucial enzymes for lignin degradation in wood-rotting fungi, the wood degradation process is complex, involving the simultaneous breakdown of various components of wood cell walls, including cellulose and hemicellulose, by a combination of enzymes secreted by these fungi. The fungi typically secrete a combination of enzymes, including cellulases and hemicellulases, in addition to ligninolytic oxidoreductases.[113] These enzymes

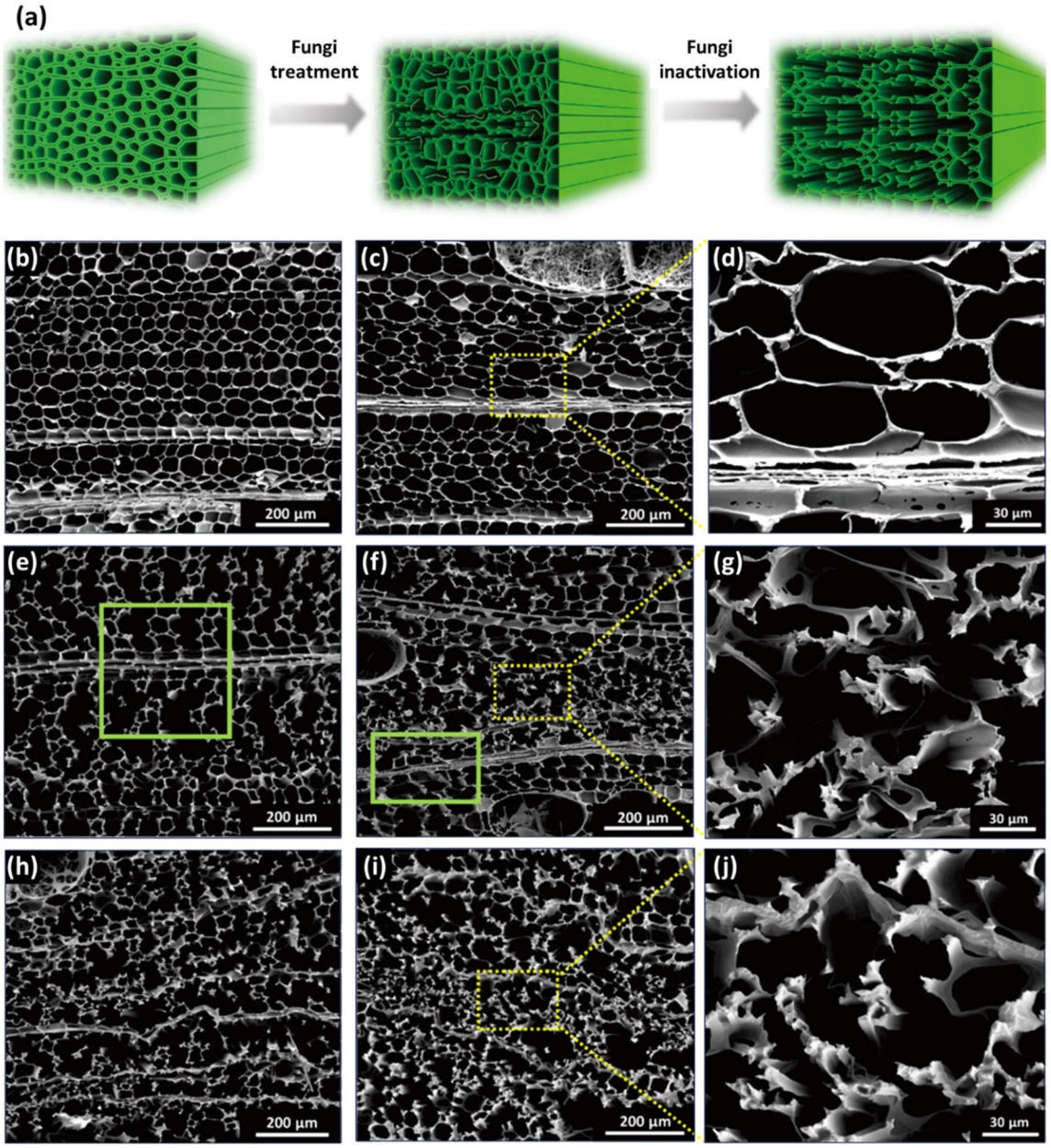

Fig. 4 Morphological changes in balsa wood decaying after exposure to *G. applanatum* fungus. (a) Schematic representation of the transformation of the wood structure during fungal treatment. (b) SEM images at different magnifications obtained from native balsa (0% weight loss). (c and d) Balsa wood after 4 weeks of exposure (15% weight loss). (e) Balsa wood after 6 weeks of exposure (25% weight loss). (f and g) Balsa wood after 8 weeks of exposure (35% weight loss). (h) Balsa wood after 10 weeks of exposure (45% weight loss). (i and j) Balsa wood after 12 weeks of exposure (55% weight loss). (Reproduced from ref. 110 with permission from Science. Copyright 2021.)

target different components of wood, including cellulose and hemicellulose, which make up the carbohydrate portion of wood cell walls. As a result, during the biological pulping (biopulping) process, not only lignin but also hemicellulose components are typically removed from the wood materials.

Compared with other delignification methods, biological depolymerization using enzymes shows a higher degree of selectivity for lignin removal, occurs under milder conditions (in terms of lower temperatures and pH), is more eco-friendly, and can significantly reduce the need for hazardous chemicals. However, it also has limitations related to reaction rate, cost, enzyme stability, yield, and scale-up challenges. Enzymatic reactions are generally slower than chemical reactions, which makes enzymatic delignification a time-consuming process. Moreover, enzymes are often expensive to produce and susceptible to environmental conditions (*e.g.*, temperature and pH), causing them to lose catalytic activity over time.[112]

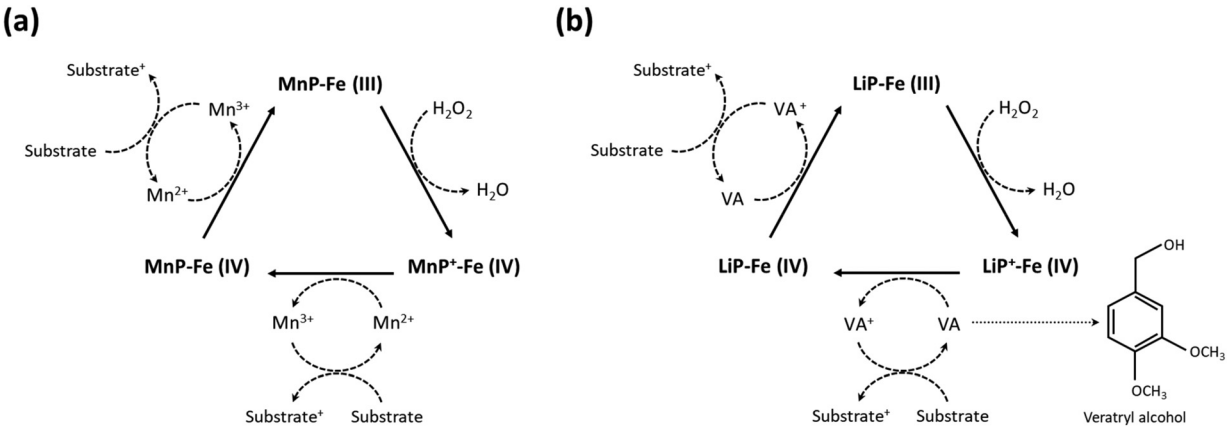

Fig. 5 Enzymatic degradation of lignin in the presence of ligninases. Schematic illustration of (a) the mechanism of lignin degradation by MnP and (b) LiP in the presence of H_2O_2 as a co-substrate. (Reproduced from ref. 112 with permission from Elsevier B.V. Copyright 2019.)

3.2.3. Chemical delignification. Chemical delignification methods that utilize reagents, such as acids or alkaline substances, are indeed the most commonly employed techniques for delignifying wood. These methods have been utilized extensively in various industrial and research applications to remove lignin from wood fibers, making the wood pulp more suitable for paper production, biofuel production, electronics, energy devices, and other applications where lignin removal is essential.[62,63,67,106,114] Wood delignification processes, comprising a range of pulping and bleaching reactions, can be systematically classified into nucleophilic and electrophilic categories based on the structural changes of lignin.[66] Nucleophilic reactions involve electron-rich species attacking electron-deficient sites, whereas electrophilic reactions involve electron-poor species targeting electron-rich centers. These distinctions play a significant role in delignification chemistry.

Pulping is primarily driven by the activity of external nucleophilic species (*e.g.*, OH^-, HS^-, HSO_3^-, and SO_3^-), which target electron-deficient centers in the carbonyl and conjugated carbonyl (enone) structures. These nucleophilic reactions involve using the delignifying reagent's electron pair to form chemical bonds with lignin. Pulping also involves neighboring nucleophilic groups attacking the β-carbon atom of side chains. In contrast, the initiation of bleaching involves electrophilic species, including cations (*e.g.*, Cl^+ from Cl_2, protonated HOCl and HO^+ from protonated H_2O_2 or CH_3COOOH) and radicals (*e.g.*, $Cl^\bullet$, $ClO_2^\bullet$, $HO^\bullet$, and $HOO^\bullet$) targeting the electron-rich centers in the aromatic nuclei and unsaturated ring-conjugated side chains. Compared with the nucleophilic-based pulping mechanism, electrophilic reactions entail the acceptance of an electron pair or an unpaired electron by the delignifying reagent to facilitate the bond formation to lignin.[66] These initial electrophilic-based bleaching reactions can be followed by nucleophilic ones, occurring either concurrently or in the subsequent bleaching stages. This systematic division is useful to form an understanding of the fundamental chemistry and mechanisms underlying delignification. It also aids in the strategic development and fine-tuning of delignification techniques tailored to specific applications.

3.2.3.1. Alkaline pulping. Wood pulping methodologies mainly comprise a series of chemical reactions taking place in alkaline media, which can be divided into soda pulping (NaOH only solution), Kraft pulping (NaOH and Na_2S), and sulfite pulping (NaOH and Na_2SO_3). In essence, the stability of the β-O-4 ether bonds, the most prominent linkage in lignin, varies under different pH conditions. Under acidic conditions, cleavage of the lignin structure primarily occurs at α-substituents, due to the lack of strong nucleophiles. However, in alkaline or even neutral media, strong nucleophilic species, including hydroxide (OH^-), sulfite (SO_3^{2-}), bisulfite (HSO_3^-), and hydrogen sulfide (HS^-) ions, are produced, making possible the cleavage of ether bonds in lignin.[66,68] During the resulting partial delignification produced by these methods, alkali treatment induces depolymerization of the lignin structures, resulting in the fragmentation and degradation of lignin macromolecules, as well as structural modification by introducing hydroxyl groups to make lignin more hydrophilic.

Generally speaking, hydroxide ions play a critical role in the delignification process by promoting the fragmentation and solubilization of lignin *via* two significant reactivity patterns in the structures. Hydroxide ions facilitate the deprotonation of hydroxyl groups in both phenolic and aliphatic moieties, as well as being involved in nucleophilic addition reactions in the aliphatic regions of lignin. These ions induce the cleavage of specific bonds, namely α-aryl ether bonds (in phenolic units) and β-aryl ether bonds (in non-phenolic units), in lignin and they catalyze the cleavage of certain C–C bonds.[115] It has also been shown that the addition of sodium sulfide (Na_2S) or sodium sulfite (Na_2SO_3) to the alkaline solution plays a significant role in lignin degradation. The sulfide ions and SO_3^{2-} form a series of active sulfur species, including hydrosulfide ions (HS^-), that can break down lignin by cleaving β-aryl-ether linkages, increasing the rate of the delignification process.[115]

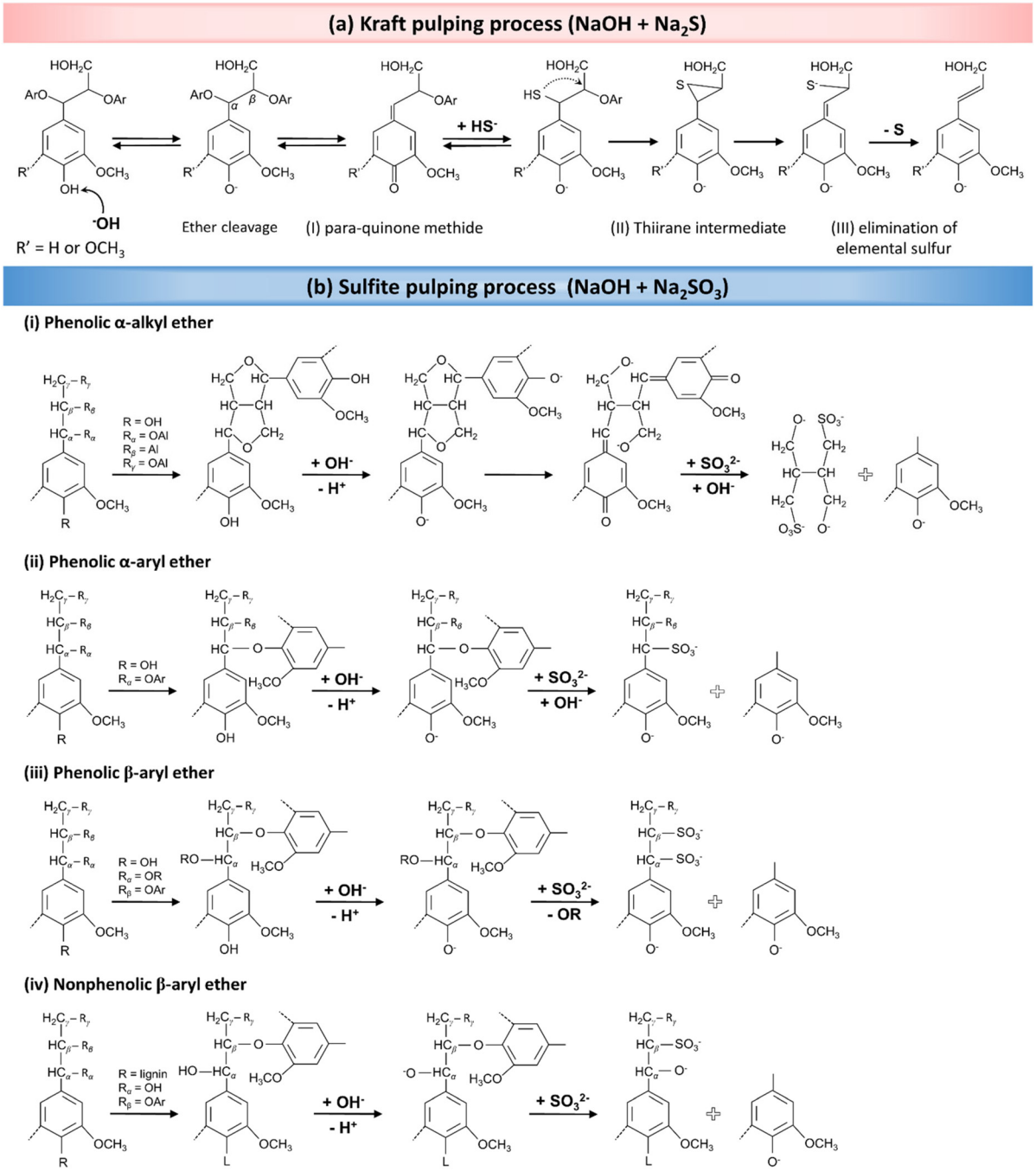

Fig. 6 The delignification mechanism during pulping processes. (a) Wood pulping reactions in the presence of an alkaline solution of Na_2S (Kraft pulping). (Reproduced from ref. 66 with permission from WILEY-VCH Verlag GmbH & Co. Copyright 2020.) (b) The mechanism for partial *in situ* lignin removal in a solution containing NaOH and Na_2SO_3 (sulfite pulping process). (Reproduced from ref. 68 with permission from the American Chemical Society. Copyright 2021.)

As presented in Fig. 6a, the Kraft pulping process utilizes OH^- and HS^- ions as nucleophiles to break down lignin macromolecules through a series of nucleophilic reactions. The process begins with the formation of para-quinone methide *via* the elimination of α-aryl ether from the phenolic β-aryl ether unit (Fig. 6a-I). Thereafter, a thiol structure is formed in the presence of hydrosulfide anions as nucleophiles, leading to the formation of a thiirane complex intermediate *via* a neighboring group participation reaction (Fig. 6a-II). Following the addition reaction, elemental sulfur in the thiirane complex gradually dissociates, resulting in the degradation of side chains of lignin molecules (Fig. 6a-III). The cleavage of phenolic β-aryl ether bonds is a key step in determining the rate of the overall reaction. These reactions

collectively result in the partial delignification of the wood.[66,68]

In the context of sulfite pulping, which employs Na_2SO_3 in an alkaline solution, a consecutive series of analogous chemical reactions occurs. As mentioned earlier, lignin exhibits a complex chemical structure primarily composed of phenolic compounds, encompassing α-alkyl, α-aryl, and β-aryl ether functional groups, along with nonphenolic β-aryl ether structures. The ionization of lignin's phenolic hydroxyl groups in an alkaline medium generates phenolate anions. These phenolate anions, carrying a negative charge, resonate with the π-electron system of the phenolic compound's aromatic ring. This resonance facilitates the formation of quinone methide structures when α-carbon atoms are cleaved, particularly in phenolic α-alkyl or α-aryl ether units. Subsequently, SO_3^{2-} (potential electrophiles) attacks the α-carbon atom in the quinone methide structure. This attack leads to the cleavage of side chains in the phenylpropane structures, ultimately resulting in the fragmentation of lignin into aryl and alkyl portions. The proposed mechanisms for these reactions are shown in Fig. 6b-i and ii.[68]

In addition to α-alkyl and α-aryl ether reactions, β-aryl ether (phenolic or nonphenolic) units also play a crucial role in partial wood delignification, undergoing nucleophilic reactions due to their high reactivity (Fig. 6b-iii and iv). The cleavage of β-aryl ether bonds in phenolic units produces lignosulfonates, which again results from the rupture of α-ether bonds and the subsequent formation of quinine methide compounds. As indicated in Fig. 6bii–iv, the cleavage of aryl ether bonds results in the formation of lignin-based structures, which are also susceptible to similar fragmentation reactions.[68,116] The ultimate result of these reactions is the enhanced solubility of lignin, achieved by introducing SO_3^{2-} (sulfonation) into its structure, leading to the partial removal of lignin from the wood. It should be taken into consideration that, although we are discussing the lignin degradation mechanisms, a significant amount of hemicellulose is concurrently removed during the delignification process.[117]

Several strategies have also been adopted in conjunction with alkaline treatment to increase the integrity and mechanical strength of the final DW. For instance, Li *et al.* presented a cross-linking method for creating porous cellulose scaffolds from spruce wood while preserving its natural cellular structure.[118] To this end, the spruce wood samples were treated by boiling in an NaOH solution (1%, w/v) for 6 h. The polysaccharides in the cell wall of the partially delignified samples were cross-linked with 1,4-butanediol diglycidyl ether (BDDE) or poly(ethylene) glycol diglycidyl ether (PEGDGE), in order to improve the adhesion between tracheids. This process enabled lignin molecules to be completely removed without causing any damage to the structural integrity of the wood. Another study conducted by Xiao *et al.* demonstrated that re-swelling the DW chips in a rapid water-shock process led to the selective opening of the vessels, creating a unique wrinkled cell wall structure.[119] Basswood samples were firstly treated by sulfite pulping (boiling in 2.5 M NaOH and 0.4 M Na_2SO_3 for 48 h), which removed significant portions of lignin (≈55%) and hemicellulose (≈67%) from the cell walls. The wood samples were dried, resulting in the vessels and fibers shrinking. A "shocking" step, immersing the chips in water for 3 min, selectively opened the vessels, creating the distinctive wrinkled structure. This process partially re-swells the cell walls and causes expansion in the dimensions of the resulting product, termed "moldable wood", which contains around 100% of its weight in water. This chemical engineering process enables the materials to be easily folded and molded into any desired shapes, while maintaining their original anisotropies.

3.2.3.2. Bleaching methods. Bleaching methods employing chlorine-based reagents (*e.g.*, $NaClO_2$ and NaClO) are among the most widely utilized delignification techniques, owing to their exceptional selectivity in targeting lignin while preserving the cellulose integrity. In an acidic solution, $NaClO_2$ undergoes conversion into chlorine dioxide (ClO_2), which serves as the primary oxidizing agent responsible for lignin removal during the delignification process. The use of buffer solutions, particularly an acetate buffer with a pH range of 4.5–4.8, is hence essential for the conversion of $NaClO_2$ into ClO_2, as well as stabilizing and controlling the pH to ensure that the reaction proceeds effectively. ClO_2, a strong oxidizing agent, can react with lignin's phenolic hydroxyl groups *via* a radical reaction, resulting in the formation of phenoxy radicals (Fig. 7a-I). This reaction typically involves one-electron transfer processes that simultaneously reduce ClO_2 to chlorite. In the next step, ClO_2 molecules can be added to the phenoxy radicals, forming hypochlorous esters (Fig. 7a-II). These esters are intermediate compounds in the degradation of lignin. Following a hydrolysis reaction at the aromatic ring moieties of lignin and the resulting aromatic ring opening, hypochlorous acid is liberated, and a muconic acid derivative generated. This aromatic ring cleavage is a significant aspect of lignin degradation during bleaching. In addition, ortho-quinone structures can be produced in another pathway. Thus, ClO_2 can disrupt the bonds between aromatic rings and side chains, resulting in the fragmentation of lignin molecules into smaller, more soluble fragments.[66,68,120]

Although chlorine-based delignification methods can be effective at achieving a high degree of lignin removal with good selectivity, they are accompanied by significant environmental drawbacks, since they produce large amount of hazardous chlorine wastes. This issue has prompted the exploration of environmentally friendly alternatives (*e.g.*, H_2O_2), which ensures effective delignification, as its decomposition yields only oxygen and water, avoiding the production of hazardous byproducts associated with chlorine-based methods.[121] As mentioned above, during bleaching methods, electrophilic species target the electron-rich centers typically found in aromatic nuclei and unsaturated ring-conjugated side chains in lignin molecules. In the presence of H_2O_2, various active species can form, including both hydroperoxide (HOO^-) ions and superoxide ($O_2^{\bullet-}$) and hydroxide ($HO^\bullet$) radicals. These species are highly reactive, and they can participate in chemical reactions, particularly in processes involving the degra-

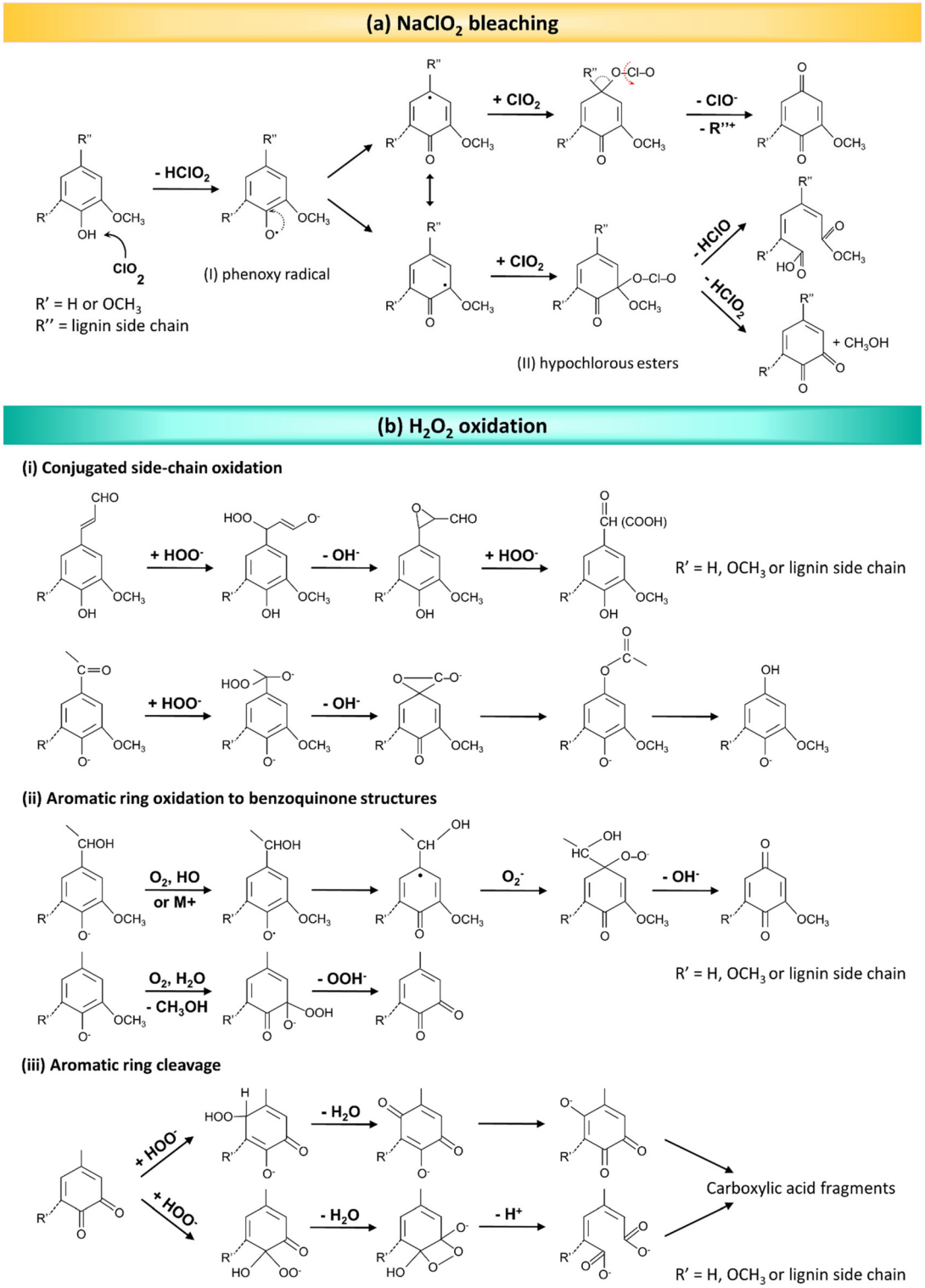

Fig. 7 The delignification mechanism during bleaching processes. (a) The lignin oxidation mechanism by ClO_2. (Reproduced from ref. 66 with permission from WILEY-VCH Verlag GmbH & Co. Copyright 2020.) (b) Various reactions that take place in the presence of H_2O_2 in the course of delignification. (Reproduced from ref. 120 with permission from WILEY-VCH Verlag GmbH & Co. Copyright 2015.)

dation or modification of organic compounds, such as lignin (Fig. 7b).[120] HOO^- ions show high chemical reactivity, and play a predominant role in the oxidative cleavage of chemical bonds in lignin molecules, including those between aromatic rings and side chains, as shown in Fig. 7b. This causes the fragmentation of lignin into small molecular aliphatic com-

pounds, along with carbonyl and carboxyl compounds. These fragments and compounds are typically more water-soluble, and they can be easily removed from the cellulose fibers, resulting in a bright and white final product.

Previous investigations have revealed that H_2O_2 is a more reactive oxidizing agent than molecular oxygen.[68] As a result, chemical reagents, such as transition metal species (*e.g.*, iron, copper, and manganese), that are capable of decomposing H_2O_2 into O_2 exert a detrimental influence on the overall delignification rate.[106] However, certain metal-based chemicals, including $MgSO_4$ and Na_2SiO_3, can act as H_2O_2 stabilizing agents, protecting the lignin from decomposition.[120] It is worthy of mention that the *in situ* delignification process using H_2O_2 is generally conducted under alkaline conditions to balance lignin removal with the protection of cellulose fibers. It has been shown that alkaline–H_2O_2 treatment can be used for wood modification by removing mainly chromophoric structures, rather than lignin removal through oxidative ring-opening reactions, as in the case of $NaClO_2$-based delignification processes.[85] The treatment of balsa wood samples using 1 wt% $NaClO_2$ in an acetate buffer solution (pH 4.6) at 80 °C for 6 h resulted in a 90% decrease in lignin content (from 23.5% to 2.5%). In terms of the H_2O_2 (in 3 wt% NaOH solution at 70 °C) method, this treatment approach led to a transparent wood after treatment for only 2 h, while preserving 80% of the initial lignin content (from 23.5% to 21.3%). Hence, this lignin treatment method is an efficient process that largely retains lignin, thereby preserving the wood structure, enhancing the mechanical properties of lignin-modified wood templates, and promoting environmental friendliness by minimizing the toxic effluents.

Another innovative strategy for *in situ* lignin modification entails oxidizing the lignin in the wood using H_2O_2 and UV light.[86] The photocatalytic oxidation approach is able to selectively remove lignin's chromophores while preserving their aromatic skeletons. By harnessing lignin's UV light-absorption and photoexcitation properties, a simple rapid yet scalable method has been proposed for the selective elimination of lignin chromophores. The process involves the generation of chromophoric radicals ($Lig^{\bullet}$) resulting from the cleavage of conjugated double bonds in lignin in the presence of UV light, which primarily acts as a photocatalyst.

UV radiation also accelerates the breakdown of H_2O_2 into oxygen/peroxy radicals ($O^{\bullet}$/$HOO^{\bullet}$). The photoexcited radicals engage in the UV-assisted photocatalytic oxidation of lignin, resulting in the formation of non-conjugated carboxyl groups. The slight decrease in the lignin content of the wood is attributed to the minor ring-opening reactions that are able to produce small soluble molecules in an H_2O_2 aqueous solution. This process maintains the lignin's structural integrity and ensures the retention of mechanical strength.

Several studies have also been conducted into the combination of pulping and bleaching methods, with the aim of increasing the delignification efficiency and producing higher quality pulp with improved strength properties. Alkaline pulping is effective at removing a significant portion of lignin from wood fibers. However, it may not achieve complete delignification on its own. Bleaching processes, which often involve the application of chlorine-based species and H_2O_2, can remove more residual lignin and brighten the pulp. Combined treatments are generally associated with the significant removal of both lignin and hemicellulose from the natural wood structure.[64,117,122–124] Table 4 lists the reaction conditions that have been used in different delignification protocols for various wood species, along with the resulting changes in the chemical composition of the wood.

3.2.3.3. Ionic liquids (ILs) and deep eutectic solvents. ILs have shown promise as potential solvents for the delignification process, and are composed of large, asymmetric organic cations and organic or inorganic anions. Their unique physicochemical properties, including low volatility, high thermal stability, and high solvating power for a wide range of compounds, make them attractive candidates for wood biomass dissolution.[106,125] ILs have demonstrated the ability to dissolve cellulose, and this property is attributed to their ability to disrupt both intermolecular (between different cellulose molecules) and intramolecular (within a single cellulose molecule) hydrogen bonds that hold cellulose fibers together. New hydrogen bonds are also formed between the hydroxyl groups of carbohydrates and the anions present in the ionic liquid. This process allows the individual cellulose chains to disperse in the ILs, effectively solubilizing them. The extent to which cellulose can be dissolved in ILs depends on various factors, *e.g.*, both the size and polarization of the anions and the specific characteristics of the cations. Different combinations of cations and anions can produce varying levels of cellulose dissolution.[5,126,127] Ionic liquid extraction has been devised for the separation of hemicellulose from wood substrates as well.[128,129]

In the same way as the holocellulose constituent, the polar components of ILs can form hydrogen bonds with lignin. The ionic parts of ILs can interact with the hydroxyl groups in lignin, weakening the hydrogen bonds that hold the lignin structure together. Taking this ability of ILs into consideration, imidazolium-based IL, namely 1-ethyl-3-methylimidazolium acetate ($[C_2mim]OAc$), has been successfully utilized to remove lignin from both softwood and hardwood species; a 26.1% and 34.9% lignin reduction was observed in southern yellow pine and red oak samples, respectively.[130] The delignification process was conducted under heat treatment at 110 °C; however, the results revealed that applying pretreatment techniques, such as microwave pulses or ultrasound irradiation, accelerated the dissolution rate. The exact IL-based delignification mechanism can vary, depending on the type of IL. The process is also influenced by factors, such as temperature, pressure, and reaction time. It is worthy noting that, although ILs offer exciting potential for lignin delignification, there are still challenges to be addressed, including the cost of ILs, the need for high temperatures (90–170 °C), and their potential environmental pollution.[63,125]

Deep eutectic solvents (DESs) are recognized as an emerging subclass of ILs based on their similar characteristics and

Table 4 Various wood delignification methods used for lignin removal from different wood species with reaction conditions

	Advantages and disadvantages	Wood species	Delignification condition	Changes in wood composition	Ref.
Alkaline pulping	**Soda pulping (NaOH)**				
	✓ Mild condition	Beech	- Immersion in an NaOH solution (15%, w/v) for 1 h, followed by washing with water while stirring for 24 h until the pH value reached 9	N/A	140
	✓ Simple process	Spruce	- Hydrothermal reaction in autoclaves using a solid to liquor ratio of 1 : 100	Lignin content:	141
	✓ Good cellulose preservation		- Cooking liquor composed of an NaOH solution (3%, w/v)	0 min: 30.7%	
	× Low delignification efficiency		- Deaerated and pressurized autoclave (under vacuum for 5 min and 5 bar with nitrogen gas for 5 min) was kept at 170 °C for different time periods	After 90 min: 19.8%	
	× Limited to certain wood types			After 180 min: 17.3%	
		Aspen woodchips	- In an M/K circulation digester with a temperature of 150 °C - In the presence of an effective alkali solution (20%, w/v) and liquor-to-wood ratio of 4.5 : 1 for 3 h	27.5% of total lignin mass	142
	Kraft pulping (NaOH + Na_2S)				
	✓ High delignification efficiency ✓ Chemical recycling × Environmental impact × Energy-intensive	Hoop pine	- An NaOH + Na_2S solution (25% active alkali, 25% sulfidity) at 120 °C or 135 °C for 4 h	Total weight loss: 20%	122
	Sulfite pulping (NaOH + Na_2SO_3)				
	✓ High-quality pulp ✓ Adaptable for different wood types × Environmental concerns	Basswood, oak, poplar, western red cedar, eastern white pine	- Immersion of natural wood blocks in a boiling aqueous solution of NaOH (2.5 M) and Na_2SO_3 (0.4 M) for 7 h - Subsequent immersion in boiling water several times to remove the chemicals	Lignin content: - Before: 20.8 ± 1.2% - After: 11.3 ± 0.5%	143
	× Limited to hardwoods	Balsa	- Immersion of wood slices in a boiling mixed aqueous solution (2.5 M NaOH and 0.4 M Na_2SO_3) at 85 °C for 2 h, then in ethanol several times to remove the chemicals	N/A	116
		Basswood	- Treating with a boiling aqueous solution of NaOH (2.5 M) and Na_2SO_3 (0.4 M) for 48 h, followed by immersion in water several times to remove the chemicals	Removed ≈55% of the lignin and ≈67% of the hemicellulose	119
		Basswood	- Dipping in a mixed solution of NaOH (2.5 M) and Na_2SO_3 (0.4 M) at 100 °C for 5 h, followed by washing with water to remove the residual chemicals	N/A	144
		Willow wood	- Boiling natural pieces in a solution of 2.5 M NaOH and 0.4 M Na_2SO_3 for 8 h, followed by rinsing with water to remove the chemicals	N/A	145

Table 4 *(Contd.)*

	Advantages and disadvantages	Wood species	Delignification condition	Changes in wood composition	Ref.
Bleaching methods	**Chlorine-based bleaching ($NaClO_2$ and NaClO)**				
	✓ Effective delignification	Hoop pine veneers	- Treating the veneers with a $NaClO_2$ solution (2%, w/v, pH = 4.5) at 45 °C for 12 h. The treatment was repeated up to 3 times and finally rinsing in running water for 2 h	Total weight loss: 24.3%	122
	✓ Low cost	Beech	- Immersion in a delignifying solution containing $NaClO_2$ (3%, w/v) in an acetate buffer solution (0.2 M, pH 4.6) at 60 °C for 48 h, followed by washing using water for 10 min	N/A	146
	× Environmental harm	Balsa	- Immersing the native wood in a solution containing NaClO (1%, w/v) in an acetate buffer (pH 4.6) for a period of 18 h, during which the buffer solution was renewed every 6 h	Lignin removal: ≈90%	147
	× Potential cellulose degradation	Balsa	- Immersion of wood blocks in an NaClO solution (1%, w/v) buffered with an acetate solution (pH = 4.6) overnight at room temperature, followed by heating at 80 °C for 24 h	N/A	148
		Natural wood	- Soaking the wood cubes in a solution of NaClO (5%, w/v) and acetic acid (1%, v/v) for 12 h, heating the samples twice in a 60 °C water bath for 8 h. The prepared white wood (WW) was soaked in 75% alcohol for 4 h and washed in water three times	Total weight loss: 24.8% (equivalent to the natural weight percentages of lignin and hemicellulose in wood)	149
	H_2O_2 oxidation				
	✓ Eco-friendly	Balsa	- Mixing chemicals in the following order: water, sodium silicate (3%, w/v), NaOH solution (3%, w/v), $MgSO_4$ (0.1%, w/v), DTPA (0.1%, w/v), then H_2O_2 (4.0%, w/v)	Lignin content	85
	✓ Effective brightening		- Submerging the wood substrates in the lignin modification solution at 70 °C until WW was achieved, followed by thorough washing with water	- Before: 23.5%	
	✓ No toxic byproducts			- After: 21.3% (weight loss: 12%)	
	× Higher cost	Balsa	- Immersion in an alkaline solution of 30% H_2O_2 containing 10 wt% NaOH	- Initial lignin content: 23.5%	86
	× Less effective when used alone		- The pretreated material was exposed to UV light (power = 20 W) until the samples became completely white	- After 2 h UV exposure: 19.29% (retaining 82.08% of the original lignin)	
	Combined delignification				
	✓ High efficiency	Balsa	- Immersion of wood slices in a 2 wt% solution of $NaClO_2$ in acetic acid (pH ≈ 4.6) and boiling for 2 h, then washing with DI water	Total weight loss: 50.3 ± 0.4 wt%	64
	✓ Tailored properties		- Reimmersion in an NaOH solution (15%, w/v) and keeping them at room temperature for 2 h, neutralizing using ethanol and distilled water		
	✓ Reduced environmental impact	Balsa	- Immersion in a boiling mixed aqueous solution (2.5 M NaOH and 0.4 M Na_2SO_3) for 7 h, followed by immersion in boiling water several times to remove the chemicals	Total weight loss: 79%	117
	× Complexity		- Treating with boiling H_2O_2 (2.5 M in water) for a few hours		
	× High costs	Hoop pine veneers	- Treatment at 45 °C with a 1 or 2% $NaClO_2$ aqueous solution (pH ≈ 4.5) for 12 h, repeated 3 times	Total weight loss: 29.8%	122
	× Integration challenges		- Soaking in a 0.1% NaOH solution at 20 °C for 24 h		

Table 4 *(Contd.)*

Advantages and disadvantages	Wood species	Delignification condition	Changes in wood composition	Ref.
	Poplar	- Immersion in an aqueous solution of NaOH (3.0 wt%) and Na_2EDTA (0.1 wt%) and heating at 70 °C for 10 min - Addition of $MgSO_4$ (0.1 wt%) followed by H_2O_2 (4.0 wt%) and further heating until WW was achieved - Boiling in DI water to remove the residual chemicals	- Before: 23.5 ± 1.1% - After: 20.6 ± 0.9% (preserving about 88% of the lignin)	150
	Balsa	- Cooking the wood blocks in a mixture solution of NaOH and Na_2SO_3 at 100 °C for 5 h - Boiling in the H_2O_2 solution to remove the residual lignin completely	Total weight loss: 65% Cellulose: 37.5% → 27.5% Hemicellulose: 14.9% → 1.9% Lignin: 26.2% → 0.2%	123
	Balsa	- Immersion in an $NaClO_2$ solution (2%, w/v) buffered with acetic acid at pH 4.6 and heating at 100 °C for 8 h - Re-immersion in an NaOH solution (5%, w/v) at 80 °C for various periods of time (4, 8, and 12 h) to remove the hemicellulose content	Relative contents: Cellulose: 41.4 → 81.3 wt% Hemicellulose: 36.3 → 9.6 wt% Lignin: 20.1 → 0.1 wt%	124
Ionic liquids (ILs)				
✓ Highly selective ✓ Eco-friendly ✓ Versatile × High cost × Limited industrial scale	Southern yellow pine (softwood), red oak (hardwood)	- Adding 0.5 g of wood chips to 10 g of $[C_2mim]OAc$ in a 50 mL beaker, heating the mixture in an oil bath under vigorous magnetic stirring (700 rpm) at 110 °C for 16 h in the open air	Reduction in lignin content: - Pine wood: ≈26.1% - Oak: ≈34.9%	130
	Balsa	- Mixing ChCl and oxalic acid at 80 °C for 1 h (molar ratio 1 : 1) - Immersion of wood chips in ChCl/oxalic acid DES with a weight ratio of 20 : 1, microwave-assisted heating (800 W) for 10 min - Bleaching with a boiling solution of sodium silicate (3%, w/v), NaOH solution (3 wt%), magnesium sulfate (0.1 wt%), EDTA (0.1 wt%), and H_2O_2 (4 wt%)	Lignin content: 27.8 → 2.3 wt% (>90 wt% of the lignin in the original wood)	132
	Poplar	- Heating the wood samples in DES (ChCl and lactic acid prepared under reduced pressure at 80 °C) to 90 °C for 12 h, washing three times at room temperature with ethanol (100 mL)	Lignin content: - Before: ≈22% - After: ≈10%	133

NA: not applicable.

properties. Although sometimes used interchangeably, the chemical composition of ILs and DESs differs, since DESs are designer solvents composed of a mixture of Lewis or Brønsted acids and bases. The strong hydrogen bonds between the hydrogen bond acceptor (HBA) and hydrogen bond donor (HBD) species give rise to solvents with distinctive characteristics, including low vapor pressure, a relatively wide liquid range, and nonflammability.[131] Compared with conventional ILs, many DESs can be synthesized using cost-effective, readily accessible, environmentally friendly compounds with low or negative toxicity. This makes them attractive options for various applications, including partial or total wood delignification.[132–134] However, the efficiency of DESs in breaking the complex connections of lignin–carbohydrate complexes (LCCs) and separating the lignin components is highly dependent on their chemical composition and capacity to form hydron bonds.[135] For instance, choline chloride (ChCl), which is a quaternary ammonium halide salt and a powerful HBA compound, has been widely used in conjunction with various HBDs (*e.g.*, oxalic, malic, and lactic acid) to prepare DESs for the efficient fractionation of lignin.[133,134] Among the three named hydrogen bond donors, lactic acid has shown a superior ability to dissolve lignin, due to the efficiency of the acid–base catalytic reactions responsible for the selective cleavage of unstable ether bonds between the phenylpropane units of lignin.[134] However, the choice of glycerol as a potential hydrogen bond donor, along with ChCl to prepare a DES, has shown inferior ability to remove lignin from wood species.[136,137] Theoretical studies using density functional theory (DFT) and the Kamlet–Taft solvatochromic method have revealed that the ChCl–glycerol (1 : 2) DES has relatively weak interaction with the linkages in the LCC network.[135] This phenomenon can be attributed to the fact that the hydrogen bonds in the ChCl–glycerol are restricted by both negatively charged anionic ($[Cl(glycerol)]^-$) and positively charged cationic ($[Ch(glycerol)]^+$) H-bonds, limiting the capacity of the anions at occupied sites to accept hydrogen bonds. The prepared DES also lacks the active protons and acidic sites required to break the ether bond linkages in the LCCs. In general, using a deep eutectic solvent with high hydrogen-bond acidity can increase delignification efficiency.[138]

Combining DESs with microwave irradiation plays a crucial role in improving the fractionation of lignocellulosic biomass, due to a notable synergistic effect.[132,138] Bi *et al.* have demonstrated that a DES prepared by mixing oxalic acid dihydrate and ChCl at a molar ratio of 1 : 1 was able to selectively remove hemicellulose and lignin from balsa wood while showing poor solubility to cellulose.[132] The results revealed that using a two-step delignification method in which wood slices were firstly immersed in DESs under microwave-assisted treatment followed by alkaline–H_2O_2 bleaching could remove the lignin content of balsa wood effectively up to more than 90 wt%. The same solvent system (*i.e.*, the ChCl–oxalic acid dihydrate DES with a hydrogen-bond acidity of 1.31) effectively extracted 80% of the total lignin of poplar wood flour after only 3 min of microwave irradiation (800 W) at 80 °C.[138]

It is worthy of mention that the delignification strategies induce structural and morphological alterations in the intricate composition of wood tissues, as well as cells and cell walls. The nanoscale arrangement of cellulose, hemicellulose, and lignin components results in a tightly interconnected network, precluding the selective removal of lignin from the cell wall *via* chemical routes. Consequently, the chemical removal of lignin also impacts hemicellulose units that are closely associated with lignin moieties. In other words, although we always refer to "delignification", all the above-mentioned processes affect and dissolve wood's hemicellulose content to a certain extent. The delignification process also likely induces modifications in the cellulose–hemicellulose network due to spatial reorganization within the cell wall, compared with native wood templates.[66,139] Special attention should be paid to the degree of delignification, since substantial removal of lignin and hemicellulose contents would cause a brittle DW without sufficient structural integrity.

4. Chemical characterization techniques: unveiling the structural transformations

The comprehensive assessment of decellularized plant tissues and DW products necessitates a precise examination of their chemical composition and structural integrity. This assessment plays a critical role in understanding the decellularization and delignification processes. To reveal the intricate transformations at both macro- and micro-level, an array of advanced characterization techniques can be employed. These techniques, ranging from staining methods to spectroscopic analysis, enable researchers to probe alterations in molecular constituents, crystalline structures, and morphological features. In this section, the objective is to shed light on each of these characterization methodologies and elucidate how they contribute to the design and optimization of decellularized plant tissues and DW products.

4.1. Characterization of decellularized plant skeletons

As mentioned earlier, the decellularization process involves removing cellular materials from plant tissues. The initial manifestation of decellularization is characterized by the transition of the plant scaffold into a translucent state, as shown in Fig. 8a–e for various plant species.[28,60] The resulting optical transparency in the decellularized matrix is due to the effective removal of cellular constituents and residual debris. The colorless, "ghost-like" structure is typically achieved by stripping away pigments and chlorophyll contents. This transformation is significant, as it provides a better view of the plant's underlying structure and extracellular matrix.[28,53]

Although pigmentation loss and color alteration can serve as initial indicators of successful decellularization, the precise extent of this process necessitates evaluation using more specialized methodologies. Morphological and

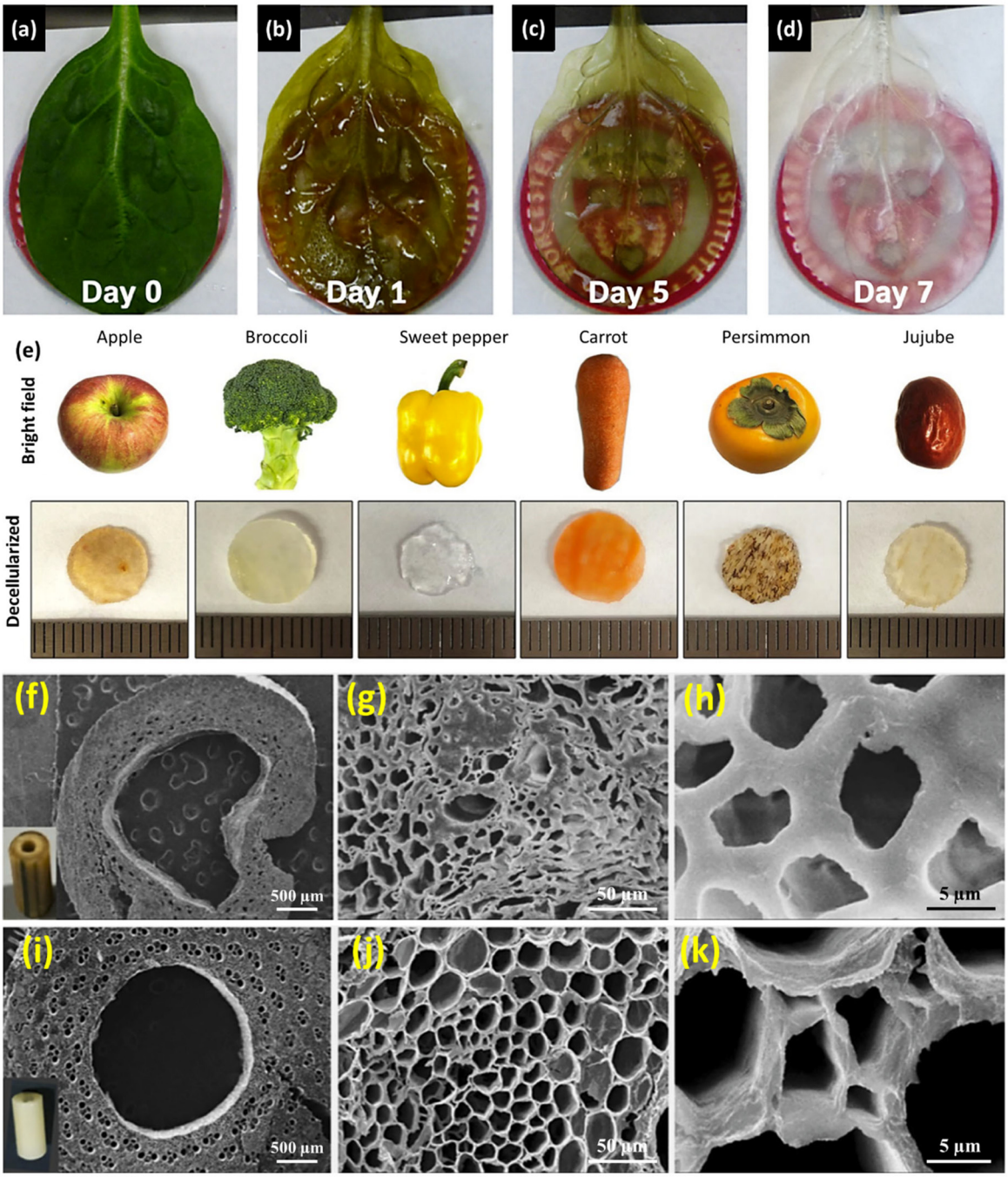

Fig. 8 Changes in the appearance and morphological structures of plant tissues before and after decellularization. (a–d) Spinach leaf decellularization after 5 days of SDS treatment, followed by 2 days of perfusion with Triton X-100/$NaClO_2$ clearing solution. (Reprinted from ref. 28 with permission from Elsevier Ltd. Copyright 2017.) (e) Various decellularized samples using an SDS solution (0.5%, w/v) for 48 h. (Reprinted from ref. 60 with permission from Springer Nature. Copyright 2019.) (f–h) SEM images of fresh bamboo stem, and (i–k) decellularized stem treated with hypochlorite for 72 h at different magnifications. (Reproduced from ref. 55 with permission from Elsevier B.V. Copyright 2020.)

structural characterization techniques, in particular SEM, have been widely utilized to assess the degree of decellularization.[33,36,48,57,60]

The decellularization process ideally entails the comprehensive removal of cellular constituents from plant tissues while preserving the native structural frameworks and vascular networks. The internal porous architecture and the hierarchical pore morphology of the scaffolds can be observed reliably by means of SEM imaging of the decellularized specimens. Successful decellularization manifests as the absence of any disruptions to pore walls or alterations in the morphological configuration, and discernible effects, such as the develop-

ment of thinner walls and enlarged pore dimensions, can also be detected from SEM images (Fig. 8f–k).[55] The changes in surface roughness after decellularization can be investigated using atomic force microscopy (AFM).[31,33,48]

Histochemical analyses utilizing fluorescent dyes represent another valuable approach for evaluating plant decellularization efficacies. This method involves the application of various dyes to enable the direct visualization of cellulose, lignin, and pectin contents in the cell walls, observed by using fluorescence microscopy. Selecting appropriate dyes enables the targeted labeling of specific cellular components or structures in the plant tissues. Calcofluor white, for instance, exhibits binding affinity to cellulose and chitin (prominent constituents of plant cell walls), thereby enabling the visualization of the residual cell wall materials in the decellularized tissues.[32,35,38,49]

Fig. 9a shows confocal fluorescence microscopy images of the isotropic cellulose scaffolds acquired in transverse directions from different vegetables and fruits post-decellularization.[35] Safranin O has been widely employed for staining cellulosic materials.[28,151] Furthermore, specific fluorescent dyes, such as fast green FCF, toluidine blue, and ruthenium red, provide specific stains for lignin, pectin/lignin, and pectin, respectively, enhancing the comprehensive assessment of the decellularization process.[28,57]

The effective elimination of genetic materials from plant structures following decellularization can be verified through histological analysis. This analytical approach is based on the utilization of dyes capable of binding to the specific cellular components, including hematoxylin and eosin (H&E), Hoechst 33342, and 4′,6-diamidino-2-phenylindole (DAPI). Hematoxylin

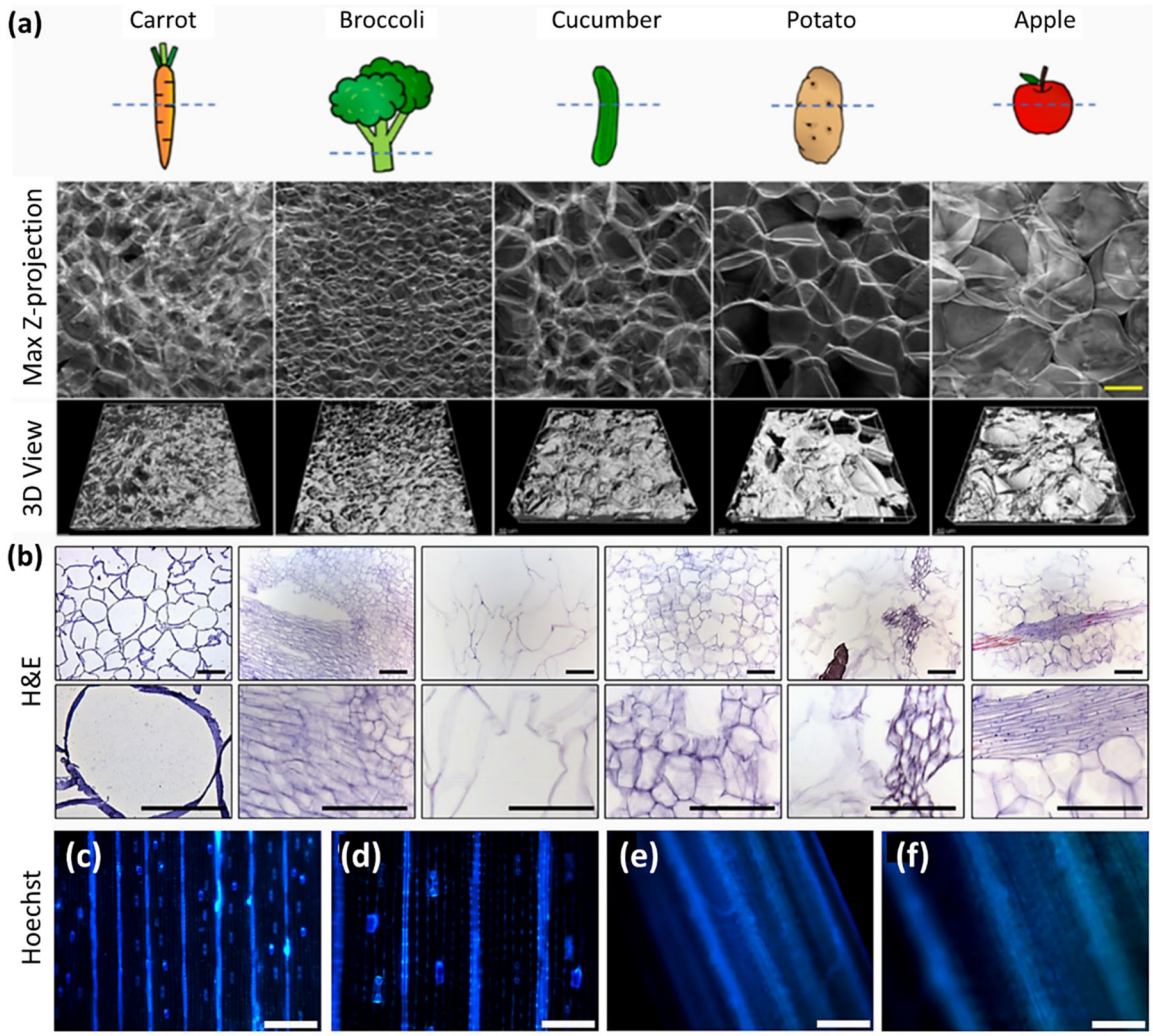

Fig. 9 Histochemical and histological analysis of decellularized plants. (a) Fluorescent images of the isotropic cellulose structure in various decellularized vegetable and fruit samples stained with Calcofluor white dye. (Reprinted from ref. 35 with permission from the American Chemical Society. Copyright 2020.) (b) H&E-stained images obtained from cellulose-based scaffolds, from left to right: apple, broccoli, sweet pepper, carrot, persimmon, and jujube samples at 200× and 400× magnification. (Reprinted from ref. 60 with permission from Springer Nature. Copyright 2019.) Hoechst 33342 staining of native grass blade (c and d) before and (e and f) after decellularization at different magnifications (scale bars = 200 μm (c, e) and 100 μm (d, f)). (Reproduced with permission from ref. 31, Elsevier B.V. Copyright 2020.)

imparts a distinctive purple hue to cell nuclei, whereas eosin stains cell membranes pink.[49,59] Fig. 9b shows the H&E-stained images of decellularized plant scaffolds, the acellular nature of which is discernible from the substantial absence of cellular entities.[60] Moreover, Hoechst 33342 and DAPI exhibit an affinity for nucleic acids, resulting in a blue-stained nucleus.[51,53,56,59,61] The discernible absence of stained nuclei in the fluorescent images subsequent to decellularization is a reliable indicator of the process's effectiveness. Fig. 9c–f show the Hoechst 33342-stained grass blade before and after decellularization: the absence of nuclei following the process can be clearly observed.[31] The disappearance of the nuclei signifies the accomplishment of the central objective of decellularization, *i.e.*, the thorough removal of genetic materials while preserving the structural integrity of plant tissues. However, to move from a qualitative histological approach to a quantitative analysis, quantifications of DNAs and proteins are employed to measure the quantity of genetic materials present in the decellularized plants. This allows for a precise measurement of the genetic content of the decellularized samples.

In general, the effectiveness of the decellularization process in biological samples is assessed based on the level of remaining DNA, which should not exceed 50 ng of double-stranded DNA per mg of dry weight.[24] This stringent criterion confirms the successful removal of protein and DNA contents from the fresh tissues, ensuring the suitability of acellular scaffolds for tissue engineering and regenerative medicine applications.[28,42,55] For this purpose, DNA is extracted from the decellularized samples, followed by quantification of the residual DNA by measuring the absorbance at 260 nm using a spectrophotometer or, alternatively, by assessing the fluorescence emission intensity.[55,57] Similarly, in the case of protein quantification, the extracted protein content is assessed using either the Bradford Assay or a Micro BCA protein assay kit.[28,41,61] The percentages of DNA and/or protein removal depend on the decellularization method, decellularization duration, and plant species. In order to provide a better understanding, Table 5 lists DNA/protein removal efficacies based on the decellularization conditions and plant species.

Other characterization techniques, such as profilometry[31] or BET (Brunauer–Emmett–Teller) investigation,[33,48] have been employed on occasion to examine the decellularization process in more detail. The removal of cellular materials during the decellularization process can produce a more porous and open structure, which in turn can result in an increased specific surface area. Using BET analysis, Salehi *et al.* reported specific surface areas of 6.787 m g^{-1} (with a total pore volume of 0.01766 cm g^{-1}) and 28.540 m g^{-1} for decellularized cabbage and spinach leaf scaffolds, respectively.[33,48] The large specific surface area and high surface roughness play a critical role in trapping the 3D cultured cells when using the decellularized plant-derived skeletons.

For biomedical applications, it is important to maintain vascular patency in decellularized scaffolds, since it is a critical parameter. The vascular patency of acellular plant tissues is evaluated using perfusion studies, facilitated predominantly by a cannula affixed to the petioles. These studies are conducted under a controlled, constant pressure regime, employing red dyes, such as Ponceau red or rhodamine, as tracers to discern and confirm patency.[28,39,40,57] In specific instances, a more rigorous examination is undertaken, utilizing red blood cells at a hematocrit level of 25% to ascertain the efficacy and functionality of the resultant vasculature in decellularized *Aptenia cordifolia* leaves.[39]

4.2. Chemical and structural evaluation of DWs

As with decellularized plant tissues, a precise characterization of the chemical compositions and structural properties of DW scaffolds is essential to delineate the physicochemical properties that underpin the biocompatibility, mechanical integrity, and biodegradable potential of such materials to ascertain their suitability for biomedical applications.

Delignification is a technical process that involves the removal of lignin from wood. Lignin is a polyphenolic polymer containing absorbent chromophoric groups (*e.g.*, quinone moieties and conjugated double bonds), which are photoactive and responsible for the characteristic brown color of wood. Delignification procedures effectively remove the majority of lignin and its associated chromophores. As a consequence, the wood's capacity to absorb and reflect specific wavelengths of light is drastically diminished.[86,147,148] This fundamental alteration in light interaction produces a discernible shift in color from the original brownish color to a notably white appearance. The resulting DW is hence referred to as "white wood" (WW) or "transparent wood" (TW).[64,84,132,144,152] This apparent color change is the preliminary indication of lignin removal after delignification. As revealed in Fig. 10a, the brightness of DW is dependent on the amount of removed lignin.[85] However, certain delignification processes (*e.g.*, UV irradiation of H_2O_2-treated wood) increased the brightness even when 82% of the lignin content was retained in the wood structures (Fig. 10b and c).[86] This is due to the fact that a photocatalytic oxidation reaction causes the formation of non-conjugated carboxyl groups, and only a small proportion of aromatic ring moieties in lignin undergo ring-opening reactions followed by the formation of H_2O_2-soluble small molecules. These observations convey the point that the removal or even structural modification of lignin will result in color changes in native wood. It is not only the removal of lignin but also the elimination of hemicellulose content that is responsible for the resulting WW post-delignification.

Chemical compositional analysis can also be used to quantify lignin content based on the standard methods established by the Technical Association of the Pulp and Paper Industry (TAPPI). The "Klason lignin" method has been extensively used in this domain, especially for lignocellulosic materials, such as wood and its derivatives.[101,108] This technique selectively measures the acid-insoluble fraction of lignin in a sample, using rigorous acid hydrolysis. During this process, the cellulose and hemicellulose constituents undergo degradation, leaving behind the acid-resistant lignin residues, referred to as "Klason lignin". It is known that wood materials

Table 5 Various wood delignification methods used for lignin removal from different wood species with reaction conditions

Plant species	Decellularization protocol	Total time	DNA content		Protein content		Ref.
			Before decellularization	After decellularization	Before decellularization	After decellularization	
Ulva sp. *Cladophora* sp.	- Boiling in acetone (60 °C) - Boiling in an $NaClO_2$ acetate buffer solution (60 °C) - NaOH treatment (60 °C) - Boiling in HCl (100 °C) for 10 min	2 days	9.6 ± 2.7 ng μl^{-1} 69.7 ± 16.5 ng μl^{-1}	5.5 ± 2.8 ng μl^{-1} 4.2 ± 0.4 ng μl^{-1}	N/A N/A	N/A N/A	49
Spinach	- Perfusion with SDS (10%, w/v) - Perfusion with a Triton X-100 (0.1%, w/v) + $NaClO_2$ (10%, w/v) solution	9 days	1129.0 ± 217.3 ng DNA per mg tissue	9.4 ± 1.3 ng DNA per mg tissue	19.1 ± 1.9 mg protein per mg tissue	2.4 ± 0.6 mg protein per mg tissue	28
Cabbage	- SDS (10%, w/v) treatment at 25 °C - Immersion in a Triton X-100 (0.1%, w/v) + $NaClO_2$ (10%, w/v) solution at 25 °C	7 days	1466 ng DNA per mg tissue	27 ng DNA per mg tissue	N/A	N/A	48
Leek	- Treatment with SDS (1%, w/v) at 37 °C - Placing in absolute ethanol at 65 °C	6 days	485.8 ± 24.3 ng DNA per L solution	78.7 ± 3.9 ng DNA per L solution	0.9 ± 0.1 ng protein per mg tissue	0.09 ± 0.01 ng protein per mg tissue	61
Tobacco BY-2 cells	- Adding lyophilized DNase I powder (1 mg mL^{-1}) to 2 mg of lyophilized BY-2 cell material in PBS containing 0.492 mM Mg^{2+} and 0.9 mM Ca^{2+}	30 min	1503 ± 459 ng DNA per sample	31 ± 5 ng DNA per sample	424 ± 70 μg protein per sample	154 ± 60 μg protein per sample	56
Spinach	- Pouring liquid CO_2 (0.56 kg per run) of 17.23 MPa and 33 °C into the vessel - Flushing with bleach	≈36 h	636.1 ng DNA per mg tissue	10.7 ng DNA per mg tissue	47.8 μg protein per mg tissue	1.5 μg protein per mg tissue	57
Ficus hispida leaves	- Placing in SDS (10%, w/v) at 20–25 °C	N/A	104.7 ± 26.2 ng DNA per mg tissue	2.5 ± 0.2 ng DNA per mg tissue	N/A	N/A	52
	- Treatment with Triton X-100 (1%, w/v) in bleach (10%) (detergent-based) - Treatment with an NaClO (5%, w/v) and $NaHCO_3$ (3%, w/v) solution at 60–70 °C (detergent-free)		104.7 ± 26.2 ng DNA per mg tissue	2.7 ± 1.6 ng DNA per mg tissue	N/A	N/A	

NA: not applicable.

typically contain two forms of lignin content: acid-soluble and acid-insoluble.[134] The procedure commences with the meticulous grinding of wood samples into fine powders. Subsequently, the samples undergo further treatment to eliminate any extractives, sugars, and non-lignin components. The prepared samples are further treated with concentrated sulfuric acid (H_2SO_4), at a typical concentration of 72% (v/v). This acid treatment process hydrolyzes the cellulose and hemicellulose components, ultimately yielding lignin as the insoluble residues. The Klason lignin residues are isolated from the soluble components using filtration and subjected to combustion. The gravimetric determination of the resulting ash contents serves as an indicator of the lignin contents. The individual constituents of the ash residues can be analyzed using inductively coupled plasma mass spectrometry (ICP-MS). The acid-soluble portion, containing monomeric sugars, is also subjected to dilution and subsequent quantification using a range of analytical techniques, including high-performance liquid chromatography (HPLC), gas chromatography (GC), and UV-Vis.[85,86,130,132]

SEM is one of the most widely used techniques for evaluating the delignification effectiveness and extent in wood, as it can provide valuable insights by revealing structural and morphological alterations in the vascular structures of native wood. Indeed, high-resolution SEM images can provide detailed visual evidence of the changes brought about by the delignification process, enabling a thorough assessment of the lignin removal degree at the microstructural level. Although multiple delignification techniques have been established, all of them aim to preserve the hierarchical porous microstructure in the DW. It is paramount that no substantial degradation or disintegration of cell walls should be discernible post-

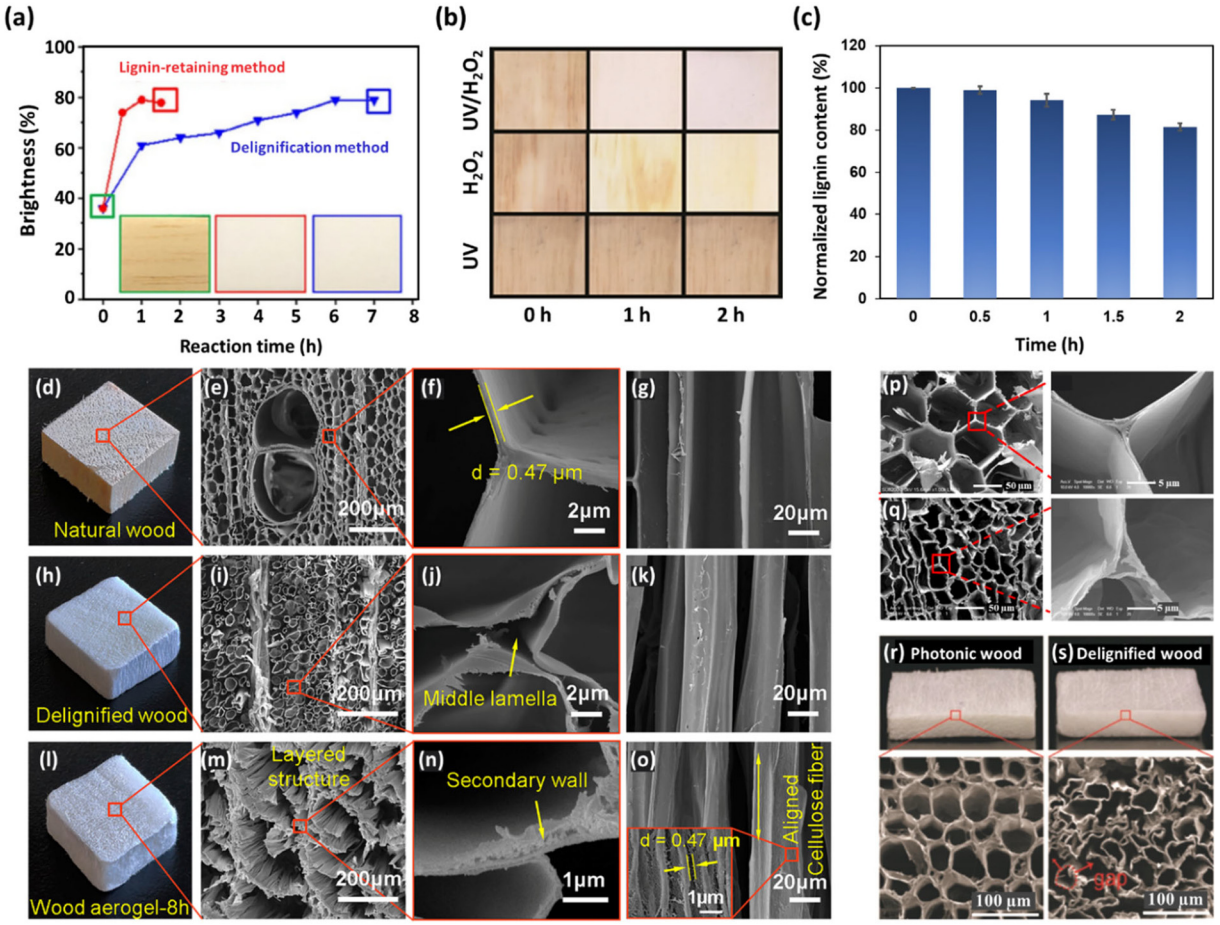

Fig. 10 Visual and morphological evaluation of DW samples. (a) Plot of balsa wood brightness against the reaction time for a delignified sample using an $NaClO_2$ solution (pH = 4.6, 1%, w/v) at 80 °C (inset: middle image) and a lignin-retained sample treated with H_2O_2 at 70 °C (inset: right image). (Reproduced from ref. 85 with permission from Wiley-VCH Verlag GmbH & Co. KGaA. Copyright 2017.) (b) Digital images of color changes in balsa wood after treatment with a H_2O_2 (30%, v/v)/NaOH (10%, w/v) solution and exposure to UV light (power = 20 W) for various time periods and (c) normalized lignin content of the resulting photonic wood. (Reproduced from ref. 86 with permission from Wiley-VCH GmbH. Copyright 2021.) (d–o) Digital photographs and SEM images of balsa wood specimens: native wood (d–g), DW with an $NaClO_2$ solution (pH 4.6, 2%, w/v) at 100 °C for 8 h and an NaOH solution (5%, w/v) at 80 °C (h–k), and wood aerogel obtained after freeze-drying at −18 °C for 24 h (l–o). (Reproduced from ref. 124 with permission from MDPI. Copyright 2020.) Cross-section SEM images of the cell wall structures of lignin-rich middle lamella of (p) native balsa wood and (q) delignified wood using a deep eutectic solvent, showing the empty middle lamella. (Reproduced from ref. 132 with permission from the American Chemical Society. Copyright 2018.) Comparison of the microstructures between photonic wood where (r) the majority of lignin content has been retained and (s) DW, revealing large pores and partial kinking. (Reproduced with permission from ref. 86, Wiley-VCH GmbH. Copyright 2021.)

delignification.[72,79,153] Lignin can generally be found in the middle lamella and concentrates at the cell wall corners.[134] Hence, as shown in Fig. 10d–o, the delamination and separation of cell walls become evident after lignin is removed from the native wood.[124] The cell wall structure becomes more pronounced in DW, emphasizing the presence of cellulose and hemicellulose components. The removal of lignin, which typically fills the spaces between cellulose fibers, results in the formation of pores in the cell wall surface and the exposure of the underlying cellulose microfibrils (Fig. 10p and q).[132] However, the resulting structural alterations in delignified samples are highly dependent on the delignification type. In certain delignification methods with retained lignin, the wood microstructures differ to a great extent. For instance, Fig. 10r shows SEM images of photonic wood after treatment with an H_2O_2 (30%, v/v)/NaOH (10%, w/v) solution and exposure to UV light irradiation (power = 20 W), which maintains the majority of lignin, resulting in an intact wood microstructure. In contrast, the cell walls of DW (treated with 5 wt% $NaClO_2$, pH = 4.6) exhibit large gaps and partial kinking (Fig. 10s), thereby compromising their structural integrity.[86] It is worth mentioning that specific methods, such as freeze-drying, play a significant role in preserving the microstructures of DW. Overall, SEM images provide visual evidence of the delignification process, highlighting the transformation of the wood microstructure from a dense, lignin-rich matrix to a porous, fiber-reinforced network predominantly composed of cellulose and hemicellulose.

Fourier-transform infrared spectroscopy (FTIR) is another appealing analytical technique used to identify functional groups. In wood, in the context of a complex composite material composed of cellulose, hemicellulose, and lignin, FTIR can be used as a powerful technique to characterize these components. Table 6 lists the main FTIR peaks associated with these components and the resulting changes that appeared in the FTIR spectra after the delignification process. A broad peak was observed in the FTIR spectra of wood samples within the 3200–3600 cm^{-1} range, attributed to the stretching vibration of O–H groups in cellulose and hemicellulose.[71,134,144] This peak underwent changes after delignification. After the treatment of *Pinus sylvestris* wood powder with a 17.5 wt% NaOH solution, the band at 3345 cm^{-1}, a characteristic peak of cellulose type I, was diminished, and two cellulose II-specific bands appeared at 3488 and 3445 cm^{-1}, indicating that the crystal structure was converted into cellulose type II.[154] Furthermore, a noticeable broadening in this band was observed in delignified balsa wood after treatment with an NaOH solution (15 wt%) for 2 h, compared with its untreated counterparts, indicating that the crystallinity of cellulose was reduced.[64] Also, Li *et al.* reported that the delignification of alkali-treated spruce chips using an $NaClO_2$ solution, (1 wt%, pH = 4.6) resulted in a strong absorption peak at 3336 cm^{-1}. The enhanced peak intensity was attributed to an increase in the amount of hydroxyl functional groups, due to the increased relative content of polysaccharides when lignin was removed.[118] The C–H stretching vibrations of aliphatic structures in cellulose and hemicelluloses appear at around 2900 cm^{-1}.[71,134,144] Another predominant peak that appeared in the FTIR spectra of wood samples was observed at ≈1700 cm^{-1} (from 1700 to 1737 cm^{-1}), corresponding to the stretching vibration of carbonyl (C=O) groups in acetyl moieties found in hemicellulose and lignin.[144,155] This characteristic absorption peak of hemicellulose was accompanied by a peak at around 1230 cm^{-1}, which could be attributed to the stretching vibration of the Ar–O bond that typically occurred in phenolic compounds such as lignin, as well as ester linkages involving carboxyl groups (a characteristic vibration in ester group-contained compounds), which could be found in both lignin and hemicellulose.[119,123,144] After delignification procedures, the intensities of these bands were significantly reduced or even disappeared, reflecting the partial or almost complete removal of hemicellulose and lignin from the structures.[64,71,110,140,154] During delignification, the hydrogen bonds and ether linkages between lignin and hemicellulose in the wood cell walls are broken, resulting in the dissolution and subsequent removal of lignin and hemicellulose. Since lignin and hemicellulose are closely associated through lignin-carbohydrate linkages, the elimination of glucomannan and xylan caused a decrease in the contents of both hemicellulose and lignin.[118,134] The peak that appeared at approximately 1150 cm^{-1} is another characteristic absorption band of cellulose and hemicellulose corresponding to the glycosidic C–O–C stretching vibrations.[144,152]

Table 6 FTIR characteristic peaks of wood constituents and changes post-delignification

Wave number range (cm^{-1})	Functional group	Post-delignification changes	Ref.
Cellulose and hemicellulose peaks			
3200–3600	O–H stretching vibration from hydroxyl groups in cellulose/hemicellulose	• Band broadening due to reduced cellulose crystallinity • Increase in the peak intensity due to the increased relative content of polysaccharides	56 and 79
≈2900	Stretching vibration of C–H in cellulose and hemicellulose	• No observable change was reported	71, 134 and 144
≈1700	C=O stretching vibration of acetyl groups in hemicellulose and lignin	• Significant decline or even disappearance due to the partial or almost complete removal of hemicellulose and lignin from the wood	56, 60, 101, 133 and 147
≈1230	Stretching vibration of the Ar–O bond in phenolic compounds (lignin) Ester linkages involving carboxyl groups in lignin and hemicellulose		
≈1150	Glycosidic C–O–C stretching vibrations, characteristic of cellulose and hemicellulose	• Retained in WW sample after $NaClO_2$ delignification of basswood	152
Lignin-specific peaks			
1460	C–H bending vibration (asymmetric C–H deformation)	• Significant decline or even disappearance due to the partial or almost complete removal of lignin from the structure	64, 116, 118, 147 and 148
1505	Skeletal vibrations of aromatic ring (symmetric stretching vibrations of C=C bonds)	• Slight changes in the peak intensities for the lignin-retaining methods	
1593	Skeletal vibrations of aromatic ring (asymmetric stretching vibrations of C=C bonds)		
1270	Guaiacyl ring breathing with C=O stretching	• Reduction after delignification	118 and 157
897	C–H out-of-plane deformation of the aromatic ring	• Typically decreases in intensity or may even disappear altogether	71 and 144

Lignin removal efficacy can be assessed from the characteristic lignin-specific FTIR peaks within the 1500–1600 cm^{-1} spectral range. Lignin manifests distinctive vibrational signatures, notably at 1460, 1505, and 1593 cm^{-1}. The 1460 cm^{-1} peak is attributed to the asymmetric C–H deformation associated with C–H bending vibrations. The peaks at 1505 and 1593 cm^{-1} correspond to the asymmetric and symmetric stretching vibrations of the C–C bonds in the aromatic skeletal structure of lignin, respectively.[144,148,153] Following the delignification of wood samples, a discernible reduction in these characteristic lignin peak intensities is observed.[64,118] This reduction persists even in cases of complete delignification, resulting in the eventual disappearance of the aforementioned lignin-associated peaks in the FTIR spectrum.[123,124,154,155] The impact of various delignification procedures on the lignin removal degree has been investigated. The findings showed a substantial reduction in lignin content, as evidenced by a corresponding decrease in the FTIR lignin peaks, when employing sodium hypochlorite and chlorite agents. In contrast, delignification processes utilizing H_2O_2 exhibit a selective affinity for chromophore structures, resulting in minimal disruption to the bulk lignin matrix. A negligible decrease in the intensity of these FTIR peaks is therefore observed, indicating substantial retention of lignin in the wood structures.[85,86]

The specific peaks and intensities can vary depending on various factors, such as wood species, sample preparation, and measurement conditions. The overlapping nature of some of these bands can make the precise identification challenging. A combination of FTIR with other techniques, including nuclear magnetic resonance (NMR) spectroscopy[95,130,156] and X-ray diffraction (XRD),[140,147,150] is therefore used for a more comprehensive analysis of wood components. XRD analysis facilitates the determination of crystallinity indexes in the delignified samples. These quantitative results entail assessing the proportion of ordered crystalline regions relative to the total mass of cellulose present in the wood samples. By leveraging XRD, researchers can precisely study the percentages of removal of amorphous constituents, providing crucial insights into the structural alterations induced by delignification processes.[71] A decrease in CIs after delignification suggests the variations of cellulose crystallinities.[140]

Cellulose exists in different crystalline forms, the two most common types being cellulose I and cellulose II. Each type exhibits distinct XRD patterns due to the differences in their crystal structures. The main XRD peaks of cellulose I are registered at 2θ (degree) of 14.8°, 16.5°, 22.5°, and 34.4°, which are attributed to specific crystallographic planes of (101), (10$\bar{1}$), (002), and (040), respectively.[64,86,124,150] The peak at around 2θ of 18° also typically corresponds to the amorphous region, representing the disordered or non-crystalline portions of the cellulose samples.[134]

The characteristic peaks associated with cellulose type I appeared to have no variations, revealing that its crystalline structures are preserved after the delignification process, specifically the β-crystalline form of cellulose I.[110,116,149] However, the observed reductions in peak intensities corresponding to the characteristic peaks of cellulose type I, along with the emergence of a broader amorphous peak, serves as indicative evidence of potential alterations in cellulose crystallinity due to the alkaline treatment and delignification of wood samples. This alteration is attributed to the disruption of the ordered crystalline lattice structures, resulting in increasing the disordered regions in the cellulose matrix.[64,147]

The transition of the crystalline structure from cellulose type I to II, which manifests as the emergence of a broad crystalline peak at approximately 2θ of 20° (corresponding to the overlapping of 20.1° (110) and 21.9° (200) peaks), can also be detected from XRD plots post-delignification. The appearance of these characteristic peaks of cellulose II reflects the transformation of cellulose crystalline structures into type II cellulosic constituents.[84,154]

Last but not least, Raman spectroscopy can be utilized to study the delignification process. The Raman spectra of lignin in wood typically exhibit several characteristic peaks associated with specific vibrational modes of the lignin molecules. The main Raman peaks associated with lignin content in wood include: 1598 cm^{-1} (ν (C=C) aromatic ring stretching), corresponding to the stretching vibration of the carbon–carbon double bonds in the aromatic rings of lignin, 1655 cm^{-1} (ν (C=C) unsaturated bonds), related to the stretching vibration of unsaturated carbon–carbon double bonds in lignin, and 1630 cm^{-1}, attributed to aldehyde functionalities.[119,157] The band at 1269 cm^{-1} (δ (C–O) stretching) is attributed to the guaiacyl (G) units of lignin. In order to investigate the regional variations in lignin depletion across different wood anatomical components, including secondary cell walls, middle lamellae, and cell corners, discernible shifts in the dominant lignin-specific vibrational modes can be analyzed, notably the aromatic ring stretching at 1598 cm^{-1} and the 1655 cm^{-1} peak associated with the polymerization degree and cross-linking density. Meanwhile, Raman spectroscopy has also been used as a semi-quantitative approach for revealing spectral evidence of lignin reduction in the basswood fiber structure following delignification using a boiling aqueous solution of NaOH and Na_2SO_3 for 48 h.[119] It was found that the reduction in lignin exhibits a gradient, with the most pronounced effect observed in the secondary cell walls, followed by the middle lamellae, and the least prominent effect in the cell corners.

Raman imaging can be used for the visual observation of lignin depletion in various parts of wood. A comprehensive Raman spectroscopic investigation was conducted by Segmehl *et al.* on thin Norway spruce wood sections, with the aim of elucidating the impact of delignification processes on distinct anatomical regions (Fig. 11a).[157] In the secondary cell wall, the primary objective is to achieve maximal lignin removal, creating space for additional functionalizing materials. Conversely, in the interconnecting layer encompassing the middle lamella and cell corner, predominantly composed of lignin, preservation is paramount to maintain the structural integrity of wood scaffolds. Raman spectra generated by integrating the signal from the principal lignin band located at 1598 cm^{-1}

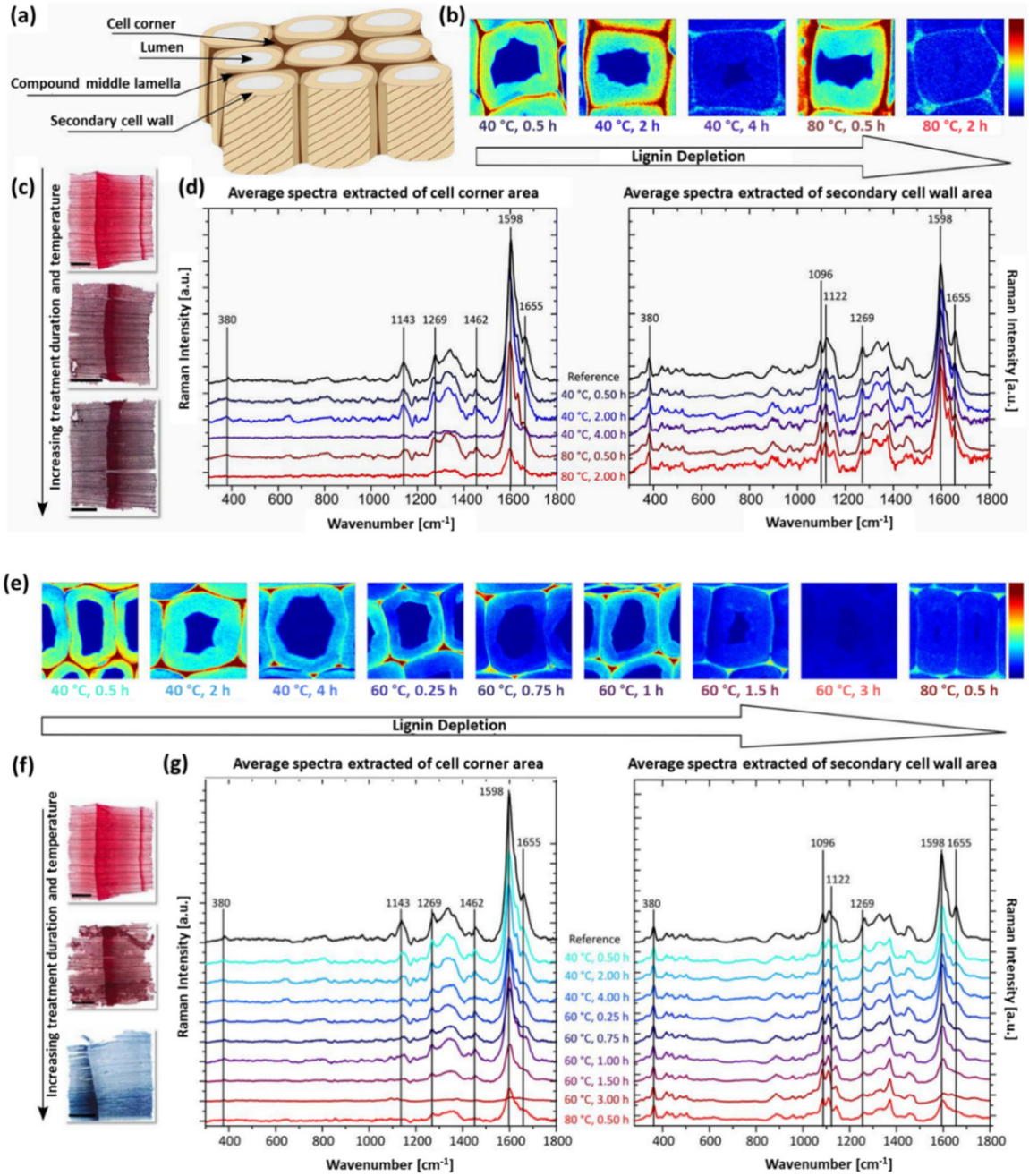

Fig. 11 Cross-section characterization of soda-pulped and acid-bleached spruce wood. (a) Schematic representation of a wood tissue model composed of various anatomical regions, Raman images based on the integration of the main lignin band at 1598 cm^{-1} obtained from various regions for (b) soda-pulped and (e) acid-bleached samples. Cross-sectional images of stained spruce wood samples utilizing safranin red and methylene blue, which resulted in cellulose appearing blue, whereas lignified tissue took on a red hue after (c) alkaline and (f) acid treatment. Calculated average Raman spectra extracted from the secondary cell wall region and cell corner area (normalized on the band at 380 cm^{-1}) after (d) soda pulping and (g) acid bleaching methods. (Reproduced from ref. 157 with permission from MDPI. Copyright 2018.)

(Fig. 11b and e) were used to determine the lignin-removal capacities of acid bleaching and soda pulping processes. The results revealed significant differences in the resulting material properties. Soda pulping showed no decrease in the aromatic content of the secondary cell wall but demonstrated higher susceptibility in the cell corner/compound middle lamella area. In soda-pulped (NaOH 10 wt%) samples, the aromatic ring stretching and unsaturated C=C double bonds at, respectively, 1598 and 1655 cm^{-1} remained unaltered in the secondary cell walls, even under severe conditions (Fig. 11b). Fig. 11d indicates that the subtle alterations observed at 1630 cm^{-1} and the reduction in the band at 1269 cm^{-1} revealed the reorganization of lignin molecules at the molecular level. These results suggest the formation of non-cleava-

ble carbon–carbon bonds due to the re-condensation and densification of lignin structures.

In contrast, the acid bleaching process resulted in a decrease in the main lignin vibration at 1598 cm^{-1} in the secondary cell wall region, strongly correlated with increasing temperature and treatment duration, indicating a gradual reduction in aromatic compounds (Fig. 11e and g).

There is a constant decrease in the 1269 and 1655 cm^{-1} peaks, along with a rise in the aldehyde-specific peak (1630 cm^{-1}). The results suggest the continuous fragmentation of lignin macromolecules into smaller aromatic entities followed by leaching from the structure as the prevailing mechanism in lignin degradation. Even at high temperatures and with long treatment durations, the induced depletion of lignin was less pronounced in the cell corner area, indicating a retention degree of the adhesive-like layer among single cells, contributing to tissue-level structural integrity even after near-complete cell wall lignin removal. Additionally, the two methods caused different scaffold swelling behaviors, offering opportunities for specific functionalization. Acid bleaching preserved scaffold volume in the wet state post-delignification, whereas soda pulping exhibited higher swelling capacity. These treatments can be applied selectively to produce tailored cellulose scaffolds, facilitating functionalization either among cells or in cell walls. This top-down approach for hierarchical scaffold formation presents a promising alternative to energy-intensive bottom-up disassembly processes, with potential for scalability.

5. Physicochemical characteristics of plant-derived skeletons

In tissue engineering and other biomedical applications, selecting an appropriate scaffold with desired properties is paramount for successful therapeutic outcomes. Structural properties play a pivotal role, as scaffolds must both provide mechanical support for cell attachment to extracellular matrix binding sites and facilitate cell growth. Adequate mechanical strength is imperative to withstand physiological forces and maintain structural integrity. Scaffold permeability is another important factor, ensuring the diffusion and transport of vital elements, including nutrients, oxygen, cell signaling molecules, and growth factors, all of which profoundly influence cell fate. Scaffolds are deliberately fabricated with a porous nature, allowing for efficient cell infiltration, nutrient exchange, and waste removal. Biocompatibility also ensures that the scaffold is well tolerated by host tissues without causing adverse reactions. Biodegradability is another critical property, as the scaffold should gradually break down as the new tissue grows. Finally, surface topography, characterized by parameters such as roughness, hydrophilicity, the size and shape of porosities, and specific surface area, significantly impacts cell behavior and adhesion. A comprehensive consideration of these factors and properties is therefore essential when selecting the optimal scaffold for tissue engineering and biomedical applications.

5.1. Mechanical properties

Plant skeletal structures exhibit a diverse array of mechanical properties, ranging from pliable soft tissues in leaves and fruits to rigid lignified woody components characterized by elevated mechanical resilience. Plant decellularization can have a significant impact on the mechanical properties in terms of stiffness and elasticity, and it often results in a reduction in the structural integrity and stiffness of plant materials.[24,28] As can be seen from Fig. 12a, a dramatic decrease is observed in the Young's modulus of the decellularized plant vegetal tissues compared with native ones.[24] This is due to the fact that the cellular components, including rigid cell walls and supporting structures, provide the plants with their inherent mechanical strength. When these components are removed, the tissues become less rigid and more pliable (Fig. 12b–d).[36] The removal of cells and cell contents can also induce a decrease in overall tissue densities, further influencing the mechanical properties. The mechanical properties of plant-derived skeletons have been shown to exert a direct influence on the cell attachment and proliferation profiles of human induced pluripotent stem cells (hiPSCs) seeded on various plant tissues.[60] Among various decellularized plants, including apple, carrot, and persimmon, only apple-derived scaffolds promoted the cultivation and proliferation of hiPSCs. Since the decellularization procedure, pore shapes, and the average pore size were the same among all species, the differences in cell behaviors were attributed to the unique mechanical properties of these decellularized tissues.

It is essential to ensure that the mechanical properties of decellularized plant tissues, including Young's modulus (YM), ultimate tensile strength (UTS), maximum tangent modulus (MTM), and strain at failure (%), closely align with those of human organ tissues to guarantee their effectiveness for implant applications.[36] Fig. 12e shows a comparative analysis of mechanical characteristics between various decellularized plant-based scaffolds and those of human tissues.[24] Compression and tensile tests are standard methods for measuring macroscopic mechanical properties. However, in cases where the evaluation of local elastic properties at the nanoscale is required, techniques such as AFM and nanoindentation become valuable.[25,43]

The surface modification of scaffolds can also exert a significant impact on their mechanical properties. For instance, the introduction of collagen I or glutaraldehyde cross-linking in apple-derived scaffolds resulted in a notable twofold to fourfold augmentation in Young's modulus compared with unmodified decellularized scaffolds or the native tissues.[25] In a separate investigation, it was observed that the elastic modulus of native and decellularized leek samples was the same, whereas the decellularized leek samples demonstrated a slight enhancement in tensile strength (1.9 ± 0.3 MPa) in contrast to native samples (1.5 ± 0.3 MPa). Both 3-aminopropyltriethoxysilane (APTES)-modified and graphene oxide (GO)-

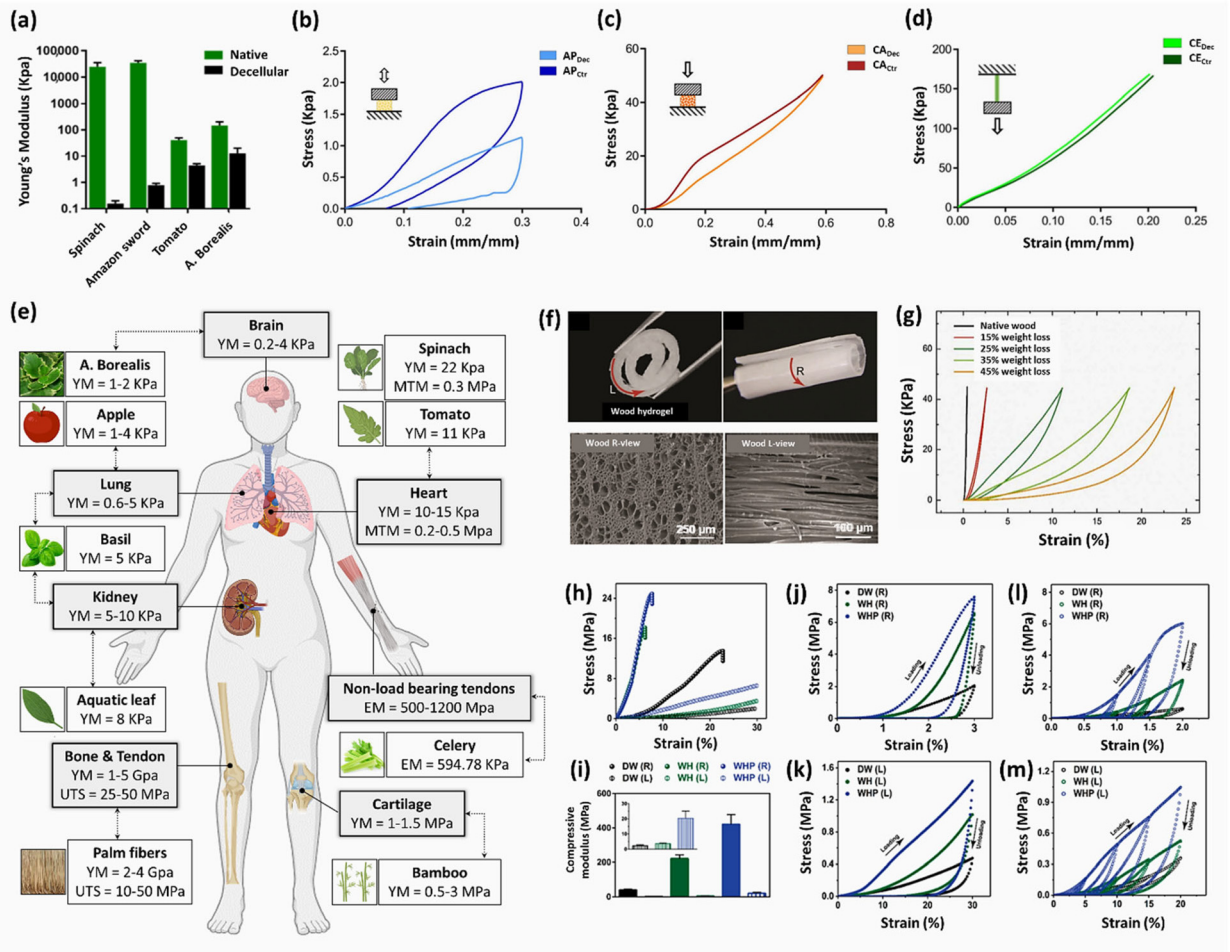

Fig. 12 Mechanical properties of various decellularized plant and DW samples. (a) Comparison of Young's modulus for various plant tissues before and after decellularization. (Reprinted from ref. 24 with permission from MDPI. Copyright 2021.) (b, c) Representative mechanical compression curves of apple- and carrot-derived scaffolds and control samples. (d) Mechanical tensile curves of celery-derived scaffold compared with control sample. (Reproduced from ref. 36 with permission from Frontiers. Copyright 2020.) (e) Correlation of mechanical parameters between decellularized plant-derived scaffolds and human tissues. (Adapted from ref. 24 with permission from MDPI. Copyright 2021.) (f) Optical images of flexible wood-PAM hydrogels after lignin removal and SEM images of wood hydrogel from the L and R directions. (Reproduced from ref. 152 with permission from WILEY-VCH Verlag GmbH & Co. Copyright 2018.) (g) The effect of various weight losses on the stress–strain curves of fungus-decayed wood. (Reprinted from ref. 110 with permission from Science. Copyright 2021.) (h–m) Mechanical properties of DW, wood–hydroxyapatite (WH) and wood–hydroxyapatite–polycaprolactone (WHP) composites along the radial and longitudinal directions. (Reprinted from ref. 146 with permission from the American Chemical Society. Copyright 2017.)

coated decellularized leek samples also exhibited increased tensile strength values.[61] These findings highlight the ability to finely tune scaffold elasticity within a range that mimics the selected mammalian tissues using appropriate surface modification.

It is worthy of mention that, in plant tissues characterized by anisotropic structures (*e.g.*, celery, chive, and asparagus), mechanical anisotropy is discernible along the longitudinal axis. The mechanical anisotropy of asparagus scaffolds arises from the linear alignment of vascular bundles along plant stems.[45] This resulted in an elastic modulus of 148 ± 53 kPa when measured parallel to the longitudinal axis, compared with 12 ± 4 kPa when measured perpendicular to it. Decellularized chive samples also showed no mechanical resilience to applied transverse tensile loadings; they demonstrated the ability to withstand tensile loading solely in the longitudinal direction.[41]

The mechanical properties of wood originate from cellulose nanofibrils (CNFs) arranged in a highly ordered and aligned manner within the cell walls. These hierarchical CNFs are embedded in a matrix of lignin–carbohydrate complexes, providing rigidity and resistance.[148,152,158] As a result, like plant decellularization, wood delignification typically results in a significant alteration in mechanical properties.[64,140,159] As indicated in Fig. 12f, the partial removal of lignin and hemicellulose during the delignification process reduced both strength and hardness, consequently yielding wood samples with enhanced flexibility.[152] Previous investigations have revealed that the alterations in mechanical properties are highly dependent on the amounts of lignin and/or hemi-

cellulose removal from the native wood specimens. For example, the mechanical compressibility of balsa wood subjected to selective decay by white-rot fungus has shown a direct correlation with the extent of weight loss (Fig. 12g).[110] The strain load obtained for native wood was only around 0.44%, whereas in the case of decayed wood samples with 15, 25, 35, and 45% weight loss, the strain load increased by 2.7, 11.1, 18.6, and 23.7%, respectively. It is important to note that the exact changes in mechanical properties depend on the specific delignification process, the delignification degree, and the wood types. Compared with intense delignification procedures, lignin modification methods obtained wood templates with higher mechanical properties, as more lignin is preserved in the structure.[85,86] Innovative strategies can also be adopted to produce moldable and flexible DW while increasing its mechanical strength. A study conducted by Xiao *et al.* found that engineering wood using a rapid water-shock process post-delignification produced a unique wrinkled cell wall structure that endows wood with an extraordinary tensile strength of ≈300 MPa (6 times higher than that of native wood) in the case of a wood veneer of ≈0.75 g cm^{-3} density.[119]

In addition to variations in mechanical characteristics before and after delignification, which are contingent upon factors such as wood species and specific delignification parameters, an essential aspect of wood's mechanical behavior is its inherent anisotropy. The majority of wood samples exhibit noticeable differences in mechanical properties along the longitudinal and transverse axes, due to the anisotropic composition of their microstructures.[160] This mechanical anisotropy arises from the arrangement of cellulose fibers within cell walls. Wood demonstrates its highest mechanical strength in the longitudinal direction (L direction), where the fibers align parallel to the grain. Conversely, the mechanical properties are notably lower in the transverse direction (R direction), where the fibers are oriented perpendicular to the growth direction. This structural disparity is a critical consideration in engineering applications, as it necessitates careful orientation of wood in order to optimize its performance for specific load-bearing requirements. Fig. 12h–m present a thorough evaluation of the mechanical properties of wood–hydroxyapatite (WH) and wood–hydroxyapatite–polycaprolactone (WHP) composites, in comparison with those of the DW samples.[146] It was observed that noticeable differences are detected in the mechanical behaviors of delignified and composite woods in the R and L directions: the calculated elastic modulus was 20 times greater in the R direction than the L direction.

The mechanical properties of wood can also be adjusted by introducing polymer matrices into its structure. Numerous studies have shown that combining wood's inherent high stiffness properties with weak yet flexible polymers yields wood hydrogels with tailored mechanical strength. The enhanced mechanical properties were attributed to the strong intermolecular interactions (hydrophobic interactions and hydrogen bonding) between the highly aligned CNFs and polymer chains, such as polyacrylamide (PAM),[152] gelatin,[148] sodium alginate (SA),[158] and regenerated silk fibroin (RSF).[149] These interactions contribute to energy dissipation during compressive and tensile processes. In addition, water content plays a key role in the mechanical properties of wood samples.[148,152] As listed in Table 7, this anisotropic mechanical behavior is observed in the case of different wood specimens when measured in the parallel *versus* perpendicular direction to the channels. It was found that various parameters, including delignification type, retained lignin amount, and modification process, exert direct influences on the final mechanical properties.

5.2. Porosity and pore size of plant scaffolds

The porous nature and vascular structure of plant skeletons are fundamental to their functionality. These structures exhibit a wide range of porosities and pore sizes in different species, facilitating the diffusion of water, nutrients, and oxygen. Specialized vascular tissues (*e.g.*, xylem and phloem) play a crucial role in regulating fluid transport. Their intricate architecture is subject to evolutionary adaptations, allowing plants to thrive in diverse environmental conditions.[54] This inherent porosity is critical for biomedical applications, especially tissue engineering, as cell adhesion, proliferation, and differentiation on the scaffolds depend on the interactions between cells and essential materials (*i.e.*, nutrients and oxygen) in an interconnected 3D structure.[38,60] Generally, the soft plant tissues (*e.g.*, leaves) possess larger pore sizes and higher porosities after decellularization, in comparison with harder parts (*e.g.*, stems).[54] However, it should be taken into consideration that using the same decellularization method, the final porosity degrees and the average pore sizes post-decellularization are highly dependent on the plant tissue types, as shown in Fig. 13a–n.

This also affects the amount of water retained in the structures.[27] The ultimate pore size exerts a substantial effect on the final cellular attachment to and proliferation on the decellularized scaffolds. In this regard, macroporous scaffolds with pore sizes in the 50–350 μm range surpass the typical cell sizes, facilitate cell infiltration, and allow cells to adhere to the flat surface areas surrounding the cavities or along the pore walls, facilitating the formation of 3D cellular organization.[49,161] Conversely, microporous scaffolds possess pore sizes between 0.1 and 10 μm, smaller than the average cell sizes. This impedes cell penetration into the pores but encourages contact primarily with pore margins,[162] which promotes cell–cell interactions and obtains a continuous sheet on the scaffold's surface.[163]

Previous investigations have revealed that not only pore sizes but also pore shapes play a significant role in cell behavior. For example, fibroblasts cultured on the surface of decellularized *Ulva* sp. with a porous structure formed monolayer sheets, while exhibiting elongated filament profusions in the form of stretched polygonal cells along the decellularized *Cladophora* sp. fibers.[49] Similar results were observed in the case of decellularized celery.[53] MSCs displayed different morphologies when cultured on the porous and fibrous celery

Table 7 Comparison of the mechanical properties of woods subjected to different delignification methods along the longitudinal and transverse directions

Plant-derived scaffold	Wood species	Delignification method	Specific properties of the final scaffold	Mechanical properties (MPa)		Application	Ref.
				Longitudinal (∥)	Perpendicular (⊥)		
Hydroxyapatite (HAp) scaffold	Pine	Thermal (1000 °C) and hydrothermal processes	Total porosity = 70%; pore diameter = 80 ± 45 μm	Compression strength 2.5–4	0.5–1	Bone	73
Optically transparent wood (TW)	Birch	Lignin-retaining method (alkaline H_2O_2) *vs.* delignification with $NaClO_2$ (1 wt%)	Weight loss (wt%) after modification = 10.6; lignin content (wt%) after modification = 20.1	Wet strength 14.4 ± 3.3	0.8 ± 0.2	Light-transmitting buildings	85
			Weight loss (wt%) after delignification = 25.3; lignin content (wt%) after delignification = 3.3	1.4 ± 0.4	0.07 ± 0.03		
Wood hydrogel (WH)	Basswood	Delignification using $NaClO_2$ (pH = 4.6) and PAM infiltration	Water content = 65 wt%	Tensile strength 36 Elastic modulus 310	0.5 0.1	Muscle	152
Carbon dots/ transparent wood (CDs-TW)	Balsa	Deep eutectic solvent (DES, oxalic acid and choline chloride)	Lignin content (wt%) = 2.3; 90 wt% lignin removal	Fracture strength 60.9 Fracture modulus 1430	27.4 1240	White LEDs (W-LEDs)	132
PAM/alkali-treated DW (A-PDM) hydrogel	Balsa	Treatment with 15 wt% NaOH	PAM (wt%) = 33.8 ± 1.3; wood (wt%) = 9.1 ± 0.4	Young's modulus 145.5 ± 12.3 Fracture strength 16.5 ± 1.4	5.5 ± 0.2 0.7 ± 0.1	—	64
Mineralized wood hydrogel (MWH)	Pine	Delignification using $NaClO_2$ (pH = 4.8) and SA impregnation followed by *in situ* mineralization of HAp nanocrystals	Lignin loss (wt%) = 23.4; reduction in density = 46%; increase in porosity = from 61% to 94%	Tensile strength 67.8 ± 1.0 Elastic modulus 670 ± 11	13.2 ± 1.2 7.4 ± 1.2	Bone	158

tissues. They formed a more rounded shape with a notably smaller size (1232 ± 407 μm^2) on the porous tissues compared with larger cells (1954 ± 601 μm^2) with a higher aspect ratio on fibrous ones. Furthermore, the dimensions and distributions of pores in the decellularized plant tissues play a crucial role in their suitability for tissue engineering applications. For instance, apple-derived scaffolds with uniformly large porosity are well suited for adipose tissue regeneration, whereas carrot-based scaffolds composed of a heterogeneous structure, featuring radially oriented pores with a smaller size (70 ± 12 μm) at the core and larger round pores (130 ± 26 μm) at the periphery, have shown potential for bone tissue regeneration.[36]

Wood is a tough material composed of nano- to macro-scale pores with a total porosity varying between 40 and 80% based on the species.[164] Delignification removes a significant proportion of lignin and a certain percentage of hemicellulose from the wood structures, releasing the tight connections between cellulose nanofibrils while preserving the hierarchical skeletons.[64] Lignin removal enhances the material's porosity and increases its specific surface area (SSA), whereas the wood density is notably reduced compared with its native state.[143,144] Lignin is a high-density polymer, whose extraction creates voids within the wood's cellular structure (Fig. 14a).[123,165] Accordingly, the resulting DW exhibits lower overall mass per unit volume. For instance, the densities of delignified basswood using an $NaOH/Na_2SO_3$ mixture and pinewood softened with $NaClO_2$ solutions have shown a reduction from 0.4 to 0.26 g cm^{-3} and 0.58 to 0.28 g cm^{-3}, respectively.[144,158] Moreover, delignification confers benefits in terms of increased surface area and improved accessibility for various chemical and biological processes.[147,148] As seen in Fig. 14b–d, the depletion of the lignin-rich middle lamella results in the appearance of empty, open voids, increasing the overall porosity.[85]

Detailed microscopic studies revealed that delignification treatment produced nanoporosities in the DW structures (Fig. 14e and f).[77,166] Similarly, $NaClO_2$-delignified pinewood demonstrated a significant increase in porosity from 61 to 94%,[158] and Brunauer–Emmett–Teller (BET) analysis revealed an increase in SSA from 0.3 m^2 g^{-1} in the native spruce to 88 m^2 g^{-1} in the alkaline-treated samples.[118]

Meanwhile, it was found that drying DW samples under ambient conditions can result in loss of surface area due to the collapse of small pores,[79] suggesting that it is important to select an appropriate drying method. The SSA of balsa wood aerogel has been shown to be remarkably influenced by the drying method, as different SSAs of 247 and 159 m^2 g^{-1} were obtained using the critical point drying (CPD) and freeze-drying methods, respectively.[147]

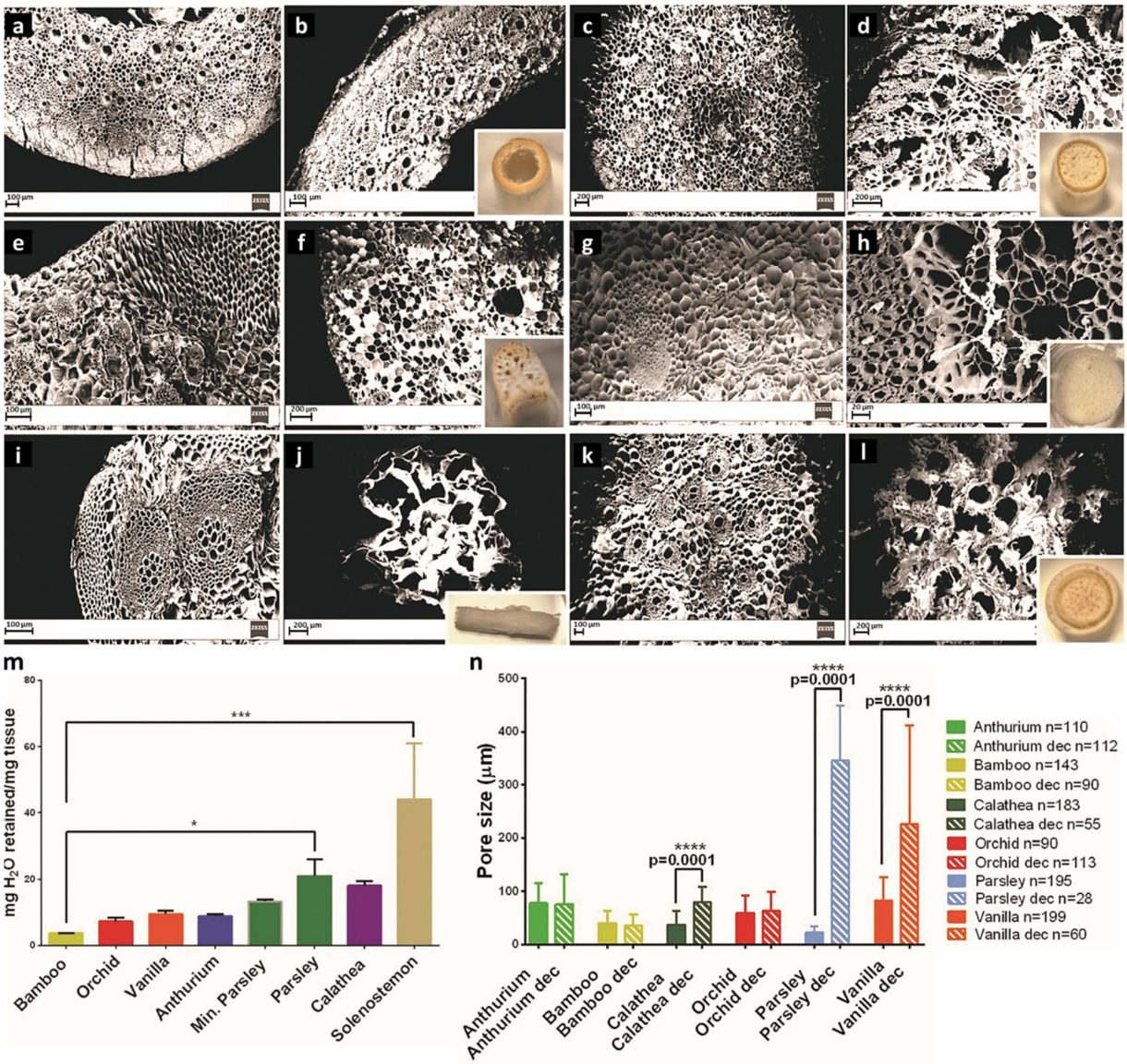

Fig. 13 Pore size and distribution profiles of various plant tissues after decellularization. SEM images of plant tissues before (left panel) and after (right panel) decellularization for: (a, b) bamboo, (c, d) *Anthurium warocqueanum*, (e, f) *Calathea zebrina*, (g, h) orchid pseudobulb, (i, j) parsley, and (k, l) vanilla. (m) The normalized water mass retained in each stem (n = 4, *p < 0.05 and ***p < 0.001. n), and (n) comparison of average pore sizes of stems pre- and post-decellularization (p < 0.05). (Reproduced from ref. 27 with permission from WILEY-VCH Verlag GmbH & Co. Copyright 2017.)

5.3. Biocompatibility and biodegradability of plant-derived scaffolds

Biocompatibility and biodegradation of biomaterials are two crucial considerations for their biomedical applications. When transitioning from experimental benchwork to clinical applications, it is imperative that the proposed scaffolds exhibit high biocompatibility and tailored biodegradability commensurate with the specific requirements of the intended application. Due to their natural origin, plant-derived scaffolds show considerable promise as viable candidates for such applications. Decellularized plant structures are typically expected to elicit a diminished immunogenic response in the host post-implantation as compared with allogeneic (from a donor of the same species) and xenogeneic (from a different species) transplants. This attenuation in immunogenicity is predominantly due to the absence of biochemical cues, as well as the thorough removal of intracellular components by the decellularization process. Eventually, the biocompatibility of decellularized plants increases, mitigating the likelihood of host rejection.[33,36]

As the decellularization process necessitates the use of a variety of reagents, such as acids, bases, and detergents, any incomplete removal of residues from these components could potentially result in cytotoxicity. Therefore, it is imperative to verify the biocompatibility of scaffolds before progressing with

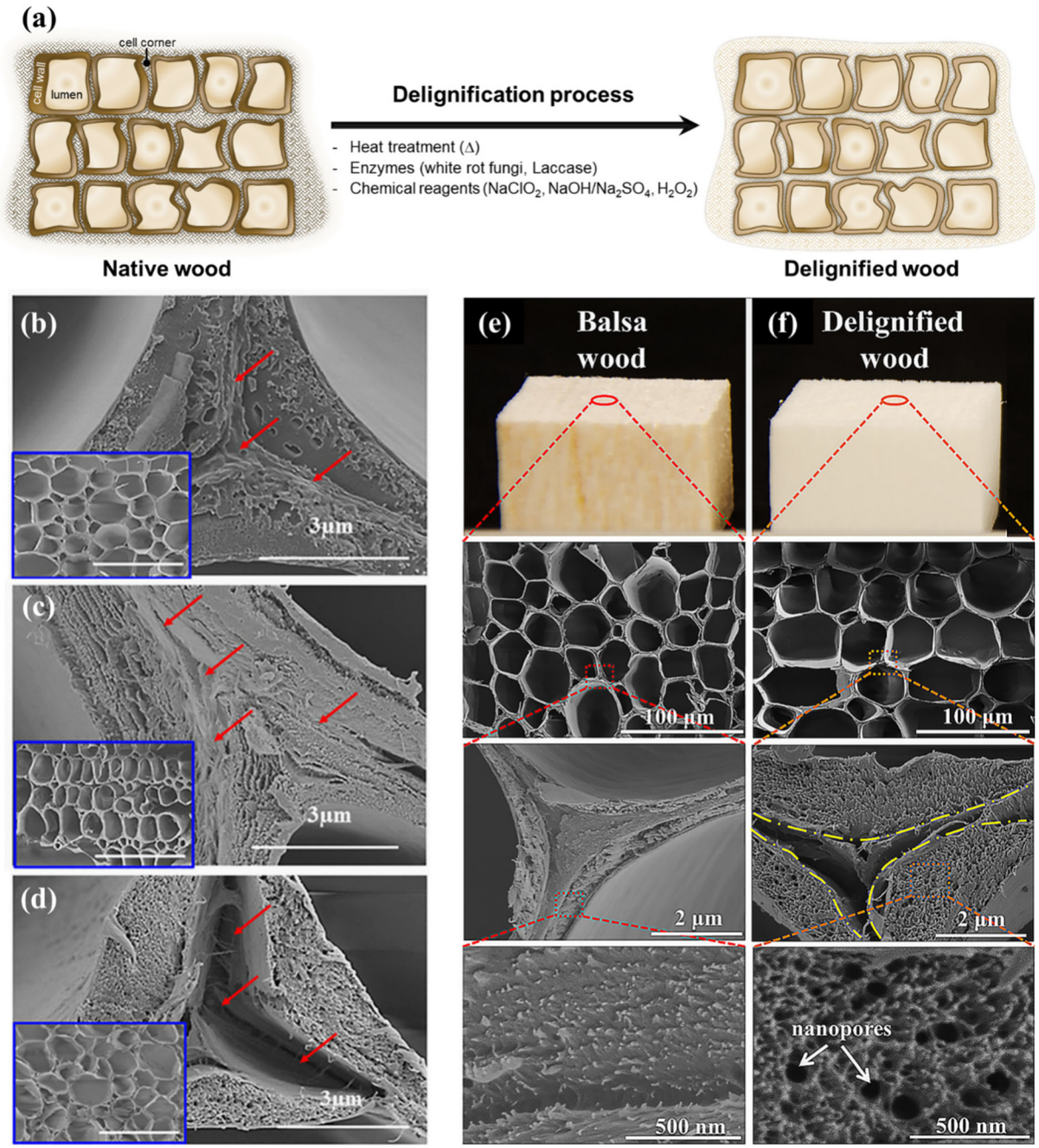

Fig. 14 The effect of delignification on the porosity and surface area of DW samples. (a) Schematic representation of lignin removal from cell wall causing a significant decrease in density. Comparative SEM images of (b) native balsa wood, (c) lignin-modified wood in alkaline–H_2O_2 media, and (d) $NaClO_2$-based delignified balsa wood. (Reproduced from ref. 85 with permission from WILEY-VCH Verlag GmbH & Co. Copyright 2017.) Low- and high-magnification SEM images of (e) native balsa wood and (f) DW with nanopores indicated by arrows. (Reproduced from ref. 77 with permission from the American Chemical Society. Copyright 2018.)

tissue regeneration applications.[42] It was detected that olive leaves, when decellularized with higher percentage SDS, exhibited higher toxicities compared with samples treated with Triton X-100 and bleach solutions.[167] These results clearly demonstrate the importance of choosing an appropriate decellularization method and thoroughly washing the decellularized tissues to ensure the complete removal of the residual reagents.

The biocompatibility of decellularized plant-derived scaffolds has been investigated both *in vitro* and *in vivo*. The *in vitro* biocompatibility of scaffold is imperative for facilitating cell attachment, migration, proliferation, and differentiation. The efficacy of cell adhesion and morphology of cultured cells can be evaluated using SEM. Adherent cells exhibit substantial spreading across the surface of decellularized scaffolds, avoiding the formation of cell aggregates.[33,48] As an additional

modality for visualizing specific cellular features, live/dead fluorescence imaging utilizing a range of dyes has been employed to evaluate the biocompatibility of decellularized plant-derived scaffolds. Apple-derived scaffolds recellularized with NIH3T3 fibroblasts, mouse C2C12 muscle myoblasts, and human HeLa epithelial cells stained with Hoechst 33342 and propidium iodide (PI),[25] murine C2C12 myoblasts cultured on the surface of decellularized grass and stained with fluorescein diacetate (FDA) and Hoechst 33342,[31] human MSCs (hMSCs) grown on *Ficus religiosa* leaf skeleton and assessed using the acridine orange/ethidium bromide (AO/EB) staining method,[50] and DAPI-stained bone marrow-derived MSCs (BM-MSCs) cultured on the surface of decellularized spinach leaf scaffold,[33] all revealed good biocompatibility and negligible cytotoxicity. Colorimetric methods, such as Alamar Blue and (3-(4,5-dimethylthiazol-2-yl)-2,5-diphenyltetrazolium bromide) (MTT) assays, can be employed to quantitatively assess cell viability and metabolic activity.[36,48,49,58,167] The cell counting kit-8 (CCK-8) assay is another valuable and versatile tool that provides reliable assessments of cell viability and proliferation.[29,42,60]

In the context of *in vivo* biocompatibility, it should be meticulously evaluated in the case of practical applications. Modulevsky *et al.* have investigated the *in vivo* biocompatibility of decellularized apple hypanthium tissues by subcutaneously implanting the scaffolds in wild-type, immunocompetent mice.[26] One week after implantation, histological examination revealed a characteristic foreign body response to the scaffolds. However, the observed mild immune responses gradually diminished, with no remaining signs in the surrounding dermal tissues by the 8th week post-implantation. The formation of blood vessels in the implanted scaffolds also exhibited their pro-angiogenic characteristics. Similar *in vivo* experiments carried out by the same group have shown that using $CaCl_2$ in the course of decellularization resulted not only in higher cell proliferation and invasion but also in the elimination of any sign of immune responses.[29]

Wood-derived composite hydrogels[149,152,158,166] and scaffolds[146,159] have also demonstrated good biocompatibility. An interwoven meshwork of bract in *Manicaria saccifera* palm fiber mats has shown robust cellular attachment and proliferation in the case of cultured NIH/3T3 mouse fibroblasts, human aortic smooth muscle cells, and human adipose-derived mesenchymal stem cells.[83] The immunogenicity of the mats was investigated by measuring the gene expression and protein secretion profiles of the typical inflammatory cytokines (IL-1β, IL-8, and TNF-α), demonstrating the high biocompatibility and low immunogenicity of the fibers. The biocompatibility of wood-based materials can be further improved by impregnating the DW templates with various biocompatible polymers, including, PAM,[152] polycaprolactone (PCL),[146] polydopamine (PDA),[166] and hyaluronic acid (HA).[145] Deposition of hydroxyapatite (HAp) nanocrystals on the surface of scaffolds has also been shown to be effective in not only cell adherence and spreading but also in their osteogenic potential.[146,158] Further studies revealed that modification of wood-derived scaffolds with chitosan quaternary ammonium salt (CQS) and dimethyloxalylglycine (DMOG) improves the cytocompatibility of scaffolds by bringing the –OH and $–NH_2$ functional groups to their surface, promoting protein absorption and acting as adhesion sites for cells.[159]

Biodegradability is crucial for scaffolds, as it ensures that the implanted biomaterials can be gradually metabolized and eliminated by the body, reducing the need for additional surgical interventions.[45,60] In mammalian organisms, cellulose itself is not a readily digestible compound, because humans and most animals lack the necessary enzymes, known as cellulases, to break down the cellulose polymers into constituent sugars.[27,35,43] As a result, the biodegradability of plant-based scaffolds is a crucial factor that needs to be precisely controlled. The degradation rate of cellulosic materials can vary, depending on diverse factors such as crystallinity states, chemical modifications, and the specific forms (*e.g.*, fiber and film). Crystalline cellulose, although provoking fewer immunological responses, degrades at a slower rate than amorphous cellulose, which exhibits an accelerated biodegradation property.[26,27,35] Previous studies found that the biodegradation rate of cellulosic materials could be improved by treating them with oxidizing agents, such as 2,2,6,6-tetramethylpiperidine1-oxyl radical (TEMPO), sodium bromide, sodium hypochlorite, and sodium periodate.[55,58] Among these oxidants, sodium periodate reacts with crystalline domains of cellulose, converting the 1,2-dihydroxyl groups into dialdehyde by selectively breaking the C2–C3 bond in the polysaccharide chain. The oxidation reaction can be assessed by employing Schiff's reagent, which produces a noticeable color change to magenta. Apart from biodegradability, periodate-mediated oxidation is able to increase the hydrophilicity of scaffolds as well.[55]

5.4. Anisotropy and the role it plays in the biomedical properties of plant skeletons

Cell alignment on the scaffold surface plays a crucial role in tissue engineering by mimicking the native structural organization of tissues. This spatial orientation of cells is vital, because many tissues in the human body (*e.g.*, muscles, tendons, blood vessels, bone, and nerves), exhibit distinct alignment patterns.[168–170] Incorporating micro- and/or nanostructured surface topographical features in scaffolds can promote cell orientation, guide tissue growth, and enhance mechanical properties in specific directions.[171] This feature facilitates the development of functional, organized tissues that closely resemble their natural counterparts. Scaffold alignment also influences cell behavior, such as migration, proliferation, and differentiation, *via* a mechanism known as "contact guidance", which is pivotal for achieving the desired tissue functionality.[172,173]

Anisotropy refers to the directional variation in the properties of scaffolds.[174,175] A fundamental design consideration is to induce cell alignment, contributing to the successful fabrication of biomimetic constructs that promote tissue regeneration and repair. Various techniques, such as electron beam lithography, photolithography, chemical etching, and 3D print-

ing, have been applied to produce micro- and nanostructured surface patterns.[176–178] These techniques, while capable of creating topographical features on the substrates, are time-consuming and laborious, often requiring specialized high-tech instrumentation. Conversely, porous plant skeletons possess inherent anisotropy, characterized by distinct orientations of fibers and vascular bundles (VBs), providing unique structural advantages in tissue engineering.[31,36,53] Different plant species have various degrees of anisotropy in their structures. For instance, cellulose structures in some plants (*e.g.*, carrot, apple, broccoli, and cucumber) display similarity in both transverse and longitudinal directions, eventually exhibiting isotropic properties. In contrast, scaffolds derived from leek, celery, asparagus, and green onion skeletons manifest anisotropic properties, exhibiting distinct structural variations when cut along the longitudinal and transverse axes.[35]

Separate investigations have demonstrated the self-alignment of seeded C2C12 murine myoblasts along the longitudinal axis of decellularized grass,[31] green onion,[35] and celery[32] surfaces. Fig. 15a–l clearly show an alignment of this kind parallel to the longitudinal axis of vascular bundles in the decellularized celery.[32] This anisotropic feature plays a critical role in myoblast orientation and the formation of aligned myotubes, as opposed to randomly oriented myoblasts on the surface of the 2D control surface (*i.e.*, tissue culture plastic, TCP).[31]

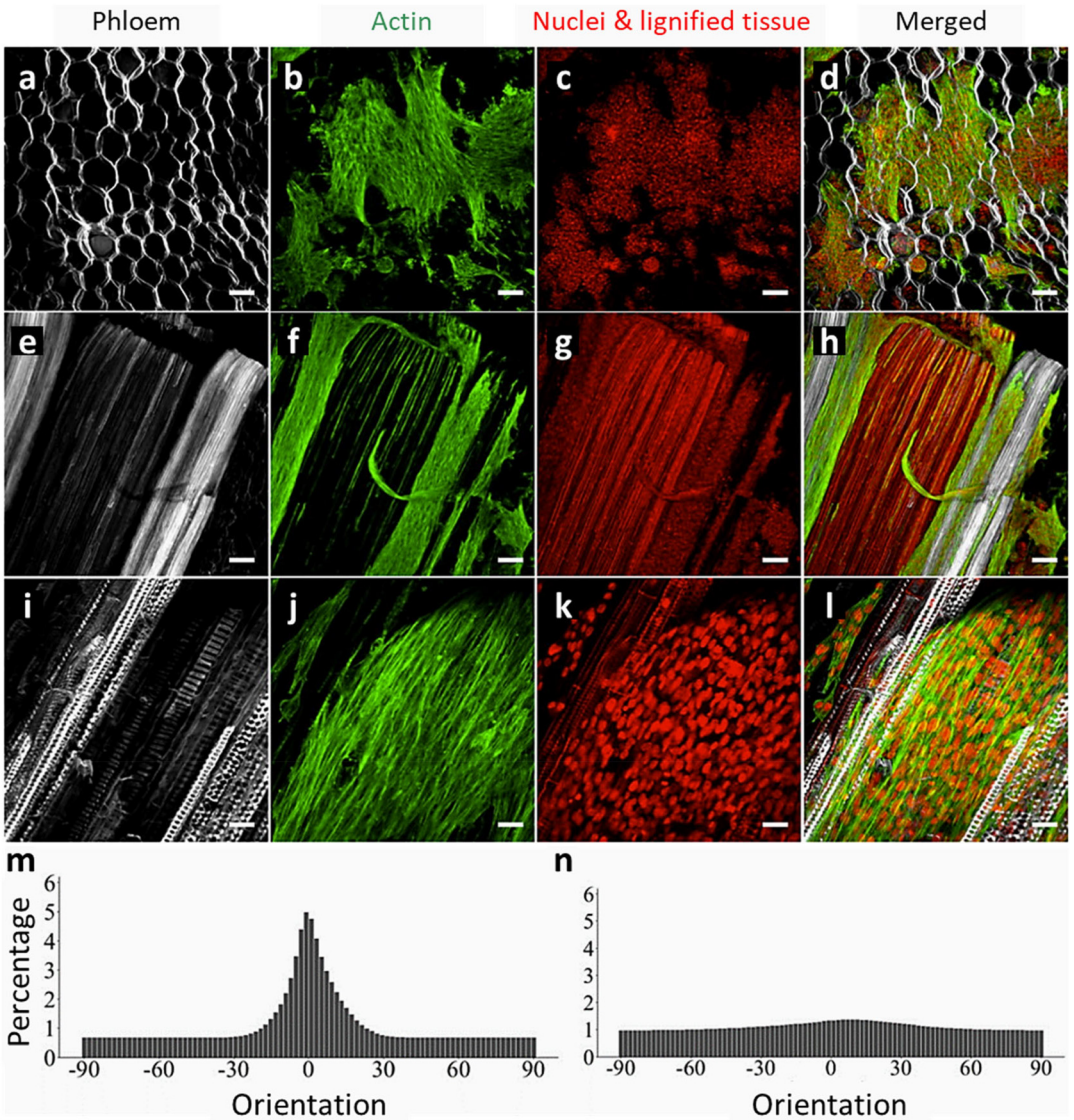

Fig. 15 The effect of plant anisotropy on the alignment of C2C12 myoblast cells. Alignment of myoblast cells cultured on different parts of decellularized celery: the unimodal distribution of aligned F-actin filaments along vascular bundles can be clearly seen. Calcofluor-labeled phloem and ground tissue in gray (a, e, i). Phalloidin Alexa fluor 488-labeled filaments (green) (b, f, j). Nuclei and lignified tissues labeled with PI in red (c, g, k), and merged images (d, h, l) (a–h: scale bar = 100 μm, i–l: scale bar = 25 μm). The histograms show the average orientation of F-actin filaments on vascular bundles, representing a clearly predominant orientation angle (anisotropy) (m), and on parenchyma with amorphous topography with uniform distribution (isotropy) (n). (*N* = 10 max projection images). (Reproduced from ref. 32 with permission from *BioRxiv*. Copyright 2020.)

The "orientation angle" (OA), an angle between the direction of plant topography and that of the attached cells, can be used to provide a good estimate of cell alignment. A smaller OA (degree) indicates higher orientation: an orientation angle of 0° would achieve perfect cell alignment, revealing that cells are oriented in the same direction as the underlying plant topography.[27] As can be seen from the histograms of average F-actin orientation on vascular bundles (Fig. 15m) and parenchyma (Fig. 15n), aligned filaments with a narrow orientation distribution were observed along VBs, whereas only a small degree of alignment and broad distribution were found in the case of randomly oriented filaments on parenchyma. Mean normalized OAs of 1.2 ± 2.0° and 8.6 ± 23.8° (N = 10) were obtained for F-actin and myotubes, respectively.

The inherent hierarchy of wood, comprising a porous radial structure and longitudinal tracheids and vessels, makes it a potential candidate for tissue engineering that requires a high degree of cell alignment. Compared with labor-intensive and time-consuming bottom-up approaches to prepare highly ordered hydrogel structures from CNFs, the natural anisotropy of wood has attracted a great deal of attention for preparing scaffolds using a straightforward top-down strategy.[147,148,152] Cell guidance and apparent polarity was confirmed by L929 and human umbilical vein endothelial cells (HUVEC) cultured on the surface of a wood–hydroxyapatite–polycaprolactone (WHP) scaffold,[146] as well as in bone marrow MSCs (BMSCs) grown on elastic wood modified with PDA–dimethyloxalylglycine–chitosan quaternary ammonium salt (EW@P-C-D).[159]

6. Modification of plant scaffolds

Surface modification through chemical functionalization or physical coating of decellularized plants and DW scaffolds can tailor their properties to facilitate tissue regeneration in engineered constructs. It not only serves to enhance their biocompatibility but also promotes cell adhesion, proliferation, and differentiation by creating customized microenvironments.[103,166,179] Surface modification can improve mechanical properties, tune the scaffold porosity and pore size, and modulate the degradation rate of scaffolds, as well as introducing biomimetic features. It also enables the controlled release of bioactive molecules.[145]

6.1. Surface-functionalized scaffolds *via* chemical reaction

Chemical functionalization of scaffolds for biomedical applications generally aims to enhance biocompatibility, control mechanical properties, and increase scaffold reactivity by bringing various functional groups to their surface. Apple-derived cellulose scaffolds modified with chemically cross-linked collagen using glutaraldehyde presented enhanced elasticity and a fourfold increase in the Young's modulus. The functionalized scaffolds also supported the growth of C2C12 cells due to their augmented cellular binding potential.[25] The process of decellularization or delignification imparts a high degree of hydrophilicity to plant-based scaffolds, owing to the presence of hydroxyl (OH) groups in the cellulose structures.[63] The OH functional group was used for chemical modification of scaffold surface with organosilanes[58,61] and various biomolecules, such as concanavalin A (Con A) and biotin.[118] Fig. 16a shows the multi-step process involved in the preparation of *Borassus flabellifer* (BF)-derived oxidized cellulose scaffolds (OCS) using sodium periodate-mediated oxidation, followed by organosilane-based surface modification with 3-aminopropyltriethoxysilane (APTES) and octadecyl trichlorosilane (OTS).[58] Organosilanes, functioning as coupling agents, established covalent bonds with the abundant OH groups on the surface of scaffolds. The interatomic linkages formed during organosilane surface modification enable electrostatic and hydrophobic interactions between the amino- and methyl-terminated functional groups of APTES and OTS molecules and cells. This in turn facilitates effective cell and protein interactions, ultimately enhancing cellular functions. Also, when decellularized leek samples were modified with graphene oxide (GO) sheets, higher cell adhesion and better neuroblastic morphologies were observed for SH-SY5Y human neuroblastoma cells, compared with surface functionalization using APTES and OTS.[61]

Li *et al.* used a chemical modification method to immobilize biomolecules on the surface of delignified spruce-derived scaffolds.[118] The structural integrity of native spruce was preserved by cross-linking the polysaccharides of the cell walls with 1,4-butanediol diglycidyl ether (BDDE) prior to delignification using acidic $NaClO_2$ solution. The surface of lumens and cell walls in the scaffolds were modified by primary amine terminal groups, enabling the covalent attachment of biomolecules (*e.g.*, Con A and biotin), as shown in Fig. 16b. The Con A-modified scaffolds showed great potential for glycoprotein enrichment and separation due to the high affinity to mannose-containing glycoproteins (*e.g.*, ovalbumin). To determine the versatility of the amination process for biofunctionalization, biotin was conjugated to the scaffold surface using *N*-hydroxysuccinimide (NHS) ester, and the successful conjugation was evaluated using fluorescence-labeled streptavidin.

TEMPO oxidation is a chemical process used to modify the surface properties of cellulose-containing materials. It involves the use of TEMPO reagent, a stable free radical, to selectively oxidize the primary hydroxyl groups of cellulose into carboxyl groups (–COOH).[180,181] Thus, TEMPO oxidation creates negative charges on the cellulose surface, making it more hydrophilic and chemically reactive. This modification facilitates the surface functionalization of wood to enhance its biocompatibility, reactivity, and structural properties. It was found that the deposition of hydroxyapatite nanocrystals on softwood pulp using a biomimetic mineralization process was improved by chemical TEMPO oxidation, due to the enhanced electrostatic interactions.[179]

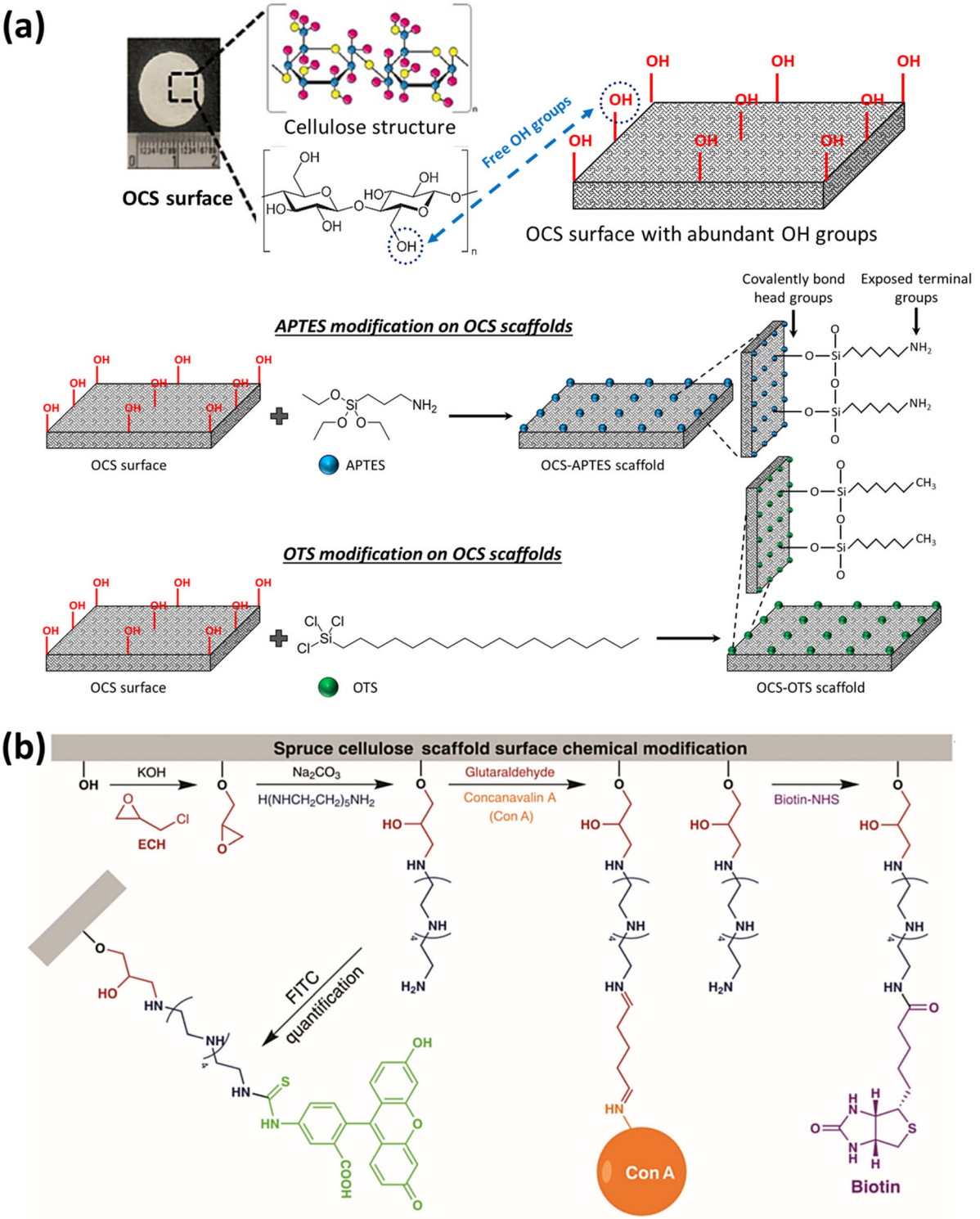

Fig. 16 Various approaches for the chemical functionalization of plant-derived scaffolds. Schematic representation of (a) the mechanism of self-assembled monolayer formation on OCS derived from *Borassus flabellifer* (BF) immature endosperm *via* chemical functionalization using APTES and OTS. (Reproduced from ref. 58 with permission from the American Chemical Society. Copyright 2022.) (b) Covalent attachment of Con A and biotin biomolecules *via* surface amination of spruce-derived cellulose scaffolds. (Reprinted from ref. 118 with permission from Wiley-VCH GmbH. Copyright 2021.)

The effect of increasing the nucleation sites on the nanoparticle (NP) deposition yield was also seen in the *in situ* growth of ZIF-8 metal–organic framework (MOF) nanocrystals on delignified beech.[140] It has been demonstrated that treating the wood substrate with NaOH would facilitate the deposition of MOF NPs by imparting negative

charges to the surface to provide binding sites for Zn^{2+} ions.

6.2. Functionalized scaffolds *via* physical method

Plant skeleton-derived scaffolds may lack specific binding sites, such as the RGD motifs, found in animal-derived ECM proteins, impeding cell attachment to their surfaces.[32] However, they can still be engineered or biofunctionalized to create an environment conducive to cell adhesion and tissue formation. One possible technique to enable cell adhesion during recellularization in plant-based scaffolds is surface modification and biofunctionalization using cell-adhesive proteins, such as poly-L-lysine,[36] fibronectin, and collagen.[28,30,35,37] It was observed that coating decellularized spinach leaves with fibronectin or a combination of fibronectin and collagen promoted cell attachment and supported the proliferation and differentiation of HUVECs[28] and prostate cancer cells (PC3),[37] respectively. Improved adhesion and cell alignment was also observed in the case of C2C12 myoblasts and human skeletal myoblasts (HSMCs) seeded on the surface of fibronectin-coated green onion-derived scaffolds.[35] Interestingly, Robbins *et al.* found that fibronectin coating had a positive effect on the development of sarcomeres in human-induced pluripotent stem cell-derived cardiomyocytes (hiPS-CM).[30] At day 14 post-recellularization, the length of hiPS-CM sarcomeres on fibronectin-coated spinach leaves was greater than that of collagen IV.

Dopamine and its derivatives have been used for the biofunctionalization of plant-derived scaffolds.[27,41,159] Dopamine was chemically conjugated with RGD peptides using an EDC/NHS as cross-linking agents.[27] The decellularized parsley stems were incubated with the RGD-dopamine conjugate (RGDOPA) under gentle agitation at room temperature. The effectiveness of the RGDOPA-coated plants in supporting cell adhesion was tested using human dermal fibroblasts (hDFs), and the results were compared with non-coated plants. This approach successfully supported hDF adhesion, whereas non-coated plants did not facilitate cell attachment. In another attempt, balsa wood was delignified with an $NaOH/Na_2SO_3$ solution to create a tough, elastic scaffold (EW) that mimics the structures of natural bone tissues. The addition of PDA served as an intermediate layer to create the EW@P scaffold. Further modifications with CQS and DMOG, either individually or simultaneously, were achieved with the aid of the introduced PDA layer. The obtained composite scaffolds exhibited an anisotropic porous structure and excellent elasticity. They not only exhibited antibacterial properties due to the presence of CQS, but also promoted vascular network and bone tissue formation as a result of DMOG. The sustained release of DMOG from the composite scaffold also contributed to its long-term osteogenic and angiogenic capabilities.

Polymers are a versatile class of materials frequently employed to physically coat plant surfaces, imparting a range of properties to plant skeleton-derived scaffolds, including enhancing optical transparency using polymers with a specific refractive index,[85,132] boosting mechanical strength,[146,152] and adjusting the scaffold's hydrophobicity or hydrophilicity.[69,149,158] The accessible surface area within DW is augmented following delignification. This increased surface area facilitates the penetration and infiltration of polymers into the wood pores. This is a crucial step in modifying the wood's properties and effectively incorporating polymers into its nanostructures. In their review article, Berglund and Burgert classified wood–polymer nanostructures based on the location of polymer layer within the materials.[80] There are several key approaches, such as surface modification at the interface between cell wall and lumen, direct cell wall modification, and lumen filling by infusing polymer into the cell's inner cavity. The modified wood cell wall can be analyzed in more detail using nanoscale characterization techniques. To prepare wood–polymer nanocomposite structures, the main adopted strategy is impregnating the wood channels with polymer solutions using a vacuum. The vacuum-assisted infiltration technique has been shown to be effective for the thorough permeation of the porous DW matrix with poly (methyl methacrylate) (PMMA)[85] and PCL,[146] as well as SA[158] and RSF[149] hydrogels. Other approaches, such as free-radical polymerization[152] and *in situ* chemical polymerization,[64] have also been employed to prepare wood–PAM composites following the infiltration of precursors (*i.e.*, acrylamide (AM) monomer along with appropriate initiators and cross-linkers) into the DW. As revealed in Fig. 17a and b, the formation of strong hydrogen bonding between CNFs and PAM chains obtains high mechanical strength along with superflexibility.[64,152]

Polymer coating is particularly valuable in the context of cell culturing applications as well, where specific scaffold characteristics can influence cell behavior and tissue formation.[29] During the polymer infiltration process in plant-derived scaffolds, maintaining the structural integrity and porosity of the scaffolds is crucial for their effective application in tissue engineering. Blocking the pores or reducing the accessible surface area can compromise the scaffold's ability to provide a suitable environment for cell growth. To achieve this goal, it is important to select and optimize the infiltration method and polymer type. Controlling parameters, such as temperature, pressure, and curing time, during the infiltration process help prevent excessive polymer aggregation that might clog the pores.[148]

Scaffolds derived from plant skeletons can be decorated with various NPs to endow them with desired properties. The mineralization of decellularized spinach and celery stems,[43] as well as delignified pine and beech wood blocks,[146,158] with hydroxyapatite (HAp) nanocrystals has shown promising results for bone regeneration and repair. Li *et al.* have demonstrated that coating decellularized plant tissues with bioactive nano-amyloids can not only improve cell adhesion, viability, and proliferation, but also induce the deposition of nano-HAp.[43] The results showed that nano-HAp crystals promoted the osteogenic differentiation of MC3T3-E1 pre-osteoblasts. In another attempt to mimic natural bone tissues, DW was coated with HAp NPs using *in situ* deposition in the channels

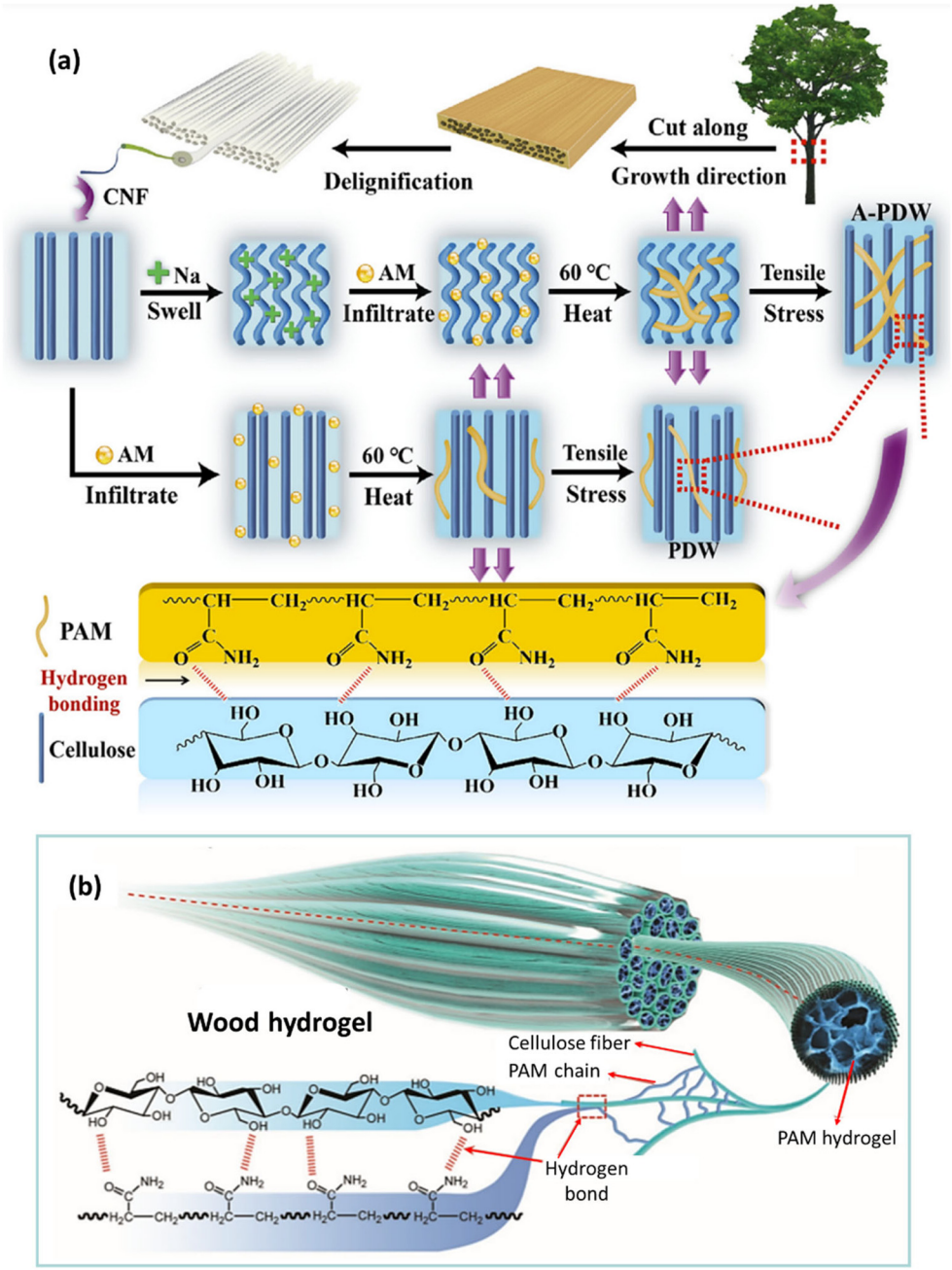

Fig. 17 Physical coating of plant-based scaffolds. Schematic illustration of wood modification with (a) a PAM polymer network using *in situ* chemical polymerization. (Reprinted from ref. 64 with permission from Elsevier B.V. Copyright 2020.) (b) Muscle-inspired wood hydrogel prepared through free-radical polymerization, showing hydrogen bonds and covalent cross-linking between PAM chains and CNFs. (Reproduced from ref. 152 with permission from WILEY-VCH Verlag GmbH & Co. Copyright 2018.)

of the DW scaffolds.[146] PCL was infiltrated into the scaffolds to improve the attachment of HAp particles to the channel walls. The synergistic effect of a PCL coating with a hydrophobic nature together with HAp NPs increased the proliferation and osteogenic differentiation of MC3T3-E1 cells.

As mentioned above, the abundant oxygen-containing functional groups on the surface of cellulose-based scaffolds can be exploited for the deposition of NPs *via* electrostatic interactions. Using this strategy, CuS NPs were immobilized on the surface of a holocellulose framework (HCFW) derived from basswood.[144] Due to the electrostatic interactions between the negatively charged oxygen functional group and electropositive copper cations, high loading efficiency (≈22.7 wt%) and uniform distribution of NPs were achieved. The prepared CuS NPs@HCFW were loaded with doxorubicin hydrochloride (DOX) to develop a drug delivery system. The composite

scaffold exhibited an almost 100% bacterial inhibition effect on *E. coli* and *S. aureus* by CuS NPs, as well as a pH-responsive drug-release behavior. Decellularized leaf and onion cellulose scaffolds also showed promise as a vascular patch loaded with polylactic-*co*-glycolic acid (PLGA)-based rapamycin NPs.[145] The vascular patch demonstrated decreased neointimal thickness when implanted in the inferior vena cava (IVC) of a rat model, associated with the release of rapamycin.

A wood hydrogel bionic scaffold has been proposed by Hu *et al.* for bone repair and osteolytic tumor therapy.[149] The platform was fabricated based on vacuum infiltration of RSF in a DW scaffold (WW/RSF), followed by the incorporation of PLGA-encapsulated black phosphorus quantum dots (BPQDs). WW/RSF provided a mechanical support for BPQDs, known to be a photothermal agent with high photothermal transformation efficiency. However, as BPQDs are susceptible to oxidation and degradation when exposed to oxygen, visible light, and water, they were encapsulated in PLGA nanospheres to maintain their photothermal stability. The prepared composite hydrogel demonstrated promising results in promoting bone regeneration by stimulating bone MSC proliferation, migration, and osteogenic differentiation, resulting in improved osteogenesis *in vivo*. Notably, the presence of BPQDs in the hydrogel scaffolds exhibited inhibitory effects on osteoclast differentiation and photothermal properties against spinal metastatic tumors.

Finally, another strategy involves converting plant-derived scaffolds into a conductive framework. To this end, wood-derived carbon templates were prepared using pyrolysis at elevated temperatures.[73,103] This approach has to be applied at high temperatures (mainly over 800 °C) with relatively slow heating rates to preserve the integrity and hierarchical morphology of wood during the carbonization process. Decorating DW with conductive nanomaterials, such as silver NPs (Ag NPs), multiwalled carbon nanotubes (MWCNTs), and poly(3,4-ethylenedioxythiophene) polystyrene sulfonate (PEDOT:PSS), is a more feasible alternative strategy for creating conductive plant-based aerogels.[116,147] The electrical conductivity of PEDOT:PSS-impregnated wood aerogel was measured as 213.7 S m^{-1} and reached 371 ± 5 S m^{-1} in the case of carbon aerogel after carbonization.[147]

7. Plant-based scaffolds for tissue regeneration

Tissue engineering strives to develop substitutes for tissues and organs in order to maintain, restore, or enhance the functions of their damaged counterparts in the body.[182,183] Scaffolds utilized in tissue engineering are constructs with specifically tailored physical and biological functions that can interact with cells through physical and biochemical signals, and these features make them essential components of tissue engineering.[184] The most desirable scaffolds should exhibit biocompatibility, interconnected porosity for fluid transport and waste removal, and biochemical properties that support cell functions, and be cost-effective.[185] They are also required to have a diversity of physical and mechanical properties that can be customized to mimic specific anatomical regions of interest. Given that *in vivo* cells are found in oriented structures[186,187] with complex extracellular matrix,[188] 3D scaffolds hold the potential to closely mimic the physical properties of the cellular microenvironment and support biochemical features with appropriate loading of cells or biomolecules into them.

There has been growing interest in the development of novel biomaterials for the fabrication of 3D scaffolds.[189–192] A wide range of methods have been established for fabricating 3D scaffolds, including 3D printing,[193] electrospinning,[194] and molding.[195,196] However, these methods involve costly, multi-step procedures with resolution limitations in micro and macro pores in the scaffolds.[7] In recent years, an alternative approach has been developed using the decellularization of animal tissues, in which after cell removal, the structural and mechanical properties of the ECM largely persist, allowing for the repopulation of the ultrastructures with human cells.[18] This process yields a tissue graft that closely mimics *in vivo* conditions. Utilizing animal-derived sources in medical research, however, entails significant economic costs, adverse environmental implications, and contentious ethical concerns. To meet these challenges, there has been a recent focus on the decellularization of plant tissues to generate scaffolds that are suitable for tissue engineering. Decellularized plant-based scaffolds have gained favor due to their ease of access, environmental friendliness, and low cost. Remarkably, these plant-based scaffolds are biocompatible, as they provoke minimal immune responses when implanted in a host. This makes them a viable choice for transplantation studies involving near-autologous tissues and organs, using cells harvested from a donor.[24] Decellularized plant scaffolds offer several distinct advantages, including their natural porosity, vascular architecture, and mechanical properties, which make them particularly suited for a variety of tissue engineering applications. For instance, plants such as spinach, bamboo, and parsley possess vascular networks that can be repurposed to support perfusion and nutrient transport, making them ideal candidates for cardiac and vascular tissue engineering.[7,27] Moreover, the cellulose-rich extracellular matrix of plants provides a robust scaffold for cell growth, and their tunable surface properties allow for biofunctionalization through coatings such as collagen or RGD peptides to enhance cell adhesion and proliferation.[27] Recent studies have demonstrated the potential of plant-based scaffolds in regenerating bone, muscle, and even organs-on-a-chip, highlighting their versatility in various biomedical applications.[7] The scalability, low cost, and environmental sustainability of these scaffolds further strengthen their position as a viable alternative to synthetic and animal-derived materials in tissue engineering. All these great features, combined with recent promising studies, have made plant-based scaffolds a highly appealing choice for tissue engineering applications.

7.1. Recellularization of decellularized scaffolds

The first step to fabricate plant-derived 3D scaffolds is to remove plant cells while minimizing cell debris, with the goal of preserving the plant skeleton, a process known as "decellularization".[23] Several decellularization techniques have been developed for various plant tissues, including leaves, roots, fruits, and wood. In the same plant tissues, different decellularization techniques result in varying characteristics in the final scaffolds. Therefore, it is essential to select optimum decellularization methods. The pioneering application of decellularized plant tissues in mammalian cell culture was undertaken by Modulevsky *et al.*, who utilized native hypanthium tissues from apples.[25] To obtain the decellularized tissues, the fruit was cut with a mandolin slicer to a uniform thickness of 1.2 ± 0.1 mm, after which the slices were cut into segments measuring 2.0 × 0.5 cm. After that, the small samples went through a decellularization process using SDS at room temperature, and the decellularized scaffolds were washed with PBS (Fig. 18a). To examine the plant-derived scaffolds' ability to support 3D mammalian cell culture, three kinds of cells, namely mouse C2C12 myoblasts, mouse NIH3T3 fibroblasts, and human HeLa epithelial cells, were seeded in the scaffolds. Confocal microscopy demonstrated that these three types of cells could completely infiltrate, proliferate, and remain viable after a long-term period of culture (12 weeks) in the surface and interior cavities of the cellulose scaffolds, and their numbers increased three to fourfold (Fig. 18b and c). Subsequently, this decellularized plant-derived cellulose scaffold was implanted in immunocompetent mice.[26] Following implantation, the immunological responses of the mice, deposition of a new collagen extracellular matrix, and new blood vessel formation were evaluated after 8 weeks. It was found that no immune response or foreign body rejection was observed in the dermis tissue at the end of the study. However, histological analysis confirmed the angiogenic effect of these native scaffolds and the presence of active fibroblasts and collagen deposition in the pores of cellulose scaffolds, demonstrating the biocompatibility and tissue regeneration potential of plant-derived cellulose scaffolds (Fig. 18d–g).

Based on the investigation of plant-derived scaffolds, Fontana *et al.* applied a decellularization process to various plant stems, including *Petroselinum crispum* (parsley), *Vanilla planifolia* (Vanilla), *Laelia ancepts* (orchid), *Anthurium warocqueanum* (Anthurium), and *Bambusoideae* (bamboo), to identify the most suitable candidate for 3D scaffolds capable of supporting the attachment and proliferation of human cells.[27] Following decellularization, the scaffolds were coated with RGD peptides and further conjugated with dopamine (RGDOPA) to facilitate cell attachment to the diverse surfaces of these plant-derived materials. The researchers also biomineralized the scaffolds using a common method for bio-functionalizing biomaterials. This enabled them to compare the effects of RGDOPA coating with mineralization, further elucidating the potential of these materials for tissue engineering. A thorough assessment of the physicochemical characteristics and biocompatibility of all the scaffolds resulted in the identification of parsley as the most promising construct. With its favorable attributes (*e.g.*, suitable porosity, topographical features, pore size, hydrophilicity, and interconnected ultra-structure), parsley stood out as the optimal choice. The researchers observed that the RGDOPA-coated and biomineralized parsley stems supported the adhesion of hDFs and MSCs, whereas non-coated scaffolds failed to facilitate cell attachment. Interestingly, the coated scaffolds not only supported cell attachment but also preserved the scaffold's original topographical features and porosity, in comparison with biomineralization, which could clog some of the small pores and change the topography of the decellularized stems. It was therefore concluded that, to provide a mechanism for cell attachment to a plant-derived scaffold, surface functionalization is a necessary part of scaffold fabrication.

However, several studies dispute the necessity of surface functionalization for cell attachment and the role it plays in cellular morphology and proliferation. For instance, Robbins *et al.* conducted a study to compare the adherence and contractile strength of hiPS-CMs on extracellular matrix protein and non-ECM protein-coated decellularized leaves.[30] It was reported that collagen IV-coated fibrin micro-threads offered a conductive surface for cardiomyocyte adherence and function.[197] In that study, spinach leaves were decellularized, sterilized, and coated with either fibronectin or collagen IV ECM protein. The hiPS-CMs were seeded onto these leaves, and the contractile strain, a crucial parameter for assessing myocardial cellular function, was quantified at days 7, 14, and 21. The results revealed that there were no significant differences in the maximum contractile strain of hiPS-CMs on ECM-coated and non-coated leaves at days 7, 14, and 21 (Fig. 18h). Immunofluorescence staining and imaging also demonstrated that hiPS-CMs adhered to the decellularized spinach leaves with and without ECM coatings at day 21 (Fig. 18i). These findings strongly suggest that the use of plant-derived ECM protein coatings is not necessary for hiPS-CM adherence, likely due to the inherent composition of the cellulose scaffold. In another study, the same group that developed the apple-derived scaffolds introduced a novel fabrication method, building on their prior research.[29] Apple hypanthium was sliced and punched to form small ring shapes, and the plant tissue was decellularized using the same SDS-based approach as in their previous study. Next, a Ca^{2+} buffer was added to the decellularized scaffold to encourage any residual SDS molecules to form micelles. The addition of Ca^{2+} changes the critical micelle concentration of the surfactant. At a certain concentration known as the "cloud point", a phase transition occurs, and the micelles become insoluble and can be easily rinsed away (Fig. 19a–d). This salt treatment is based on speculation that the residual surfactant is responsible for insufficient cell proliferation and adhesion in the scaffolds. The detergent washing process helps to remove detergents from scaffolds. However, it is time-consuming, especially in the case of larger scaffolds. Quantification of cell density using CCK-8 assays showed a higher number of viable cells attached to the

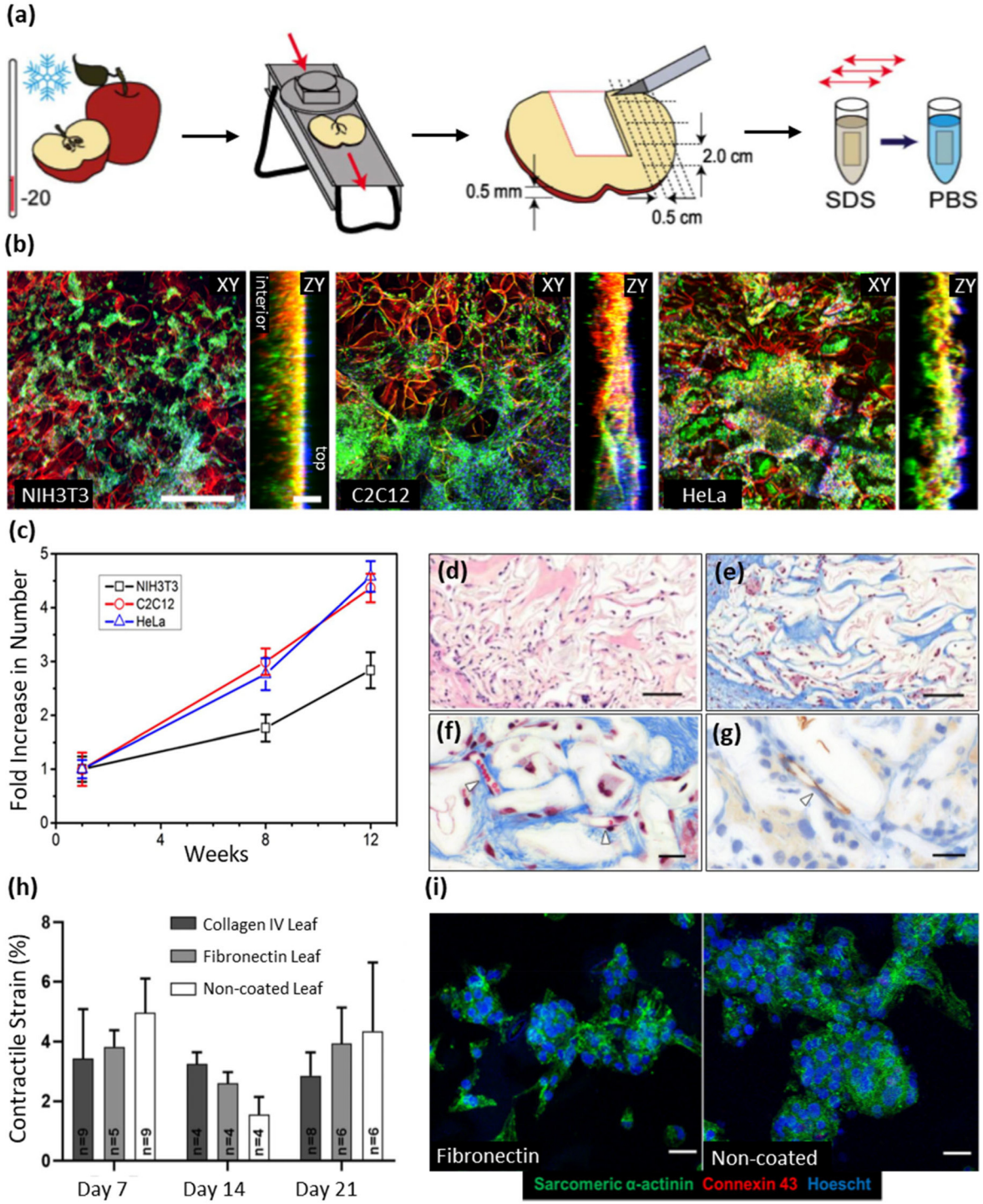

Fig. 18 Using decellularized plant tissues for recellularization purposes. (a) Schematic representation of apple tissue preparation and decellularization. (b) Fluorescent staining and laser scanning confocal microscopy analysis of NIH3T3, C2C12, and HeLa mammalian cells in cellulose scaffolds: the cellulose structure is highlighted in red, mammalian cell membranes in green, and nuclei in blue. Confocal volumes were obtained and visualized in the XY and ZY planes. The ZY orthogonal views provide insights into the depth of cell proliferation in the cellulose scaffold, with clear demarcation of the scaffold's top and bottom surfaces (scale bars: XY = 300 mm, ZY = 100 mm). (c) The increase in NIH3T3, C2C12, and HeLa cell populations was calculated from confocal microscopy image analysis of stained cells (Hoechst 33342). (Reproduced from ref. 25 with permission from PLOS. Copyright 2014.) (d and e) Cross-section of apple-derived scaffold stained with H&E (d) and Masson's trichrome (e) 8 weeks after implantation, respectively (scale bar = 100 μm). (f and g) Cross-sectional images of scaffold stained with Masson's trichrome (f) and anti-CD31 (g) to identify endothelial cells in the cellulose scaffold. Initial blood vessels are indicated by white arrows (scale bar = 20 μm). (Reproduced from ref. 26 with permission from PLOS. Copyright 2016.) (h) Maximum contractile strain analysis for hiPSCMs on ECM-coated and non-coated decellularized spinach leaves at 7, 14, and 21 days. All values are mean ± S.E.M. (i) Confocal microscopy images of fibronectin and non-coated spinach leaves after 21 days. Samples were stained for sarcomeric α-actinin (green), connexin-43 (red), and Hoescht 33342 (blue) (scale bar = 25 μm). (Reproduced from ref. 30 with permission from WILEY-VCH Verlag GmbH & Co. Copyright 2020.)

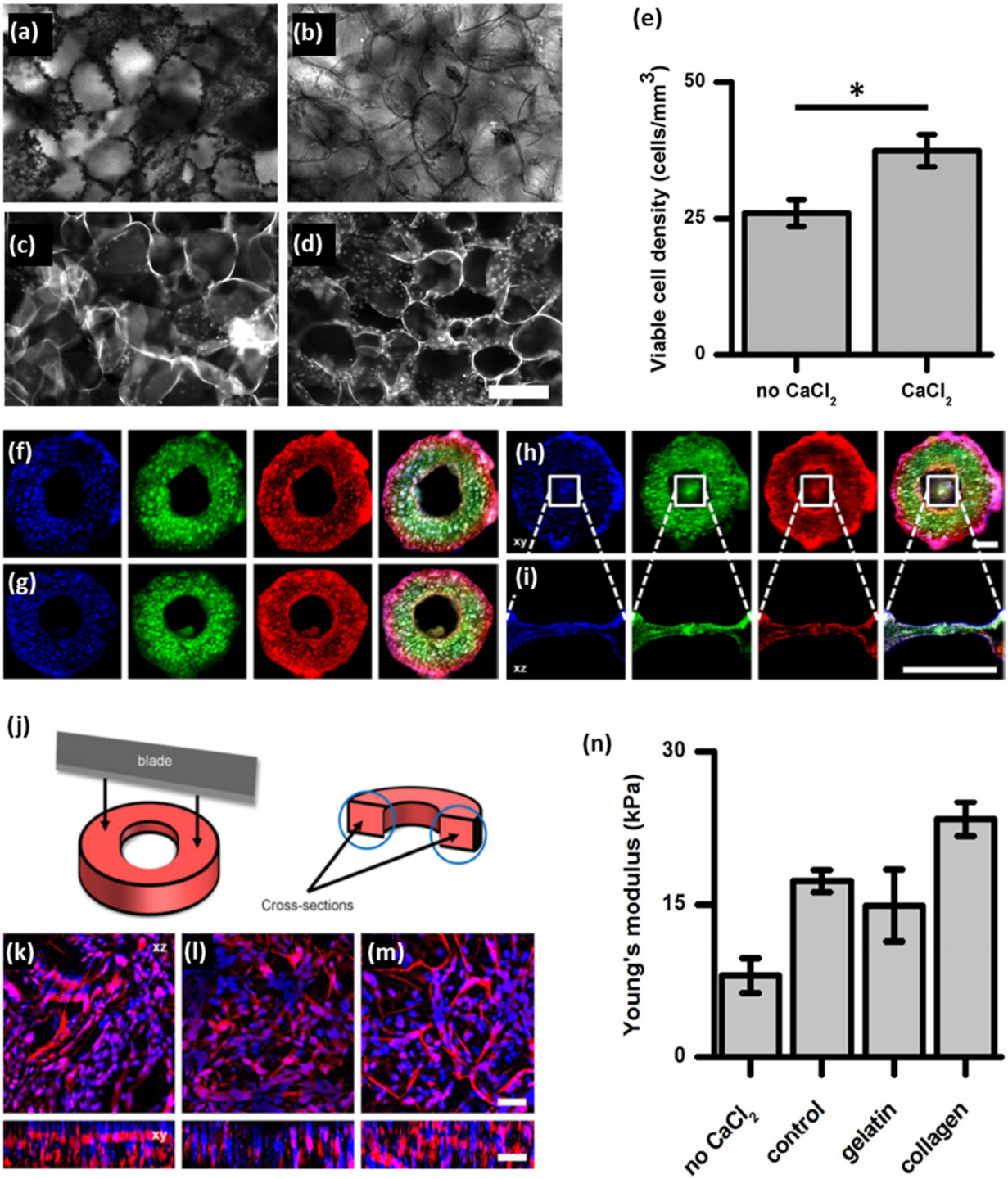

Fig. 19 Customizing the shape and microenvironment biochemistry of apple-derived scaffolds (a–e). $CaCl_2$ pretreatment: the salt/micelles crash out of solution onto the scaffold (a). Removal of the salt residue (b). C2C12 myoblasts cultured on the scaffold without $CaCl_2$ pretreatment (c). C2C12 myoblasts cultured on the scaffold with $CaCl_2$ pretreatment (d). (e) CCK-8 quantification of cell density after 2 days of culture. ($P = 1.8 \times 10^{-2}$, $N = 5$). All values are mean ± S.E.M. (scale bar = 200 μm). (f–i) Confocal microscopy images of control (f), gelatin (g) and collagen (h and i) scaffolds. The scaffolds were stained for the nuclei (blue), cell membrane (green), and cellulose (red). Also, all the stained parts merged in an image. The permanent collagen hydrogel created a compacted collagen suspension over the ring-hole (h and i). It should be noted that the collagen gel suspended over the ring-hole contained cells as well (scale bar = 1000 μm). (j) The rings were sectioned with a razor blade to reveal their cross-sectional areas. (k–m) Cross-sectional areas XZ and XY, maximum projections of confocal images of the control (k), gelatin (l), and collagen (m) biomaterials. Blue = nuclei, red = cellulose (scale bar = 50 μm). (n) The Young's modulus of the scaffolds. ($P = 4.9 \times 10^{-2}$ for no $CaCl_2$ and control. No $CaCl_2$: $N = 5$, $CaCl_2$: $N = 6$) ($P > 0.05$, for gelatin and collagen, both $N = 6$). (Reproduced from ref. 29 with permission from American Chemical Society. Copyright 2018.)

salt-treated scaffolds, compared with their non-salt-treated counterparts, after 2 days of C2C12 mouse myoblast cell culture (Fig. 19e). Remarkably, these results were achieved without the need for deliberate surface functionalization, unlike in other studies. The researchers also achieved a groundbreaking advance by combining plant-derived scaffolds with hydrogels. This involved designing two scenarios for hydrogel integration: temporary and permanent hydrogel casting. Because of gelatin's melting point of 32 °C, gelatin hydrogels were employed in the temporary case. When placed in an incubator at 37 °C, the gelatin slowly diffused out of the scaffolds. This exposed the cells to a distinct biochemical cue during the attachment process. On the other hand, collagen hydrogel was used as the permanent hydrogel; unlike gelatin, collagen remains in its gel state at 37 °C. Collagen hydrogel encompasses the scaffold, resulting in a composite biomaterial where cells occupy two distinct regions: in the cellulose and collagen ring, or suspended in the collagen gel in the ring's central cavity. Confocal microscopy revealed a dramatic improvement in the cell invasion and proliferation rate, as compared with the previous investigation (Fig. 19f–m). The CCK-8 assay, conducted one day after cell seeding, quantified and compared the initial cell attachment on different scaffolds. It was found that a significantly greater population of viable cells remained in the biomaterial used in combination with the permanent hydrogel. The mechanical properties of the scaffolds were assessed by measuring the Young's modulus. The results revealed that the $CaCl_2$ treatment increased the Young's modulus of the scaffolds, whereas the addition of the hydrogels exerted a negative impact (Fig. 19n). The increase in the Young's modulus after salt treatment can presumably be attributed to the presence of residual salt adsorbed on the surface. The *in vivo* investigation ensured that the salt treatment did not adversely affect the biocompatibility of scaffolds or the vascularization process, thereby confirming the previous study's findings.

These studies have raised the possibility of achieving biocompatible plant-derived scaffolds that can support the adherence and proliferation of cells without surface biofunctionalization. The selection of biofunctionalization methods depends on the ultimate application of the scaffold or the specific type of cells. In some cases, biofunctionalization may indeed prove to be a game-changer, whereas in others its impact may be less pronounced. For example, as a method of biofunctionalization, biomineralization is capable of modifying and enhancing the mechanical properties of the final scaffolds. These mechanical features are crucial in influencing cell behaviors. In particular, in the context of regenerating rigid tissues (*e.g.*, bone), mechanical properties play a paramount role that necessitates careful consideration. Similarly, the type of cell employed is a critical determinant of cell attachment, proliferation, and functionality within the scaffolds. Considering the example of C2C12 myoblasts, they are able to deposit their own ECM during culture on 3D scaffolds.[198] In such cases, the need for biofunctionalization may be limited or even non-existent, as the cells inherently contribute to the scaffold's ECM. Nevertheless, many questions about surface biofunctionalization remain to be answered, and this ongoing controversy calls for further investigation to provide clarity and insight into various aspects of this issue.

Eliminating biofunctionalization could reduce the manufacturing time and cost of scaffold fabrication. This approach could simplify the process of creating new regenerative scaffolds, making them more accessible and cost-effective. However, this is not the only way to reach this goal. Narayanan *et al.* pioneered the development of a 3D micropatterned scaffold that does not require any decellularization or surface modification, resulting in a cost-effective and environmentally friendly solution.[199] The scaffold was fabricated by cutting small segments from the pseudostem sheath of the banana plant, followed by freeze-drying and sterilization using ethylene oxide. After this sterilization process, the scaffold becomes ready for use. The SEM images of the final scaffolds revealed their composition, consisting of a micro rectangular cavity (0.5 mm × 1 mm × 0.5 mm) interconnected with porous septa (0.05 mm in diameter) arranged in a series resting on a robust base. It seems that the topographical features of the scaffolds favor the 3D attachment and proliferation of cells. To assess the potential of scaffolds for supporting cell attachment and proliferation, various cell types, including hMSCs, mouse primary cortical neurons, human pancreatic cancer cells, and mouse fibroblasts, were introduced into the scaffold. Imaging analysis demonstrated that all cell types successfully attached and proliferated on the surface of scaffolds. A hepatocyte differentiation protocol was also applied to the hMSCs that seeded into the scaffolds, and after differentiation, the cells were observed for 30 days. Bright-field microscopy images displayed opaque spherical outlines on the scaffolds, with some spheroid cells observed spilling into the cell culture medium. This observation confirmed the successful formation of spheroids, which confirmed effective differentiation. The surface of the scaffolds was subsequently scanned, and SEM images of the scaffolds revealed the presence of a substantial population of primary human hepatocyte-like cells. These cells exhibited numerous bud-like projections on the surface, resembling a berry-like morphology, with a central invagination. An initial assessment of the presence of cell surface markers for hepatocytes, human hepatocyte-like cell-specific markers, and Cytochrome P450 was performed, and the confocal microscopy images confirmed the presence of these markers. To evaluate *in vivo* biocompatibility, the scaffold was subcutaneously implanted in Sprague Dawley rats for 8 weeks. Histopathological analyses were conducted at various time intervals during this period. The levels of polymorphs (cells involved in the material's phagocytosis) and C-reactive protein were quantified and compared with both sham-operated and sham-unoperated groups. Although an initial immune response was observed following implantation, no toxicity was found after 4 weeks, thus confirming the biocompatibility of the scaffolds. Nevertheless, more comprehensive investigation is required to evaluate the biocompatibility of scaffolds when seeded with autologous cells and their potential to support

these cells in an *in vivo* environment. Despite the limitations of this study, it highlights the feasibility of creating plant-based scaffolds without the necessity of decellularization and surface modifications. The study highlights the importance of selecting a plant skeleton with innate topographical characteristics and a chemical conformation capable of easing the fabrication process and ultimately reducing the cost of the final product. Previous studies have found that cells are not only sensitive to the chemical composition of their surroundings but also responsive to the topographical cues of their environment.[200] This observation holds true for plant-based scaffolds as well, emphasizing the importance of choosing suitable materials, given that the properties of the scaffolds should be tailored to specific tissue engineering objectives.[27] As an example, Bar-Shai *et al.* chose two different kinds of marine macroalgae species, *Ulva* sp. and *Cladophora* sp., to fabricate a decellularized cellulose scaffold.[49] SEM images of the decellularized seaweed matrices revealed their diverse structural composition. The *Ulva* sp. matrix showed hollow cavities, organized in a comb-like network, with highly interconnected pores (Fig. 20a), whereas imaging of *Cladophora* sp. matrix showed an entangled mesh, a bundled fibrillar matrix (Fig. 20d). After the recellularization of scaffolds with mouse embryonic NIH-3T3 fibroblasts, the *Cladophora* sp. scaffold encouraged elongated cells to spread along the axis of its fibers, and gradual linear cell growth (Fig. 20e and f), whereas the *Ulva* sp.'s porous surface facilitated rapid cell growth in all directions, reaching saturation at week 3 (Fig. 20b and c). The microporous surface area of the *Ulva* sp. scaffold provides cells with the opportunity to migrate in all directions. However, at higher concentrations of initially seeded cells, the proliferation rate decreases, due to early surface cell saturation in the scaffolds. In contrast, the structure of *Cladophora* sp. facilitates the migration of cells along the elongated axis of the fibers, guided by microfibrils overlaying the fiber surface. This guidance mechanism results in a linear increase in proliferation rates as the initial concentration of seeded cells increases (Fig. 20g). These studies demonstrate that topographical features of plant-based scaffolds can influence cell behaviors.

However, topographical cues are not the only physical parameters that can impact cell behavior. Certain tissues in the human body are subject to distinct biomechanical forces, such as shear stress and cyclic strain. Scaffolds intended to replace such tissues must possess the ability to withstand these forces, while also providing support for the residing cells. This is a crucial issue in lung tissue engineering, where the biomaterials must be able to harmonize with the forces generated by ventilation and the strain experienced by the lung tissues. The mechanical strain and forces indeed alter cell behaviors. Harris *et al.* showed that cells seeded on a spinach leaf scaffold perceived and responded to mechanical strain.[201] In their prior study, they delved into the stiffness of spinach leaf scaffolds, recognizing the importance of aligning the mechanical properties of scaffolds with the target tissues.[37] The elastic feature, another critical mechanical characteristic of tissue engineering scaffolds, was also investigated in the context of the spinach leaf scaffold. In order to assess elasticity, the researchers constructed a custom-built device to stretch decellularized tissue in the cell culture environment and characterize the response of decellularized plant-based scaffolds to such strains within the physiological range of the normal human adult lung during breathing. After seeding human lung epithelial cells on the scaffold, the cellular response to stretching was also examined. The results showed that stretching the scaffold in the range of normal human adult breathing increased the strain at failure and ultimate tensile strength, as compared with an unstretched scaffold, while preserving the initial porosity after 24 h of cyclic strain (Fig. 20h). Importantly, the cell behavior changes after cyclic strain showed nuclear reorientation perpendicular to the strain direction, nuclear location of YAP, and increased expression of YAP target genes, a high cytoplasmic calcium level, and an elevated expression level of collagen genes, with increased collagen secretion at the protein level (Fig. 20i and j). These findings demonstrated that the decellularized plant leaf tissues possessed an inherent elastic property similar to that observed in the mammalian system. This property allowed cells to perceive and react to mechanical cues, highlighting the potential for these plant-based scaffolds in tissue engineering applications. It has created significant interest in exploring the elastic properties of other decellularized vegetal biomaterials and understanding how they might align with the requirements of specific anatomical areas (*e.g.*, the skin, tendons, or blood vessels).

In the next section, we explore plant-based scaffolds and biomimetic substrates designed to replicate the ECM environment and facilitate the establishment of human tissue patterns after recellularization. We provide a comprehensive overview that includes discussions of bone, neural, and cardiovascular tissue engineering applications, along with insights into angiogenesis modelling.

7.2. Bone tissue regeneration

Bone tissue engineering has emerged as a cutting-edge field at the intersection of biology, engineering, and materials science, offering innovative solutions to address the challenges posed by bone defects and injuries.[202] The limitations of conventional treatment methods, including autografts, allografts, and synthetic materials, have paved the way for the development of alternative strategies for bone regeneration.[203] One such strategy involves the use of scaffolds to enable new bone tissue to grow. Although scaffold design has conventionally been dominated by synthetic materials, attention has recently turned towards harnessing the unique merits of plant skeletons for bone tissue engineering.[24] Plant skeletons offer a promising approach for scaffold development, providing the requirements for successful bone regeneration.[36] Plant tissues are similar to animal tissues in the sense of involving a sequence of soft and hard components organized in a complex hierarchical structure. The anisotropic structures of plant skeletons provide desirable mechanical properties, which are critical features of bone tissue engineering scaffolds.[58] Plant skeletons

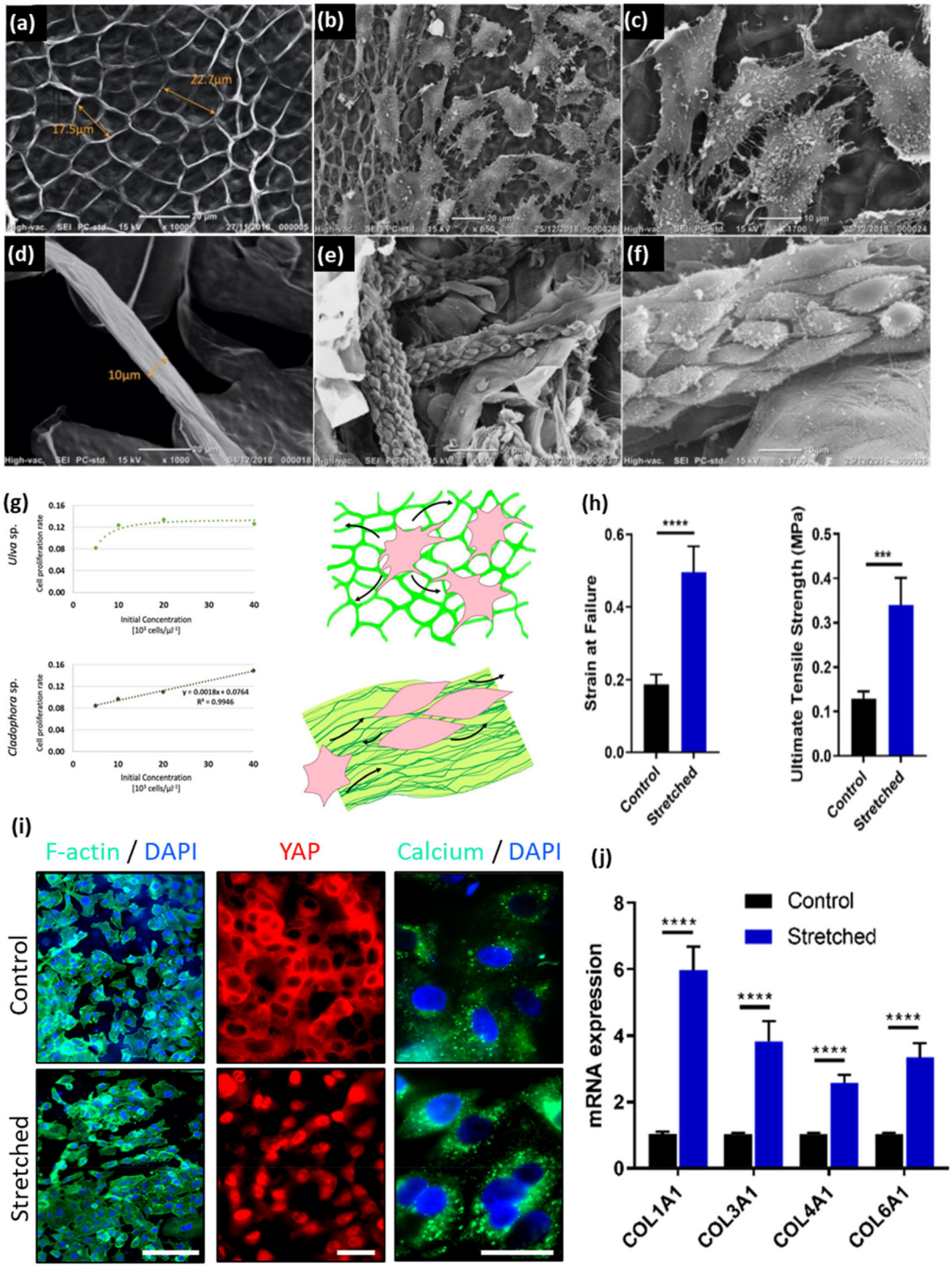

Fig. 20 (a) SEM image of an *Ulva* sp. acellular scaffold. (b, c) SEM images of a recellularized *Ulva* sp. scaffold after 4 weeks of cell seeding. (d) SEM image of *Cladophora* sp. acellular fiber. (e, f) SEM images of a recellularized *Cladophora* sp. scaffold after 4 weeks of cell seeding. (g) Cell growth in correlation to initial seeding cell concentrations, graphs and schematics of growing pattern. (Reproduced from ref. 49 with permission from Nature Springer. Copyright 2021.) (h) Comparison of strain at failure and ultimate tensile strength of decellularized spinach leaf scaffolds exposed to strain conditions for 24 h and unstretched controls (n = 10). (i) The biological response to mechanical deformation observed in A549 cells seeded on spinach leaf scaffolds and exposed to lung-relevant strain (11.7% strain, 0.3 Hz) for 24 h from observing immunofluorescent microscopic images of the morphology (F-actin, green) and nucleus (DAPI, blue) of A549 cells seeded on unstretched (control) and stretched scaffolds, immunofluorescent microscopic images of YAP protein (red) and nuclei (blue) localization in A549 cells, and immunofluorescent microscopic images of Fluo-4 probe (green) localization to detect intracellular calcium in A549 cells counterstained with DAPI (blue). (Scale bars: (F-actin/DAPI) = 100 µm, (YAP and Calcium/DAPI) = 20 µm.) (j) Relative expression levels of the four main collagen genes expressed in lung cells (COL1A1, COL3A1, COL4A1, and COL6A1), measured in A549 cells seeded on stretched scaffolds and normalized to unstretched (control) scaffolds. (****p < 0.0001) (reproduced from ref. 201 with permission from the American Chemical Society. Copyright 2022).

can also be easily decellularized, repopulated with mammalian cells, or loaded with active biomolecules to serve as scaffolds with advantageous capabilities, such as biocompatibility, biodegradability, and natural porosity, resulting in effective tissue repair.[36] Plant-derived scaffolds could bypass challenges associated with immune responses and scaffold degradation and offer an eco-friendly alternative to synthetic materials for bone regeneration. Numerous studies have assessed the efficiency of plant-based bone tissue engineering utilizing various parts of plants, including fruits, leaves, and stems, which can closely resemble bone and offer an ideal environment for promoting osteogenic differentiation.[33,60,158]

7.2.1. Fruit-derived scaffolds for bone tissue engineering. Decellularized fruit-derived scaffolds can provide a 3D biomimetic microenvironment for cell growth and tissue regeneration.[36,204,205] Given these capabilities, Modulevsky *et al.* employed native hypanthium tissues from apples and utilized decellularization approaches to obtain porous plant-derived cellulose scaffolds for 3D culture of mammalian cells *in vitro*, including NIH3T3 fibroblasts, mouse C2C12 muscle myoblasts, and human HeLa epithelial cells. They found that cell viability remained high even after 12 weeks of culture.[25] Inspired by these promising *in vitro* results, this decellularized plant-derived cellulose scaffold was further implanted in immunocompetent mice.[26]

Following implantation, the immunological responses of the mice, the deposition of a new extracellular collagen matrix, and new blood vessel formation were evaluated after 8 weeks. No immune response or foreign body reactions were observed within the dermis tissues at the end of investigations. However, histological analysis confirmed the angiogenic effect of these native scaffolds and the presence of active fibroblasts, as well as collagen deposition in the pores of cellulose scaffolds, demonstrating the biocompatibility and promising potential of plant-derived cellulose scaffolds for tissue regeneration. Similarly, Contessi Negrini *et al.* selected carrot-derived scaffolds for bone tissue engineering, due to the presence of two different porosity ranges in the same structure (radially oriented pores (70 ± 12 mm average size) in the central region and round larger pores (130 ± 26 mm average size) in the peripheral region). The prepared scaffolds supported MC3T3-E1 pre-osteoblast adhesion, proliferation, and osteogenic differentiation without cytotoxic effects. However, they noticed that decellularized carrot-derived scaffolds can only serve as bone fillers in non-load-bearing conditions, due to their lower mechanical properties compared with natural bone tissues.[36] Building on the research into the *in vivo* potential of plant-derived scaffolds for bone tissue engineering, Lee *et al.* used decellularized cellulose scaffolds of various plants, including apple, broccoli, sweet pepper, carrot, persimmon, and jujube, to incubate with hiPSCs, stimulated to differentiate as osteoblasts in culture (Fig. 21a).[60] The residual cellulose structures contained pores of diverse shapes and dimensions (Fig. 21b); apple scaffolds possessing regular 300 μm pores seemed to provide the best construction (Fig. 21c). After being seeded with hiPSCs, only the cells cultivated in the apple scaffolds were able to survive (Fig. 21d); in the other types of scaffolds, cells did not proliferate well. *In vitro* osteoblastic (OB) differentiation of hiPSCs in the decellularized apple scaffolds was evaluated by Alizarin red S and Von Kossa staining, which confirmed calcium deposition and bone formation (Fig. 21e). They also observed a time-dependent increase in osteocalcin (OCN) expression as an osteogenic marker compared with hiPSCs (Fig. 21f). OB-differentiated plant scaffolding also improved bone regeneration *in vivo* in a rat calvarial defect model. Histologically, the bone organoids showed successful engraftment, evidenced by the presence of type I collagen (Col-I) deposition, as verified by Masson's trichrome stain after 8 weeks, which signifies a promising development in the context of new bone formation (Fig. 21g). In addition, vascular ingrowth, which is essential for successful implantation, was observed in apple scaffolding (Fig. 21h). For effective bone regeneration, scaffolds must possess interconnected and highly porous (≥90%) structures, with adequately sized openings (≥100 μm).[206] The apple-derived scaffolds provided these desired features, with pores approximately 200 μm in diameter, which makes them suitable for bone regeneration applications to promote cell growth, tissue integration, vascularization, and delivery of nutrients and oxygen to the developing tissues.

Moreover, plant-derived cellulose scaffolds provide a versatile platform that can be easily carved into the desired shapes and modified by surface treatments to improve their surface biochemistry.[29] Latour *et al.* coated decellularized apple-derived cellulose scaffolds with collagen, which is widely used for bone tissue engineering.[38] MC3T3-E1 pre-osteoblasts were seeded in the bare cellulose scaffolds or composite cellulose–collagen scaffolds to evaluate their capacity for *in vitro* mineralization. They found cell adherence and higher levels of calcium deposition and alkaline phosphatase (ALP) in both the bare cellulose scaffolds and the composite hydrogel scaffolds, as compared with the control (non-seeded) scaffolds. However, the presence of collagen hydrogel in the composite scaffolds did not have any noticeable effect on the increase in Young's modulus.

Despite the increase in the Young's modulus of both types of scaffolds when cultured in a differentiation medium, the moduli remained lower than those of bones, indicating that these scaffolds may not be suitable for load-bearing applications. They nevertheless remain a promising option for non-load-bearing applications (*e.g.*, hand and wrist fractures). An *in vivo* comparison should be done, however, to increase the relevance of any studies. Given the challenge of healing in the interfacial zone between tissues in regenerative medicine, Hickey *et al.* also fabricated modular "blocks" using computer numerical controlled milling techniques, employing decellularized plant-derived scaffolds with varying shapes and sizes (Fig. 22a).[34] Each block was seeded with MC3T3-E1 pre-osteoblasts and assembled like LEGO™ bricks, forming an engineered tissue interface (ETI) to study the interaction between lab-grown bones and connective tissues (Fig. 22b). *In vitro* cell migration assays indicated that, when a scaffold containing preloaded fibroblast cells was interlocked with a bare subunit,

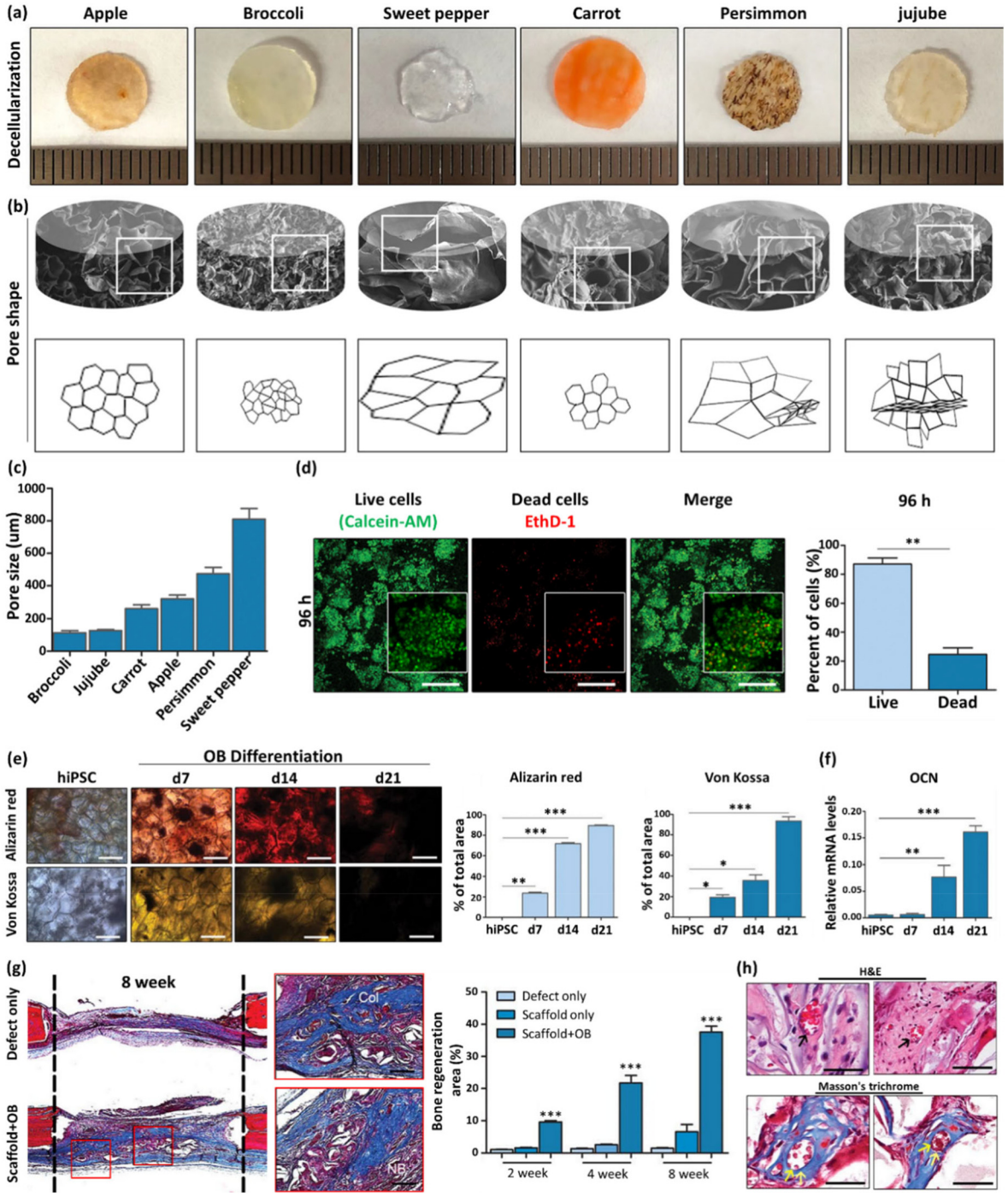

Fig. 21 (a) Images of different plants after decellularization. (b) SEM images and drawings of various plant scaffolds showing shape and pore sizes. (c) Pore sizes of different scaffolds. (d) Views and proportions of live and dead cells in cultures after 96 h, respectively. (e) Alizarin red staining and Von Kossa staining of hiPSCs before and after osteoblastic differentiation and proportions of positively stained areas. (f) Expression levels of osteocalcin by hiPSCs before and after osteoblastic differentiation (*p < 0.01; **p < 0.005; and ***p < 0.001). (g) Masson's trichrome staining of defect sites 8 weeks after implantation, and proportion of bone regeneration 2 weeks, 4 weeks, and 8 weeks after implantation. (h) Assessment of vascularization in graft (H&E and Masson's trichrome stains). (Reproduced from ref. 60 with permission from Springer Nature Copyright 2019.)

the cells moved across the interface and penetrated the bare scaffold, as it is crucial for cells to traverse the interface and interact with the adjacent population (Fig. 22c). They also replicated the bone/connective tissue interface by repopulating each subunit with the appropriate cell type: osteoblasts for the bone region and fibroblasts for the connective tissue region. The osteoblast cells mineralized the bone segment, resulting in a stiffness of 115.00 kPa, whereas the fibroblast cell-popu-

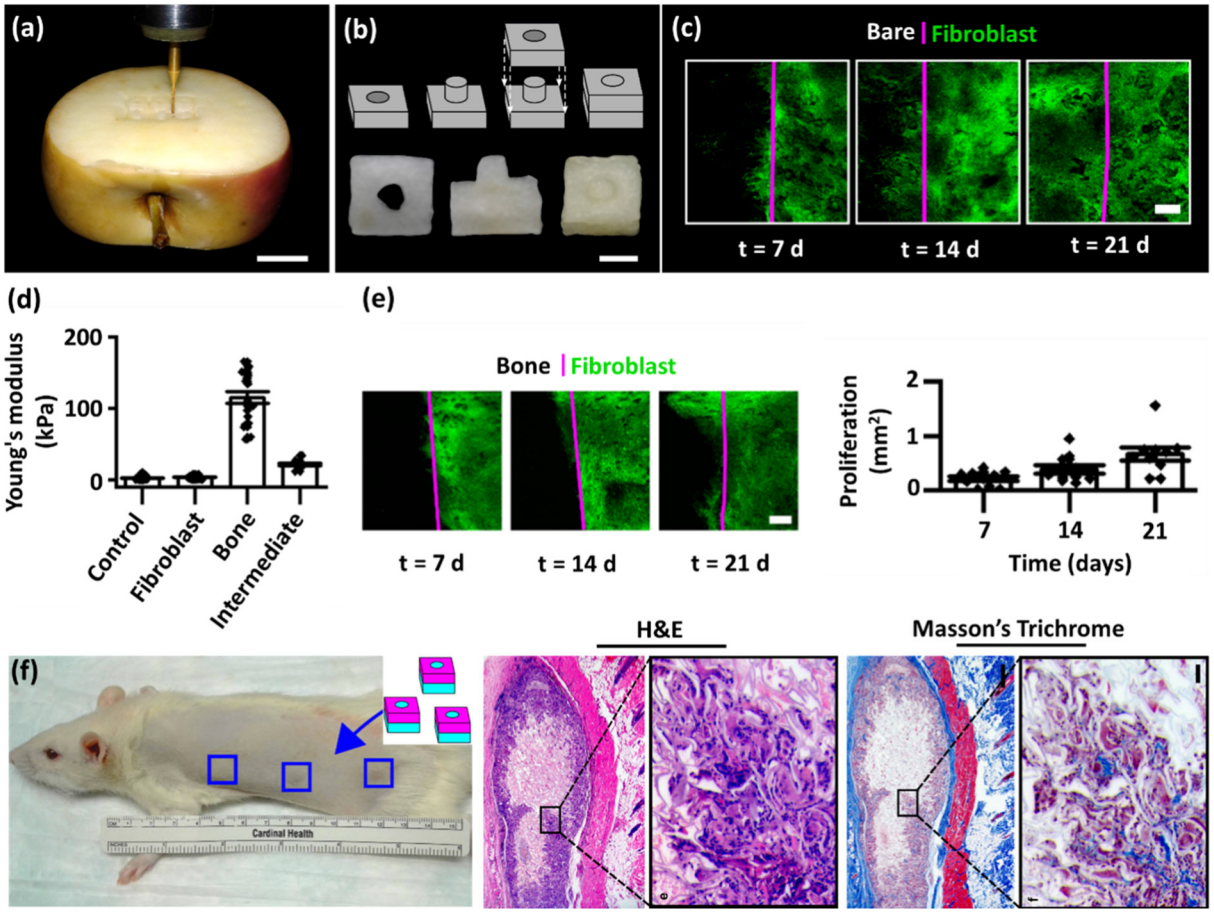

Fig. 22 (a) A CNC router was used to carve the interlocking materials (scale = 15 mm). (b) Geometry of both the single stud and anti-stud interlocked units and the decellularized subunits and the combined entity (scale = 2.5 mm). (c) Fibroblast cell (green) migration across the interface (magenta) of the interlocked unit. The image shows one subunit preloaded with cells, whereas the other remains void of cells (scale = 500 μm). (d) Compressive moduli of the bone–fibroblast ETI (N = 5). (e) Fibroblast cell (GFP NIH 3T3) migration across the bone connective tissue ETI (scale = 500 μm) and quantification of cell migration (N = 10). (f) Schematic representation of the location of 3 subcutaneously implanted ETIs in a rat model and corresponding H&E and Masson's trichrome staining on the scaffolds (scale = 500 and 50 μm, respectively) (reproduced from ref. 34 Copyright 2020).

lated region was not mineralized and had a lower modulus of 3.90 kPa (Fig. 22d). In addition, the results of cell migration from the fibroblast component to the bone section showed that the cells intermixed at the interface and exhibited a similar proliferation rate to those in the natural bone–connective tissue interface, which increased in a time-dependent manner (Fig. 22e). The interlocked composite was finally implanted subcutaneously in an immunocompetent rat model, and histological analysis after 4 weeks showed cell invasion in the peripheral regions of the biomaterials, vascularization, and collagen deposition in the cellulose-based scaffold (Fig. 22f). It was therefore concluded that decellularized plant scaffolds can be selected based on a specific property and subsequently modified to match the desired microenvironment features. In another attempt, Mahendiran *et al.* explored the potential of cellulose scaffolds derived from immature *Borassus flabellifer* endosperm for bone tissue regeneration.[58] The prepared scaffolds were modified with two organosilanes: amino-terminated aminopropyltriethoxysilane (APTES) and methyl-terminated octadecyltrichlorosilane (OTS). As a result, the scaffolds acquired a foamy architecture and, as compared with unmodified controls, both APTES and OTS treatment showed a significant improvement in the material's compressive modulus, increasing it from approximately 0.3 MPa to 0.9 MPa and 1.2 MPa, respectively, as well as enhanced osteoinductive properties. Collectively, the bulk-like plant parts (*e.g.*, apple fruits) provide a noteworthy advantage in the field of tissue regeneration.

7.2.2. Leaf-derived scaffolds for bone tissue engineering. The cell walls of leaves are composed of cellulose, containing pores that enable the transfer of nutrients and water throughout the plant structures. This characteristic of plant leaves is the most important feature in any type of scaffold.[8] Thus, decellularized plant leaf can be used as a scaffold to resemble vascularization in bone tissue engineering. To this end, Salehi *et al.* provided a decellularized spinach leaf scaffold and evaluated its osteoinductivity by culturing human bone marrow-derived MSCs (BM-MSCs) on it.[33] SEM images from the

surface (Fig. 23a) and transverse sections (Fig. 23b) showed uniform porosity throughout the structure: the pores were about 50 micrometers in size. AFM results showed the surface roughness of scaffolds, which could induce stem cell differentiation and osteogenic cell adhesion (Fig. 23c). To assess the biocompatibility of the scaffolds, human BM-MSCs were cultured on the decellularized spinach leaf scaffold. It was observed that cells grew well and spread over the surface of the scaffolds without aggregation (Fig. 23d). The ALP activity, calcium content, and expression fold change of osteocalcin and Runt-related transcription factor 2 (Runx2) in BM-MSCs cultured on the decellularized spinach leaf scaffold were significantly higher, in comparison with BM-MSCs clustered on the tissue culture polystyrene (TCPS) groups as a control on day 18 as markers of osteogenic differentiation (Fig. 23e and f). Hence, a decellularized spinach leaf scaffold can be considered a good substrate for cell attachment, growth, and differentiation in bone tissue engineering. While spinach leaves are one example of plant vasculature structures, plant materials provide a variety of vascular networks, with different designs and structures for tissue engineering. Cabbage is another source, being a leafy vegetable, and its leaves consist of expanded blades (the lamina) and veins (the midvein or primary vein and secondary vein) that can feed and oxygenate the cells cultured on it after decellularization. In view of this, a decellularized cabbage leaf scaffold co-cultured with BM-MSCs was investigated for osteogenic differentiation by Salehi *et al.* (Fig. 23g and h).[48] SEM images presented the regular geometrical grids of the scaffold surface; however, cross-sectional images showed a multilayered structure with irregular geometrical grids, providing plenty of space for cell growth and proliferation due to the 3D structures (Fig. 6i and j). A tensile test demonstrated the potential of the prepared scaffold to mimic spongy bone tissues. *In vitro* investigations showed a notable increase in ALP activity and mineralization of BM-MSCs cultured on the scaffold, as compared with BM-MSCs cultured on TCPS as a control group (Fig. 23k). Higher gene expression of osteocalcin was also observed in the cells cultured on a decellularized cabbage leaf scaffold, as compared with those cultured in Petri dishes (Fig. 23l). In conclusion, given the osteogenic potential of the fabricated scaffold, it is evident that a decellularized cabbage leaf scaffold can provide an exceptional ECM-mimicking structure for bone tissue engineering. However, *in vivo* tests are needed for the comprehensive evaluation of the application potential of these leaf-derived scaffolds in bone regeneration. The biggest challenge with these plant-derived scaffolds, moreover, is that they have to provide appropriate biomechanical support to simulate the mechanical properties of the reconstructed tissue.

7.2.3. Stem-derived scaffolds for bone tissue engineering. Progress in the field of plant-derived scaffolds for bone tissue engineering is currently facing a challenge related to the strength of the plant-derived scaffolds, which is insufficient to mimic natural bones. The remarkable biomechanical properties of bones are a result of its hierarchically organized structures, which enable them to adapt to constantly changing mechanical needs.[103,207] To achieve successful bone regeneration, hierarchical structure-mimicking scaffolds are therefore required to enable the production of well-structured bones. In light of this necessity, it is important to recognize that wood and bone share several notable similarities as anisotropic heterogeneous composites (Fig. 24). Both osteons and tree cells exhibit alignment along the long axis of bone and wood, respectively, featuring multiple concentric layers of parallel fibers or fibrils. These layers, characterized by varying orientations, collectively contribute to their mechanical strength.[208–210]

Functional wood implants are mostly prepared by chemically and thermally treating hierarchical natural templates (wood cell walls), possibly selectively modifying the wood cell wall structures (fine pore spaces and inner lumen surface area) for different applications.[73,80] The early studies of birch wood implants pretreated with ethanol showed new bone formation around the wood implants and into their pores; however, the tissues produced a foreign body reaction, which cannot be prevented by ethanol pretreatment.[211]

Years later, Aho *et al.* investigated a novel wood pretreatment method, involving preheating birch implants at different temperatures (140, 200, and 220 °C) for 2 h and implanting them into drilled cavities of rabbit femurs.[72] At the end of the experiments, they observed that the preheating of birch implants improved osteoconductivity, as compared with untreated implants. Notably, applying the highest temperature achieved reduced biomechanical characteristics of the implants. Moreover, researchers noticed that pretreating wood with heat slightly reduces the surface roughness of the implants.[212] Implant surface roughness can provide a basis for the interfacial integration of an implanted material and host bone, as well as increasing mechanical interlocking.[213,214] One of the possible mechanisms that reduces surface roughness is the transformation of wood lignin to a thermoplastic condition, which densifies the cell surfaces.[212] Recent research relevant to DW has expanded to develop wood-based functional scaffolds by removing the embedded lignin from the wood cell wall structures, while maintaining the natural hierarchical cellulose structures.[63] In order to achieve complete lignin removal, an additional bleaching procedure that removes hemicelluloses from the cell wall is required. Consequently, after the elimination of lignin and hemicellulose, the obtained cellulose scaffold exhibited enhanced biocompatibility and a porous structure conducive to cell attachment and proliferation, making wood-derived cellulose scaffolds an ideal candidate for bone tissue engineering. However, the robustness of the cellulosic system is altered. In particular, it exhibits a loose, unstable nature in a wet state, affecting the mechanical properties of wood as well as limiting its application as bone repair material alone. By incorporating hydrogels or minerals, its mechanical properties can be fine-tuned to optimize the stability, flexibility, and mechanical and biological activities of cellulose scaffolds, providing promising resources for various applications in the field of tissue engin-

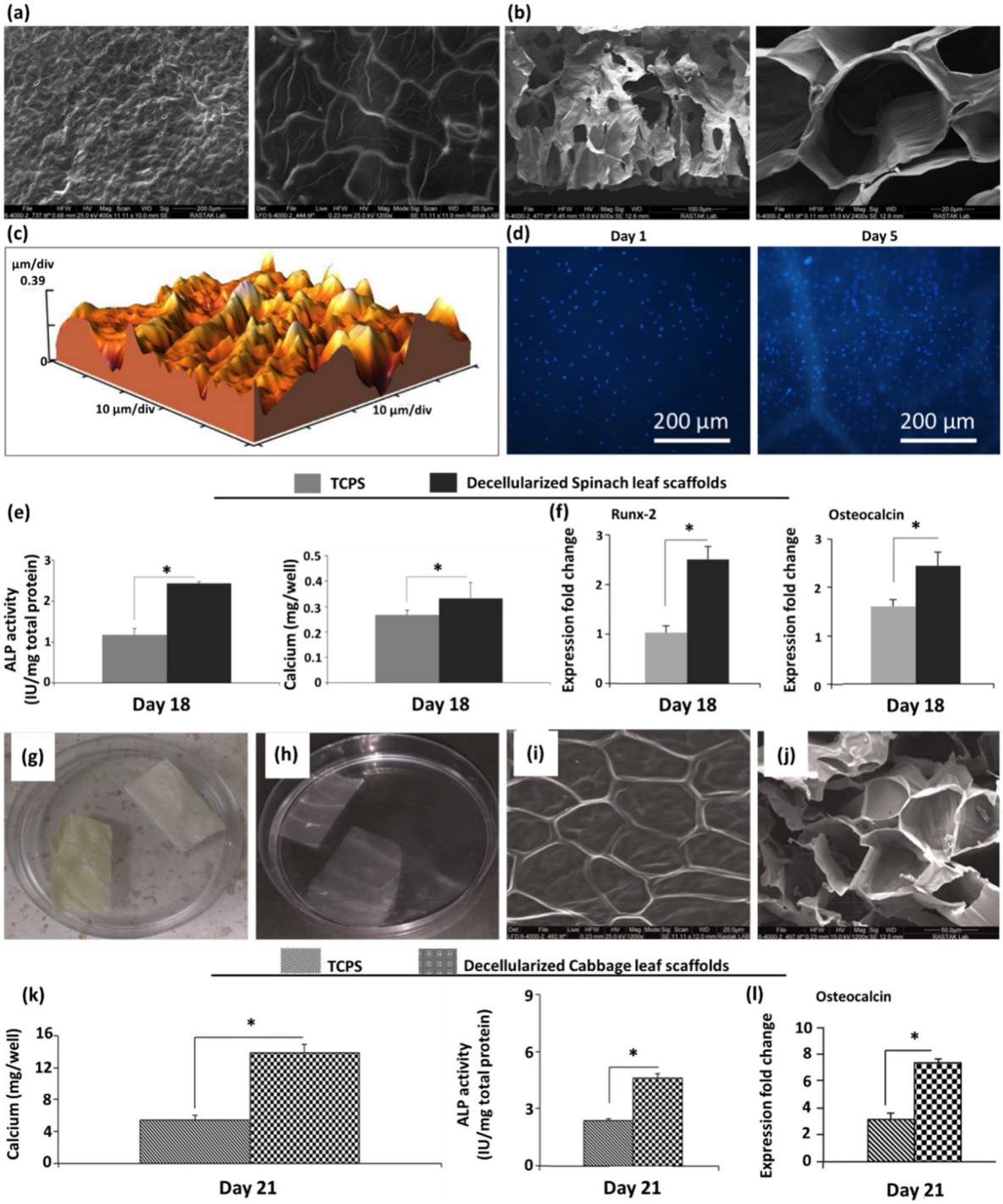

Fig. 23 (a, b) SEM images of the surface and transverse sections of decellularized spinach leaf scaffolds at two magnifications, respectively. (c) Microscope representative AFM image of the decellularized spinach leaf scaffold surface, with a surface roughness average (R_a) of 11.50 nm. (d) DAPI staining results of human BM-MSCs cultured on the decellularized spinach leaf scaffold on days 1 and 5. (e) ALP activities and calcium content assays of BM-MSCs cultured on the decellularized spinach leaf scaffolds (SP) and TCPS as a control on day 18 under osteogenic differentiation medium ($P < 0.05$). (f) Expression fold changes of Runx-2 and osteocalcin gene markers in BM-MSCs cultured on SP and TCPS as a control on day 18 under osteogenic differentiation medium ($P < 0.05$). (Reproduced from ref. 33 with permission from Elsevier. Copyright 2020.) (g) Photographs of cabbage leaf fragments and (h) decellularized cabbage leaf fragments. (i, j) SEM images of the surface and cross-section of the decellularized cabbage scaffold. (k) Calcium content, ALP activity of BM-MSCs, and (l) osteocalcin expression level when differentiated on the TCPS and decellularized cabbage (Cb) scaffold on day 21. ($P < 0.05$). (Reproduced from ref. 48 with permission from WILEY-VCH Verlag GmbH & Co. Copyright 2020.)

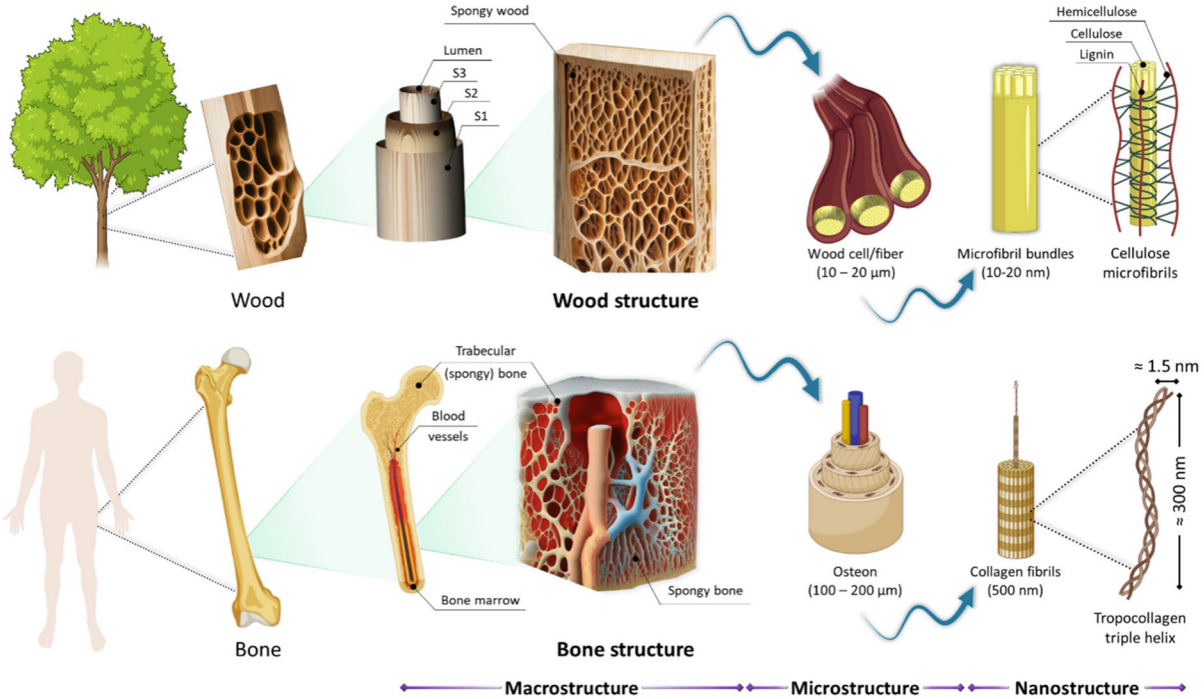

Fig. 24 Schematic structures of bone and wood at the macro, micro, and nano scale. (Reproduced from ref. 210 with permission from MDPI, Copyright 2023.)

eering and regenerative medicine.[63,159,166] To assess this potential for mechanical tunability, Koch *et al.* exploited a straightforward methodology for creating an anisotropic and mechanically adjustable scaffold by saturating delignified spruce wood with an aqueous gelatin solution, followed by a chemical cross-linking step using glutaraldehyde. Then the unreacted glutaraldehyde was removed by thorough washing to obtain the final DW-Gel (Fig. 25a).[215] The cross-linking process enabled adjustment of the mechanical characteristics of composites by altering the cross-linking period. Microscopic images of native wood, DW, and DW-Gel are shown in Fig. 25b. Following delignification treatment, the intact natural wood tissue structure was preserved, the wood cell lumina remained accessible, and the DW samples were effectively infiltrated with hydrogel. Rheological strain sweep experiments indicated that the resultant DW-Gel exhibited relatively high shear moduli, attributed to its anisotropic tubular array structure (Fig. 25c). The cross-linking degree of the DW-Gel samples correlated with their storage (G') and loss moduli (G'').

The DW-Gel shear moduli range from 10^5 to 10^6 Pa, falling within the viscoelastic range of dense connective tissues, which is beneficial for absorbing higher-impact loads. In addition, temperature sweep experiments exhibited the stability of all cross-linked DW-Gel samples over a temperature ranging from 10 to 50 °C; however, the non-cross-linked DW-Gel lost structural integrity at temperatures higher than 34 °C, the onset temperature of gelatin dissolution (Fig. 25d). The results of this study suggest that the cellulose scaffold loaded with hydrogel by varying cross-linking degrees provides adjustable mechanical properties for potential tissue engineering applications.

In view of this, and inspired by the hierarchical anisotropic structures of natural bone and wood, Wang *et al.* designed a highly anisotropic, ultrastrong, stiff, hydrophilic, and osteoconductive hydrogel composite using natural pinewood.[158] To this end, the WW with aligned cellulose fibril skeletons was fabricated using a straightforward one-pot chemical treatment. SA hydrogel precursor solution was infiltrated into the WW microchannels by vacuum impregnation, yielding excellent biocompatibility, a structural similarity to ECM, and a high-water content (WH samples); this was followed by mineralization with HAp nanocrystals (MWH) (Fig. 26a and b). Following gelation, the SA hydrogel effectively occupied the WW lumina, as verified by SEM images of the transverse (Fig. 26c) and longitudinal sections (Fig. 26d). The DW cell walls and the SA hydrogel within the channels can be clearly distinguished. Notably, the original wood texture framework remained intact following hydrogel impregnation. The cross-linked SA network structure is shown in Fig. 26e. As shown in Fig. 26f, HAp nanocrystals precipitated on the networks of SA hydrogel and the surface of the MWH became much rougher than the WH, enhancing osteogenic cell adhesion. It is noteworthy that the deposition of HAp on wood-derived cellulose scaffolds enhanced scaffold biocompatibility, provided a bioactive surface that encouraged the osteogenic differentiation of stem cells, and improved the mechanical properties of the scaffolds.[43,153] Mechanical analysis showed that the tensile

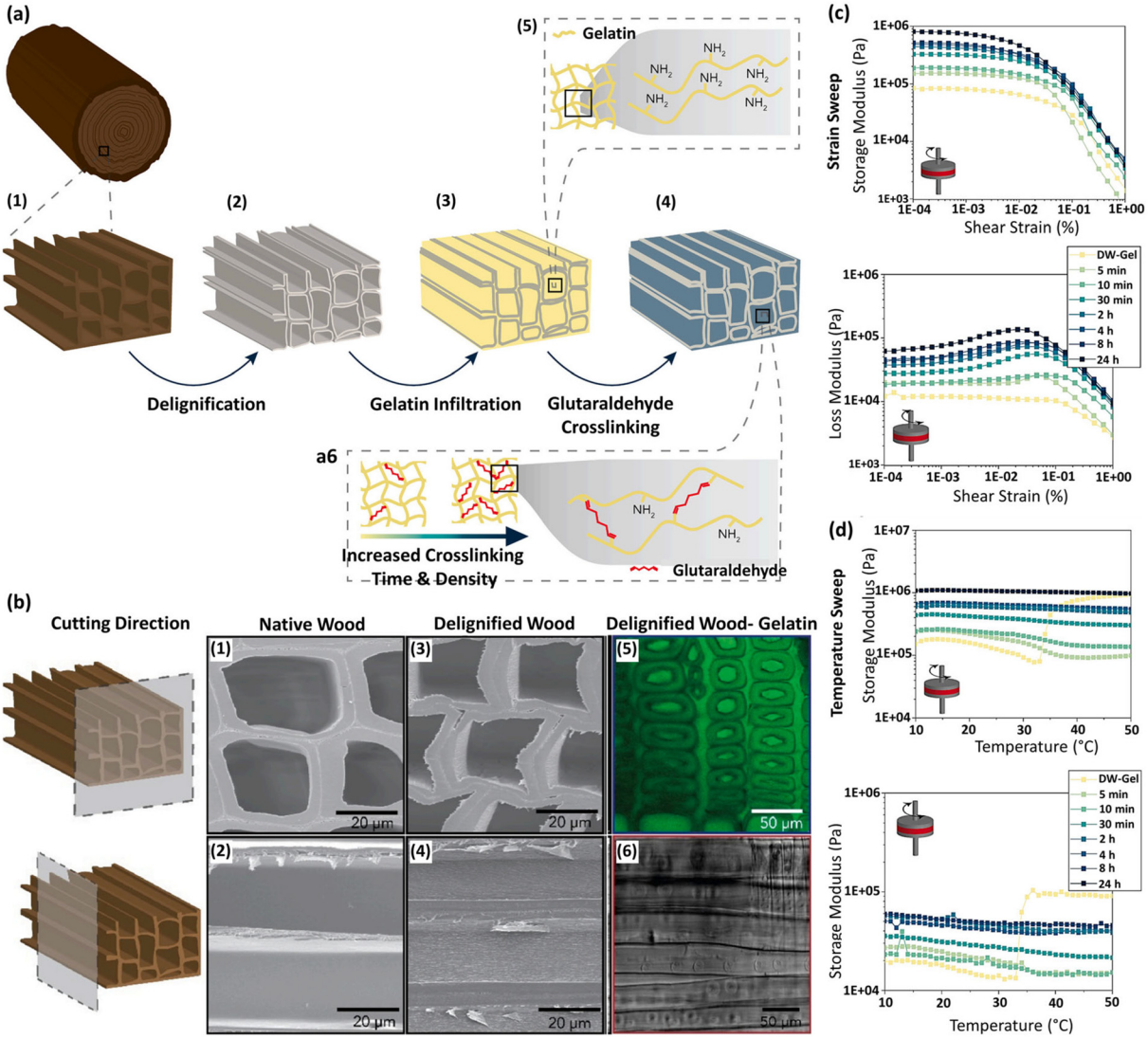

Fig. 25 (a) Manufacturing process of the cross-linked DW-gelatin composite (DW-Gel): (a1) native wood, (a2) DW, (a3) infiltration with gelatin, and (a4) additional cross-linking in an aqueous glutaraldehyde solution. (a5) Gelatin protein chains with lysine residues and free amino groups integrated into the DW structures. (a6) Tuning the cross-linking degrees of gelatin protein chains by adjusting cross-linking time in the glutaraldehyde solution. (b) SEM images of (b1, b2) the cross-section and longitudinal-tangential surface of native spruce and (b3, b4) the cross-section and longitudinal-tangential surface of delignified spruce. (b5, b6) Confocal fluorescence microscopy and phase contrast images of the DW-Gel cross-section, respectively. (c) Storage and loss modulus *versus* shear strain. (d) Temperature-dependent storage and loss modulus in different groups. (Reproduced from ref. 215 with permission from Elsevier, Copyright 2023.)

strength of WH was higher than that of WW in both L and R directions, which could be attributed to the presence of intermolecular bonds among the aligned cellulose fibrils and the robust hydrogen bonds formed between the SA hydrogel and the WW (Fig. 26g). Cross-sectional analysis of the microstructures of the WH before mineralization revealed interfacial bonding between aligned cellulose fibrils and cross-linked SA networks (Fig. 26h). The delignification of the wood resulted in the presence of aligned cellulose fibrils with a large surface area, enabling the formation of strong interfacial hydrogen bonds with the SA chains, thus enhancing the mechanical properties (Fig. 26i). In addition, the mechanical properties of MWH were significantly increased in comparison with the WH, confirming that the mechanical properties were further improved by the mineralization of HAp nanocrystals in the hydrogel matrix. Therefore, the highest strength was observed in the MWH scaffolds, at the same level as that of natural compact bone, making them promising candidates for load-bearing bone repair. Moreover, the *in vitro* evaluations demonstrated the potential of MWH to promote preosteoblast adhesion, proliferation, and osteogenic differentiation, as well as increased mineralization due to the presence of HAp (Fig. 26j). The *in vivo* analysis after 60 days of scaffold implantation in the rabbit femoral defect models showed a calcified shadow in the defect site of the MWH-treated group in X-ray images (Fig. 26k), and new bone regeneration both in the

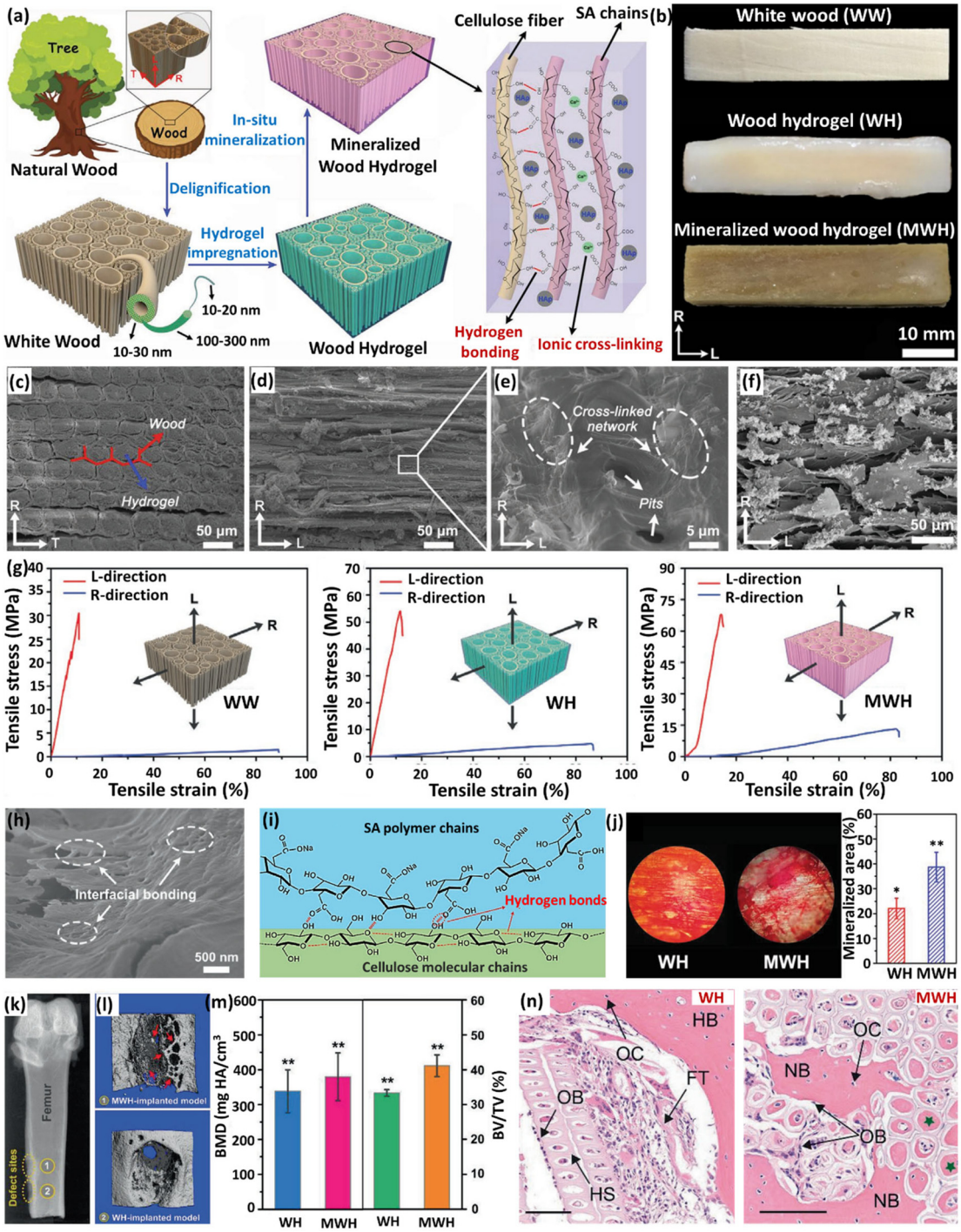

Fig. 26 (a) Schematic representation of the fabrication approach and the structure of the MWH. L, R, and T define the longitudinal (parallel to tree growth/cellulose axial direction), radial, and tangential directions of the tree trunk, respectively. (b) Photographs of the fabricated WW, WH, and MWH. (c, d) SEM images of the transverse and longitudinal sections of the WH scaffold, respectively. (e) A SEM image of the microscopic structure of the SA hydrogel. (f) A SEM image of the transverse section of MWH. (g) Tensile stress–strain curves of WW, WH, and MWH along both the L and R directions, respectively. (h) A representative SEM image of the WH showing the linkage between cellulose fibers and SA hydrogel. (i) Schematic representation of the hydrogen bonding between SA polymers and cellulose molecular chains. (j) *In vitro* ECM mineralization of MC3T3-E1 pre-osteoblasts after 21 days of incubation with WH and MWH in osteoinductive conditional medium using Alizarin red S staining, and the quantitative mineralized areas of WH and MWH. (N = 5, *P < 0.05, **P < 0.01). (k) X-ray image of two neighboring bone defect sites implanted with WH and MWH, respectively. (l) Micro-CT reconstructed models of the femoral defects treated with MWH and WH scaffolds. Red arrows indicate new bone ingrowth into the MWH scaffold. (m) Quantitative BMD and BV/TV assessment of the bone defects implanted with WH and MWH. (N = 5, **P < 0.01). (n) Histological analysis of bone formation 60 days after implantation with WH and MWH, respectively. (Abbreviations: FT, fibrous tissue; NB, new bone; HB, host bone; HS, hydrogel scaffold; OB, osteoblast; OC, osteocyte.) (Scale bar = 100 μm.) (Reproduced from ref. 158 with permission from WILEY-VCH Verlag GmbH & Co, Copyright 2021.)

outer edges of the implanted MWH scaffold and within it (Fig. 26l and m), as confirmed by histological analysis (Fig. 26n). The wood-derived delignified scaffold containing SA and HAp described here can therefore facilitate new bone formation and improve osteointegration, while providing satisfactory mechanical properties and porosities for the infiltration of host cells.

In another study based on the same concept, researchers demonstrated that the anisotropic nature of delignified beech wood resulted in unique static and dynamic mechanical properties.[146] A combination of hydrophobic polycaprolactone and HAp enhanced cell proliferation and osteogenic differentiation, aided by the hydroxyl groups in cellulose fibers. These properties, combined with the aligned channels, facilitate directional cell transport and osteogenic differentiation with minimal cytotoxicity.

It is noteworthy that as well as hydrogels, incorporating a drug into DW scaffolds can provide additional advantages, such as anti-inflammatory, antibacterial, angiogenesis-promoting, and osteogenesis-enhancing effects. As a result, the drug-loaded hydrogel-filled DW provides a comprehensive strategy for successful bone tissue regeneration, addressing both the desirable structural aspects and therapeutic effects, and preventing bacterial infections and inflammatory responses.[144,159,216] To explore this possibility, Chen *et al.* incorporated curcumin and phytic acid in a polyvinyl alcohol (PVA) hydrogel with a wood-derived cellulose scaffold.[216] The drug-loaded PVA hydrogel enhanced the flexibility of DW, as well as providing sustained drug release. Phytic acid demonstrated a notable ability to enhance the bioavailability of curcumin and the mechanical properties of the wood-derived scaffold, due to strong hydrogen bonding interactions. Even more important was the evident synergy between curcumin and phytic acid, particularly in their combined antibacterial, anti-inflammatory, and osteogenic activities. The further experimental results revealed that this platform retarded the growth of bacteria, inhibited inflammatory responses, and facilitated the adhesion, proliferation, and osteogenic differentiation of bone marrow mesenchymal stem cells. However, one of the major unmet challenges in designing hydrogel-loaded DW-derived scaffolds is that the hydrogel has to occupy the porous channels of the wood, restricting the growth of new blood vessels, which is needed for efficient tissue growth by facilitating the diffusion of nutrients, gas exchange, and waste product removal.[217] To overcome this challenge, Chen *et al.* treated natural wood with an alkaline solution to obtain a highly elastic and porous-oriented CNF scaffold, followed by depositing CQS and dimethyloxalylglycine (DMOG) on the wood surface using the PDA layer.[159] The CQS and DMOG on the wood surface inhibited bacterial growth and angiogenesis, enhancing cell osteogenic differentiation. Being a small angiogenic molecule, DMOG can actually be constantly released from the scaffold, which is beneficial for endowing the scaffold with relatively long-term angiogenic and osteogenic abilities.

In another step forward, the innovative use of DW-derived scaffolds in combinatory approaches for bone repair and tumor therapy (photothermal therapy) represents a significant advance in regenerative medicine and oncology treatment. Thus, a novel, robust therapeutic system has been innovatively designed by Hu *et al.*[149] It entails the integration of black phosphorus quantum dots (BPQDs) encapsulated in PLGA nanospheres (NSs) in a scaffold formed from WW/RSF hydrogel (referred to as BP/WW/RSF), yielding multifunctional composites to inhibit osteoclastogenesis, facilitate photothermal therapy for early-stage spinal metastases upon implantation and subsequently promote bone tissue regeneration (Fig. 27a). To achieve this, BPQDs with high photothermal transformation efficiency were initially encapsulated in PLGA-based NPs using an oil-in-water emulsion solvent evaporation method, resulting in BPQD/PLGA NSs. The model materials employed encompassed aligned cellulose fibril skeletons and RSF hydrogel infused with BPQD/PLGA NSs, enhancing the mechanical properties of the scaffold. BPQD/PLGA and RSF hydrogel were used to simulate the phosphates and collagen fibrils in the bone tissues, respectively, while the WW mimicked the scaffold's hierarchical anisotropic structure. The tough frame structure of the cellulose fiber in RSF hydrogel, along with intermolecular forces, such as hydrophobic interactions and hydrogen bonding between cellulose and RSF, improved the mechanical properties of the hydrogel scaffold (Fig. 27b and c). This can be attributed to the increased formation of β-sheet domains in the RSF within an alcohol-rich environment. At the same time, the introduction of an oriented DW skeleton provided the composite hydrogel scaffold with anisotropic mechanical characteristics. In addition, the mechanical properties of the composite hydrogel scaffold matched those of natural compact bones, making it a promising candidate for bone repair applications. Moreover, BPQD/PLGA degraded into non-toxic phosphate ions in the physiological environment, possibly enhancing the expression of genes that are crucial for cell proliferation in osteoblast-like cells. The presence of BPQD/PLGA thus notably boosted the proliferation of BMSCs. The protein expression levels of RUNX2, Col-1, OCN, and osteopontin (OPN) were upregulated in the BPQD/PLGA-containing groups, as compared with others, indicating that the degradation products of the BPQD/PLGA in the medium could induce the increased expression of osteogenesis-related proteins (Fig. 27d). In addition, the osteogenic differentiation and mineralization of BMSCs in the final platform was confirmed using Alizarin red staining (Fig. 27e). The osteogenic effect was evaluated on a critical-size femur defect model, and two implantation methods were studied to assess the effects of the anisotropic structure on bone formation. In the vertical implantation system, the wood hydrogel scaffold was implanted perpendicular to the longitudinal axis of the bone, whereas in the parallel implantation system, it was implanted in parallel. Both cancellous and cortical bone promotion was observed in the 200BP/WW/RSF group in the parallel implantation system. This may be due to the porous structure of the platform, as well as the simulation of the Haversian system, which is suitable for efficient bone repair. Moreover, the presence of BPQDs could enhance the biomineralization of the

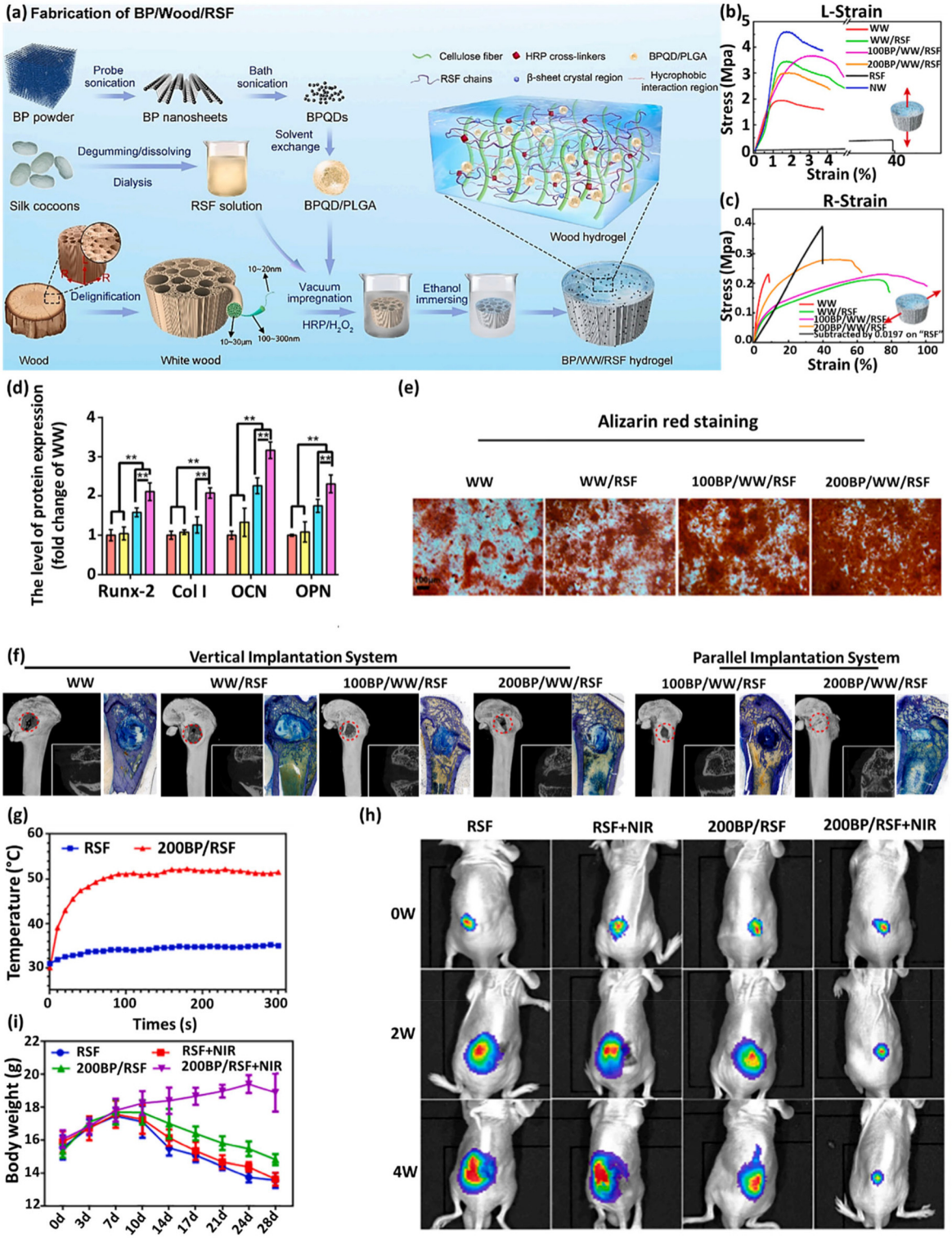

Fig. 27 (a) Schematic illustration of the fabrication process of the BP/WW/RSF hydrogel scaffold, (b, c) the tensile stress–strain curves of all groups in both L-direction and R-direction, (d) quantitative analysis of the expression levels of Runx-2, Col-1, OCN, and OPN, (e) representative images of alizarin red staining results, (f) 3D and 2D reconstruction of micro-CT, and toluidine blue staining of undecalcified femoral sections of different groups after implantation for 12 weeks, (g) real-time temperature recording in spinal metastasis tissue, (h) time-dependent body weight curves of tumor-bearing mice, (i) luminescence images of mice before and after treatments with and without NIR irradiation. Data are presented as the mean ± S.D. (N = 3), ** P < 0.01. (Reproduced from ref. 149 with permission from Elsevier, Copyright 2022.)

platform and its mechanical properties (Fig. 27f). In addition, owing to the highly efficient photothermal conversion of the BPQDs in the wood hydrogel scaffolds, resulting in the generation of strong hyperthermia in the tumor site, this platform exhibited a promising metastatic tumor ablation effect and reduced the loss of weight caused by tumor-related cachexia (Fig. 27g–i). In conclusion, incorporating BPQD/PLGA in the Haversian-like wood hydrogel scaffold system provides a favorable therapeutic approach to bone repair, specifically focusing on the treatment of bone metastasis.

In addition to the need to optimize the architectural structures, mechanical features, and biological activities of wood-based scaffolds, significant unresolved challenges remain, such as scaffold degradation. An optimal platform for implantable tissue engineering has to exhibit controlled biodegradability in line with the rates of cellular remodeling and vascular integration. However, cellulose, a key component of the scaffold, can only be broken down by cellulase enzymes, which are not naturally present in mammals.[218,219]

In order to overcome this challenge, a proposal is to pretreat the cellulose-based scaffold with oxidizing agents, such as 2,2,6,6-tetramethylpiperidine1-oxyl radical (TEMPO), sodium hypochlorite, sodium bromide and sodium periodate, which can enhance cellulose degradation.[204,220–222] Among these agents, sodium periodate-mediated oxidation facilitates the conversion of 1,2-dihydroxyl groups into dialdehydes.[221] Given this factor, Aswathy *et al.* decellularized bamboo stem, followed by oxidation using sodium periodate, and evaluated its biodegradation and biocompatibility for bone tissue engineering.[55] Despite a decrease in compressive strength post-oxidation, it still remained within the compressive strength range of cancellous bone. The oxidized bamboo fiber was notably coated with sericin, resulting in enhanced cell adhesion, cell viability, and ALP activity compared with non-oxidized bamboo fiber *in vitro*. Subsequent *in vivo* assessments in a rat model demonstrated an improvement in angiogenesis, biocompatibility, and biodegradability in the scaffold-treated group. The degradation percentages increased with implantation time and promoted sodium periodate concentration, thereby underlining its promising potential as a bone scaffold for non-load-bearing applications.

Another approach for the development of bone implants involves subjecting the wood to high-temperature treatment to create a charcoal-like material. A study involving bamboo charcoal as a bone substitute demonstrated favorable biocompatibility and osteoconductivity without inflammatory responses.[223] However, pure carbonized wood lacks mechanical strength, rendering it impractical as a biomaterial for bone tissue engineering. There were subsequent efforts to enhance the mechanical properties of carbonized wood by impregnating it with silicon carbide (SiC), resulting in a biomaterial known as ecoceramics. In this process, natural wood was pyrolyzed at 1000 °C using argon gas, resulting in a 75% weight loss and a 60% volume reduction. The remaining scaffold was infiltrated with melted Si at 1550 °C, which reacted with the carbon in the pyrolyzed wood to form SiC.[224–227] One *in vivo* study of SiC scaffolds was performed by Filardo *et al.* to investigate the regenerative potential of the bio-ceramization process for bone regeneration in long diaphyseal defects in a sheep model.[103] The prepared biomorphic silicon carbide (BioSiC) showed hierarchically organized porosity and high mechanical strength. The surface of the hollow cylinder was also made more bioactive by electrodeposition of a uniform layer of collagen fibers that were mineralized with biomimetic HAp. Meanwhile, the internal portion was filled with a biohybrid composite comprising HAp and collagen to enhance cell adhesion and osseointegration. The results indicated both suitable scaffold-to-bone adhesion and new bone formation inside the scaffolds.

In conclusion, plant-based scaffolds hold tremendous promise for advancing bone regeneration strategies, offering unique advantages in mimicking the anisotropic nature of natural bone and remarkable potential in supporting cell adhesion, promoting osteogenesis, and facilitating osseointegration. While challenges, including scaffold degradation and mechanical properties, require further refinement, the utilization of these plant-based materials represents an environmentally friendly and sustainable approach for bone tissue engineering.

7.3. Wound healing using plant-derived dressings

Plant-based platforms for wound healing have gained considerable attention for their potential therapeutic benefits, providing eco-friendly wound care alternatives. Wound healing is a complicated process that involves four continuous, overlapping phases, comprising hemostasis, inflammation, proliferation, and remodeling.[228] For the purpose of wound healing, considering the wide application of cellulose as a natural biomaterial in wound dressings, Yang *et al.* studied the hemorrhage-controlling effect of carbonized cellulose aerogel derived from *Agaricus bisporus* after a series of processes, comprising cutting, carbonization, purification, and freeze-drying.[229] The results showed effective hemostatic ability in serious hemorrhage models based on both small and large animals due to high hemoglobin binding efficiency, red blood cell absorption, and platelet absorption and activation. The prepared carbonized cellulose-based aerogel hemostatic material can be used for the hemostasis stage, resulting in skin repair. However, during the wound healing process, the body is vulnerable to bacterial infections, resulting in abscess formation, inflammation, and persistent necrosis of the wound tissues, which can hinder the wound recovery.[230,231] This vulnerability highlights the importance of wound dressings with antibacterial properties, which add substantial value by mitigating infection risks and facilitating the healing process. Hydrogels are an excellent choice for wound dressings due to their structural resemblance to soft tissues and ability to absorb wound exudate, and the fact that they provide an effective microbial barrier while preserving a consistently moist wound environment. However, pure hydrogel lacks the required mechanical properties. DW can be considered a new material in the field of wound dressings, due to its great bio-

compatibility and safety, excellent mechanical properties, and its porous and anisotropic structure that provides a good substrate for hydrogels and enhances cell proliferation, differentiation, and transport functions. To this end, He *et al.* prepared a pH-responsive flexible *Triplochiton scleroxylon* (TS) wood-based hydrogel (FTS-G@PC) comprising PVA and chitosan (CS) cross-linked wrapped gentamicin (GS) in order to effectively solve the wound infection issue by harnessing the unique properties of wood (Fig. 28a).[232] Fig. 28b shows the ability of FTS to be rolled up along the fiber direction without cracking, due to lignin removal and cytosolic pore contraction after chemical modifications performed on TS. Moreover, the hydrogel-modified FTS-G@PC showed excellent flexibility, as it can be rolled up in the direction of the fibers and stretched, making it a useful tool for hemostasis during the healing process, as well as providing superior mechanical properties. The modification of TS and lignin removal resulted in a reduction in maximum tensile strength in the FTS samples. However, the penetration of hydrogel in the scaffolds slightly increased elongation at break (Fig. 28c and f). The nominal stress, proof strength, and bending strength decreased in the treated wood samples, compared with TS, confirming the desirable flexibility, which is associated with a decrease in stiffness caused by the reduction in lignin following dual aldehyde treatment (Fig. 28d and g). Moreover, the relaxation elastic modulus results were consistent with those of the tensile and three-point bending tests, mainly owing to the reduced lignin and hemicellulose content, and the lower friction resistance between polymer chains compared with that of cellulose chain molecules, requiring less external effort to achieve the same deformation (Fig. 28e and h). In conclusion, the wood reinforces the mechanical stability of the hydrogel and provides a superior combination of strength and flexibility, while the hydrogel enhances the surface properties of the wood, rendering it more compatible with the skin. The addition of GS also provided antibacterial activity against *S. aureus* or *E. coli*, enabling infected wounds to heal quickly (Fig. 28i and j). The epidermis layer of FTSG@PC-treated infected wounds also recovered faster, and the superficial dermal appendages were more intact, demonstrating good potential for treating infected wounds (Fig. 28k). In summary, the fabricated flexible wood-based hydrogel exhibited remarkable biocompatibility, mechanical, and antibacterial performances, and a strong therapeutic effect on the infected wounds.

In another attempt, benefiting from the unique structures and characteristics of wood, photothermal therapy was used to treat infected wounds.[233] This employed a platform composed of a flexible PVA-loaded wood enriched with black phosphorus with excellent photothermal conversion properties and the photodynamic ability to produce singlet oxygen, which can rapidly inhibit wound infection. This formulation was enhanced with clarithromycin, ensuring sustained and extended release to effectively prevent infection recurrence at the wound site.

Collectively, the use of wood-based platforms containing hydrogel is a promising strategy for wound treatment, due to the desirable mechanical properties, porosity, and anisotropic structure of wood, which can result in better cell proliferation and provide a substrate for incorporating drugs or photothermal agents in these structures, leading to faster recovery.

7.4. Neural tissue engineering

Neural stem cell (NSC) transplantation has been regarded as a promising treatment option for various central nervous system disorders. However, there are major obstacles to the effectiveness of NSC therapies, including low transplant survival and poor efficiency of neuronal differentiation.[234,235] In the context of nerve tissue engineering, the application of naturally derived plant cellulose scaffolds is particularly desirable due to their porous structure with appropriate mechanical features that can be harnessed to manipulate NSC differentiation, anisotropic structure for axonal extension, and providing an ECM-mimicking microenvironment for cell adhesion and migration.[236,237] Couvrette *et al.* prepared a 3D cell culture scaffold for the attachment, proliferation, and differentiation of rat adult neural stem cells, using decellularized *Asparagus officinalis* stalks. This scaffold is biocompatible, and can support neural stem cell growth due to the presence of well-structured channels of varying diameters in the scaffold.[238] In another attempt, researchers assessed the use of plant-derived scaffolds in the treatment of traumatic spinal cord injuries, an area that currently lacks a standard of care.[45] To this end, they developed microscale channels within the asparagus stalk-derived scaffolds to enhance axon regrowth while minimizing scar tissue formation. The plant-derived channeled scaffolds were implanted in rats with complete spinal cord injuries, without any additional interventions. These animals showed notable improvements in motor function over 6 months, along with minimal scarring and axonal regrowth through the scaffolds. This innovative strategy can harness natural plant microarchitectures to facilitate functional spinal cord tissue repair. Altogether, the outcomes indicated the application potential of plant-derived scaffolds in the treatment of nerve injury.

7.5. Cardiovascular tissue engineering

The circulatory systems in living organisms are meticulously designed to facilitate the transportation of blood throughout the body. This system comprises two key components that enable the primary fluid transport function: vascular networks and hearts. Ischemic diseases (*e.g.*, atherosclerotic cardiovascular disease) remain the leading cause of mortality and morbidity across the world.[239] This has created an enduring need for vascular conduits to reconstruct or bypass vascular occlusions and aneurysms. Vascular tissue engineering is a recent development in biomedical sciences that addresses the demand for vascular replacement and reconstruction. Vascular tissue engineering is not limited to the macrovasculature. It can also address the demand for microvascular replacement that is a critical challenge with engineered tissues.

Decellularized plant-based scaffolds are emerging as a novel approach for vascular tissue engineering, taking advan-

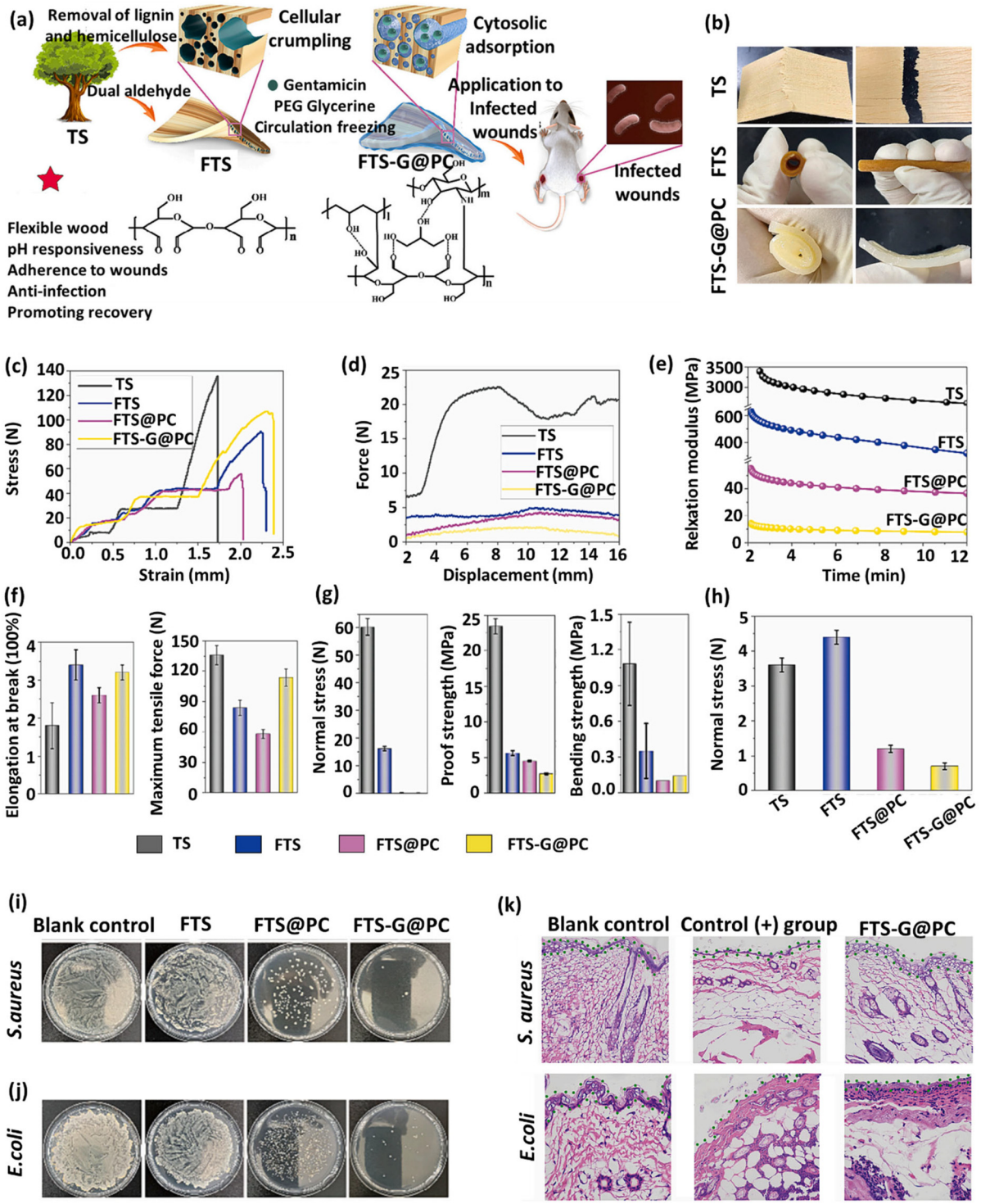

Fig. 28 (a) Schematic illustration of the fabrication and application of FTS-G@PC in infected wound treatment. (b) Flexibility analysis of different samples. (c) Tensile test. (d) Three-point bend test. (e) Tensile stress at 5% deformation in a stress relaxation test. (f) Maximum tensile strength and elongation at break. (g) Nominal stress, proof strength, and bending strength diagrams. (h) Maximum tensile stress at 5% deformation with stress relaxation. (i, j) Antibacterial test for *S. aureus* and *E. coli*. (k) H&E staining of the wound section from different treated groups. (Reproduced from ref. 232 with permission from Elsevier, Copyright 2023.)

tage of their prefabricated branched hierarchical structure that mimics the micro and macro architecture of human vasculature. The main function of the vascular system is to transport oxygen and nutrients to tissues, while removing waste products from them. This need for an input and output flow of fluids is the issue that Wang *et al.* addressed in their study.[39]

To achieve this goal, two plant leaves were grafted in opposite but horizontal directions, with phytohormone treatments producing trans-leaf vascular connections that provided the vascular system with a flow input and output. The merged leaves were decellularized by inserting a cannula into one end of the leaf stem and washing with chemicals to extract the cells and cuticles. The cell residues and other decellularization waste exited from the other end of the grafted tissues (Fig. 29a). After multiple washing of decellularized grafted leaves, to assess the fluid perfusion ability of the merged leaves, Ponceau red dye (Fig. 29b) and human red blood cells (hRBCs) (Fig. 29c) were perfused through the input petiole. In both perfused red dye and hRBC experiments, it was observed that, after input through the petiole of the first leaf, they diffused through the veins in the grafted leaf margins and ultimately exited through the midrib veins from the petiole of the second leaf. Notably, there was no leakage during perfusion onto the outside surface of the grafted leaves. Intact hRBCs were collected from the exit petiole (Fig. 29e), and no morphological differences were observed upon comparison with the hRBC morphology before perfusion (Fig. 29d). These data demonstrated that the leaf graft connections remained patent, allowing for input and output flow into one petiole and out of the other. However, it is important to note that this was an initial study exploring the potential of vascularized plant-based structures as perfusionable systems. The results of this study are promising and demonstrate the potential utility of vascularized grafted plant scaffolds in tissue engineering. These types of scaffolds can also be combined with non-vascularized scaffolds to meet the oxygen and nutritional requirements while facilitating the removal of CO_2 and waste products.

Support for the adherence and proliferation of vascular endothelial cells is a critical characteristic for a vascular graft. *In vivo* angiogenesis and subsequent initial vascularization were detected in apple hypanthium tissue-derived cellulose scaffolds.[26,29] To evaluate the potential of plant-based scaffolds for facilitating vascular endothelial cell proliferation and attachment meticulously, Walawalkar *et al.* conducted an investigation using *Brassica oleracea* (cabbage) leaves.[240] The cabbage leaf underwent a decellularization process and was coated with fibrin glue to support cell adhesion (Fig. 29f–i). Furthermore, angiography was employed to evaluate the vascular structure of the scaffold. The images revealed a functioning vascular network in the scaffold, confirming the creation of a prevascularized biomaterial ready for subsequent investigation (Fig. 29j). Endothelial cells, specifical HUVECs, were seeded on the fibrin glue-coated cabbage surface to recellularize the scaffold. The aim of this recellularization was to assess the vascularization potential and confirm the retention of cell-specific phenotypes. Cytotoxicity tests, including live–dead assay, MTT assay, and lactose dehydrogenase activity, were carried out to confirm the biocompatibility of the scaffolds. As von Willebrand factor (vWF) expression is a hallmark of endothelial cells, vWF staining was performed because of its specificity for identifying HUVECs. Confocal microscopy images showed that vWF was found to be present in both cell culture media and scaffold expansions. This highlighted the preservation of HUVEC phenotypes and their functionality in the formation potential of new blood vessels on the plant-derived scaffolds (Fig. 29k and l). This study concludes that plant-based scaffolds, cabbage leaf in this case, can support the establishment and proliferation of endothelial mammalian cells while leveraging their inherent vasculature.

Recently, vascular patches based on decellularized scaffolds have received significant attention for treating vascular defects.[241,242] During this period, plant-based scaffolds have emerged as one of the innovative options under investigation, and the outcomes appear promising.[243] In a pioneering study, Bai *et al.* fabricated vascular patches using plant leaf and onion as scaffolds, examining their drug delivery ability in a rat venoplasty model.[40] To achieve a biocompatible scaffold, the plant leaf and onion were both decellularized (Fig. 30a) and functionalized with PLGA-based rapamycin NPs. Rapamycin, an immunosuppressant, was incorporated to inhibit neointimal hyperplasia in a rat inferior vena cava (IVC) patch venoplasty model (Fig. 30b). In the case of the leaf scaffolds, rapamycin NPs were slowly introduced through the main trunk of the leaf, whereas in that of the decellularized onions, the NPs were applied to the surface. To assess the effectiveness of the patch in animal models, the IVC was punctured, the patches were surgically implanted in the venotomy area, and observations were carried out over a 14-day period. At day 14, the patches were incorporated into the rat's IVC without any sign of thrombosis formation. H&E staining showed a notably thinner neointima in NP-conjugated patches than in the control patches (Fig. 30c). The study also observed the migration and infiltration of cells into the scaffolds. These findings collectively demonstrated the successful modification of leaf- and onion-based decellularized scaffolds into vascular scaffolds with potent drug delivery capabilities. However, they lacked the mechanical strength required for larger vascular patches (*e.g.*, aorta patches). To address this issue, the same group that developed the leaf and onion vascular patches investigated rapamycin-coated DW as a vascular patch, based on the same concept as described in their previous study.[145] *In vivo* studies were carried out using a rat IVC model, as outlined in their earlier work. An evaluation of the harvested tissues using H&E staining demonstrated the successful integration of the rapamycin-coated and control scaffolds with the IVC, without any significant foreign body reactions. There was well-formed tissue on both sides of the scaffolds, the luminal side (neointima) and the abdominal cavity side (adventitia). Although cell migration and proliferation were observed on both sides of the scaffolds, notable differences were identified in the rapamycin-coated group as compared with the control group. Some wood patches were loaded with rapamycin. Those without rapamycin (the control patch) showed a thick neointima and adventitia, whereas those coated with rapamycin showed a significantly thinner neointima and adventitia (Fig. 30d). In addition, in the neointima and adventitia, there were significantly fewer neocapillaries near the rapamycin-coated patches than the control patches (Fig. 30e). These data

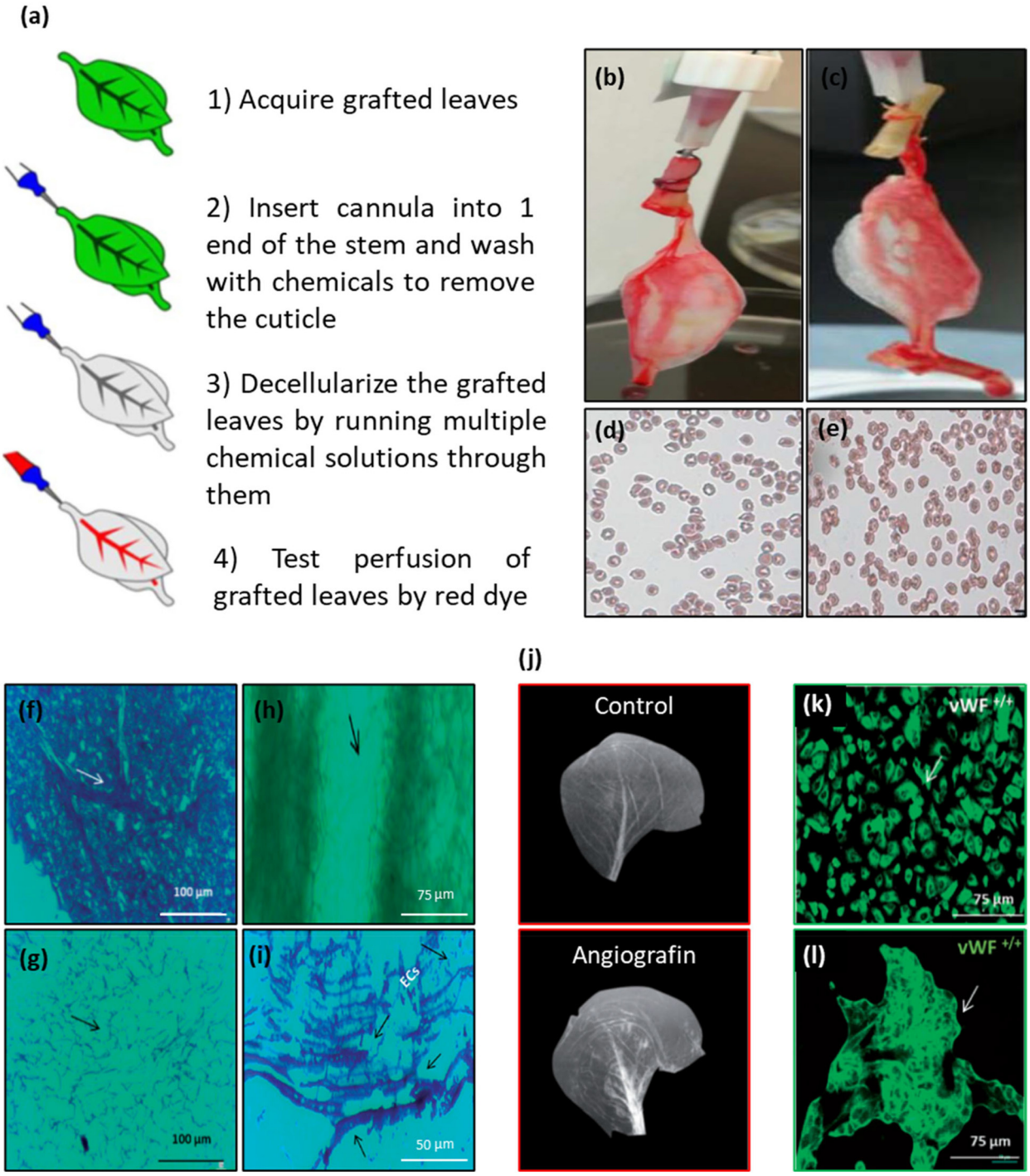

Fig. 29 (a) Schematic representation of the grafted leaf decellularization process. (b) Image of Ponceau red dye perfusion in the front side of grafted leaf scaffold. (c) Image of human red blood cell perfusion in the front side of the grafted leaf scaffold. (d) The optical microscopy image of red blood cells before perfusion. (e) The optical microscopy image of red blood cells after perfusion (×40 magnification). (Reproduced from ref. 39 with permission from Nature Springer. Copyright 2020.) (f and g) The optical microscopy image of hematoxylin and safranin (HS)-stained cabbage leaf (f) and decellularized leaf (g). The white arrow indicates the inherent vascular system of the natural leaf. The black arrow indicates the absence of cells in the ECM scaffold (scale bar = 100 μm). (h) Phase contrast microscope images of decellularized scaffold with a cobblestone appearance. The arrow indicates the absence of cells in intact ECM walls (scale bar = 75 μm). (i) The optical image of the HS-stained decellularized scaffold (nuclei were stained in dark blue color and cytoplasm with pink (HS staining)) seeded with HUVECs. The stained cells with dark blue nuclei are present in both the parenchymatous and as xylem zones (scale bar = 50 μm). (j) The radiological image (angiogram) visualizing the vascular architecture and the patency of the decellularized scaffold. An image without angiographic dye was taken as a control image. The angiographic dye perfusion showed the presence of fluorescence throughout the patent leafy venation of the decellularized scaffold. (k and l) Confocal images of vWF staining as an endothelial-specific marker showing HUVECs both in the tissue culture plastic (k) and on the decellularized scaffold (l) (scale bar = 75 μm) (reproduced from ref. 240 with permission from American Chemical Society, Copyright 2022).

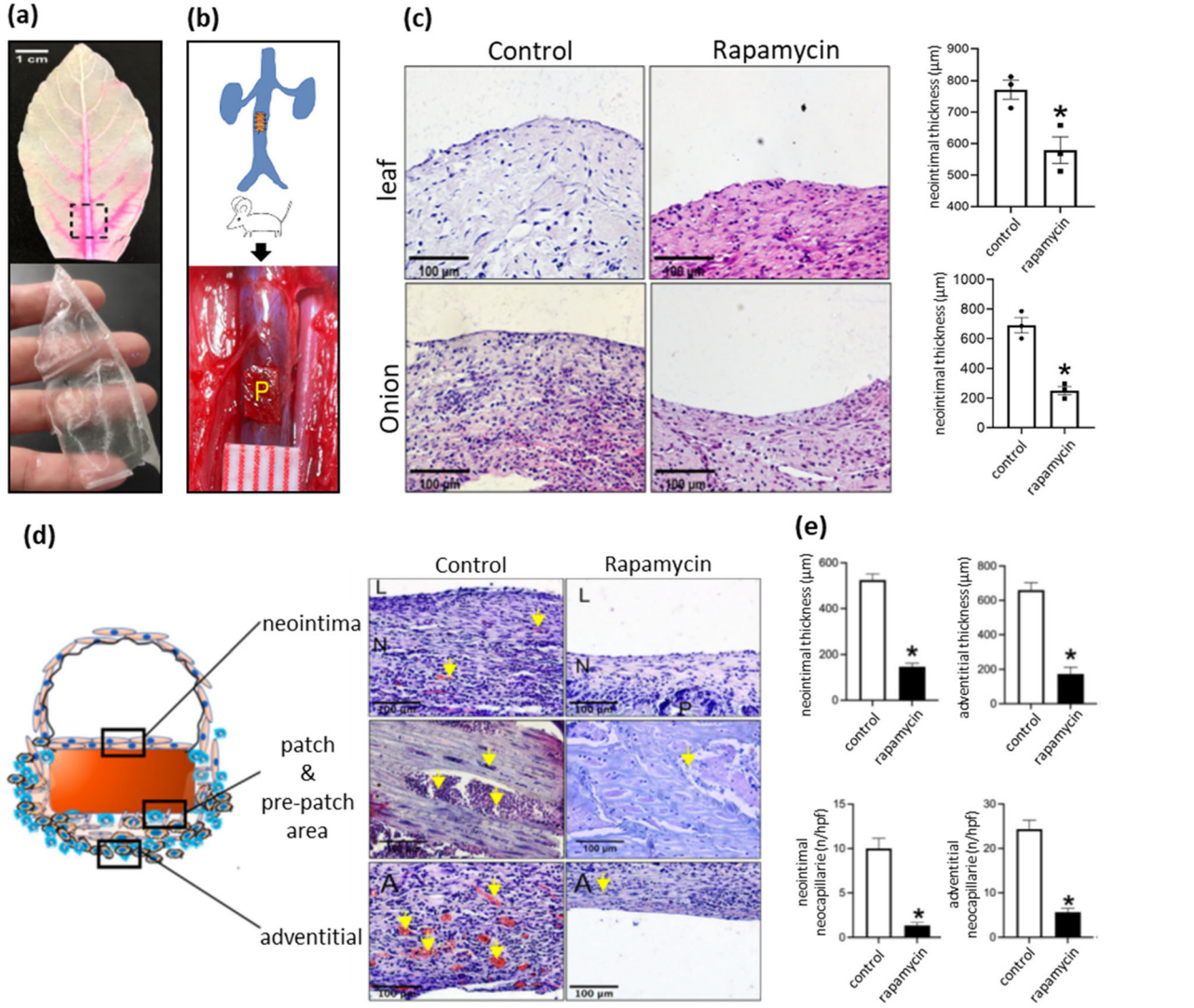

Fig. 30 (a) The photograph of the decellularized leaf perfused with rhodamine water (upper image) and decellularized onion (lower image). (b) Illustration of the design of rat inferior vena cava venoplasty. (c) Photographs of H&E staining of the leaf and onion patches after venoplasty at day 14, showing neointima in both the control and rapamycin-functionalized leaf patches, as well as in the control and rapamycin-functionalized onion patches. Bar graph showing the neointimal thickness in the venoplasty models at day 14 for leaf (upper graph) and onion (lower graph)-based patches. For leaf patches: *p = 0.0210; n = 3, for onion patches: *p = 0.0019; n = 3 (scale bar = 100 μm). (Reproduced from ref. 40 with permission from American Chemical Society. Copyright 2021.) (d) Microphotographs of H&E staining, illustrating the control and rapamycin-coated wood patches harvested on day 14: the first row shows the neointima, the second row the patch and prepatch, and the third row the adventitia. P denotes the patch, N corresponds to the neointima, L signifies the lumen, and the yellow arrow highlights neocapillaries or infiltrated cells (scale bar = 100 μm). (e) Bar graphs showing neointimal thickness (*p = 0.0001, t-test), adventitial thickness, neointimal neocapillaries (*p = 0.0001, t-test), and adventitial neocapillaries (*p = 0.0001, t-test); n = 3. (Reproduced from ref. 145 with permission from Frontiers Editorial Office; Frontiers Media SA, Copyright 2022.)

show that rapamycin-coated scaffolds effectively decrease cell proliferation and reduce neointimal hyperplasia, even better than in their earlier study of coated plant leaf and onion. All in all, plant-based materials can be used as vascular patches, potentially replacing current approaches for vascular regenerative materials.

As regards heart disease, in the United States alone, nearly 5 million people live with heart failure, and approximately 550 000 new cases are diagnosed each year, and the number of new patients with a heart failure diagnosis is increasing annually.[244] Heart transplantation remains the ultimate treatment for end-stage heart failure, but the supply of donor organs is limited. Due to the rise in and prevalence of cardiovascular diseases and the need for tissue replacement and reconstruction, cardiovascular tissue engineering has rapidly emerged as one of the fastest-growing subdisciplines. Attempts to engineer heart tissues have involved numerous approaches. It is also important to acknowledge that the heart itself comprises various functional parts, including atria, ventricles, and valves, each of which possesses unique character-

istics, and these complexities make the engineering of heart tissues even more challenging. In the context of the application of plant-based scaffolds in heart tissue engineering, decellularized spinach leaves were used to support the attachment and functioning of human stem cell-derived cardiomyocytes (hPS-CMs).[28] In detail, spinach leaves were decellularized and coated with fibronectin on both the surface and inner cannula to functionalize the scaffold and enhance cell attachment. Following this preparation, hPS-CMs were seeded onto the scaffold, and cell clusters formed after a 3-day incubation. At day 5, the contractile behavior of cells was detected and assessed. Contractile analysis demonstrated an approximately 1% contractile strain at a rate of 0.8 Hz in the myocytes seeded on leaf scaffolds by day 10. Notably, these constructs retained their contractile function for up to 21 days, but with a reduction in contractile strain to 0.6% by day 21. The researchers also explored the impact of omitting surface coating and functionalization, along with reducing the surfactant concentration during the decellularization process, on the functionality of hPS-CMs.[30] The results showed that not only did these modifications not disrupt cell activity and attachment, the contractile analysis also yielded higher values (3.9 ± 1.2% at day 21), as compared with the previous fabrication methods. This suggests that higher surfactant (*e.g.*, SDS) concentrations may impact the stiffness of leaf substrates and potentially reduce the contractility of adherent cardiomyocytes. Although cardiomyocyte contractility increased, hiPS-CMs contractile strains on the decellularized leaves were still less than in the human myocardium (15.9–22.1%).[245] These findings show that the plant-based scaffold is able to support myocardial cells even without surface functionalization, contributing to our understanding of the design principles and coordination mechanisms in biological systems. Further investigation is needed to enhance the contractile strain so as to approach the contractile strain observed in the human myocardium. Additionally, further research should explore various types of plant-based scaffolds that could support the development of multiple cell layers. In conclusion, the plant kingdom is significantly expanding the range of biomaterials available for cardiovascular tissue engineering, providing numerous advantages in terms of sustainability and cost-effectiveness, as well as leveraging the innate prevascularized complex network for potential applications in the field.

7.6. Skeletal muscle and tendon tissue regeneration

Large skeletal muscle defects profoundly impact patients' quality of life by reducing the functionality of the injured muscles due to trauma, aging, or disease.[246] A notable focus has thus been placed on the development of skeletal muscle tissue engineering and regenerative medicine approaches. Decellularized plants can be considered a potential source of highly structured cellulose-rich scaffolds, which can support cell adhesion, alignment, growth, and differentiation to achieve the organization and function of engineered tissues. A study was performed involving the construction of a low-cost scaffold using the unique cellulose structures of green onion to enable the engineering of organized muscle tissues.[35] Green onion-derived cellulose scaffolds showed anisotropic structures that differed when cut longitudinally *versus* transversely, which facilitated myoblast differentiation and myotube alignment (Fig. 31a). In an isotropic control within a 2D setup, C2C12 cells were cultured on glass coverslips to assess their alignment. Cell growth and alignment were observed on cellulose scaffolds sourced from white bulbs and green leaves. Cells on glass coverslips exhibited random orientation. Following this, the C2C12 cells were directed to differentiate into myotubes with a well-organized structure, as demonstrated by the presence of αMHC (Fig. 31b). The same results were achieved with HSMCs that grew on the outer white bulb-derived cellulose scaffolds. The formation of HSMC myotubes was also observed on the outer white bulb-derived cellulose scaffolds, verified using positive staining for αMHC following the transition to differentiation media (Fig. 31c). This study concluded that the architecture of the green onion's white bulb serves as an effective guide for aligning mouse and human muscle cells, making it a suitable choice for engineering well-aligned human skeletal muscle tissues. In another study, Allan *et al.* showed that a decellularized grass leaf scaffold with natural morphology provided a conducive environment for the differentiation and proliferation of C2C12 myoblasts, facilitating the alignment of these cells (Fig. 31d–f).[31]

In another step forward, using plant-derived scaffolds for tendon regeneration has also emerged as a promising strategy in regenerative medicine. For example, decellularized celery-derived scaffolds were used to regenerate tendons, due to their ability to vertically align cells in a tubular, anisotropic scaffold with desirable mechanical properties.[36]

7.7. Other tissue engineering applications

Recent advancements in the biomedical application of plant-based scaffolds have demonstrated their significant potential for designing cost-effective and resilient cell models, which can be assembled into tissue-engineered alternatives. Inspired by the natural microstructures of hepatic lobules, a novel decellularized celery-derived scaffold was fabricated and cultured with human-induced pluripotent stem cell-derived hepatocytes (hiPSC-Heps) to construct bioengineered liver tissues.[42] The structure of the human hepatic lobule contains a central vein surrounded by hepatocytes radiating in all directions, and clusters of vessels at its periphery resembling the composition of celery stems, which consist of numerous thin tubes surrounding a central one. The integration of decellularized celery stems and hiPSC-Heps that can differentiate into hepatocytes was therefore considered to develop a tissue-engineered liver. A decellularization process was performed to make the stem suitable for further functionalization (Fig. 32a). The SEM images of the prepared scaffolds showed the desirable pore sizes for hepatocyte proliferation and migration (Fig. 32b). GFP-positive hiPSC-Heps were embedded in the matrigel, followed by infusion into the decellularized celery

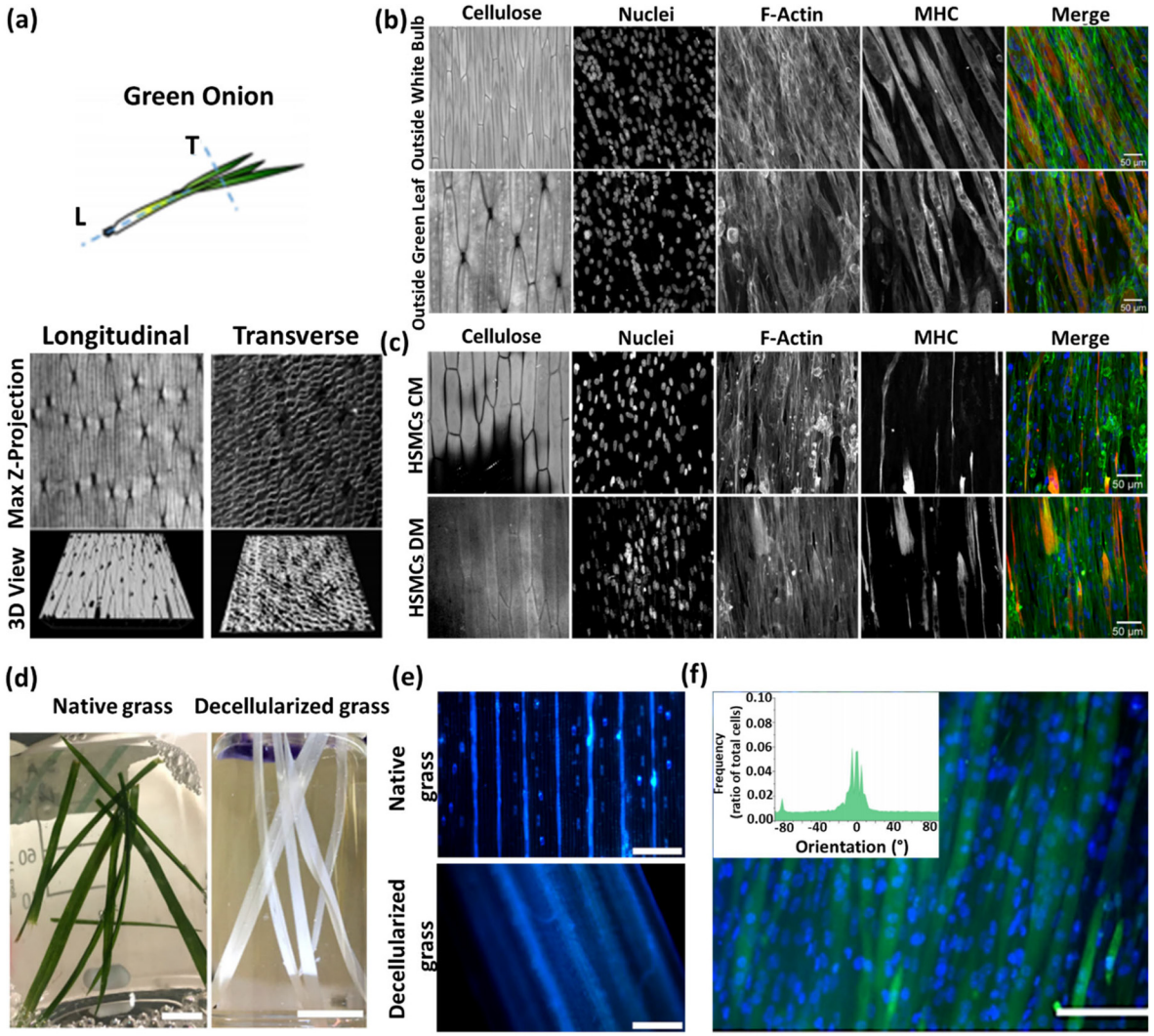

Fig. 31 (a) Anisotropic cellulose structures and 3D reconstruction of the cellulose scaffolds for both transverse and longitudinal preparations (scale bars: 100 and 50, respectively). (b) C2C12 cells exhibiting uniaxial alignment and directed movement along the cellulose scaffold topology when cultured on green onion's white bulb or green leaf scaffolds, as indicated by myotube expression (nuclei, NucGreen 488, blue; F-actin, phalloidin, green; myotubes, αMHC, red; scale bar = 50 μm). (c) HSMCs exhibiting remarkable alignment and differentiation along the cellulose scaffold topology when cultured on outer green onion's white bulb scaffolds, under both control medium (CM) and differentiation medium (DM) conditions (nuclei, NucGreen 488, blue; F-actin, phalloidin, green; myotubes, αMHC, red; scale bar = 50 μm). (Reproduced from ref. 35 with permission from American Chemical Society (ACS) Copyright 2020.) (d) Images of native grass and decellularized grass (scale bar = 1 cm). (e) Hoechst 33342 staining (blue) for nuclei in native and decellularized grass (scale bar = 200 μm). (f) Fluorescence images of C2C12 myotubes, stained green with FDA, and nuclei, stained blue with Hoechst 33342. (b) Quantified myotube alignment frequency, represented as a ratio of the total myotube count, employing the ImageJ Directionality plug-in (scale bar = 100 μm). (Reproduced from ref. 31 with permission from WILEY-VCH Verlag GmbH & Co, Copyright 2021.)

scaffold, and showed an increased number of GFP-positive cells over time (Fig. 32c). The prepared scaffold also displayed increased expression of Albumin (ALB) compared with the control group, and expression of Cytochrome P450 (CYP) enzymes needed for drug metabolism, indicating appropriate liver cell function (Fig. 32d and e). The hiPSC-Heps-loaded decellularized scaffolds were used for ectopic transplantation on the liver, spleen, and omentum in nude mice (Fig. 32f and g). Histological examination of the omentum grafts showed normal liver cell morphology and the presence of vascular-like structures, indicating their potential to generate blood vessels, and further immunohistochemical and immunofluorescence staining of ALB confirmed the retention of liver functions; hiPSC-Heps from both liver and spleen grafts also exhibited notable proliferation activity. It can be concluded that this celery-derived scaffold offers outstanding prospects in the field of liver transplantation and other regenerative medicine.

Another study applied a plant-derived membrane as an effective carrier of corneal epithelial cells for corneal epithelium regeneration.[247] It aimed to investigate the potential

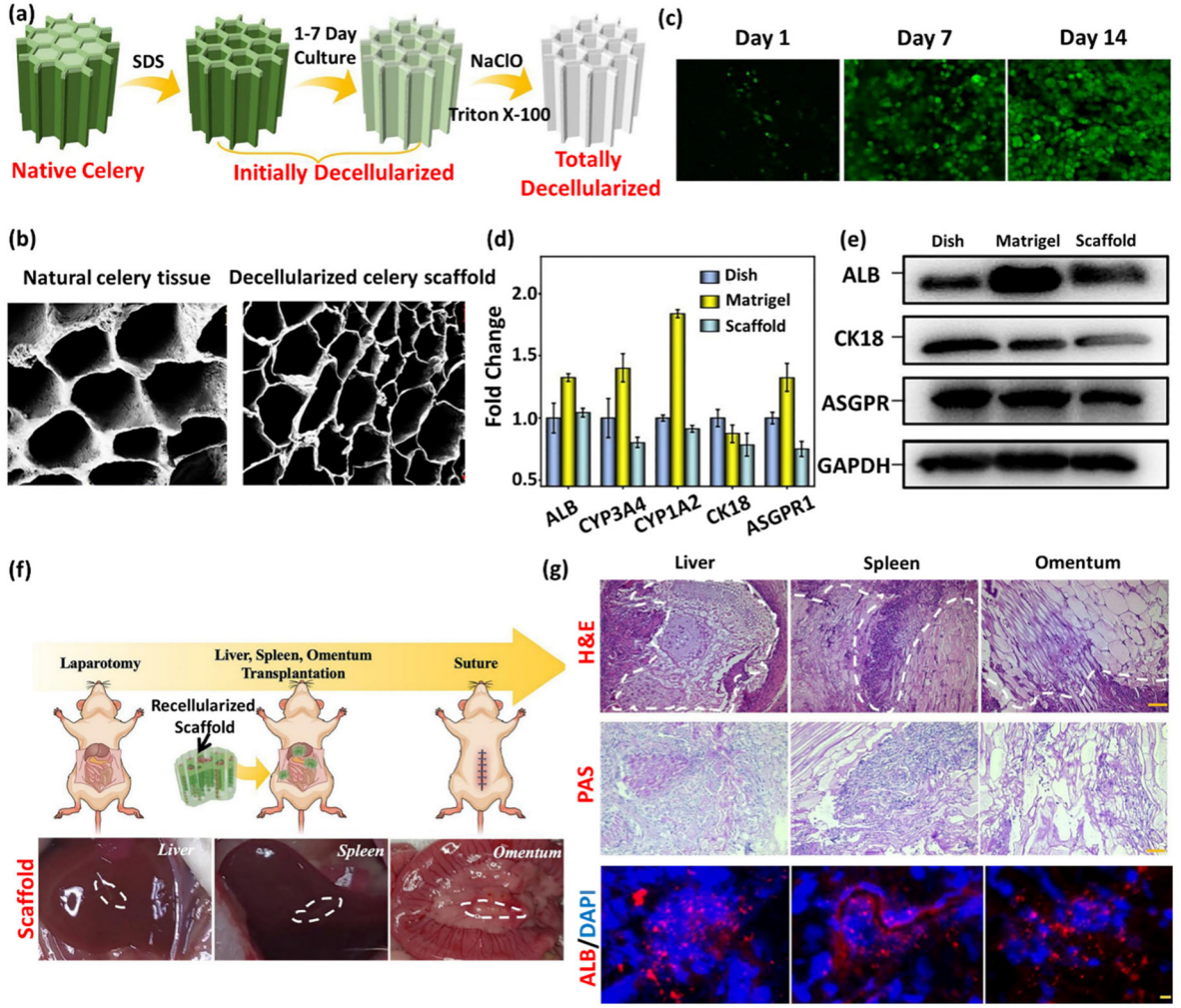

Fig. 32 (a) Schematic representation of the natural celery decellularization process. (b) SEM images of natural celery tissues and decellularized celery scaffolds (scale bar = 5 μm). (c) Confocal laser scanning fluorescence images during the 14-day culture of hiPSC-Heps on decellularized celery scaffolds. (d) The expression of hepatic function factors of hiPSC-Heps in 2D dish, matrigel, and decellularized celery scaffold. (e) The western blot results of ALB, CK18, and ASGPR expression in hiPSC-Heps in 2D dish, matrigel, and decellularized celery scaffold. (f) Schematic representation of the animal study design and the corresponding photographs of the transplanted scaffolds wrapped in host tissues (liver, spleen, and omentum). (g) H&E, PAS immunohistochemical, and ALB (red) immunofluorescence staining of hiPSC-Heps in each group (scale bar = 10 μm), periodic acid–Schiff stain. (Reproduced from ref. 42 with permission from WILEY-VCH Verlag GmbH & Co, Copyright 2022.)

of onion epithelial membranes (OEM) as scaffolds for cell cultures and their impact on rabbit corneal epithelial cells (RCECs). The results showed that OEM effectively maintained the phenotypic characteristics, proliferative potential, and stemness of RCECs. This suggests that OEM is cost-effective and viable for corneal epithelial transplantation surgery. Transplanting RCECs expanded on OEM onto limbal stem cell-deficient rabbits significantly accelerated wound healing and resulted in a more compact, stratified epithelium, as compared with the untreated group. These findings hold promise for clinical wound treatment and warrant further examination in relevant animal models. Another study presented a breakthrough in constructing intervertebral discs (IVDs) by developing a complete wood framework IVD (WFIVD) containing elastic nanocomposite hydrogel-based nucleus pulposus (NP) and anisotropic wood cellulose hydrogel-based annulus fibrosis (AF).[166] The innovative composite structure exhibited remarkable properties, characterized by cross-linked flexible polymer chains and strong hydrogen bonds with cellulose chains, enabling the integral construction of complex structures. The cellulose–PAM–PDA composite hydrogels provided high elasticity and favorable mechanical compatibility. The final WF-IVD closely matched the mechanical properties of native IVD. Comprising biocompatible materials, the wood IVD is non-cytotoxic, making it a safe and viable option. This nature-inspired approach simulates the intricate two-phase structure of native IVD, achieving an organic fusion of naturally aligned materials and polymers. It represents an innovative pathway in designing advanced structural biomimetic materials.

Recently, decellularized *Opuntia ficus-indica* tissue (commonly known as "nopal") has been exploited as a promising scaffold in tissue engineering, regenerative medicine, and dentistry.[248] This is due to nopal's unique structural qualities, controlled degradation properties, mechanical strength, ability to stimulate cell growth, and downregulation of pro-inflammatory cytokines. Therefore, these scaffolds have been regarded as a compelling candidate for advancing the field of biomaterials and regenerative applications. In addition to various applications of plant-derived scaffolds in the field of tissue engineering, these scaffolds could also be used to address the challenges associated with engineering complex tissues (*e.g.*, kidney tissue) due to its structural and functional complexity.[41] To this end, Jansen *et al.* studied the potential of spinach leaf vasculature and chive stems for kidney tubule engineering. However, the recellularization of spinach and chive vasculature using current methods is restricted, owing to inherent anatomical limitations. Further research is therefore needed to address this limitation.

In conclusion, it is worthwhile to integrate plant-derived scaffolds and tissue engineering, given the above-mentioned advantages. However, further research and exploration are imperative in this field, in order to overcome the current challenges.

8. Plant-based scaffolds for biosensing applications

8.1. An introduction to biosensors

Biosensors, as analytical devices, integrate a biomolecular recognition element or bioreceptor with the sensing platform to confer selectivity, along with a transducer or signal transduction element to enable quantitative bioanalysis. This conjugation of biological components with signal transducers facilitates complex and precise bioanalytical measurements characterized by their simplicity, ease of use, sensitivity, and specificity. The conceptualization of biosensors traces back to Leyland C. Clark's 1962 revelation, where he introduced the Clark oxygen electrode as the foundation for an "enzyme electrode" by immobilizing glucose oxidase (Gox) enzyme. Originally designed for detecting oxygen or hydrogen peroxide, this oxygen electrode was adapted to convert a simple platinum electrode into a bioanalytical device for glucose detection in diabetic patients.[249] Subsequently, the field evolved by incorporating various biological elements, such as nucleic acids, cells, and antibodies, resulting in the transformation of the term "enzyme electrode" into "biosensor".

Biosensors, characterized by their rapidity, selectivity, portability, and reusability, demand minimal sample processing before analysis. As depicted in Fig. 33, a typical biosensor is conceptually composed of three essential components: a detector, a transducer, and an output system. Biorecognition elements, including enzymes, antibodies, DNA/RNA, whole cells, hormones, and tissues, serve as interpretive biosensing tools due to their specific interactions with analyte molecules. The interaction between analyte molecules and biorecognition elements initiates transduction, manifesting as a measurable physicochemical change, such as electrical or optical signals, current flow, heat transfer, and alterations in mass or refractive index.[250]

Affinity biosensors rely on the binding interactions between bioreceptors and analytes, exemplified by immunosensors (antibody–antigen), nucleic acid biosensors (complementary nucleic acid binding), and aptamer biosensors (synthetic oligonucleotide binding). In contrast, catalytic biosensors operate based on chemical reactions that produce detectable products, encompassing enzymatic, cell-based, and DNAzymes (catalyti-

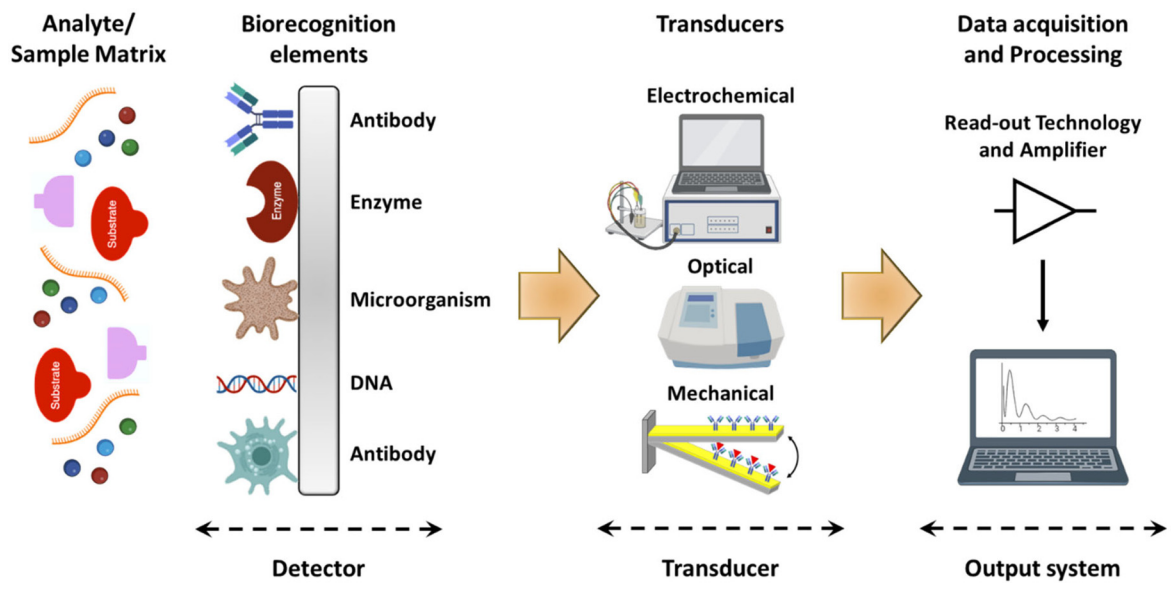

Fig. 33 Schematic representation of biosensor. (Reproduced from ref. 251 with permission from Springer Nature, Copyright 2023.)

cally active polynucleotides) biosensors. Catalytic biosensors, particularly advantageous for trace analysis, exhibit amplified product generation from a single analyte.[250] The intrinsic catalytic activity of enzymes imparts high sensitivity and selectivity to biosensing platforms. However, challenges such as denaturation, high costs, and low stability are associated with isolated enzymes.

Biosensor classification extends beyond biorecognition elements to encompass transduction techniques. Transducers, categorized as electrochemical (potentiometry and amperometry), optical (colorimetry, fluorescence, and bioluminescence), heat-based (thermistor), and mass-sensitive (piezo), define biosensor types. Biosensors find diverse applications in medical diagnostics, detecting biomarkers in cancer diagnosis and cardiovascular monitoring, drug discovery, environmental monitoring, process control, food safety, and security/defence contexts.[252] The growth of biosensors has been remarkable, transitioning from laboratory instruments to widespread manufacturing for home use. In 2022, the biosensor market surpassed $28.5 billion, as reported by Global Market Insights, garnering significant attention from diagnostic companies.[253]

8.2. Importance of plant tissue-based biosensors

In 1981, Kuriyama and Rechnitz pioneered the development of a glutamic acid biosensor utilizing a CO_2 electrode coupled with a yellow squash slice incorporating glutamate decarboxylase.[254] Subsequently, diverse biosensors have been introduced, employing plant tissue slices as bioreceptors and enzyme reservoirs to facilitate specific catalytic reactions.

Phytochemicals, a diverse array of natural compounds inherent to plants, present appealing candidates for targeted interactions with analytes owing to the distinct chemical structures encompassing carbohydrates, lipids, alkaloids, phenolics, terpenoids, and other nitrogen-containing compounds. In biosensor design, phytochemicals emerge as an alternative to isolated enzymes, offering a spectrum of applications facilitated by their chemical diversity, optical and electrochemical properties, and biocatalytic potential within plant tissues.[255] Beyond their attractive analytical features, the simplicity and cost-effectiveness associated with utilizing plant-derived materials have stimulated the development of biosensors.[256]

The utilization of plant tissue in biosensor development affords notable advantages, characterized by increased stability and sustained enzyme activity, attributed to inherent self-maintenance mechanisms. The higher availability of plant tissues at lower costs circumvents the need for laborious and time-intensive purification and enzyme extraction procedures, simplifying the biosensor construction process. Nevertheless, plant-based biosensors are not without limitations. They exhibit prolonged response times and diminished specificity, attributable to the diffusion barriers posed by intact tissue components, including proteins and other constituents, as opposed to the primary enzymes. Typically, the construction of plant-based biosensors involves the integration of plant tissue onto the conductor surface, encapsulated within a dialysis membrane to prevent enzyme leakage while facilitating analyte diffusion into the biosensor tissue. Simultaneously, the incorporation of tissue into a carbon paste matrix is employed. However, the aforementioned diffusion impediments contribute to extended response times, contrasting with the expeditious performance of carbon paste electrodes (CPEs).

Electrochemical detection methods have found widespread application in plant tissue-based biosensors. Nonetheless, optical methods, specifically chemiluminescence or fluorescence, exhibit notable advantages, including faster response times and higher sensitivities.[257] Electrochemical transducers leverage the redox activity of either the electroactive analyte or a label, with the ensuing redox process generating a current proportional to the analyte concentrations. Signal transduction in electrochemical biosensors can then occur *via* voltammetry or amperometry.

In contrast, optical methods, another prevalent signal transduction approach for biosensing, typically require an optically active label affixed to the analyte. The simplest optical method, colorimetry, involves correlating relative light absorbance intensity at visible wavelengths with analyte concentration after passing through a sample. Fluorescence, on the other hand, involves the emission of light following absorption or excitation from fluorescent species. Both absorbance and fluorescence transducers necessitate external light sources. Notably, chemiluminescence, an alternative in catalytic biosensors, operates without such external illumination.[250]

Harnessing plants as natural biocatalysts, biocatalytic sensors can be constructed using plant tissues containing various enzymes such as polyphenol oxidases (PPOs), ascorbate oxidase, peroxidase, urease, asparaginase, acid phosphatase and glycolate oxidase. The following section provides an overview of biosensing platforms based on plant matrices for the determination of diverse analytes, including catecholamine neurotransmitters, amino acids, and biomarkers. The discussion encompasses the working principles of modified bioelectrodes employing plant tissues, electrochemical techniques (amperometric, potentiometric, and voltammetry), and chemiluminescence (CL) coupled with flow injection analysis.

In the realm of enzyme-containing plant tissues for sensing applications, a diverse array of enzymes with distinct catalytic activities has been harnessed to facilitate targeted and responsive detection mechanisms (Fig. 34).

These enzymes, strategically classified into various groups, encompass oxidoreductases such as polyphenol oxidases, peroxidases, oxalate oxidase, ascorbate oxidase, and sulphite oxidase, primarily involved in redox (oxidation–reduction) reactions. Additionally, hydrolases including acid phosphatase, urease, pectinesterase, and diamine oxidase contribute their hydrolytic capability to sensing applications. Furthermore, the transferase asparaginase plays a role in the transfer of functional groups.

8.2.1. Oxidoreductases

8.2.1.1. Polyphenol oxidases (PPOs). The category of polyphenol oxidases encompasses a group of enzymes pivotal in plant tissues, catalyzing the oxidation of polyphenolic com-

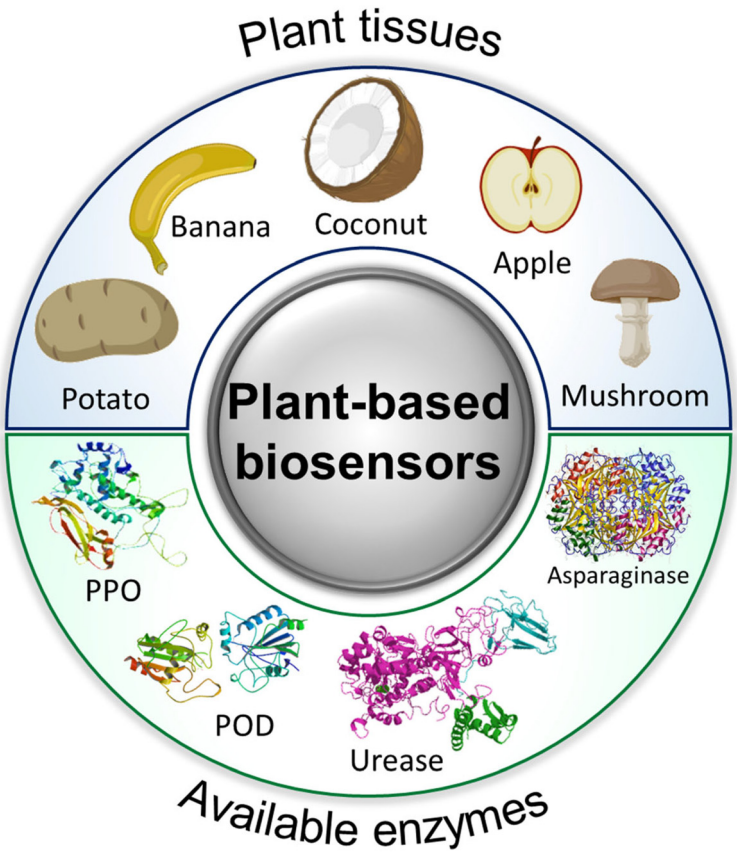

Fig. 34 Schematic depiction of various plant tissues and enzymes used in the construction of plant-based biosensors.

pounds and contributing to various physiological processes, as well as playing a significant role in the development of tissue-based biosensors. In 1985, Sidwell and Rechnitz pioneered the development of a plant tissue-based sensor for the electrochemical detection of dopamine. This method involved the utilization of banana pulp slices due to their richness in PPOs, enabling the recognition of mono- and poly-phenols. As shown in Fig. 35a, the experimental setup involved the construction of a biocatalytic membrane electrode by integrating a thin banana slice with a Clark electrode, referred to as "*Bananatrode*", facilitating the detection of oxygen decline through the conversion of dopamine into 1,2-benzoquinone. The prepared amperometric sensor demonstrated notable biocatalytic activity, robust time stability, and favourable selectivity.[258]

In 1988, further advancements were made by incorporating banana tissue into a CPE, aimed at reducing response times. This modification enabled the measurement of the reduction of the quinone derivative to catechol.[259] Eggins *et al.* expanded on this methodology by incorporating banana into a CPE and comparing its performance with apple and potato tissues for the detection of flavanols in commercial samples. The evaluation of beer quality was conducted by measuring catechins. Despite its potential, the banana electrode yielded less satisfactory and uncertain results, attributed to interference from residual flavanols in the banana matrix. Conversely, wet and dried apples and potatoes, both containing PPO, exhibited comparable results to conventional colorimetric and chromatographic methods.[260] A similar methodology was employed to detect flavanols and phenolic compounds in beer, employing apple tissue in a CPE (Fig. 35b). Through amperometric analysis, the biosensor was optimized, with an observed trend that increasing tissue ratios in the CPE led to enhanced water penetration, impacting PPO and catalytic site accessibility. Despite these improvements, the developed biosensors faced challenges related to specificity and selectivity.[261]

In 1997, an innovative approach was introduced involving the utilization of coconut tissue (*Cocus nucifera*) for an amperometric-based biosensor. Notably, the coconut tissue was encapsulated within a glass reactor body, differing from conventional practices of immobilization onto the working electrode surface. This unique biorecognition element was applied in a flow injection system for catechol analysis. Despite the absence of direct contact between the biomolecule and the transducer, the system demonstrated utility by determining catechol content at −0.10 V *vs.* Ag/AgCl, achieving a detection limit (LOD) of 2 μM in river and wastewater samples. However, the biosensor was not considered optimal due to challenges arising from tissue fouling *via* phenolic polymer adsorption during biocatalysis, resulting in a decline in activity. Additionally, it was suggested that a separation pretreatment

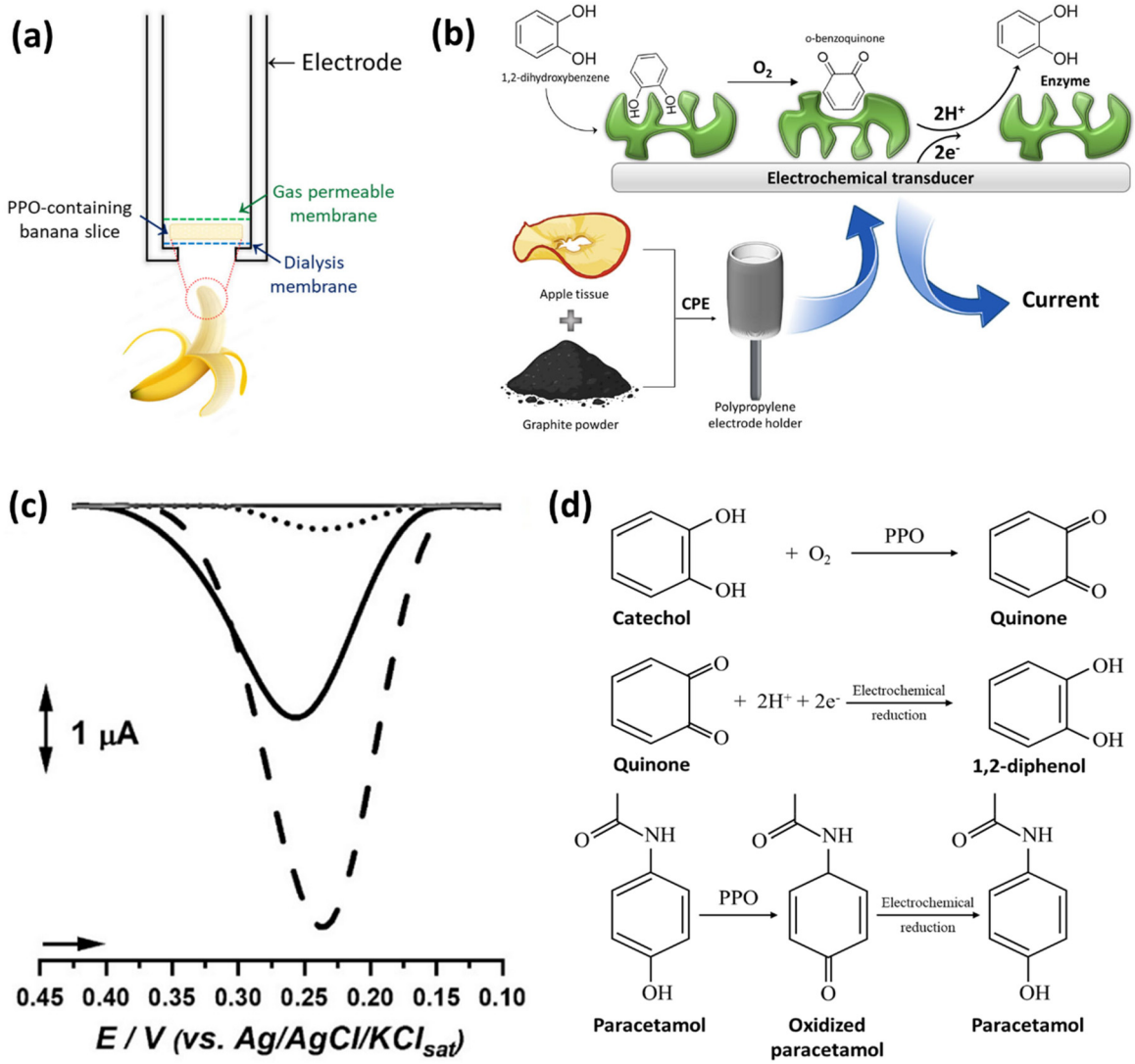

Fig. 35 (a) Schematic representation of "*Bananatrode*" assembly (reproduced from ref. 258 with permission from Springer Nature, Copyright 1985), (b) carbon paste biosensor based on PPO-containing apple tissue for electrochemical determination of flavanol content in beer samples (reproduced from ref. 261 with permission from Royal Society of Chemistry, Copyright 1998), (c) differential pulse voltammograms of catechol on the surface of bare CPE (●●●), mature-ripe fruits (—), and immature fruits biosensors (---), (d) catechol and paracetamol oxidation mechanism in biosensors. (Reproduced from ref. 266 with permission from Tabriz University of Medical Sciences, Copyright 2021.)

step might be necessary for applications requiring individual phenolic content analysis.[262]

Moreover, avocado tissue (*Persea americana*), known for its rich PPO content, was utilized in conjunction with a vaseline/graphite mixture to construct a chronoamperometric biosensor for the detection of paracetamol in pharmaceutical dosage forms. The PPO catalyzed the oxidation of paracetamol to *N*-acetyl-*p*-benzoquinone and its further reduction to paracetamol, resulting in a biosensor with a rapid 40-second response time and a LOD as low as 88 μM in pharmaceutical formulations. This approach proved advantageous in circumventing the need for time-consuming sample preparation, particularly due to the absence of phenolic compounds as pharmaceutical excipients in paracetamol dosage forms. The biosensor's performance was systematically evaluated in terms of repeatability, reproducibility, and operational lifespan.[263]

A biosensing platform utilizing fibers derived from the fruits of the palm tree (*Livistona chinensis*) was introduced for the determination of epinephrine. The biosensor operates through the catalysis of epinephrine oxidation to epinephrine quinone by PPO, followed by electrochemical reduction at −0.10 V *vs.* Ag/AgCl. The CPE configuration demonstrated a LOD of 15 μM in conjunction with a flow injection analysis system. This biosensor was successfully applied to quantify epinephrine in an inhaler as a pharmaceutical product, showcasing enhanced specificity compared with the official spectrophotometric method due to mitigated interference from benzoic acid in the pharmaceutical formulation.[264]

In an alternative strategy, Mazzei *et al.* proposed a biosensor utilizing potato (*Solanum tuberosum*) in combination with a commercial Clark electrode. In this approach, herbicides served to inhibit PPO, and this inhibition was leveraged for the quantification of atrazine, diverging from conventional phenol catalysis. Notable for its simplicity and cost-effectiveness, the biosensor demonstrated good stability, addressing the short lifespan associated with other pesticide sensors. The biosensor selectively quantified atrazine with a LOD of 10 μM, even in the presence of organophosphorus or carbamate pesticides. However, the biosensor's lifespan was reduced compared with catechol or phenol biosensors, a limitation partially mitigated by washing atrazine traces from the electrode. The application of plant tissues provided a practical and economically viable replacement in the biocatalytic layer compared with pure enzymes, rendering it suitable for applications in aqueous solutions, such as rivers or water-washed soils.[265]

Additionally, a voltammetric biosensor was devised utilizing PPO-containing myrtle tree fruits, for the determination of epinephrine in pharmaceutical samples. The biosensor involved the immobilization of tissue homogenate on a glassy carbon electrode crosslinked with glutaraldehyde. The enzymes present in plant fibers catalyzed the oxidation of epinephrine to epinephrine quinone.[267] Furthermore, a PPO biosensor was developed using *Solanum lycocarpum* fruit extracts (both immature and mature ripe) for the detection of paracetamol. As depicted in Fig. 35c and d, employing the differential pulse voltammetry (DPV) technique, the biosensor exhibited varying performance levels based on the maturity of the fruit extract, with immature fruit extract demonstrating superior performance in tablet formulations.[266]

Mushroom tissues, renowned for their abundant PPO content, also served as promising biorecognition elements in biosensors designed for the quantification of *o*-diphenol, achieving faster and higher responses.[268] In a specific application, mushroom tissue was incorporated onto a Clark oxygen electrode using gelatine and glutaraldehyde to engineer a phenol biosensor. The methodology suggested versatility by proposing its applicability to the determination of thiourea and benzoic acid concentrations in beverages and juices.[269]

8.2.1.2. Peroxidases (PODs). The utilization of PODs-containing plant tissues has been introduced in the development of plant-based biosensors, given their widespread occurrence in various plant species and their suitability for biosensor construction. In this regard, Wang *et al.* employed horseradish root tissue, a predominant source of PODs, coupled with a graphite disk transducer. Employing the amperometry technique, the biosensor demonstrated the ability to detect 2-butanone peroxide in the organic phase with submillimolar concentrations within 20 seconds. This methodology marked a significant advancement, attributing its success to the simplicity, speed, and reproducibility of enzyme immobilization on transducers.[270]

Gilo (*Solanum gilo*), recognized for its rich POD content, was immobilized within a chitosan matrix and then incorporated into a CPE to engineer electrochemical biosensors for hydroquinone[271] and rutin.[272] The interaction between the amine groups on chitosan and the enzyme resulted in the creation of a reproducible, remarkably stable, and sensitive biosensor with a LOD of 2 μM and 20 nM for hydroquinone and rutin, respectively.

Furthermore, the same researchers coupled green bean (*Phaseolus vulgaris*) tissue homogenate with chitin to construct a caffeic acid biosensor for white wine analysis. This biosensor exhibited comparable quality in terms of sensitivity, stability, and reproducibility. Additionally, asparagus tissue, characterized by a high POD content, was immobilized with ferrocene as a redox mediator on a CPE to develop a hydrogen peroxide biosensor. Operating at 0 V *vs.* SCE, the biosensor presented a LOD of 0.4 μM with a rapid 2-second response time.[273] A similar approach was adapted for the determination of fluoride in real samples, exhibiting performance comparable to fluoride-selective electrodes even in the presence of potential interferences[274] (Fig. 36a).

An organic-phase plant-based biosensor was proposed based on modifying a CPE with POD-containing *Ipomoea batatas* (sweet potato) tissue, to detect hydroquinone in cosmetic creams *via* cyclic voltammetry. POD catalyzed the oxidation of hydroquinone to *p*-quinone, followed by the reduction back at −0.22 V *vs.* Ag/AgCl in the presence of hydrogen peroxide as a natural substrate, as depicted in Fig. 36b. This methodology facilitated the direct determination of hydroquinone with a LOD of 8.1 μM, obviating the need for hydroquinone extraction following cream solubilization, akin to pharmacopeial procedures.[275]

An innovative hydrogen peroxide biosensor was engineered by incorporating coconut fibers into a carbon paste electrode, demonstrating applicability in the amperometric determination of hydrogen peroxide in pharmaceutical products such as contact lens cleaning solutions, antiseptic solutions, and hair coloring creams. The biosensor exhibited a remarkable sensitivity, detecting hydrogen peroxide concentrations as low as 40 μM, and maintained functional integrity for at least three months. The findings exhibited a robust correlation with the spectrophotometric method, validating the biosensor's accuracy and longevity.[276]

Traditionally, plant-based biosensors have been developed using commercially sourced tissues, yet concerns arise regarding the reproducibility of results due to uncertainties surrounding the freshness and growth conditions of these tissues. To address this limitation, a pioneering approach involving *in vitro* cultured callus tissues was initiated, beginning with tobacco (*Nicotiana tabacum*), recognized for its abundance of fresh peroxidase enzymes. Explants obtained from the plants were isolated and inoculated under controlled growth conditions, nutrients, and medium to cultivate uniform tissues. The amperometric responses of hydrogen peroxide in carbon paste electrodes, incorporating tissue and ferrocene, were systematically compared across various biosensors developed using tobacco tissues, callus tissues, and agar-grown tissues. Notably, *in vitro* cultured tissues demonstrated superior sensitivities and precision, underscoring the

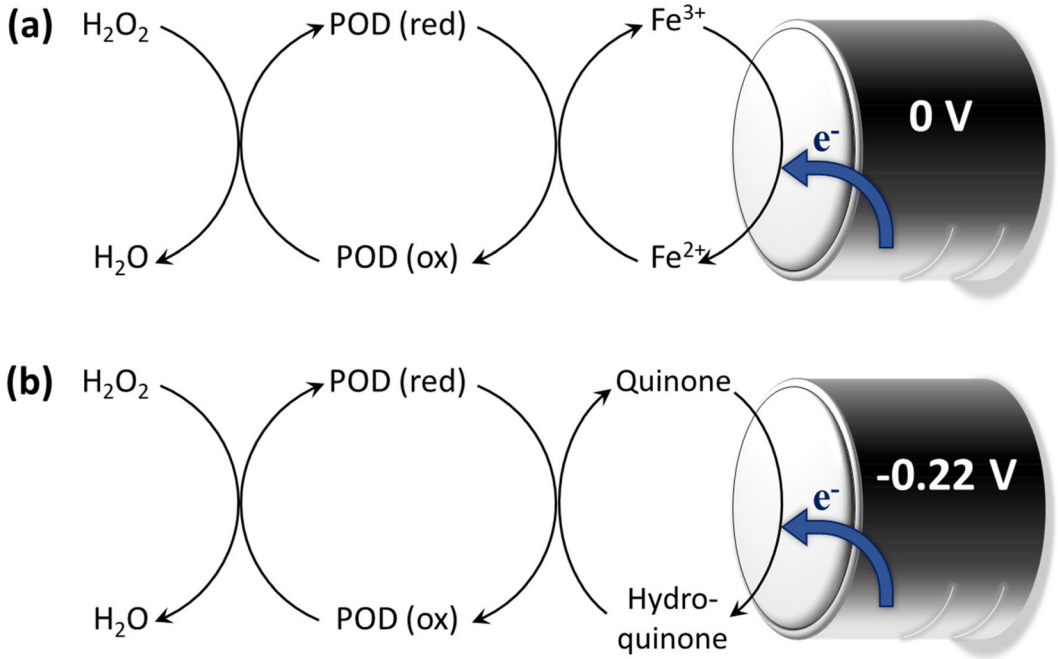

Fig. 36 Enzymatic processes of hydrogen peroxide reduction in (a) ferrocene-mediated (reproduced from ref. 274 with permission from Elsevier, Copyright 2001) and (b) quinone-mediated peroxidase catalysis. (Reproduced from ref. 275 with permission from Elsevier, Copyright 2000.)

advantages of this approach for enhancing the reliability and reproducibility of plant-based biosensors.[277]

8.2.1.3. Oxalate oxidase. Spinach (*Spinacia oleracea*) enriched in oxalate oxidase content was incorporated onto a Clark electrode through gelatine and glutaraldehyde cross-linkage for the purpose of oxalate detection in urine, relying on its oxidation with subsequent oxygen consumption. The biosensor demonstrated notable specificity and achieved a significantly reduced detection limit compared with bi-enzymatic biosensors.[278]

8.2.1.4. Ascorbate oxidase. Cucumber (*Cucumis sativus*), renowned for its elevated ascorbate oxidase content, has emerged as a promising candidate for the development of plant-based biosensors tailored for the quantification of reduced glutathione (GSH). Following tissue homogenization, cucumber tissue was affixed onto a pre-treated Teflon membrane through a process involving glutaraldehyde and gelatine cross-linkage. GSH, pivotal in cellular defence against free radicals, amino acid transport, and protein and DNA synthesis, was detected without the need for derivatization. The modulation of oxygen levels, induced by the inhibition of ascorbate oxidase by glutathione, facilitated GSH detection in real samples such as tomato, broccoli, and potato. The biosensor exhibited an impressive 0.1 μM detection limit and yielded results comparable to those obtained *via* Ellman's method.[279] Additionally, the mesocarp of squash (*Cucurbita pepo*) or cucumber was integrated with a Clark-type oxygen electrode to design an amperometric biosensor for the determination of ascorbic acid. Ascorbate oxidase-catalyzed oxidation of the analyte led to increased oxygen consumption at a potential of −650 mV *vs*. Ag/AgCl. The reduction in electrical current was indicative of this consumption and was monitored during the analysis of various fruit juices and vitamin tablets.[280]

8.2.1.5. Sulfite oxidase. In the realm of antioxidant additives, the application of sulfite is restricted due to potential hypersensitivity reactions in certain individuals. To address this limitation, *Malva vulgaris*, harnessed as a source of sulfite oxidase, was employed to establish an electrochemical sulfite biosensor. The biosensor operates by catalyzing the oxidative degradation of cysteine and methionine, sulfur-containing amino acids, resulting in the generation of hydrogen peroxide. The analytical technique employed for sulfite quantification involved amperometry, wherein oxygen consumption was monitored and correlated with the sulfite concentration.[281]

8.2.1.6. Other oxidases (alcohol oxidase, laccase). The use of mushroom tissue containing alcohol oxidase has been explored for the detection of ethyl alcohol in biological fluids, with considerations for clinical and toxicological applications.[282] A chemiluminescence biosensor based on mushroom tissue has been proposed for the detection of ethanol in both beverages and biological fluids. This biosensor relies on the reaction involving luminol, potassium hexacyanoferrate(III), and hydrogen peroxide.[283]

Moreover, serving as a source of laccase oxidase, mushroom tissues have been leveraged for the development of biosensors targeting phenolic compounds. Various sensors originating from three distinct plant sources, namely *Trametes versicolor* laccase from the white-rot fungus, *Agaricus bisporus* tissue, and *Aspergillus Niger* laccase produced through genetic engineering, were constructed and subjected to comparison. Notably,

the tissue biosensor exhibited superior activity attributed to the enhanced performance of PPO at elevated pH values.[284]

8.2.2. Hydrolases

8.2.2.1. Diamine oxidase. Diamine oxidase (DAO) present in pea or lentil cotyledons catalyzes the oxidation of diamines such as cadaverine and putrescine, resulting in the production of hydrogen peroxide. Electrochemical transducers were employed to quantify this enzymatically generated hydrogen peroxide. A biosensor, utilizing cotyledon as the biological matrix, was developed for the precise measurement of diamines. Additionally, hybrid biosensors were engineered using lentil tissue in conjunction with ornithine decarboxylase (ODC) or lysine decarboxylase (LDC) for the selective detection of ornithine or lysine, as illustrated in Fig. 37a.[285]

Moreover, the chemiluminescence of luminol and Co^{2+} was employed to detect hydrogen peroxide generated through diamine oxidation. This approach offers advantages over enzyme electrodes, including simplified sensor construction, rapid response times, lower detection limits, and reduced costs.[286]

8.2.2.2. Acid phosphatase. Potato tissue exhibits the potential to serve as a reservoir for acid phosphatase (AF), distinct from PPO and POD enzymes. In a research study, a bi-enzymatic biosensor was developed utilizing slices of potato (*Solanum tuberosum*) and glucose oxidase (Gox) with an amperometric Clark electrode to quantitatively assess phosphate levels. The enzymatic cascade involves AF catalyzing the conversion of glucose-6-phosphate to glucose, subsequently oxidized by Gox in the presence of oxygen. The inhibition of AF activity correlates with phosphate concentration. The devised biosensors were effectively employed for phosphate detection in diverse real samples, including pharmaceutical products, human urine, powdered milk, bovine milk, mashed tomatoes, and red wine. This methodology aligns with the

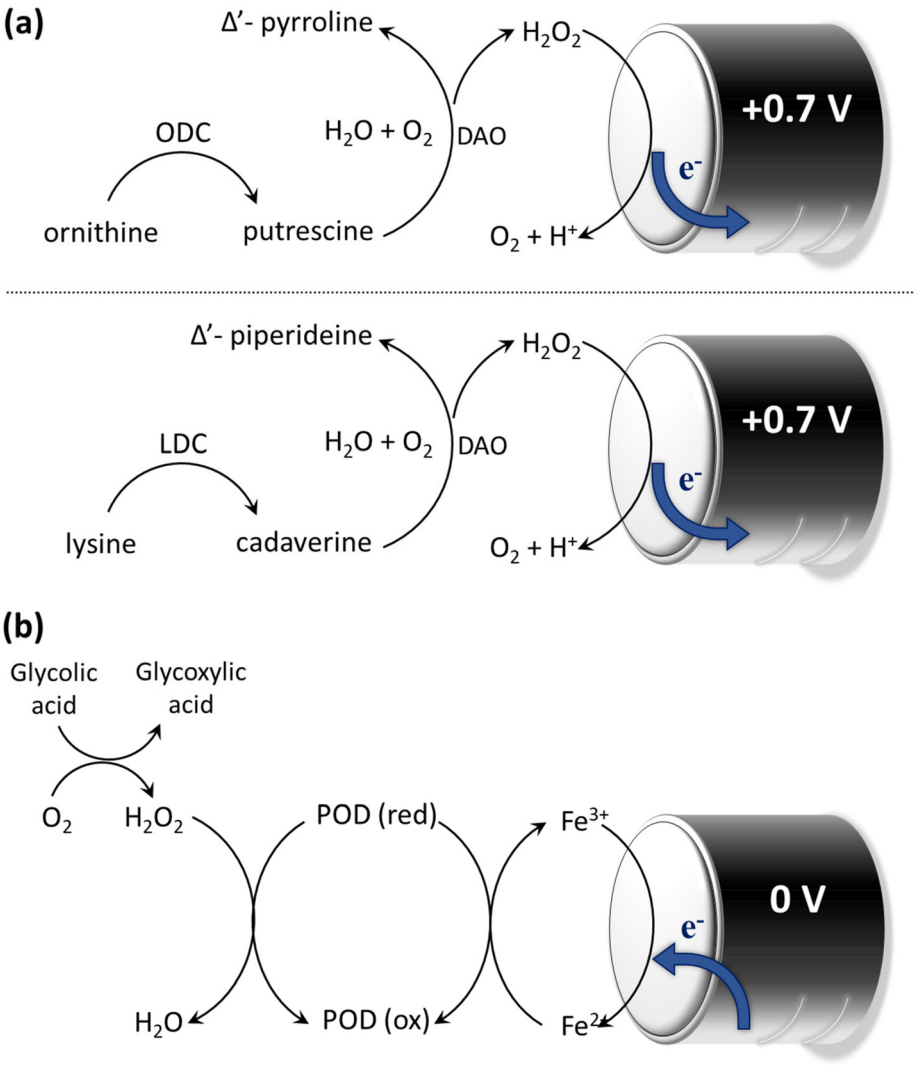

Fig. 37 Enzymatic mechanisms in (a) the legume cotyledon tissue biosensors (reproduced from ref. 285 with permission from Elsevier, Copyright 1993) and (b) ferrocene-mediated spinach tissue-based bienzymatic biosensor. (Reproduced from ref. 293 with permission from Elsevier, Copyright 1994.)

spectrophotometric approach outlined in previous studies.[287,288]

8.2.2.3. Urease. An innovative chemiluminescence (CL) biosensor, integrated with a flow injection analysis system, has been developed utilizing soybean tissue characterized by a notable urease content for the purpose of urea detection. The soybean tissue, encapsulated within a glass column, was immobilized through the use of permanganate and luminol, facilitating the determination of urea levels in urine samples through a flow-based system. Urea undergoes hydrolysis catalyzed by urease, yielding HCO_3^- and NH_4^+; the released luminol subsequently reacts with permanganate. This reaction between luminol and permanganate generates a distinctive chemiluminescence signal. The application of flow injection chemiluminescence exhibited heightened sensitivity and rapid response times.[289]

8.2.2.4. Pectinesterase. Fruits, including apples and oranges, as well as vegetables, are abundant sources of pectin, a substantial polysaccharide characterized by a molecular weight ranging from 20 000 to 400 000. Pectin solutions, known for their high viscosity, pose challenges for conventional pectin biosensors as they tend to foul the electrode surface. This limitation has been effectively addressed by employing plant tissue biosensors, which offer improved tolerance and facile replacement mechanisms. A novel pectin hybrid biosensor was devised through the synergistic integration of alcohol oxidase and orange peel tissue, notable for its elevated pectinesterase content. This hybrid biosensor engages in a reaction with pectin, generating methanol as a byproduct, subsequently oxidized by alcohol oxidase to produce hydrogen peroxide. Detection of hydrogen peroxide necessitates the utilization of high-potential oxidizing compounds such as ascorbic acid. To mitigate interference from ascorbic acid, Teflon membranes were employed instead of dialysis membranes. However, the slow diffusion of methanol led to increased response times, necessitating daily replacement of the electrode surface. Despite these challenges, the study concluded that plant-based biosensors exhibit robust capability in handling high molecular-weight analytes.[290]

8.2.3. Transferases

8.2.3.1. Asparaginase. Asparaginase, a therapeutic agent employed in the treatment of cancers like lymphosarcoma and acute lymphoblastic leukaemia (ALL), is derived from diverse sources such as bacteria, fungi, algae, and plants. This enzyme catalyzes the conversion of asparagine to aspartic acid. Notably, Ashwagandha (*Withania somnifera* (L.) *Dunal*), characterized by its richness in asparaginase, presents an opportunity for the development of a biosensor dedicated to the quantification of asparagine. This biosensor holds potential for application in assessing asparagine levels in fruit juices and leukemic blood samples from ALL patients.[291,292] Various immobilization techniques, including gelatine, agarose, agar, and calcium alginate, were explored to enhance the stability of asparaginase. Among these techniques, the calcium alginate method emerged as the most effective, demonstrating the shortest response time. The authors underscored the significance of the plant-based biosensor as an expedient, cost-effective, innovative, user-friendly, portable, and nanolevel method for detecting asparagine.[292]

8.2.4. Bi-enzymatic biosensors. Bi-enzymatic biosensors offer the potential for intricate designs involving two enzymes, with an added layer of interest when both enzymes are sourced from a single plant. In this context, ground spinach leaves, renowned for their richness in glycolate oxidase, peroxidase, and ferrocene, were co-immobilized on a carbon paste electrode. This process facilitated the construction of an amperometric plant tissue biosensor explicitly engineered for the determination of glycolic acid. The biosensor plays a crucial role in the differential diagnosis of hyperoxaluria syndrome, engaging in a series of reactions illustrated in Fig. 37b.[293]

Utilizing spinach leaves enriched in glycolate oxidase (GlOD) and luminol, a chemiluminescence biosensor, coupled with flow injection analysis, was developed for the detection of glycolic acid. GlOD catalyzed the production of hydrogen peroxide, and in tandem with a positive potential, initiated luminol electrochemiluminescence (ECL) directly correlated to the concentration of hydrogen peroxide.[294,295] Additionally, a chemiluminescence biosensor was devised for the determination of dopamine, leveraging potato root tissue containing PPO and POD. The oxidation of dopamine, catalyzed by PPO, generated hydrogen peroxide, which in turn reacted with luminol, generating a chemiluminescent signal. This system allowed for the real-time, *in vivo* monitoring of dopamine levels in rabbit blood by deploying a microdialysis probe into the rabbit's ear edge vein.[296]

9. Conclusions and future perspectives

In essence, tissue engineering and regenerative medicine are highly interdisciplinary fields that require consideration of multiple factors when designing suitable scaffolds for various applications. Despite significant advancements in scaffold construction aimed at achieving optimal properties such as enhanced biocompatibility, controlled biodegradability, customizable mechanical strength mirroring native tissue, and tailored bioactivity, several unresolved challenges still remain that hinder the clinical translation of scaffolds. Plant-derived skeletons exhibit promising structural characteristics, rendering them attractive candidates for a wide range of biomedical applications. The inherent anisotropy, biocompatibility inherited from cellulose, and structural diversity, including pore size and shape distribution, have stimulated scientists to explore plant-based scaffolds. While plant-based scaffolds offer numerous advantages, they also present several drawbacks that must be overcome for their widespread application.

One challenge in utilizing plant-derived scaffolds lies in their fabrication process. Due to the unique characteristics of plant-based materials, specialized processing techniques are often necessary to create scaffolds with tailored properties. This process, whether through decellularization or delignifica-

tion, must effectively remove cellular and lignin content while preserving structural interconnectivity and integrity.[63,297] Achieving this balance demands careful execution to ensure optimal scaffold performance. In the meantime, the variability in composition is another concern that should be taken into consideration. Plant-derived materials can exhibit variability in composition due to factors such as species, growth conditions, and processing methods, which may affect their mechanical properties and biocompatibility.[298] Moreover, there may be a lack of standardized protocols for processing and characterizing plant-derived materials, leading to difficulties in ensuring consistency and reproducibility across different batches.[299]

Tuning the biodegradation rate of the prepared scaffolds (pristine or functionalized) also needs more profound investigations. The rate of biodegradation of plant-derived materials may not always align with the desired tissue regeneration timeline, leading to challenges in scaffold degradation and tissue integration kinetics.[24,300] Another significant challenge associated with plant-derived scaffolds is scaling up their production to meet the demands of large-scale biomedical applications. While laboratory-scale fabrication methods may be feasible for research purposes, transitioning to commercial-scale production requires addressing numerous logistical and technical considerations. Scaling up plant-derived scaffold production involves optimizing processing techniques, and implementing efficient manufacturing practices. Additionally, ensuring consistency, quality control, and regulatory compliance becomes increasingly complex at larger scales. Overcoming these challenges is essential for realizing the potential of plant-derived scaffolds in clinical settings and industrial applications.

Last but not least, the absence of Glycosaminoglycans (GAGs) in plant-based scaffolds represents another limitation in their application for certain biomedical contexts. GAGs are crucial components found in native ECM that play vital roles in cell signalling, adhesion, and tissue regeneration. Their absence in plant-derived scaffolds may hinder the biomimetic properties necessary for optimal cell–matrix interactions and tissue development.[7,8] Researchers may focus on exploring strategies to incorporate GAG-like molecules into plant-based scaffolds or engineer alternative bioactive components to enhance their functionality and promote specific tissue regeneration processes. Addressing this limitation will be pivotal for expanding the utility of plant-based scaffolds in tissue engineering and regenerative medicine applications.

Despite these drawbacks, the unique features inherent in plant structures hold significant promise for their expansion and adoption in diverse biomedical applications. Researchers can actively investigate methods to enhance the bioactivity of plant-based scaffolds by incorporating bioactive molecules, such as growth factors, peptides, and ECM components. This approach aims to mimic the native tissue microenvironment more closely and promote specific cellular responses for improved tissue regeneration. Furthermore, composite scaffolds combining plant-derived materials with polymers, ceramics, or other natural materials offer the potential to synergistically leverage the unique properties of each component. By strategically designing composite scaffolds, researchers can achieve improved mechanical properties, enhanced bioactivity, and tailored degradation profiles. Efforts to translate plant-based scaffolds from bench to bedside are underway, with a focus on addressing regulatory challenges, conducting preclinical studies, and optimizing manufacturing processes for scalability and reproducibility. Successful clinical translation would pave the way for the widespread adoption of plant-based scaffolds in various therapeutic applications, including wound healing, drug delivery, and organ regeneration.

Abbreviations

AF	Acid phosphatase
AFM	Atomic force microscopy
ALB	Albumin
ALL	Acute lymphoblastic leukemia
ALP	Alkaline phosphatase
APTES	3-Aminopropyltriethoxysilane
Ar	Argon
BDDE	1,4-Butanediol diglycidyl ether
BET	Brunauer–Emmett–Teller
BF	*Borassus flabellifer*
BPQDs	Black phosphorus quantum dots
CCK-8	Cell counting kit-8
ChCl	Choline chloride
CI	Crystallinity index
CL	Chemiluminescence
CNFs	Cellulose nanofibrils
CPD	Critical point drying
CPE	Carbon paste electrode
CQS	Chitosan quaternary ammonium salt
CYP	Cytochrome P450
DAPI	4′,6-Diamidino-2-phenylindole
DESs	Deep eutectic solvents
DMOG	Dimethyloxalylglycine
DOX	Doxorubicin hydrochloride
DPV	Differential pulse voltammetry
DTA	Differential thermal analysis
DW	Delignified wood
ECL	Electrochemiluminescence
ECM	Extracellular matrix
EGFP	Enhanced green fluorescent protein
ETI	Engineered tissue interface
FDA	Fluorescein diacetate
FTIR	Fourier-transform infrared spectroscopy
G	Guaiacyl
GAGs	Glycosaminoglycans
GC	Gas chromatography
GO	Graphene oxide
Gox	Glucose oxidase
GS	Gentamicin
H	4-Hydroxyphenyl
H&E	Hematoxylin and eosin

HA	Hyaluronic acid
HAp	Hydroxyapatite
HBA	Hydrogen bond acceptor
HBD	Hydrogen bond donor
HCFW	Holocellulose framework
hDFs	Human dermal fibroblasts
hFFs	Human foreskin fibroblasts
hiPSCs	Human-induced pluripotent stem cell-derived
Heps	Hepatocytes
HPLC	High-performance liquid chromatography
hRBCs	Human red blood cells
HSMCs	Human skeletal muscle cells
HUVEC	Human umbilical vein endothelial cells
ICP-MS	Inductively coupled plasma mass spectrometry
IL	Ionic liquid
iPSCs	Induced pluripotent stem cells
IVC	Inferior vena cava
IVDs	Intervertebral discs
LCCs	Lignin–carbohydrate complexes
LDC	Lysine decarboxylase
LOD	Limit of detection
MOF	Metal–organic framework
MSCs	Mesenchymal stem cells
MTM	Maximum tangent modulus
MTT	(3-(4,5-Dimethylthiazol-2-yl)-2,5-diphenyltetrazolium bromide)
MWCNTs	Multiwalled carbon nanotubes
NMR	Nuclear magnetic resonance spectroscopy
NPs	Nanoparticles
NSC	Neural stem cell
OA	Orientation angle
OB	Osteoblastic
OCN	Osteocalcin
ODC	Ornithine decarboxylase
OEM	Onion epithelial membranes
OTS	Octadecyl trichlorosilane
PAM	Polyacrylamide
PC3	Prostate cancer cells
PCL	Polycaprolactone
PDA	Polydopamine
PEDOT:PSS	Poly(3,4-ethylenedioxythiophene) polystyrene sulfonate
PEGDGE	Poly(ethylene) glycol diglycidyl ether
PI	Propidium iodide
PLGA	Polylactic-*co*-glycolic acid
PMMA	Poly(methyl methacrylate)
POD	Peroxidases
PPO	Polyphenol oxidase
PVA	Polyvinyl alcohol
RCECs	Rabbit corneal epithelial cells
RSF	Regenerated silk fibroin
S	Syringyl
SA	Sodium alginate
scCO2	Supercritical carbon dioxide
SDS	Sodium dodecyl sulfate
SEM	Scanning electron microscopy
SSA	Specific surface area
TAPPI	Technical Association of the Pulp and Paper Industry
TEMPO	2,2,6,6-Tetramethylpiperidine1-oxyl radical
TS	Triplochiton scleroxylon
TW	Transparent wood
UTS	Ultimate tensile strength
VBs	Vascular bundles
WH	Wood–hydroxyapatite
WHP	Wood–hydroxyapatite–polycaprolactone
WW	White wood
XRD	X-ray diffraction
YM	Young's modulus

Data availability

No primary research results, software or code have been included and no new data were generated or analysed as part of this review.

Conflicts of interest

The authors declare no conflict of interest.

Acknowledgements

H. A. S. and M. A. S acknowledge UMCG Research Funds for financial support.

References

1 E. Jacques and E. J. Suuronen, *Clin. Transl. Sci.*, 2020, **13**, 440–450.
2 J. Hunsberger, O. Harrysson, R. Shirwaiker, B. Starly, R. Wysk, P. Cohen, J. Allickson, J. Yoo and A. Atala, *Stem Cells Transl. Med.*, 2015, **4**, 130–135.
3 H. Kaul and Y. Ventikos, *Tissue Eng., Part B*, 2015, **21**, 203–217.
4 A. L. Predeina, M. S. Dukhinova and V. V. Vinogradov, *J. Mater. Chem. B*, 2020, **8**, 10010–10022.
5 R. Mohammadinejad, H. Maleki, E. Larraneta, A. R. Fajardo, A. B. Nik, A. Shavandi, A. Sheikhi, M. Ghorbanpour, M. Farokhi and P. Govindh, *Appl. Mater. Today*, 2019, **16**, 213–246.
6 J. K. R. Mutra, S. E. Jujjavarapu and N. Verma, *ACS Sustainable Chem. Eng.*, 2023, **11**, 6485–6497.
7 A. C. Bilirgen, M. Toker, S. Odabas, A. K. Yetisen, B. Garipcan and S. Tasoglu, *ACS Biomater. Sci. Eng.*, 2021, **7**, 926–938.
8 S. Iravani and R. S. Varma, *Green Chem.*, 2019, **21**, 4839–4867.
9 X. Liu, Q. Sun, H. Wang, L. Zhang and J.-Y. Wang, *Biomaterials*, 2005, **26**, 109–115.

10 R. Cancelliere, F. Zurlo, L. Micheli and S. Melino, *Talanta*, 2021, **223**, 121671.
11 J. Beltrán, P. J. Steiner, M. Bedewitz, S. Wei, F. C. Peterson, Z. Li, B. E. Hughes, Z. Hartley, N. R. Robertson and A. V. Medina-Cucurella, *Nat. Biotechnol.*, 2022, **40**, 1855–1861.
12 F. Pampaloni, E. G. Reynaud and E. H. K. Stelzer, *Nat. Rev. Mol. Cell Biol.*, 2007, **8**, 839–845.
13 J. Lee, M. J. Cuddihy and N. A. Kotov, *Tissue Eng., Part B*, 2008, **14**, 61–86.
14 M. Kapałczyńska, T. Kolenda, W. Przybyła, M. Zajączkowska, A. Teresiak, V. Filas, M. Ibbs, R. Bliźniak, L. Luczewski and K. Lamperska, *Arch. Med. Res.*, 2018, **14**, 910–919.
15 M. Mabrouk, H. H. Beherei and D. B. Das, *Mater. Sci. Eng., C*, 2020, **110**, 110716.
16 J. J. Chung, H. Im, S. H. Kim, J. W. Park and Y. Jung, *Front. Bioeng. Biotechnol.*, 2020, **8**, 586406.
17 A. Gilpin and Y. Yang, *BioMed Res. Int.*, 2017, **2017**, 9831534.
18 A. Neishabouri, A. Soltani Khaboushan, F. Daghigh, A. M. Kajbafzadeh and M. Majidi Zolbin, *Front. Bioeng. Biotechnol.*, 2022, **10**, 805299.
19 D. E. Heath, *Regen. Eng. Transl. Med.*, 2019, **5**, 155–166.
20 M. Kasravi, A. Ahmadi, A. Babajani, R. Mazloomnejad, M. R. Hatamnejad, S. Shariatzadeh, S. Bahrami and H. Niknejad, *Biomater. Res.*, 2023, **27**, 1–24.
21 B. S. Kim, H. Kim, G. Gao, J. Jang and D.-W. Cho, *Biofabrication*, 2017, **9**, 034104.
22 T. J. Keane, I. T. Swinehart and S. F. Badylak, *Methods*, 2015, **84**, 25–34.
23 T. W. Gilbert, T. L. Sellaro and S. F. Badylak, *Biomaterials*, 2006, **27**, 3675–3683.
24 A. F. Harris, J. Lacombe and F. Zenhausern, *Int. J. Mol. Sci.*, 2021, **22**, 12347.
25 D. J. Modulevsky, C. Lefebvre, K. Haase, Z. Al-Rekabi and A. E. Pelling, *PLoS One*, 2014, **9**, e97835.
26 D. J. Modulevsky, C. M. Cuerrier and A. E. Pelling, *PLoS One*, 2016, **11**, e0157894.
27 G. Fontana, J. Gershlak, M. Adamski, J. S. Lee, S. Matsumoto, H. D. Le, B. Binder, J. Wirth, G. Gaudette and W. L. Murphy, *Adv. Healthc. Mater.*, 2017, **6**, 1601225.
28 J. R. Gershlak, S. Hernandez, G. Fontana, L. R. Perreault, K. J. Hansen, S. A. Larson, B. Y. K. Binder, D. M. Dolivo, T. Yang and T. Dominko, *Biomaterials*, 2017, **125**, 13–22.
29 R. J. Hickey, D. J. Modulevsky, C. M. Cuerrier and A. E. Pelling, *ACS Biomater. Sci. Eng.*, 2018, **4**, 3726–3736.
30 E. R. Robbins, G. D. Pins, M. A. Laflamme and G. R. Gaudette, *J. Biomed. Mater. Res., Part A*, 2020, **108**, 2123–2132.
31 S. J. Allan, M. J. Ellis and P. A. De Bank, *J. Biomed. Mater. Res., Part A*, 2021, **109**, 2471–2482.
32 S. Campuzano, N. B. Mogilever and A. E. Pelling, BioRxiv, 2020, 2020–2002.
33 A. Salehi, M. A. Mobarhan, J. Mohammadi, H. Shahsavarani, M. A. Shokrgozar and A. Alipour, *Gene*, 2020, **757**, 144852.
34 R. J. Hickey, M. L. Latour, J. L. Harden and A. E. Pelling, bioRxiv, 2020.
35 Y. W. Cheng, D. J. Shiwarski, R. L. Ball, K. A. Whitehead and A. W. Feinberg, *ACS Biomater. Sci. Eng.*, 2020, **6**, 3046–3054.
36 N. Contessi Negrini, N. Toffoletto, S. Farè and L. Altomare, *Front. Bioeng. Biotechnol.*, 2020, **8**, 723.
37 J. Lacombe, A. F. Harris, R. Zenhausern, S. Karsunsky and F. Zenhausern, *Front. Bioeng. Biotechnol.*, 2020, **8**, 932.
38 M. L. Latour, M. Tarar, R. J. Hickey, C. M. Cuerrier, I. Catelas and A. E. Pelling, BiorXiv, 2020, 2020–2001.
39 Y. Wang, T. Dominko and P. J. Weathers, *In Vitro Cell. Dev. Biol.: Plant*, 2020, **56**, 765–774.
40 H. Bai, B. Xie, Z. Wang, M. Li, P. Sun, S. Wei, W. Wang, H. Wu, L. Bai and J. Li, *ACS Omega*, 2021, **6**, 11595–11601.
41 K. Jansen, M. Evangelopoulou, C. Pou Casellas, S. Abrishamcar, J. Jansen, T. Vermonden and R. Masereeuw, *AAPS J.*, 2021, **23**, 1–7.
42 J. Wang, X. Qin, B. Kong and H. Ren, *Smart Med.*, 2022, **1**, e20220002.
43 Y. Li, Y. Fu, H. Zhang, X. Wang, T. Chen, Y. Wu, X. Xu, S. Yang, P. Ji and J. Song, *Adv. Healthcare Mater.*, 2022, **11**, 2102807.
44 R. Guruswamy Damodaran and P. Vermette, *Biotechnol. Prog.*, 2018, **34**, 1494–1505.
45 D. J. Modulevsky, C. M. Cuerrier, M. Leblanc-Latour, R. J. Hickey, R.-J. K. Obhi, I. Shore, A. Galuta, K. L. A. Walker, E. C. Tsai and A. E. Pelling, BioRxiv, 2020, 2020–2010.
46 L. J. White, A. J. Taylor, D. M. Faulk, T. J. Keane, L. T. Saldin, J. E. Reing, I. T. Swinehart, N. J. Turner, B. D. Ratner and S. F. Badylak, *Acta Biomater.*, 2017, **50**, 207–219.
47 P. M. Crapo, T. W. Gilbert and S. F. Badylak, *Biomaterials*, 2011, **32**, 3233–3243.
48 A. Salehi, M. A. Mobarhan, J. Mohammadi, H. Shahsavarani, M. A. Shokrgozar and A. Alipour, *J. Cell. Physiol.*, 2021, **236**, 5306–5316.
49 N. Bar-Shai, O. Sharabani-Yosef, M. Zollmann, A. Lesman and A. Golberg, *Sci. Rep.*, 2021, **11**, 11843.
50 V. S. Periasamy, J. Athinarayanan and A. A. Alshatwi, *Sustainable Chem. Pharm.*, 2020, **18**, 100321.
51 K. Varhama, H. Oda, A. Shima and S. Takeuchi, in *2019 IEEE 32nd International Conference on Micro Electro Mechanical Systems (MEMS)*, 2019.
52 M. Adamski, G. Fontana, J. R. Gershlak, G. R. Gaudette, H. D. Le and W. L. Murphy, *J. Visualized Exp.*, 2018, e57586.
53 K. Driscoll, M. S. Butani, K. A. Gultian, A. McSweeny, J. M. Patel and S. L. Vega, *Cell. Mol. Bioeng.*, 2022, **15**, 439–450.
54 Y. Zhu, Q. Zhang, S. Wang, J. Zhang, S. Fan and X. Lin, *Front. Bioeng. Biotechnol.*, 2021, **9**, 712262.
55 S. H. Aswathy, C. C. Mohan, P. S. Unnikrishnan, A. G. Krishnan and M. B. Nair, *Mater. Sci. Eng., C*, 2021, **119**, 111500.

56 N. V. Phan, T. Wright, M. M. Rahman, J. Xu and J. M. Coburn, *ACS Biomater. Sci. Eng.*, 2020, **6**, 822–832.
57 A. F. Harris, J. Lacombe, S. Liyanage, M. Y. Han, E. Wallace, S. Karsunky, N. Abidi and F. Zenhausern, *Sci. Rep.*, 2021, **11**, 3643.
58 B. Mahendiran, S. Muthusamy, G. Janani, B. B. Mandal, S. Rajendran and G. S. Krishnakumar, *ACS Biomater. Sci. Eng.*, 2022, **8**, 2000–2015.
59 B. Mahendiran, S. Muthusamy, R. Selvakumar, N. Rajeswaran, S. Sampath, S. N. Jaisankar and G. S. Krishnakumar, *Carbohydr. Polym.*, 2021, **272**, 118494.
60 J. Lee, H. Jung, N. Park, S.-H. Park and J. H. Ju, *Sci. Rep.*, 2019, **9**, 20194.
61 M. Toker, S. Rostami, M. Kesici, O. Gul, O. Kocaturk, S. Odabas and B. Garipcan, *Cellulose*, 2020, **27**, 7331–7348.
62 C. Liu, P. Luan, Q. Li, Z. Cheng, P. Xiang, D. Liu, Y. Hou, Y. Yang and H. Zhu, *Adv. Mater.*, 2021, **33**, 2001654.
63 A. Kumar, T. Jyske and M. Petrič, *Adv. Sustain. Syst.*, 2021, **5**, 2000251.
64 C. Chen, Y. Wang, Q. Wu, Z. Wan, D. Li and Y. Jin, *Chem. Eng. J.*, 2020, **400**, 125876.
65 P. Niemz, A. Teischinger and D. Sandberg, *Springer Handbook of Wood Science and Technology*, Springer, 2023.
66 T. Keplinger, F. K. Wittel, M. Rüggeberg and I. Burgert, *Adv. Mater.*, 2021, **33**, 2001375.
67 T. Farid, M. I. Rafiq, A. Ali and W. Tang, *EcoMat*, 2022, **4**, e12154.
68 J. Li, C. Chen, J. Y. Zhu, A. J. Ragauskas and L. Hu, *Acc. Mater. Res.*, 2021, **2**, 606–620.
69 S. I. Abd Razak, N. F. A. Sharif, N. H. M. Nayan, I. I. Muhamad and M. Y. Yahya, *BioResources*, 2015, **10**, 4350–4359.
70 R. C. Rajak and R. Banerjee, *RSC Adv.*, 2015, **5**, 75281–75291.
71 J. de Aguiar, T. J. Bondancia, P. I. C. Claro, L. H. C. Mattoso, C. S. Farinas and J. M. Marconcini, *ACS Sustainable Chem. Eng.*, 2020, **8**, 2287–2299.
72 A. J. Aho, J. Rekola, J. Matinlinna, J. Gunn, T. Tirri, P. Viitaniemi and P. Vallittu, *J. Biomed. Mater. Res., Part B*, 2007, **83**, 64–71.
73 A. Tampieri, S. Sprio, A. Ruffini, G. Celotti, I. G. Lesci and N. Roveri, *J. Mater. Chem.*, 2009, **19**, 4973–4980.
74 Z. Fang, H. Zhang, S. Qiu, Y. Kuang, J. Zhou, Y. Lan, C. Sun, G. Li, S. Gong and Z. Ma, *Adv. Mater. Technol.*, 2021, **6**, 2000928.
75 W. Schutyser, a. T. Renders, S. Van den Bosch, S. F. Koelewijn, G. T. Beckham and B. F. Sels, *Chem. Soc. Rev.*, 2018, **47**, 852–908.
76 S. B. Jamaldheen, M. B. Kurade, B. Basak, C. G. Yoo, K. K. Oh, B.-H. Jeon and T. H. Kim, *Bioresour. Technol.*, 2022, **346**, 126591.
77 Q. Fu, F. Ansari, Q. Zhou and L. A. Berglund, *ACS Nano*, 2018, **12**, 2222–2230.
78 Y. Li, Q. Fu, S. Yu, M. Yan and L. Berglund, *Biomacromolecules*, 2016, **17**, 1358–1364.
79 C. S. Junior, A. M. F. Milagres, A. Ferraz and W. Carvalho, *Cellulose*, 2013, **20**, 3165–3177.
80 L. A. Berglund and I. Burgert, *Adv. Mater.*, 2018, **30**, 1704285.
81 R. Ajdary, B. L. Tardy, B. D. Mattos, L. Bai and O. J. Rojas, *Adv. Mater.*, 2021, **33**, 2001085.
82 P. Grönquist, M. Frey, T. Keplinger and I. Burgert, *ACS Omega*, 2019, **4**, 12425–12431.
83 B. D. James, W. N. Ruddick, S. E. Vasisth, K. Dulany, S. Sulekar, A. Porras, A. Marañon, J. C. Nino and J. B. Allen, *Mater. Sci. Eng., C*, 2020, **108**, 110484.
84 C. Sriwong, S. Boonrungsiman and P. Sukyai, *Ind. Crops Prod.*, 2023, **192**, 115979.
85 Y. Li, Q. Fu, R. Rojas, M. Yan, M. Lawoko and L. Berglund, *ChemSusChem*, 2017, **10**, 3445–3451.
86 Q. Xia, C. Chen, Y. Yao, S. He, X. Wang, J. Li, J. Gao, W. Gan, B. Jiang and M. Cui, *Adv. Mater.*, 2021, **33**, 2001588.
87 R. Parthasarathi, R. A. Romero, A. Redondo and S. Gnanakaran, *J. Phys. Chem. Lett.*, 2011, **2**, 2660–2666.
88 D. Moon, S.-J. Shin, J. W. Choi, J.-S. Park, W. Kim and M. Kwon, *For. sci. Technol.*, 2011, **7**, 53–59.
89 M. Scott, P. J. Deuss, J. G. de Vries, M. H. G. Prechtl and K. Barta, *Catal. Sci. Technol.*, 2016, **6**, 1882–1891.
90 B. Esteves, *BioResources*, 2009, 370–404.
91 M. Brebu and C. Vasile, *Cellul. Chem. Technol.*, 2010, **44**, 353.
92 S. Laurichesse and L. Avérous, *Prog. Polym. Sci.*, 2014, **39**, 1266–1290.
93 J.-J. Weiland and R. Guyonnet, *Holz Roh- Werkst.*, 2003, **61**, 216–220.
94 B. Esteves, J. Graca and H. Pereira, *Holzforschung*, 2008, **62**, 344–351.
95 H. Sivonen, S. L. Maunu, F. Sundholm, S. Jämsä and P. Viitaniemi, *Holzforschung*, 2002, 56.
96 M. J. Boonstra and B. Tjeerdsma, *Holz Roh- Werkst.*, 2006, **64**, 204–211.
97 H. Wikberg and S. L. Maunu, *Carbohydr. Polym.*, 2004, **58**, 461–466.
98 C. Hill, M. Altgen and L. Rautkari, *J. Mater. Sci.*, 2021, **56**, 6581–6614.
99 C. Hill, M. Altgen and L. Rautkari, *J. Mater. Sci.*, 2021, **56**, 6581–6614.
100 M. T. R. Bhuiyan, N. Hirai and N. Sobue, *J. Wood Sci.*, 2000, **46**, 431–436.
101 J.-M. Ha, K.-R. Hwang, Y.-M. Kim, J. Jae, K. H. Kim, H. W. Lee, J.-Y. Kim and Y.-K. Park, *Renewable Sustainable Energy Rev.*, 2019, **111**, 422–441.
102 J. Zakzeski, P. C. A. Bruijnincx, A. L. Jongerius and B. M. Weckhuysen, *Chem. Rev.*, 2010, **110**, 3552–3599.
103 G. Filardo, E. Kon, A. Tampieri, R. Cabezas-Rodríguez, A. Di Martino, M. Fini, G. Giavaresi, M. Lelli, J. Martínez-Fernández, L. Martini, J. Ramírez-Rico, F. Salamanna,

M. Sandri, S. Sprio and M. Marcacci, *Tissue Eng., Part A*, 2014, **20**, 763–773.
104 Y. Zheng, J. Zhao, F. Xu and Y. Li, *Prog. Energy Combust. Sci.*, 2014, **42**, 35–53.
105 B. Jos, S. Sumardino and S. Nurfaizin.
106 A. Tribot, G. Amer, M. A. Alio, H. de Baynast, C. Delattre, A. Pons, J.-D. Mathias, J.-M. Callois, C. Vial and P. Michaud, *Eur. Polym. J.*, 2019, **112**, 228–240.
107 J. Rekola, PhD Thesis, *Thesis for the degree of Dentist*, University of Turku, Turku, Finland, 2011.
108 G. Henriksson and T. Teeri, *Wood chemistry and biotechnology*, 2009, p. 273.
109 R. A. Blanchette, L. Otjen, M. J. Effland and W. E. Eslyn, *Wood Sci. Technol.*, 1985, **19**, 35–46.
110 J. Sun, H. Guo, G. N. Schädli, K. Tu, S. Schär, F. W. M. R. Schwarze, G. Panzarasa, J. Ribera and I. Burgert, *Sci. Adv.*, 2021, **7**, eabd9138.
111 R. Zhang, C. Li, J. Wang and Y. Yan, *Biochemistry*, 2018, **58**, 1501–1510.
112 C. Chio, M. Sain and W. Qin, *Renewable Sustainable Energy Rev.*, 2019, **107**, 232–249.
113 M. Andlar, T. Rezić, N. Marđjetko, D. Kracher, R. Ludwig and B. Šantek, *Eng. Life Sci.*, 2018, **18**, 768–778.
114 H. Zhu, W. Luo, P. N. Ciesielski, Z. Fang, J. Y. Zhu, G. Henriksson, M. E. Himmel and L. Hu, *Chem. Rev.*, 2016, **116**, 9305–9374.
115 E. Bränvall, *BioResources*, 2017, **12**, 2081–2107.
116 W. Zhang, B. Wang, J. Sun, Y. Li, J. Zhao, Y. Liu and H. Guo, *Adv. Mater. Interfaces*, 2022, **9**, 2101727.
117 C. Chen, J. Song, S. Zhu, Y. Li, Y. Kuang, J. Wan, D. Kirsch, L. Xu, Y. Wang and T. Gao, *Chem*, 2018, **4**, 544–554.
118 K. Li, S. Wang, S. Koskela and Q. Zhou, *Adv. Mater. Interfaces*, 2021, **8**, 2100787.
119 S. Xiao, C. Chen, Q. Xia, Y. Liu, Y. Yao, Q. Chen, M. Hartsfield, A. Brozena, K. Tu and S. J. Eichhorn, *Science*, 2021, **374**, 465–471.
120 R. Ma, Y. Xu and X. Zhang, *ChemSusChem*, 2015, **8**, 24–51.
121 L. A. Beeman and J. S. Reichert, *Peroxides in pulp bleaching processes*, EI du Pont de Nemours & Company, 1951.
122 H. Yano, A. Hirose, P. J. Collins and Y. Yazaki, *J. Mater. Sci. Lett.*, 2001, **20**, 1125–1126.
123 J. Song, C. Chen, Z. Yang, Y. Kuang, T. Li, Y. Li, H. Huang, I. Kierzewski, B. Liu and S. He, *ACS Nano*, 2018, **12**, 140–147.
124 H. Sun, H. Bi, X. Lin, L. Cai and M. Xu, *Polymers*, 2020, **12**, 165.
125 N. Muhammad, Z. Man and M. A. Bustam Khalil, *Eur. J. Wood Wood Prod.*, 2012, **70**, 125.
126 R. P. Swatloski, S. K. Spear, J. D. Holbrey and R. D. Rogers, *J. Am. Chem. Soc.*, 2002, **124**, 4974–4975.
127 A. Pinkert, K. N. Marsh, S. Pang and M. P. Staiger, *Chem. Rev.*, 2009, **109**, 6712–6728.
128 C. Froschauer, M. Hummel, M. Iakovlev, A. Roselli, H. Schottenberger and H. Sixta, *Biomacromolecules*, 2013, **14**, 1741–1750.
129 A. Roselli, S. Asikainen, A. Stepan, A. Monshizadeh, N. Von Weymarn, K. Kovasin, Y. Wang, H. Xiong, O. Turunen and M. Hummel, *Holzforschung*, 2016, **70**, 291–296.
130 N. Sun, M. Rahman, Y. Qin, M. L. Maxim, H. Rodríguez and R. D. Rogers, *Green Chem.*, 2009, **11**, 646–655.
131 E. L. Smith, A. P. Abbott and K. S. Ryder, *Chem. Rev.*, 2014, **114**, 11060–11082.
132 Z. Bi, T. Li, H. Su, Y. Ni and L. Yan, *ACS Sustainable Chem. Eng.*, 2018, **6**, 9314–9323.
133 Z. Chen, B. Dang, X. Luo, W. Li, J. Li, H. Yu, S. Liu and S. Li, *ACS Appl. Mater. Interfaces*, 2019, **11**, 26032–26037.
134 Y. Wu, L. Yang, J. Zhou, F. Yang, Q. Huang and Y. Cai, *ACS Omega*, 2020, **5**, 22163–22170.
135 Q. Xia, Y. Liu, J. Meng, W. Cheng, W. Chen, S. Liu, Y. Liu, J. Li and H. Yu, *Green Chem.*, 2018, **20**, 2711–2721.
136 C. Fang, M. H. Thomsen, C. G. Frankær, G. P. Brudecki, J. E. Schmidt and I. M. AlNashef, *Ind. Eng. Chem. Res.*, 2017, **56**, 3167–3174.
137 A. Procentese, E. Johnson, V. Orr, A. G. Campanile, J. A. Wood, A. Marzocchella and L. Rehmann, *Bioresour. Technol.*, 2015, **192**, 31–36.
138 Y. Liu, W. Chen, Q. Xia, B. Guo, Q. Wang, S. Liu, Y. Liu, J. Li and H. Yu, *ChemSusChem*, 2017, **10**, 1692–1700.
139 D. Tarasov, M. Leitch and P. Fatehi, *Biotechnol. Biofuels*, 2018, **11**, 1–28.
140 K. Tu, B. Puértolas, M. Adobes-Vidal, Y. Wang, J. Sun, J. Traber, I. Burgert, J. Pérez-Ramírez and T. Keplinger, *Adv. Sci.*, 2020, **7**, 1902897.
141 A. Wagih, M. Hasani, S. A. Hall and H. Theliander, *Holzforschung*, 2021, **75**, 754–764.
142 H. Lu, R. Hu, A. Ward, T. E. Amidon, B. Liang and S. Liu, *Biomass Bioenergy*, 2012, **39**, 5–13.
143 J. Song, C. Chen, S. Zhu, M. Zhu, J. Dai, U. Ray, Y. Li, Y. Kuang, Y. Li and N. Quispe, *Nature*, 2018, **554**, 224–228.
144 C. Wan, Y. Jiao, W. Tian, L. Zhang, Y. Wu, J. Li and X. Li, *Chem. Eng. J.*, 2020, **393**, 124637.
145 B. Xie, L. Zhang, C. Lou, S. Wei, J. a. Li, H. Bai and A. Dardik, *Front. Bioeng. Biotechnol.*, 2022, **10**, 933505.
146 J. Liu, P. Yu, D. Wang, Z. Chen, Q. Cui, B. Hu, D. Zhang, Y. Li, H. Chu and J. Li, *ACS Appl. Mater. Interfaces*, 2020, **12**, 17957–17966.
147 J. Garemark, X. Yang, X. Sheng, O. Cheung, L. Sun, L. A. Berglund and Y. Li, *ACS Nano*, 2020, **14**, 7111–7120.
148 S. Wang, K. Li and Q. Zhou, *Sci. Rep.*, 2020, **10**, 17842.
149 Z. Hu, J. Lu, A. Hu, Y. Dou, S. Wang, D. Su, W. Ding, R. Lian, S. Lu and L. Xiao, *Chem. Eng. J.*, 2022, **446**, 137269.
150 A. N. S. Rao, G. B. Nagarajappa, S. Nair, A. M. Chathoth and K. K. Pandey, *Compos. Sci. Technol.*, 2019, **182**, 107719.
151 V. De Micco and G. Aronne, *Biotech. Histochem.*, 2007, **82**, 209–216.
152 W. Kong, C. Wang, C. Jia, Y. Kuang, G. Pastel, C. Chen, G. Chen, S. He, H. Huang, J. Zhang, S. Wang and L. Hu, *Adv. Mater.*, 2018, **30**, 1801934.

153 S. Jiawei, B. Xuemeng, Z. Yahui, C. Jianfei and X. Yinghong, *Compos. Interfaces*, 2023, **30**, 323–340.
154 H. Wang, C. Chen, L. Fang, S. Li, N. Chen, J. Pang and D. Li, *Cellulose*, 2018, **25**, 7003–7015.
155 H. Yang, Y. Wang, Q. Yu, G. Cao, R. Yang, J. Ke, X. Di, F. Liu, W. Zhang and C. Wang, *Appl. Energy*, 2018, **212**, 455–464.
156 H. Nishimura, A. Kamiya, T. Nagata, M. Katahira and T. Watanabe, *Sci. Rep.*, 2018, **8**, 6538.
157 J. S. Segmehl, V. Studer, T. Keplinger and I. Burgert, *Materials*, 2018, **11**, 517.
158 X. Wang, J. Fang, W. Zhu, C. Zhong, D. Ye, M. Zhu, X. Lu, Y. Zhao and F. Ren, *Adv. Funct. Mater.*, 2021, **31**, 2010068.
159 J. Chen, X. He, T. Sun, K. Liu, C. Chen, W. Wen, S. Ding, M. Liu, C. Zhou and B. Luo, *Adv. Healthcare Mater.*, 2023, **12**, 2300122.
160 Z. Liu, Z. Zhang and R. O. Ritchie, *Adv. Funct. Mater.*, 2020, **30**, 1908121.
161 G. C. Reilly and A. J. Engler, *J. Biomech.*, 2010, **43**, 55–62.
162 C. S. Ranucci, A. Kumar, S. P. Batra and P. V. Moghe, *Biomaterials*, 2000, **21**, 783–793.
163 X. Wang, T. Lou, W. Zhao, G. Song, C. Li and G. Cui, *J. Biomater. Appl.*, 2016, **30**, 1545–1551.
164 I. Varivodina, N. Kosichenko, V. Varivodin and J. Sedliačik, *Wood Res.*, 2010, **55**, 59–66.
165 T. Li, J. Song, X. Zhao, Z. Yang, G. Pastel, S. Xu, C. Jia, J. Dai, C. Chen, A. Gong, F. Jiang, Y. Yao, T. Fan, B. Yang, L. Wågberg, R. Yang and L. Hu, *Sci. Adv.*, 2018, **4**, eaar3724.
166 J. Liu, D. Wang, Y. Li, Z. Zhou, D. Zhang, J. Li and H. Chu, *ACS Appl. Mater. Interfaces*, 2021, **13**, 15709–15719.
167 A. Ahangar Salehani, M. Rabbani, E. Biazar, S. Heidari Keshel and B. Pourjabbar, *Eng. Rep.*, 2023, **5**, e12560.
168 P. Datta, V. Vyas, S. Dhara, A. R. Chowdhury and A. Barui, *J. Bionic Eng.*, 2019, **16**, 842–868.
169 S. Jana, S. K. L. Levengood and M. Zhang, *Adv. Mater.*, 2016, **28**, 10588–10612.
170 N. Khuu, S. Kheiri and E. Kumacheva, *Trends Chem.*, 2021, **3**, 1002–1026.
171 H.-I. Chang and Y. Wang, in *Regenerative medicine and tissue engineering-cells and biomaterials*, InTechOpen, 2011.
172 G. Chauhan, A. Lujambio Ángeles, E. Gonzalez-González, M. M. Kulkarni, G. Trujillo-de Santiago, M. M. Alvarez, M. Madou and S. O. Martinez-Chapa, *Ad. Mater. Interfaces*, 2020, **7**, 2000913.
173 S. J. P. Callens, R. J. C. Uyttendaele, L. E. Fratila-Apachitei and A. A. Zadpoor, *Biomaterials*, 2020, **232**, 119739.
174 G. R. Mitchell and A. Tojeira, *Procedia Eng.*, 2013, **59**, 117–125.
175 J. Xing, N. Liu, N. Xu, W. Chen and D. Xing, *Adv. Funct. Mater.*, 2022, **32**, 2110676.
176 J. J. Norman and T. A. Desai, *Ann. Biomed. Eng.*, 2006, **34**, 89–101.
177 C. J. Bettinger, R. Langer and J. T. Borenstein, *Angew. Chem., Int. Ed.*, 2009, **48**, 5406–5415.
178 M. Ermis, E. Antmen and V. Hasirci, *Bioact. Mater.*, 2018, **3**, 355–369.
179 Y. Qi, Z. Cheng, Z. Ye, H. Zhu and C. Aparicio, *ACS Appl. Mater. Interfaces*, 2019, **11**, 27598–27604.
180 Z. Tang, W. Li, X. Lin, H. Xiao, Q. Miao, L. Huang, L. Chen and H. Wu, *Polymers*, 2017, **9**, 421.
181 K. Li, S. Wang, H. Chen, X. Yang, L. A. Berglund and Q. Zhou, *Adv. Mater.*, 2020, **32**, 2003653.
182 A. Khademhosseini and R. Langer, *Nat. Protoc.*, 2016, **11**, 1775–1781.
183 N. Almouemen, H. M. Kelly and and C. O'Leary, *Comput. Struct. Biotechnol. J.*, 2019, **17**, 591–598.
184 H. Campo, X. Santamaria, I. Cervelló and C. Simón, in *Handbook of Tissue Engineering Scaffolds: Volume Two*, ed. M. Mozafari, F. Sefat and A. Atala, Woodhead Publishing, 2019, pp. 283–316.
185 E. J. Lee, F. K. Kasper and A. G. Mikos, *Ann. Biomed. Eng.*, 2014, **42**, 323–337.
186 W. R. Frontera and J. Ochala, *Calcif. Tissue Int.*, 2015, **96**, 183–195.
187 Y. Feng, R. J. Okamoto, R. Namani, G. M. Genin and P. V. Bayly, *J. Mech. Behav. Biomed. Mater.*, 2013, **23**, 117–132.
188 L. G. Griffith and M. A. Swartz, *Nat. Rev. Mol. Cell Biol.*, 2006, **7**, 211–224.
189 P. Szczepańczyk, M. Szlachta, N. Złocista-Szewczyk, J. Chłopek and K. Pielichowska, *Polymers*, 2021, **13**, 946.
190 E. Stratakis, *Int. J. Mol. Sci.*, 2018, **19**, 3960.
191 R. Derda, A. Laromaine, A. Mammoto, S. K. Tang, T. Mammoto, D. E. Ingber and G. M. Whitesides, *Proc. Natl. Acad. Sci. U. S. A.*, 2009, **106**, 18457–18462.
192 K. M. Yamada and E. Cukierman, *Cell*, 2007, **130**, 601–610.
193 A.-V. Do, B. Khorsand, S. M. Geary and A. K. Salem, *Adv. Healthcare Mater.*, 2015, **4**, 1742–1762.
194 J. Lannutti, D. Reneker, T. Ma, D. Tomasko and D. Farson, *Mater. Sci. Eng., C*, 2007, **27**, 504–509.
195 H.-Y. Mi, M. R. Salick, X. Jing, B. R. Jacques, W. C. Crone, X.-F. Peng and L.-S. Turng, *Mater. Sci. Eng., C*, 2013, **33**, 4767–4776.
196 L. Wu, H. Zhang, J. Zhang and J. Ding, *Tissue Eng.*, 2005, **11**, 1105–1114.
197 K. J. Hansen, M. A. Laflamme and G. R. Gaudette, *Front. Cardiovasc. Med.*, 2018, **5**, 52.
198 V. Chaturvedi, D. E. Dye, B. F. Kinnear, T. H. van Kuppevelt, M. D. Grounds and D. R. Coombe, *PLoS One*, 2015, **10**, e0127675.
199 D. Narayanan, S. G. Bhat and G. Baranwal, *Appl. Biol. Chem. J.*, 2021, **2**, 76–88.
200 M. M. Stevens and J. H. George, *Science*, 2005, **310**, 1135–1138.
201 A. F. Harris, J. Lacombe, N. M. Sanchez-Ballester, S. Victor, K. A. J. Curran, A. R. Nordquist, B. Thomas, J. Gu, J.-L. Veuthey, I. Soulairol and F. Zenhausern, *ACS Appl. Bio Mater.*, 2022, **5**, 5682–5692.
202 A. R. Amini, C. T. Laurencin and S. P. Nukavarapu, *Crit. Rev. Biomed. Eng.*, 2012, **40**, 363–408.

203 A. G. Abdelaziz, H. Nageh, S. M. Abdo, M. S. Abdalla, A. A. Amer, A. Abdal-hay and A. Barhoum, *Bioengineering*, 2023, **10**, 204.
204 M. Leblanc Latour and A. E. Pelling, *J. Biomech.*, 2022, **135**, 111030.
205 L. Maxime Leblanc, T. Maryam, J. H. Ryan, M. C. Charles, C. Isabelle and E. P. Andrew, bioRxiv, 2021, DOI: **10.1101/2021.07.07.451476**.
206 S. Saravanan, R. S. Leena and N. Selvamurugan, *Int. J. Biol. Macromol.*, 2016, **93**, 1354–1365.
207 D. J. Hadjidakis and I. I. Androulakis, *Ann. N. Y. Acad. Sci.*, 2006, **1092**, 385–396.
208 A. Anil and V. Ali Serdar, in *Wood in Civil Engineering*, ed. C. Giovanna, IntechOpen, Rijeka, 2017, ch. 8.
209 S. Zhao, J. X. Zhao and G. Z. Han, *IOP Conf. Ser.: Mater. Sci. Eng.*, 2016, **137**, 012036.
210 V. Nefjodovs, L. Andze, M. Andzs, I. Filipova, R. Tupciauskas, L. Vecbiskena and M. Kapickis, *J. Funct. Biomater.*, 2023, **14**, 266.
211 Z. C. Lum, S. Dennison, H. V. Le, C. O. Bayne and C. A. Lee, *J. Am. Acad. Orthop. Surg. Glob. Res. Rev.*, 2024, **8**, e24.00038.
212 J. Rekola, L. V. Lassila, S. Nganga, A. Ylä-Soininmäki, G. J. Fleming, R. Grenman, A. J. Aho and P. K. Vallittu, *Bio-Med. Mater. Eng.*, 2014, **24**, 1595–1607.
213 S. Hansson, *J. Biomech.*, 2000, **33**, 1297–1303.
214 S. Hansson and M. Norton, *J. Biomech.*, 1999, **32**, 829–836.
215 S. M. Koch, C. Goldhahn, F. J. Müller, W. Yan, C. Pilz-Allen, C. M. Bidan, B. Ciabattoni, L. Stricker, P. Fratzl, T. Keplinger and I. Burgert, *Mater. Today Bio*, 2023, **22**, 100772.
216 J. Chen, J. Chen, Z. Zhu, T. Sun, M. Liu, L. Lu, C. Zhou and B. Luo, *ACS Appl. Mater. Interfaces*, 2022, **14**, 50485–50498.
217 R. K. Jain, P. Au, J. Tam, D. G. Duda and D. Fukumura, *Nat. Biotechnol.*, 2005, **23**, 821–823.
218 S. E. Lee and Y. S. Park, *Mol. Cell. Toxicol.*, 2017, **13**, 257–261.
219 T. Miretta, J. Anne, P. Risto and E. Erika, in *Cellulose*, ed. V. Theo van de and G. Louis, IntechOpen, Rijeka, 2013, ch. 5.
220 Q. Cui, Y. Zheng, Q. Lin, W. Song, K. Qiao and L. Shumin, *RSC Adv.*, 0001, **4**, 1630.
221 U. J. Kim, S. Kuga, M. Wada, T. Okano and T. Kondo, *Biomacromolecules*, 2000, **1**, 488–492.
222 W. Konkumnerd, S.-H. Hyon and K. Matsumura, *MRS Online Proc. Libr.*, 2014, **1621**, 191–196.
223 W. Kosuwon, W. Laupattarakasem, S. Saengnipanthkul, B. Mahaisavariya and S. Therapongpakdee, *J. Med. Assoc. Thailand*, 1994, **77**, 496–500.
224 I. Polozov, N. Razumov, D. Masaylo, A. Silin, Y. Lebedeva and A. Popovich, *Materials*, 2020, **13**, 1766.
225 M. Singh and J. Salem, *J. Eur. Ceram. Soc.*, 0012, **22**, 2709–2717.
226 M. Gordic, D. Bucevac, J. Ružić, S. Gavrilovic, R. Hercigonja, M. Stankovic and B. Matovic, *Ceram. Int.*, 0003, **40**, 3699–3705.
227 G. Filardo, A. Roffi, T. Fey, M. Fini, G. Giavaresi, M. Marcacci, J. Martínez-Fernández, L. Martini, J. Ramírez-Rico, F. Salamanna, M. Sandri, S. Sprio, A. Tampieri and E. Kon, *J. Biomed. Mater. Res., Part B*, 2020, **108**, 600–611.
228 S. Guo and L. A. Dipietro, *J. Dent. Res.*, 2010, **89**, 219–229.
229 G. Yang, Z. Huang, A. McCarthy, Y. Huang, J. Pan, S. Chen and W. Wan, *Adv. Sci.*, 2023, **10**, 2207347.
230 X. Yue, S. Zhao, M. Qiu, J. Zhang, G. Zhong, C. Huang, X. Li, C. Zhang and Y. Qu, *Carbohydr. Polym.*, 2023, **312**, 120831.
231 A. Luqman and F. Götz, *Int. J. Mol. Sci.*, 2021, **22**, 4996.
232 L. He, Y. Liu, F. Chen, J. Shi, P. Song, F. Feng, J. Cui, J. Zhang, X. Ma and J. Shen, *React. Funct. Polym.*, 2023, **192**, 105707.
233 L. He, Y. Liu, P. Song, F. Feng, G. Li, Y. Ma, J. Cui, X. Ma, J. Shen and J. Zhang, *ACS Sustainable Chem. Eng.*, 2023, **11**, 11529–11540.
234 X. Li and E. Sundström, *Stem Cells Transl. Med.*, 2022, **11**, 14–25.
235 Y. Tang, P. Yu and L. Cheng, *Cell Death Dis.*, 2017, **8**, e3108.
236 S. D. Subramony, B. R. Dargis, M. Castillo, E. U. Azeloglu, M. S. Tracey, A. Su and H. H. Lu, *Biomaterials*, 2013, **34**, 1942–1953.
237 W. Li, Q. Y. Tang, A. D. Jadhav, A. Narang, W. X. Qian, P. Shi and S. W. Pang, *Sci. Rep.*, 2015, **5**, 8644.
238 L. J. Couvrette, K. L. A. Walker, T. V. Bui and A. E. Pelling, *Bioengineering (Basel)*, 2023, **10**, 1309.
239 L. Nedkoff, T. Briffa, D. Zemedikun, S. Herrington and F. L. Wright, *Clin. Ther.*, 2023, **45**, 1087–1091.
240 S. Walawalkar and S. Almelkar, *J. Biomater. Appl.*, 2021, **36**, 165–178.
241 C. Liu, H. Gao, G. Sun, X. Jiang, S. Song, J. Zhang and J. Shen, *ACS Appl. Bio Mater.*, 2023, **6**, 1071–1080.
242 J. Chlupac, R. Matejka, M. Konarik, R. Novotny, Z. Simunkova, I. Mrazova, O. Fabian, M. Zapletal, Z. Pulda, J. F. Lipensky, J. Stepanovska, K. Hanzalek, A. Broz, T. Novak, A. Lodererova, L. Voska, T. Adla, J. Fronek, M. Rozkot, S. Forostyak, P. Kneppo, L. Bacakova and J. Pirk, *Int. J. Mol. Sci.*, 2022, **23**, 3310.
243 B. Xie, X. Bai, P. Sun, L. Zhang, S. Wei and H. Bai, *Front. Bioeng. Biotechnol.*, 2021, **9**, 742285.
244 H. C. Ott, T. S. Matthiesen, S.-K. Goh, L. D. Black, S. M. Kren, T. I. Netoff and D. A. Taylor, *Nat. Med.*, 2008, **14**, 213–221.
245 T. Yingchoncharoen, S. Agarwal, Z. B. Popović and T. H. Marwick, *J. Am. Soc. Echocardiogr.*, 2013, **26**, 185–191.
246 J. M. Grasman, M. J. Zayas, R. L. Page and G. D. Pins, *Acta Biomater.*, 2015, **25**, 2–15.
247 G. Wang, P. Chen, Y. Wang, Y. Wang, P. S. Reinach, Y. Xue, Z. Liu and C. Li, *Adv. Healthc. Mater.*, 2020, **9**, e2000469.
248 R. B. Zamudio-Ceja, R. Garcia-Contreras, P. A. Chavez-Granados, B. Aranda-Herrera, H. Alvarado-Garnica, C. A. Jurado and N. G. Fischer, *J. Funct. Biomater.*, 2023, **14**, 252.

249 L. C. Clark Jr and C. Lyons, *Ann. N. Y. Acad. Sci.*, 1962, **102**, 29–45.
250 D. G. Rackus, M. H. Shamsi and A. R. Wheeler, *Chem. Soc. Rev.*, 2015, **44**, 5320–5340.
251 S. Bag and D. Mandal, in *Next Generation Smart Nano-Bio-Devices*, ed. G. Dutta and A. Biswas, Springer Nature Singapore, Singapore, 2023, pp. 29–60.
252 A. V. Kabashin, V. G. Kravets and A. N. Grigorenko, *Chem. Soc. Rev.*, 2023, **52**, 6554–6585.
253 Personal communication.
254 G. A. Rechnitz, *Science*, 1981, **214**, 287–291.
255 T. Naghdi, S. Faham, T. Mahmoudi, N. Pourreza, R. Ghavami and H. Golmohammadi, *ACS Sens.*, 2020, **5**, 3770–3805.
256 Y. E. Li and I. C. Lee, *Biosensors*, 2020, **10**, 88.
257 N. Verma, A. K. Singh and M. Singh, *Biochem. Biophys. Rep.*, 2017, **12**, 228–239.
258 J. S. Sidwell and G. A. Rechnitz, *Biotechnol. Lett.*, 1985, **7**, 419–422.
259 J. Wang and M. S. Lin, *Anal. Chem.*, 1988, **60**, 1545–1548.
260 B. R. Eggins, C. Hickey, S. A. Toft and D. M. Zhou, *Anal. Chim. Acta*, 1997, **347**, 281–288.
261 E. A. Cummings, P. Mailley, S. Linquette-Mailley, B. R. Eggins, E. T. McAdams and S. McFadden, *Analyst*, 1998, **123**, 1975–1980.
262 A. W. O. Lima, V. B. Nascimento, J. J. Pedrotti and L. Angnes, *Anal. Chim. Acta*, 1997, **354**, 325–331.
263 O. Fatibello-Filho, K. O. Lupetti and I. C. Vieira, *Talanta*, 2001, **55**, 685–692.
264 H. M. Ozcan and A. Sagiroglu, *Artif. Cells, Blood Substitutes, Immobilization Biotechnol.*, 2010, **38**, 208–214.
265 F. Mazzei, F. Botrè, G. Lorenti, G. Simonetti, F. Porcelli, G. Scibona and C. Botrè, *Anal. Chim. Acta*, 1995, **316**, 79–82.
266 R. S. Antunes, D. V. Thomaz, L. F. Garcia, E. S. Gil and F. M. Lopes, *Adv. Pharm. Bull.*, 2021, **11**, 469–476.
267 A. Ayna and E. Akyılmaz, *Hacettepe J. Biol. Chem.*, 2018, **46**, 321–328.
268 T. Yifeng, *Anal. Lett.*, 1993, **26**, 1557–1566.
269 H. M. Ozcan and A. Sagiroglu, *Artif. Cells, Blood Substitutes, Biotechnol.*, 2010, **38**, 208–214.
270 J. Wang, N. Naser, H.-S. Kwon and M. Y. Cho, *Anal. Chim. Acta*, 1992, **264**, 7–12.
271 I. R. W. Z. de Oliveira and I. C. Vieira, *Enzyme Microb. Technol.*, 2006, **38**, 449–456.
272 I. R. Z. de Oliveira, S. C. Fernandes and I. C. Vieira, *J. Pharm. Biomed. Anal.*, 2006, **41**, 366–372.
273 S. C. Fernandes, I. R. W. Z. de Oliveira and I. C. Vieira, *Enzyme Microb. Technol.*, 2007, **40**, 661–668.
274 S. Liawruangrath, W. Oungpipat, S. Watanesk, B. Liawruangrath, C. Dongduen and P. Purachat, *Anal. Chim. Acta*, 2001, **448**, 37–46.
275 I. Cruz Vieira and O. Fatibello-Filho, *Talanta*, 2000, **52**, 681–689.
276 J. V. B. Kozan, R. P. Silva, S. H. P. Serrano, A. W. O. Lima and L. Angnes, *Anal. Chim. Acta*, 2007, **591**, 200–207.
277 A. Navaratne and G. A. Rechnitz, *Anal. Chim. Acta*, 1992, **257**, 59–66.
278 M. K. Sezgintürk and E. Dinçkaya, *Talanta*, 2003, **59**, 545–551.
279 M. K. Sezgintürk and E. Dinçkaya, *Biosens. Bioelectron.*, 2004, **19**, 835–841.
280 L. Macholán and B. Chmelíková, *Anal. Chim. Acta*, 1986, **185**, 187–193.
281 M. K. Sezgintürk and E. Dinçkaya, *Talanta*, 2005, **65**, 998–1002.
282 E. Akyilmaz and E. Dinckaya, *Talanta*, 2000, **53**, 505–509.
283 Y. Huang and F. Wu, *Anal. Sci.*, 2006, **22**, 965–969.
284 S. Timur, N. Pazarlıoğlu, R. Pilloton and A. Telefoncu, *Sens. Actuators, B*, 2004, **97**, 132–136.
285 F. Botrè, C. Botrè, G. Lorenti, F. Mazzei, F. Porcelli and G. Scibona, *Sens. Actuators, B*, 1993, **15**, 135–140.
286 Y. Mei, L. Ran, X. Ying, Z. Yuan and S. Xin, *Biosens. Bioelectron.*, 2007, **22**, 871–876.
287 L. Campanella, M. Cordatore, F. Mazzei, M. Tomassetti and G. Volpe, *Food Chem.*, 1992, **44**, 291–297.
288 L. Campanella, M. Cordatore, F. Mazzei and M. Tomassetti, *J. Pharm. Biomed. Anal.*, 1990, **8**, 711–716.
289 W. Qin, Z. Zhang and Y. Peng, *Anal. Chim. Acta*, 2000, **407**, 81–86.
290 H. Horie and G. A. Rechnitz, *Anal. Chim. Acta*, 1995, **306**, 123–127.
291 K. Kumar, M. Kataria and N. Verma, *Artif. Cells, Nanomed., Biotechnol.*, 2013, **41**, 184–188.
292 N. Verma, M. Kataria, K. Kumar and J. Saini, *Ann. Biol. Res.*, 2013, **4**, 265–270.
293 W. Oungpipat and P. W. Alexander, *Anal. Chim. Acta*, 1994, **295**, 37–46.
294 B. Li, Z. Zhang and Y. Jin, *Anal. Chem.*, 2001, **73**, 1203–1206.
295 L. Zhu, Y. Li and G. Zhu, *Sens. Actuators, B*, 2004, **98**, 115–121.
296 B. Li, Z. Zhang and Y. Jin, *Biosens. Bioelectron.*, 2002, **17**, 585–589.
297 A. Khakalo, A. Tanaka, A. Korpela and H. Orelma, *ACS Appl. Mater. Interfaces*, 2020, **12**, 23532–23542.
298 M. Toker-Bayraktar, B. Erenay, B. Altun, S. Odabaş and B. Garipcan, *Cellulose*, 2023, **30**, 2731–2751.
299 Y. Dai, K. Qiao, D. Li, P. Isingizwe, H. Liu, Y. Liu, K. Lim, T. Woodfield, G. Liu, J. Hu, J. Yuan, J. Tang and X. Cui, *Adv. Healthcare Mater.*, 2023, **12**, 2202827.
300 C. C. Ferranti, E. D. Alves, C. S. Lopes, L. H. Montrezor, A. J. F. Carvalho, P. S. Cerri and E. Trovatti, *Biomed. Phys. Eng. Express*, 2023, **9**, 015003.

